# Characterising Graphene Suspensions for Drug Delivery

A thesis submitted to the University of Manchester for the degree of Doctor of Philosophy in the Faculty of Biology, Medicine and Health

2020

**Fai A. Alkathiri**

School of Health Sciences

# Contents

## Figures

## TABLES

## ABBREVIATIONS

| | |
|---|---|
| **AFM** | Atomic force microscopy |
| **ANOVA** | Analysis of variance |
| **BCNU** | 1,3-Bis (2-chloroethyl)-1-nitrosourea |
| **BPBA** | Biotin-adorned poly-(ethylene oxide) bis-(amine) |
| **BSA** | Bovine serum albumin |
| **CPT** | Camptothecin |
| **EA** | Ellagic acid |
| **EG** | Epitaxial graphene |
| **CHA** | Cholesteryl hyaluronic acid |
| **CNTs** | Carbon nanotubes |
| **DAPI** | 4,6-diamidino-2-phenylindole |
| **DESs** | Deep eutectic solvents |
| **DFT** | Density functional theory |
| **DLS** | Dynamic light scattering |
| **DMF** | N,N-Dimethylformamide |
| **Dox** | Doxorubicin |
| **EDC** | N-(3-Dimethylaminopropyl)-N'- ethylcarbodiimide hydrochloride |
| **EE** | Entrapment efficiency |
| **FA** | Folic acid |
| **FBS** | Foetal bovine serum |

| | |
|---|---|
| **FDA** | Federal drug association |
| **FTIR** | Fourier transform infrared spectroscopy |
| **GBMs** | Graphene-based materials |
| **GO** | Graphene oxide |
| **GRAS** | Generally recognised as safe |
| **HA** | Hypocrellin A |
| **HCl** | Hydrochloric acid |
| **His** | Histidine |
| $\boldsymbol{k_B}$ | Boltzmann's constant |
| **LE** | Loading efficiency |
| **MD** | Molecular dynamics |
| **MDx** | Maltodextrin |
| **MOE** | Molecular Operating Environment |
| **MTS** | 3-(4,5-dimethylthiazol-2-yl)-5-(3-carboxymethoxyphenyl)-2-(4-sulfophenyl)-2H-tetrazolium, inner salt assay |
| **MTT** | Methylthiazolyldiphenyl–tetrazolium bromide assay |
| **NMP** | N-methyl-2-pyrrolidone |
| **PAA** | Polyacrylic acid |
| **PBS** | Phosphate buffered saline |
| **PEG** | Polyethylene glycol |
| **PEI** | Polyethyleneimine |
| **PG** | Pristine graphene |
| **Phe** | Phenylalanine |
| **PLL** | Poly-L-lysine |

| | |
|---|---|
| **pNIPAM** | Poly(N-isopropylacrylamide) |
| **PVP** | Polyvinylpyrrolidone |
| **RBF** | Round bottom flask |
| **rGO** | Reduced graphene oxide |
| $\boldsymbol{R_h}$ | Hydrodynamic radius |
| **RICS** | Raster image correlation spectroscopy |
| **SDBS** | Sodium dodecylbenzenesulfonate |
| **SDS** | Sodium lauryl sulphate |
| **SGNFs** | Stacked graphene nanofibres |
| **THF** | Tetrahydrofuran |
| **Tf** | Transferrin |
| **Trp** | Tryptophan |
| **Trp2** | Tryptophan dipeptides |
| **Trp3** | Tryptophan tripeptides |
| **Tyr** | Tyrosine |
| **UFH** | Unfractionated heparin |
| **UV-Vis** | Ultraviolet-Visible spectroscopy |
| **uwGO** | Unwashed GO |
| **Val** | Valine |
| **VMD** | Visual Molecular Dynamics |
| **wGO** | Washed GO |

## Abstract

In biomedical applications, one of the most attractive properties of graphene-based materials (GBMs) is their 2D geometry, which maximises the high surface-to-volume ratio characteristic of nanomaterials. That particular property, along with their versatile functionalisation, suggests they may be designed as multifunctional therapeutics carriers. Here, two types of GBMs, including either pristine graphene (PG) or graphene oxide (GO), were prepared to form suspensions suitable for drug delivery.

In the first experimental chapter, in search for GRAS excipients to exfoliate PG and stabilise the suspension, three amino acids (valine, tyrosine and tryptophan) were considered both in computer modelling and experimentally. A strong correlation was observed between the amino acid's hydrophobicity and the existence of at least one aromatic ring in the amino acid to enhance the exfoliation efficacy, both in terms of the suspension's concentration s and thinness of the flakes. Together, these results suggested amino acids in particular tryptophan may contribute to the preparation of PG suspensions suitable for drug delivery.

In the following chapter, building upon the aforementioned study, tryptophan (Trp), di-Trp and tri-Trp peptides were used to form and stabilise PG suspensions which were also used as doxorubicin carriers. Computer modelling and experimental studies revealed that peptides with ample residues e.g. tri-Trp could accommodate more PG flakes in suspension than Trp. Furthermore, tri-Trp PG complexes had the highest drug content and were better at inhibiting the growth of MDA-MB-231 breast cancer cells more than Trp PG complexes.

In the final chapter, three preparations of GO, far more thoroughly studied than PG were characterised with traditional methods and, exploiting the intrinsic fluorescence of GO, with

raster image correlation spectroscopy. The results suggests GO's inherent fluorescence can be used to enhance the characterisation of suspensions as fluorescence measurements can be realised in different media e.g. cell media or in presence of excipients.

The research discussed herein demonstrated the complexity of applying GBMs in biomedicine as well as their potential for expansion in medical applications, especially in drug delivery supported. Altogether, this work demonstrates the importance of investigating novel approaches to characterising GBMs and has identified strategies that may be developed to enhance biomedical applications of the materials.

## DECLARATION

I hereby declare that no portion of the work referred to in this thesis has been submitted in support of an application for another degree or qualification of this or any other university or institute of learning.

## COPYRIGHT STATEMENT

# CONTRIBUTIONS TO THESIS CHAPTERS

Primary supervisor Alain Pluen, provided guidance and feedback for the Introduction (Chapter 1), Aims and Objectives (Chapter 2) and General Conclusions (Chapter 6).

**Chapter 3**

Fai Alkathiri, Catriona McCallion, Alain Pluen and Richard Bryce planned the study.

Fai Alkathiri and Catriona McCallion performed the experiments.

Fai Alkathiri analysed the data.

Fai Alkathiri and Catriona McCallion prepared the manuscript, with comments from Alain Pluen, Richard Bryce and Alexander Golovanov.

**Chapter 4**

Fai Alkathiri, Alain Pluen and Richard Bryce planned the study.

Fai Alkathiri performed the experiments with assistance from Chen Zhao.

Fai Alkathiri analysed the data.

Fai Alkathiri and Alain Pluen prepared the manuscript, with comments from Richard Bryce.

**Chapter 5**

Fai Alkathiri and Alain Pluen planned the study.

Fai Alkathiri performed the experiments and completed all the data analysis.

Fai Alkathiri prepared the manuscript with comments from Alain Pluen and Richard Bryce.

## Acknowledgements

I'd first like to thank my supervisors, Dr Alain Pluen, Dr Richard Bryce and Dr Sasha Golovanov for their patience and guidance. I'd also like to thank Dr Annalisa Tirella and Ms. Chen Zhao for their kindness and patience during all their time spent teaching me about cell biology.

To all my friends – both inside science and out – who have been lovely and made Manchester a lovely place to be. My colleagues/friends at the University – Rupesh, Irfan, Solmaz, Ismaeel, Ataul, Linghan, Yang, Lekha, Wia and Aminah – thank you for your support and I wish you all the very best in your journeys. Finally, I'd like to thank my family, who has loved and supported me throughout my education, my parents, my husband Mohammed aljallal, and my daughter Noura, for all love and support throughout my PhD, and for just making my life better.

## RECENT PUBLICATIONS RELEVANT TO THIS STUDY

**Presented in full as chapter 2 in this thesis:**

### [1] Solvation of Pristine Graphene using Amino Acids: a Molecular Simulation and Experimental Analysis

F. A. Alkathiri, C. McCallion, A. P. Golovanov, J. Burthem, A. Pluen, and R. A. Bryce, *The Journal of Physical Chemistry C*, vol. 123, no. 50, pp. 30234-30244, 2019/12/19 2019.

*Research Article*

# 1. A Review on Graphene-Based Materials in Drug Delivery

Fai A. Alkathiri[a], Alexander P. Golovanov[b], Richard A. Bryce[a, *] and Alain Pluen[a *]

[a] *Division of Pharmacy and Optometry, School of Health Sciences, University of Manchester, Manchester, UK*

[b] *Manchester Institute of Biotechnology, and School of Chemistry, Faculty of Science and Engineering, University of Manchester, Manchester, UK*

Corresponding Authors

*Alain Pluen, Division of Pharmacy and Optometry, School of Health Sciences, University of Manchester, Manchester, M13 9PT, U.K. Email: Alain.Pluen@manchester.ac.uk, Tel: (0)161-275-1792

*Richard Bryce, Division of Pharmacy and Optometry, School of Health Sciences, University of Manchester, Manchester, M13 9PT, U.K. Email: Richard.Bryce@manchester.ac.uk, Tel: (0)161-275-8345

## 1.1. Abstract

After being discovered in 2004, graphene has garnered significant attention as a material with potential for drug delivery [1]. With a unique structure and geometry, graphene is a giant polyaromatic molecule that exhibits exceptional physico-chemical properties, including robust mechanical strength, large specific surface areas (appro x. 2600 $m^2/g$) [2] and high thermal and electrical conductivity [3]. Those properties make graphene an ideal material for various applications, including in bioimaging, nanoelectronics, quantum physics, nanocomposite engineering and platforms for transporting different therapeutic agents such as DNA, small drug molecules, proteins, antibodies and genes [4].

In this chapter, the different types of graphene and their applications in drug delivery are introduce. First, briefly describe the physico-chemical properties and structural features of the types, their toxicity and biocompatibility and different approaches to their synthesis, mechanical exfoliation and graphene dispersion. After that, a review of some theoretical experiments that modelled interactions between graphene and amino acids in search of promising approaches to drug delivery. Last, a summary of current advances in biomedical applications of graphene, with a particular focus on drug delivery.

## 1.2. Graphene-based materials (GBMs)

The classification of GBMs depends on their surface chemistry, number of layers, oxygen content and chemical modification. Graphene is a single layer of $sp^2$-hybridised carbon atoms arranged in a 2D, honeycomb-like structure of crystal lattices [3]. As shown in Figure 1.1, graphene is the building block of graphite allotropes, with geometries that include being stacked in graphene layers to form 3D graphite, rolled into 1D carbon nanotubes (CNTs) and wrapped to form spherical, dimensionless structures known as fullerenes. GBMs include pristine graphene (PG), graphene oxide (GO) and reduced GO (rGO) [5].

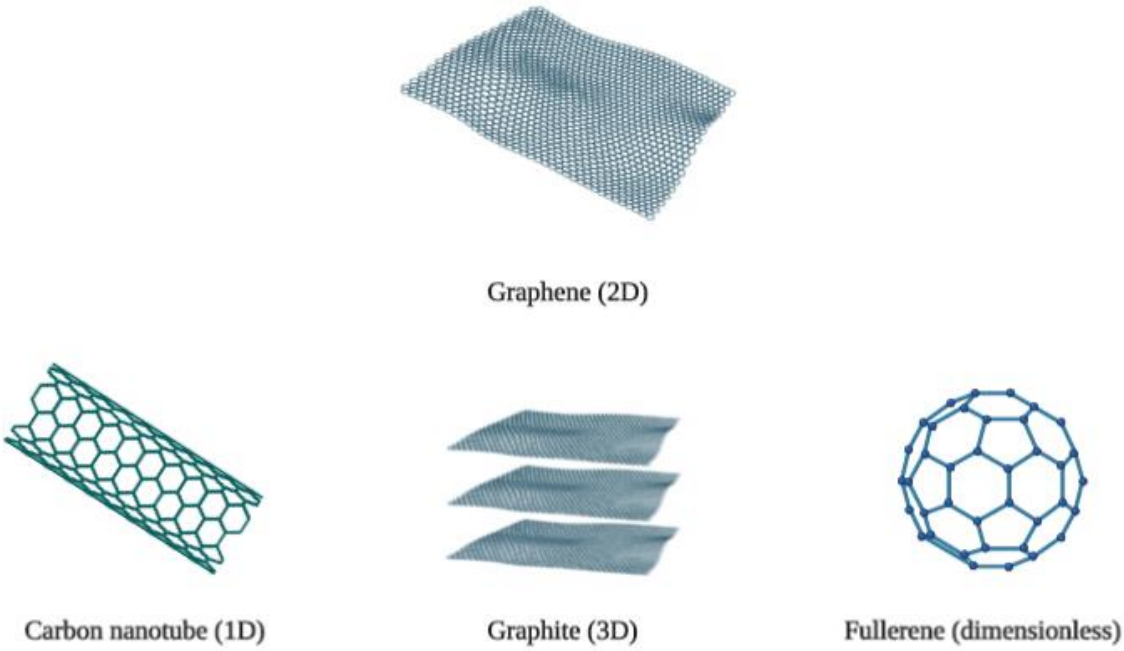


**Figure 1. 1-** Graphene structures and derivatives including, fullerene (0D), CNT (1D), graphene (2D) and graphite (3D) [6].

Regarding the term itself, *graphene* was recommended by the relevant IUPAC commission to replace the older term *graphite layers* that did not accommodate single-layered carbon

structures whose 3D stacking structure is known as graphite. The current definition of *graphene* is thus a 2D monolayer of carbon atoms that acts as the basic building block of graphitic materials, including as fullerenes, CNTs and graphite[7].

Graphene can be synthesised by using bottom–up synthetic methods such as chemical vapour deposition and epitaxial growth from silicon carbide, SiC, as shown in Table 1.1 [8]. Despite having not been used in commercial applications, those approaches can be used to produce high-quality PG for basic studies on transport physics [9, 10]. The most common approach for the large-scale manufacture of graphene and GO is Hummers et al.'s top–down method entailing the physical, mechanical and chemical exfoliation of graphite with strong acids and oxidants, including sodium nitrate, sulphuric acid and potassium permanganate oxidants [11, 12]. Those methods involve extensively oxidising the aromatic structure to weaken the van der Waals interactions that connect graphene sheets before exfoliation and dispersion in solution (Table 1.1) [13]. The resulting single- or multi-layered GO sheets contain high-density carboxylic acid groups (COOH) and hydroxyls groups (OH), albeit needing further reduction to convert GO to rGO or PG. Graphene sheets produced by that method usually have uncontrolled geometrical shapes and retain more defects due to the harsh environment used for oxidation [10].

**Table 1. 1**- Different approaches for GBMs manufacturing including synthetic techniques and materials used.

| GBM | Synthetic techniques | Materials | Reference(s) |
|---|---|---|---|
| **PG** | Top–down and bottom–up approaches with peptides, proteins, fungi, plants and bacteria | Highly oriented pyrolytic graphite, $SiO_2$ substrate and strong oxidising agents such as $KMnO_4$ and $NaNO_3$ in $H_2SO_4$ and/or $H_3PO_4$ | [1, 14] |
| **GO** | Chemical exfoliation | Oxidative exfoliation of graphite using $H_2SO_4$ and/or KMnO4 | [15] |
| **rGO** | Thermal or chemical reduction | Reducing agents such as hydrazine, hydrazine hydrate and *L*-ascorbic acid | [16] |

## 1.3. Physico-chemical properties and structural features of GBMs

GBMs vary in their surface chemistry, oxygen content, purity, composition, number of layers, defect density and lateral dimensions, the last of which can contribute to toxicity [10]. Despite those differences, the high surface areas of GBMs—2600 $m^2$ /g, generally afford efficient drug-loading capacity [2].

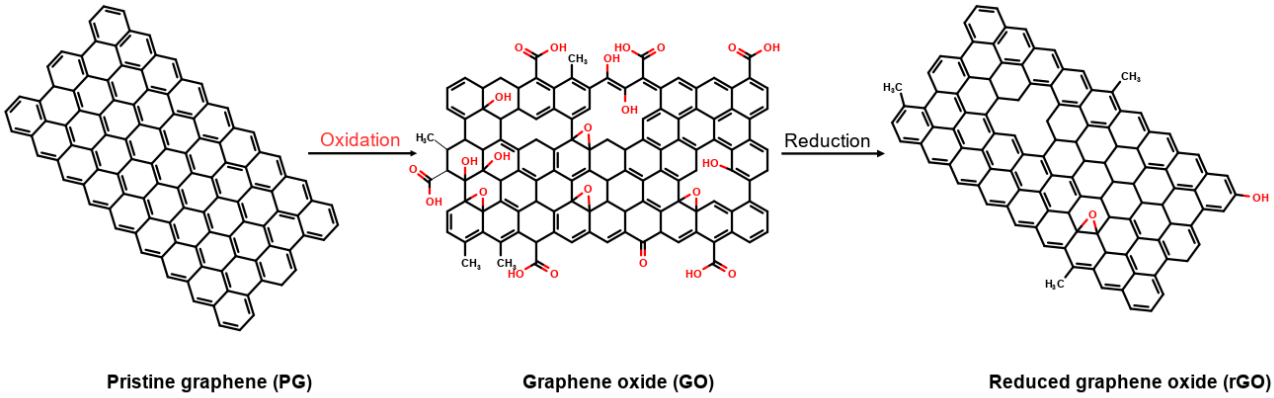


**Figure 1. 2-** Conversion of graphene oxide (GO) and reduced graphene oxide (rGO) from graphene[17].

### 1.3.1. Pristine graphene (PG)

An atomically flat sheet with a van der Waals thickness of 0.34 nm [3], PG is hydrophobic, incompatible with organic polymers and fails to form homogeneous composites [3, 18]. As it has no oxygen groups with defect-free planes, PG's optical and electrical conductivity are outstanding, as shown in Table 1.2. Furthermore, irreversible aggregates form in aqueous media due to its hydrophobic nature, van der Waals interaction and strong π–π stacking between PG flakes, to prevent the aggregation a covalent and noncovalent interactions have been used to functionalise PG using surfactant before use in drug delivery and will be reviewed in section 1.6.1 [18].

**Table 1. 2**- Comparison of the structural features and physico-chemical properties of GBMs.

| GBM | Hydrophobia or hydrophilia | Functional groups | Functional group's effect | Reference |
|---|---|---|---|---|
| **PG** | Hydrophobic | No functional groups (i.e. no oxygen groups) | Poorly soluble in water | [17] |
| | | | π–π stacking | |
| | | Polyaromatic networks | Hydrophobic interactions | |
| **GO** | Hydrophilic | Epoxide groups (–O–) | Soluble in water | |
| | | Hydroxyl groups (–OH) | Hydrogen bonding | [19] |
| | | Carboxylic acid groups (–COOH) | Electrostatic interactions | |
| | Hydrophobic | Polyaromatic networks | Hydrophobic interactions | |
| **rGO** | Less hydrophilic than GO | Few functional oxygen groups | π–π stacking | |
| | | | Hydrophobic interactions | |
| | | Polyaromatic networks | Less water soluble than GO but not as much as PG | [20] |

### 1.3.2. Graphene oxide (GO)

In theory, GO consists of one layer, only a single atom thick, of graphene with epoxide, hydroxyl groups and carboxylic acid groups. Of all chemically modified forms of graphene, GO is the most highly oxidised one [19]. Peripheral carboxylate groups influence its pH-dependent negative surface charge and, consequently, its colloidal stability [21]. Meanwhile,

hydroxyl (–OH) and epoxide (–O–) groups on the basal plane are polar but uncharged, which allows hydrogen bonding and other surface reactions [10]. Unmodified areas on GO's basal plane contain free, hydrophobic π-electrons capable of π–π interactions and available for non-covalent functionalisation and drug loading (Table 1.2). As such, GO is an amphiphilic molecule that may be adsorbed onto interfaces and reduce both interfacial and surface tension, hence its use as a surfactant in aqueous solutions able to stabilise hydrophobic molecules such as anticancer drugs [13, 22].

Shown in Figure 1.3, the most common model of GO is described by the Lerf− Klinowski [19]. That model consists of unoxidised benzene rings and areas with aliphatic six-membered rings. By contrast, other models, including Dékány's, propose that GO's structure consists of two regions: one with trans-linked cyclohexane chairs containing 1,3-epoxide and tertiary hydroxyl groups, the other with corrugated hexagon ribbons containing cyclic ketones and quinones. To justify GO's acidity, additional phenolic groups were added to that model [23].

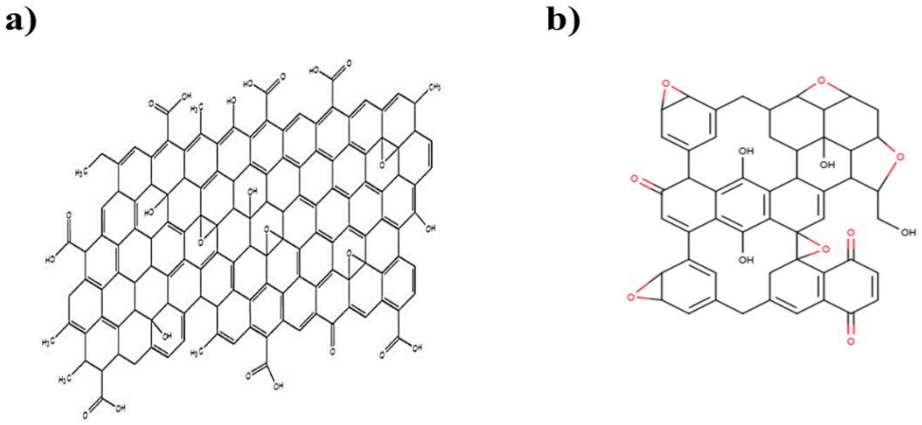


**Figure 1. 3**- Proposed structure models of GO a) Lerf–Klinowski model has carboxyl, hydroxyl and epoxy functionalise the GO surface and b) Dekany model consists of ribbons of flat hexagons with C=C double bonds and trans linked cyclohexane chairs and functional groups such as phenol (aromatic diol), ketone, tertiary hydroxyl, 1,3-ether, and quinone [19].

### 1.3.3. Reduced graphene oxide (rGO)

In the presence of reducing agents such as hydrazine, GO reduces to become rGO (Table 1.1), which differs structurally from GO by having fewer functional oxygen groups as shown in Figure 1.2 [20]. Their structural differences also explain their different physico-chemical properties, including rGO's higher electrical conductivity and optical absorbance compared with GO's higher surface charge and hydrophilicity[10, 12] .

## 1.4. Methods of graphene dispersion

Many approaches to preparing a stable, uniform graphene suspension have been undertaken often focusing on reducing any agglomeration resulting from GBMs' hydrophobic nature and strong van der Waals forces between their layers. Graphite powder and GO are precursors of graphene dispersion, for which physical and chemical methods are available. Ball milling, mechanical stirring and ultrasonic treatment typical physical methods, whereas covalent and non-covalent modification are typical chemical ones. For more efficient dispersion, both methods can be used together.

### 1.4.1. Physical methods

#### 1.4.1.1. Mechanical dispersion

The mechanical dispersion of graphene generally involves ball milling and stirring. When a liquid is stirred mechanically, energy is transferred from the stirrer to the surrounding liquid moving at a certain speed. To prepare suspensions of GBMs, Paton et al. [24] reported using the high-shear mixing of graphite in aqueous sodium cholate surfactant solutions and in *N*-methyl-2-pyrrolidone (NMP) as a solvent for exfoliating graphite. Their results included large numbers of defect-free PG at a shear rate exceeding $10^4$ $s^{-1}$. By contrast, León et al. [25] studied the interactions of the ball-milling agent (i.e. melamine under solid condition) to exfoliate PG

with few defects and disperse it into various solvents, including fresh water and *N*,*N*-dimethylformamide (DMF), by non-covalent or covalent modification. Among their results, hydrogen bonding formation with multipoint at PG surface can be used for the exfoliation of PG and the stabilization of PG in various solvents. Zhao et al. [26] used a range of organic solvents—tetramethyluren, formamide, *N*,*N*-DMF, acetone, ethanol, tetrahydrofuran (THF) and NMP—to exfoliate PG by ball milling and ultimately produced stable suspensions of single and few layer of PG with yield higher than 38.0 wt% . Beyond that, other research has suggested that a simple mechanical technique used in conjunction with a chemical method can produce excellent yields of PG flakes [27].

#### 1.4.1.2. Sonication

Sonication exfoliates graphene sheets into graphene flakes by creating cavitation and shear stresses in solvents [28]. In that process, both the sonication power and duration of sonication affect the dispersion [29]. Graphite's oxidation functionalises individual graphene flakes in the graphitic stack, thereby lowering the frequency of inter-flake interactions, such that the graphite oxide can be exfoliated simply by stirring [19]. Stronger inter-flake interactions in pristine graphite require more significant mechanical force to separate the flakes, hence the widespread use of ultrasonic exfoliation[30]. If the liquid is exposed to ultrasonic vibrations, then any dissolved gas in the liquid can act as weak points where bubbles develop due to the oscillating pressure and coalescence of micro-bubbles, which subsequently oscillate in a series of compression and rarefaction events. The type of sonication experienced can be broadly divided into stable cavitation and inertial cavitation. Inertial cavitation is considered to be more aggressive than stable cavitation, because the bubbles are often less stable and thus more likely to collapse, which causes the ejection of powerful micro-jets[30, 31]. Nevertheless, even during stable cavitation, the bubbles are expected to expand over time due to coalescence, to a point

where they become unstable and undergo violent collapse. Inertial cavitation may also result in the development and retention of several micro-bubbles that, upon collapsing, are unlikely to generate micro-jets as strong as the larger bubbles [31]. In that process, an immersed tube loaded with the suspension to be sonicated is exposed to ultrasonic waves transmitted from the bottom of the bath, where a signal transducer sits, and passes through the water to the sample. Interference may result in regions of low and high amplitude within the water bath, and the reflection from the tube's surface could significantly decrease the intensity of the waves that reach the sample [30].

To produce stable dispersions of graphene, NMP is the most widely used to alter the polarity of the solution thus favours suspensions (act as co-solvent), one that can yield dispersions ranging from 0.01 to 2.0 mg/mL [29, 32]. The intense conditions created from sonication allow graphene to disperse in solvents with low boiling points (e.g. cyclohexanone, acetone and chloroform), such that the concentration of the dispersed graphene increases with the square root of the duration of sonication [33, 34]. The graphene sheet's quality and size are affected by longer durations, which can introduce defects into the sheet [33, 35, 36]. When Bracamonte et al. [37] examined how the duration of sonication affected the dispersion of graphene, they found that durations less than 2 h caused the development of defects on the graphene's edge, whereas ones greater than 2 h caused defects on its basal plane.

More recently, Paton et al. [24] and Liu et al.[38] studied the use of a high-shear mixer to prepare dispersions of graphene using NMP as a solvent at concentrations 0.07 mg/mL and 0.27 mg/mL, respectively. Among their results, Paton et al.[24] found that exfoliation occurred when local shear rates exceeded $10 \times 10^4$ $s^{-1}$. High-shear mixing seemed to be more promising than sonication, because it produced a large amount of high-quality, defect-free GBMs[24].

In another recent study, Raju et al. [39] investigated the aqueous exfoliation of graphene from graphite using sonication and the influence of water with only residual organic solvents: DMF,

NMP and different surface adsorbates, including bile acids, serum albumin and phospholipids. The final three surface adsorbates were expected to yield PG with few layers (less than 5 layers) and size between 100 to 400 nm. Ultimately, the authors found that dispersions in aqueous media with a neutral pH remained stable with negative zeta potentials (i.e. -20 mV to -60 mV).

Other research groups have successfully prepared dispersions of graphene at low costs and with minimal environmental impacts. Among them, Yi et al.[40] have proposed that liquid-exfoliated graphene can be stably dispersed in water. As the average thickness of small graphene flakes is 1 nm, a controllable area of flakes generally suffers from defected edges, thereby affording fairly high quality, high conductivity and considerable increases in absolute zeta potential. Beyond that, the authors showed that using water to disperse graphene while preserving its quality offered several benefits, including lack of toxicity, low cost, low boiling points, no need for stabilisers, easy handling and better biocompatibility than other graphene dispersion in organic solvents. In other work, Ricardo et al. [41] prepared a surfactant-free exfoliation of natural graphite into multi-layered PG in a weakly basic aqueous solution and found that graphene flakes were stabilised by electrostatic repulsion at room temperature for several months. The stability of graphene's dispersion depended on the solution's pH, such that a pH of 11 produced the optimal exfoliation yield and zeta potential. Bepete et al. [42] combine grahenide ( negatively charged graphene ) in THF with degassed water and evaporating the organic solvent, resulting in efficiently dispersed graphene in degassed water with no additives as true single layers in a concentration of 400 $m^2$ /L and with a shelf life of several months.

### 1.4.2. Chemical methods

The covalent modification of graphene's surface and GO results from the presence of defects and reactive oxygen groups in the graphene's lattice. Such modifications can be used in electrophilic addition, nucleophilic substitution, addition and condensation, among other

techniques. GO contains epoxy groups as the principal reactive sites for nucleophilic substitution, and the bonding of groups exhibiting amino functionality ($–NH_2$) with lone pairs of electrons allows them to attack those epoxy groups (Figure 1.4). Such a simple, promising method induces the reaction in aqueous media and occurs at room temperature. A broad range of molecules allowing nucleophilic substitution have been tested, including amino acids, amines and polymers[3, 19, 43].

Although few, functional groups on PG can also be modified with covalent approaches by using several polymers, including poly-L-lysine (PLL) and polyacrylic acid (PAA). When Shan et al. [44] studied the addition of biocompatible PLL to covalently functionalise PG, the result was a complex with high water solubility and large number of free active amino groups. PG sheets work to assemble PLL's active amino groups, which offer a biocompatible medium for the additional functionalisation of, for example, bioactive molecules. After Gollavelli and Ling [45] developed multifunctional graphene as a probe for biomedical diagnostics, they further covalently modified it to make a PAA bridge linking fluorescein *O*-methacrylate to yield multifunctional graphene.

In a study addressing the displacement of hydrogen atoms with electrophiles in electrophilic reactions with graphene[46], diazonium salt chemistry using para-aminobenzoic acid has been functionalised with rGO to form diazonium ions. Bekyarova et al. [47], for instance, functionalised the surface of epitaxial graphene (EG) with nitrophenyl groups, thereby altering EG's transport properties and electronic structure from near-metallic to semiconducting. By comparison, Stankovich et al. [48] treated GO's surface with organic isocyanates in a condensation reaction followed by exfoliation into functionalised GO nano-platelets able to form a stable dispersion in polar aprotic solvents. Treatment with isocyanate functionalised (–COOH) and (OH) in GO via the formation of carbamate esters and amides. In addition, GO's

chemical modification with organic di-isocyanates revealed that di-isocyanate molecules can serve as covalently linked nanoscale spacers between GO sheets [49].

The most efficient way to functionalise a GBM's surface is using polymers with pyrene functional groups or organic molecules and π–π stacking interactions. Applying that approach, Liu et al. [50] synthesised pH-sensitive rGO with polymers PAA and pyrene-terminated poly(2-*N*,*N*-dimethyl amino ethyl acrylate) via π–π interaction, for rGO–PAA composites that showed phase transfer behaviour between organic and aqueous media at different pH values. In another example, Feng et al. [51] functionalised the negatively charged GO with polyethylenimine (PEI) polymers via electrostatic interactions, which yielded strong positive charges GO–PEI complexes with high stability in physiological solutions. These strong positive charge complexes allow effective loading of DNA plasmid (pDNA) via a layer-by-layer assembly process and reduced cytotoxicity to cells. DNA bound to that complex allowed intracellular gene delivery, thereby showing that graphene may be a promising nano-carrier for safe, efficient gene transfection.

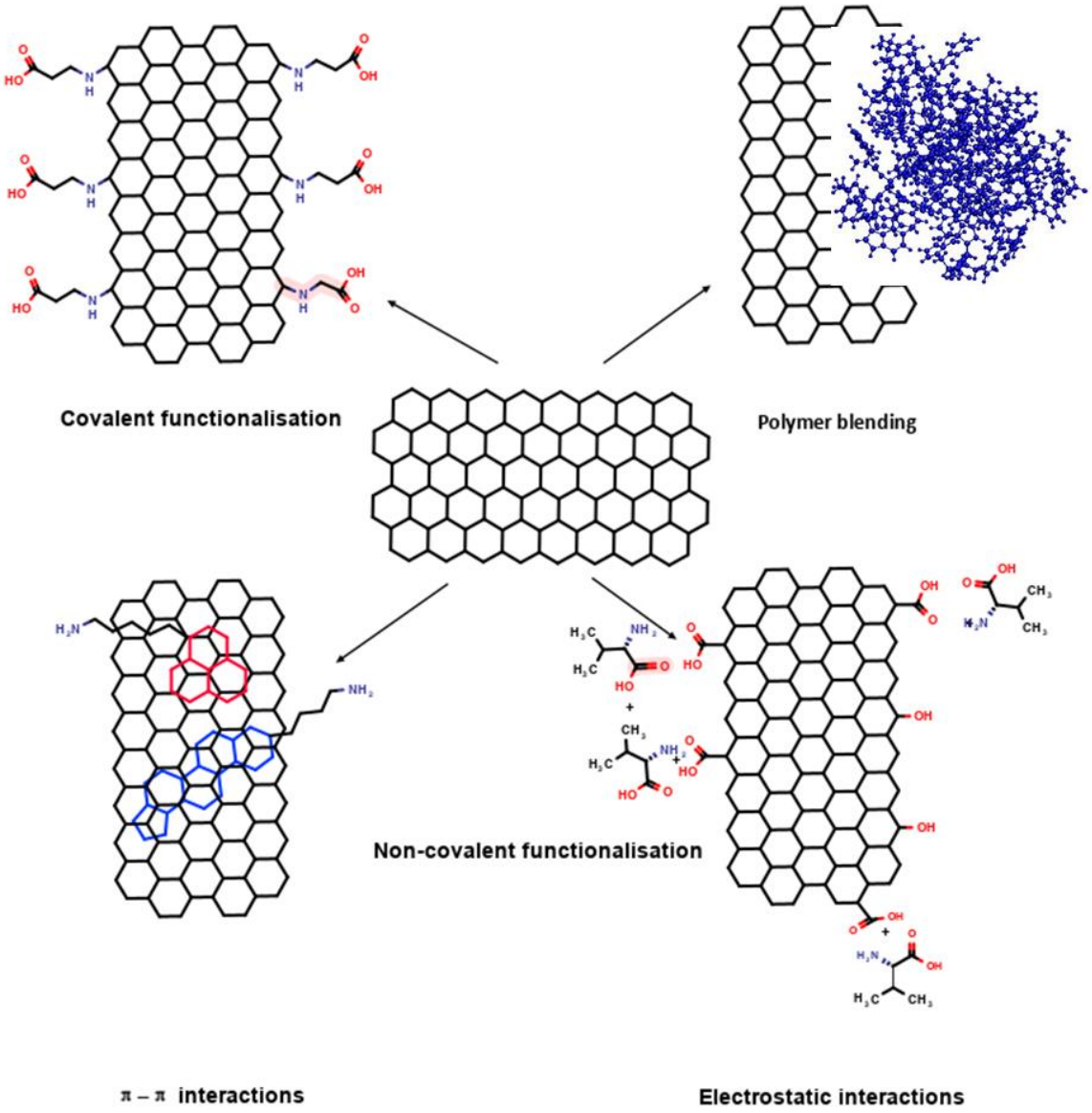


**Figure 1. 4**- Graphene structure displaying different types of interactions including covalent and non-covalent functionalisation. Figure adapted from Terrones et al. [52].

Forces widely used in modifying GBMs include π–π stacking interactions, van der Waals forces, hydrogen bonding, and electrostatic interaction. Non-covalent functionalisation can occur via interactions with biomolecules (e.g., peptides and DNA) or porphyrins, via the adsorption of small molecules or surfactants and via polymer wrapping. As a case in point,

Stankovich et al. [53] prepared stable aqueous dispersions of rGO coated with an amphiphilic polymer, poly(sodium 4-styrenesulphonate), using non-covalent functionalisation.

Surfactants are widely used to facilitate the exfoliation of GBMs, prevent their agglomeration, and enhance their solubility. Having exfoliated PG in the presence of an array of surfactants in aqueous solutions, Guardia et al. [54] showed that non-ionic surfactants—for example, Tween 80 and Pluronic P-123—exfoliated PG better than ionic ones, including sodium deoxycholate and sodium dodecylbenzenesulphonate (SDBS), given their suspending ability in concentrations of 1 mg/mL. Such results confirmed that steric repulsion is more efficient than electrostatic repulsion in PG stabilised aqueous solutions.

In another study, Hsieh et al. [55] used conductometric surfactant titration to study the adsorption of sodium lauryl sulphate (SDS) onto rGO surfaces with a range of surfactant concentrations. They also examined several phases that occur with increased concentrations of SDS, including the adsorption of SDS at concentrations <12 μM at rGO's basal plane edges and rGO's full surface coverage at approximately 12 μM, as well as measured the critical surface aggregation concentration for the formation of micelles on rGO at approximately 1.5 mM of SDS. They estimated that the surface area available for SDS's adsorption on rGO was approximately 600 $m^2/g$—that is, less than expected—and showed that SDS did not adsorb on regions of rGO with chemical functionalities but only onto $sp^2$-hybridised ones. In a different study, the same group examined the stability of rGO's dispersion in the presence of different concentrations of SDS in aqueous solutions. SDS solutions at 10 μM of rGO reaggregated rapidly, and aggregation reduced as the concentration of SDS increased. Consequently, the concentration of suspensions greater than 40 μM were stable for more than a year [56]. Comparing a wide range of zwitterionic, anionic and non-ionic surfactants to assess rGO's stability at different pHs in aqueous media (Fernández–Merino et al. [57]) showed that the

capacity of surfactants for π–π bonding and flat hydrophobic tail surfactants, especially SDBS, were best when dispersing rGO in water.

One of the most commonly used non-ionic surfactant is polyvinylpyrrolidone (PVP). Wang et al. [58] prepared aqueous dispersions of PG exfoliated from graphite using PVP to facilitate PG's exfoliation and thereby retain its flat structure, which resulted in an excellent crystalline structure. Green et al. [59] and Bourlinos et al. [60] used PVP as a stabilising polymer with PG to aid exfoliation, and PVP has also aided PG's exfoliation in numerous organic solvents—for instance, isopropanol, NMP, DMF, dimethyl sulphoxide, water, methanol and ethanol—while showing excellent stability against agglomeration [61]. Moreover, PVP is known to improve the stability of the negative charged graphene dispersion. Last, PVP has additionally been used to prepare stable aqueous dispersions of rGO, and its hydrophobic interaction with rGO resulted in stable aqueous dispersion [62]. However, PVP itself was not used for the solubilisation of chemically rGO due to, it is not ionic in nature. Thus, it interacts with graphene plate via hydrophobic interaction.

## 1.5. Characterisation of GBMs

Several approaches have been used to define GBMs. Some of the most common approaches will be reviewed in this section.

### 1.5.1. Brightfield reflective optical microscopy

Standard optical microscopy's range of applications has contributed to the development of numerous modes of imaging. The most common mode is brightfield imaging, in which images are created by uniformly illuminating the whole sample such that it appears as a dark image against a bright background. Brightfield imaging is used as a general imaging technique for observing and inspecting samples.

In our experiment, suspensions were deposited onto silicon wafers with a 290-nm oxide layer purchased from IDB Technologies (UK), followed by spin-coating onto silicon substrates using a WS-650-23 spin coater (Laurell Technologies, USA). The substrates were cleaned by submersion, first in acetone, second in distilled water and third in 70% isopropyl alcohol, followed by sonication in a bath for 10 min. Afterwards, the substrates were dried in a warming oven to remove any residue from the solvents. Next, the GO suspensions were diluted to approximately 800 μg/mL whenever possible, and a droplet of the suspension large enough to cover the substrate's surface was left on top of the silicon wafer, followed by vacuum fixation in the spin coater. After the substrate was spun at 3000 rpm for 2 min under nitrogen, the dry substrate was visualised using white brightfield reflective optical microscopy with an Eclipse LV100ND upright reflective microscope (Nikon Instruments, USA). The digital images were captured using NIS-Elements software (Nikon Instruments), for which the colour balance was adjusted for optimal contrast. Images were analysed using ImageJ (NIH, USA). For images without a significant degree of overlap, automatic particle sizing was used, whereas in images with a high degree of overlap, manual particle sizing was performed.

### 1.5.2. Atomic force microscopy

AFM is a type of scanning probe microscopy widely used to analyse the topography of a sample in order to determine the morphology of liquid exfoliated graphene. In AFM, a sharp tip mounted on a flexible raster scans across a sample, the topography of which is determined by the movement of a laser spot on a photodetector reflected by the back of the cantilever, as demonstrated in Figure 1.5.

Atomic resolution can be acquired by using various set-ups, with different tip radii and means of vibration isolation, and most set-ups can determine atomic resolution within 5 nm. With that information, it is possible to investigate the thickness and lateral dimensions of prepared flakes,

which is essential for suspensions used in biological applications, particularly because many graphene suspensions prepared with liquid exfoliation are highly polydisperse.

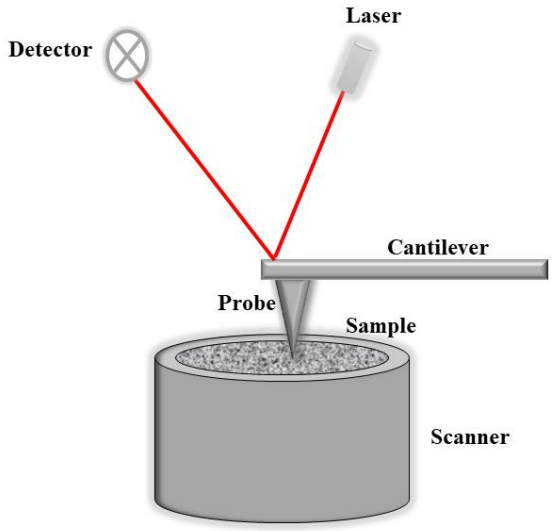


**Figure 1. 5**- Schematic of an AFM probe measuring an object's topography. A detector records the change in the cantilever's position because the surface topography varies, which allows an image of the sample's surface to be constructed [63].

As it scans a sample's surface, the AFM tip can interact with the sample in various ways, usually determined by the nature of the sample, particularly its fragility. In our experiment, the morphologies of GO were examined via AFM using a Bruker Multimode in ScanAsyst mode (Bruker, UK) with the following dimensions: cantilever, 450 μm × 50 μm × 2 μm; tip height, 17 μm; tip radius, <10 nm; cantilever, 115 μm × 25 μm × 0.65 μm; tip height, 2.5–8.0 μm; tip radius, approximately 2 nm. Images were analysed by using Gwyddion analysis software (Czech Metrology Institute, Czech Republic) for scanning probe microscopy and automatic thresholding techniques for particle analysis.

### 1.5.3. Dynamic light scattering

DLS is another common method of measurement used to characterise the size of not only macromolecules and nanoparticles in suspension but also graphene. DLS depends upon the scattering of laser light through small particles in suspension and demonstrating Brownian motion. The movement of the particles with incident light indicates that the scattered light is emitted in different phases and frequencies due to Doppler broadening. As a result, the scattered light affects the incident light either destructively or constructively, which produces a spot pattern that changes over time according to the movement of the particles [64, 65]. The apparent hydrodynamic radii ($R_h$) of the flakes is derived using the Stokes–Einstein equation, whereas the volume fraction of the various sizes measured can be determined with reference to the Mie theory [64, 65]. Both the Stokes–Einstein equation and the Mie theory assume that the particles present are hard spheres that scatter light elastically. Although that hypothesis is valid for many macromolecules and nanoparticles, which are essentially globular, it proves invalid for rods and flakes, because the diffusion coefficient can vary depending on the direction of the body's movement, which can become significant due to rotational diffusion, as shown in Figure 1.6. For those purposes, the measurements observed using DLS should be carefully handled and compared with measurements determined with direct methods such as AFM [66]. In the study reported here, DLS was used only to evaluate the propensity of the flakes to aggregate, not to measure individual flakes.

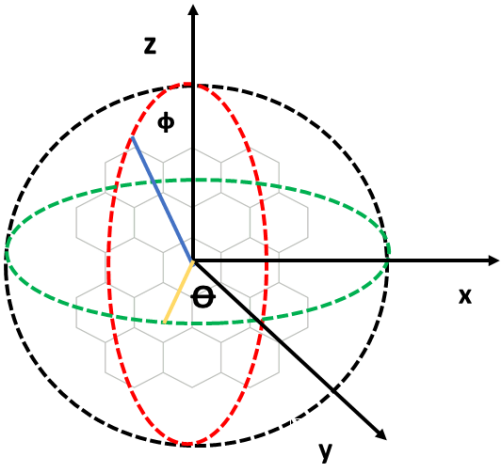


**Figure 1. 6**- Example of the diffusional degrees of freedom of a flake, showing the scattering angle [67].

In DLS, after the scattered laser light interacts with the sample, its varying intensity can be correlated with time by applying a correlation function, which determines the time needed by the intensity signal to become uncorrelated to its initial value, expressed as:

$$\boldsymbol{G^{(2)}(\tau)} = \left( < I\,(0)\mathrm{I}\,(\,\tau\,) > = \lim_{T\to\infty} \frac{1}{2T}\int_{-T}^{T} I\,(t).I\,(t+\quad\tau\,) \right) dt \qquad \textbf{Equation 1.1}$$

$$\boldsymbol{G^{(2)}(\tau)} = B\left(1 + f \mid g^{(1)}\,(\tau)\mid^2\right) \qquad \textbf{Equation 1.2}$$

For a colloid with a dilute monodispersity, $g^{(1)}$, it can also be approximated to:

$$\boldsymbol{g^{(1)}(\tau)} = e^{-Q^2 Dt} \qquad \textbf{Equation 1.3}$$

in which $D_m$ is the mutual diffusion coefficient, $I$ is intensity, $\tau$ is correlation time, $t$ is time, $B$ and $f$ are experimental factors, $Q = \frac{4\pi\, n_0}{\lambda} \sin\left(\frac{\vartheta}{2}\right)$ is the strength of the light–particle interaction, $\lambda$ is the incident light's wavelength, $\theta$ is the scattering angle, and $n_0$ is the medium's refractive index.

From that calculation, the diffusion coefficient can be correlated to the $R_h$ of the particle by using the Stokes–Einstein equation:

$$\boldsymbol{R_h} = \frac{k_B\, T}{6\, \pi\, \eta_0\, D_m} \qquad \textbf{Equation 1.4}$$

in which $\eta_0$ is the solvent's viscosity, $k_B$ is Boltzmann's constant (i.e. $1.38 \times 10^{-23}$ $m^2\, kgs^{-2}\, K^{-1}$) and $T$ is the absolute temperature.

In DLS based on the Doppler broadening of the monochromatic laser light scattered from the objects moving in the suspensions, the random phase distribution of the scattered light induced by the objects moves randomly relative to each other, resulting in a unique interference pattern captured by the spectrophotometer [64, 65], as shown in Figure 1.7. For suspensions in which significant aggregation has appeared, instead of precipitating (Figure 1.7a), the large aggregates may slow moving in a Brownian (i.e. random) manner when suspended; otherwise, they will occupy most of the focal plane (Figure 1.7b). If a particle becomes so large that the phase distribution is no longer random (i.e. because the same particle emanates several scattered light points) or if the movement of the particle is directional, then the model breaks down, as indicated by the degradation of the correlation curve in analysis. The curve for such suspension is no longer sigmoidal; strong oscillations may be detected, the tail may no longer reach 1, or significant peaks or troughs can disrupt the decay region (Figure 1.7c). During our analysis, although the software used provided residuals, we could not determine the $\chi^2$ value for the fit—that is, the value that would not likely indicate whether the curve's baseline was at 1. Therefore, qualitative evaluations of the curve were made, as illustrated in Figure 1.8. Those differences were used to assess the overall quality of the suspensions.

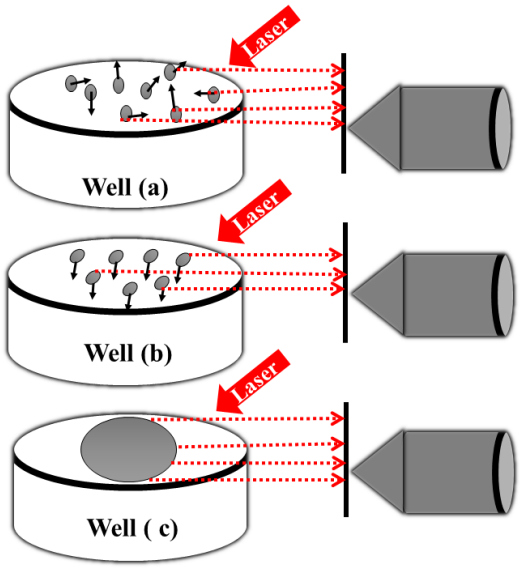


**Figure 1. 7**- Schematic of DLS function for different types of particle distributions. a) Particles remain small relative to the laser but are not well behaved; their motion is directional due to sedimentation. b) A well-behaved suspension, in which the particles are small relative to the laser point and demonstrate Brownian motion. c) Particles are large relative to the laser point, meaning that light scattered off the same particle may interfere with itself.

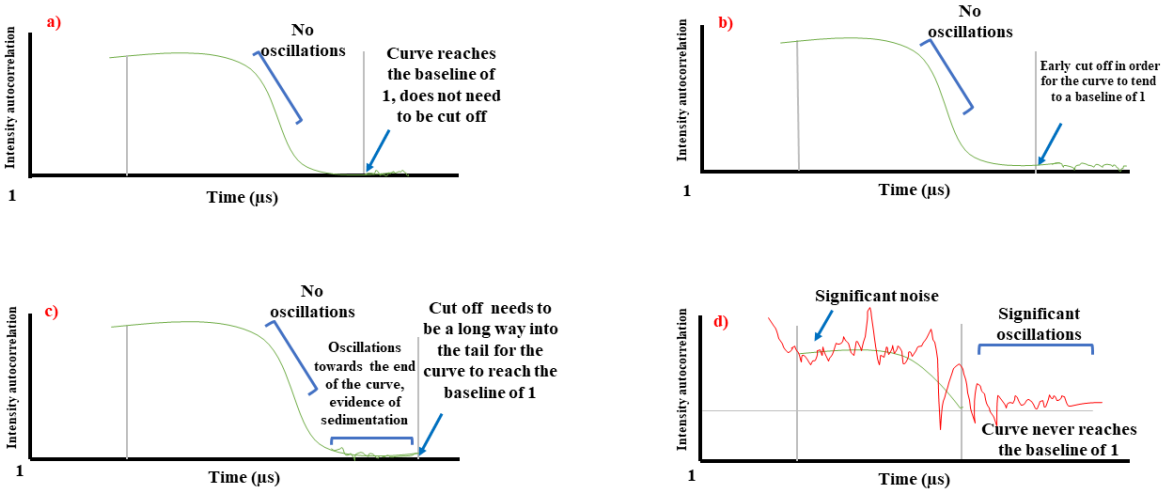


**Figure 1. 8**- DLS correlation curves representing different samples: a) good, b) and c) satisfactory and d) poor.

Performed using a DynaPro Plate Reader II (Wyatt Technology Corporation, USA), DLS entailed diluting samples to approximately 50 μg/mL, and 100 μL was aliquoted into a 384-well microtitre plate transparent to U/V light. All samples were measured in triplicate by following an events schedule set on the DynaPro plate reader using the software Dynamics. The laser was auto-attenuated for each reading, and all acquisitions were performed during a period of 10 s; 10 acquisitions were performed on each well, and the temperature was maintained at 25 °C. For the software that enabled real-time data filtering, correlation function cut-offs were set at 0.93 and $1.33 \times 10^6$ as the low and high passes, respectively, whereas peak radius cut-offs were set at 0.5 nm and 10 μm.

GO flake analysis was also performed in Dynamics, which facilitated CONTIN regularization analysis to match the correlation curve and determine the apparent $R_h$ distribution. The user-defined correlation curve region used for fitting. The accepted values were those where the curve's level decayed such that its tail was either 1.0 or projected to and where the residuals were reduced. From that curve, the software generated a distribution in the form of a histogram of apparent $R_h$.

### 1.5.4. Raster image correlation spectroscopy

In RICS, as best explained by Digman *et al.* [68, 69], confocal microscopy uses a raster-scanning laser to generate fluorescence images, which enables RICS to use the hidden time structure in the images. In that structure, three levels of coarseness appear within the images made by a confocal microscope—microsecond, millisecond and second—defined by the line rate, pixel dwell time and the frame rate, respectively, as shown in Figure 1.9.

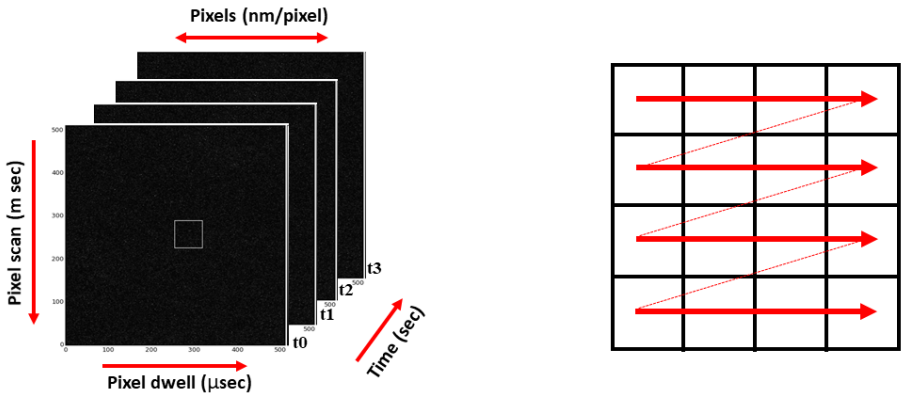


**Figure 1. 9**- An illustration of the fundamental theory of RICS, adapted from Digman et al**.** [68]. A schematic view of the a) a temporal z-stack of images, with the three levels of temporal coarseness indicated, and b) raster scanning pattern that the laser uses to form a 2D image.

Using that information, RICS involves using the scan function as well:

$$\boldsymbol{\tau(\xi,\psi)} = \tau_p(\xi) + \tau_l(\psi) \qquad \textbf{Equation 1.5}$$

in which $\tau l$ is the line rate, $\tau p$ is the pixel dwell time, $\psi$ is the spatial displacement in the y-direction in a raster image, and $\xi$ is the spatial displacement in the x-direction. A 2D autocorrelation can be developed from Equation 1.5:

$$\mathbf{Gs(\xi,\psi)} = \mathrm{G(\xi,\psi)} \cdot \mathrm{G(\xi,\psi)} = \frac{\langle \delta \mathrm{I(x,y)} \delta \mathrm{I(x+\xi, y+\psi)} \rangle \mathrm{x,y}}{\langle \mathrm{I(x,y)} \rangle^2_{x,y}} \qquad \textbf{Equation 1.6}$$

in which $\delta I(x, y) = I(x, y) - \langle I(x, y) \rangle_{x,y}$ , which is the fluorescence intensity variation around the mean, and *I(x,y)* is the pixel fluorescence intensity.

By extension, a 3D diffusion autocorrelation function can additionally be generated:

$$\mathbf{Gs(\xi,\psi)} = \frac{\gamma}{N}\left(1 + \frac{4D_s(\tau_p \xi + \tau_l \psi)}{\omega_0^2}\right) \cdot \left(1 + \frac{4D_s(\tau_p \xi + \tau_l \psi)}{\omega_z^2}\right)^{-\frac{1}{2}} \qquad \textbf{Equation 1.7}$$

$$\tau_D = \frac{\omega_0^2}{D_s} \qquad \textbf{Equation 1.8}$$

in which $N$ is the number of particles in a confocal volume, $D_s$ is the self-diffusion coefficient, $\gamma$ is $1\sqrt{8}$, $\omega_0$ if the lateral beam waist, $\omega_z$ is the axial beam waist, and $\tau_D$ is the diffusion time. The diffusion coefficient, number of particles and goodness of fit ($R^2$) are provided for each ROI interrogated using the Levenberg–Marquardt algorithm. From the diffusion coefficient, the apparent $R_h$ can be determined by again using the Stokes–Einstein equation (Equation 1.4). RICS was performed using a Zeiss LSM510 confocal laser scanning microscope with a C-Apochromat 40×/NA 1.2 water-immersion objective. After samples were excited at $\lambda_{ex}$ = 488 nm, spectra were analysed using the in-house software ManICS [70]. Suspensions were prepared at concentrations of approximately 50 μg/mL, and 300 μL was aliquoted into a Lab-Tek Nunc® 8-well chamber slide (Fisher Scientific, UK). Fluorescence images were taken following excitation with a 488-nm argon laser (30 mW) and measured with a broadband filter. For each sample, a stack of 30 images were acquired. The region of interest was approximately 28 μm × 28 μm, with a pixel size of 54.9 nm and a pixel dwell time of 6.4 μs, which yielded a line time of 7.7 ms and a frame time of 3.94 s. All experiments were performed at 21 °C in a climate-controlled environment.

## 1.6. Biomedical applications of GBMs

With high intrinsic mobility, high biocompatibility, large surface areas, high thermal stability and a high Young's modulus, graphene has recently been developed in biomedical applications as a possible drug carrier via π–π stacking and both electrostatic and hydrophobic interactions[71]. Supporting its use as such, GO's outstanding properties include its amphiphilicity, ability to quench fluorescence, surface functionality and surface-improved Raman scattering. In biomedical applications, its hydrophobicity, large surface areas and grain limits on defect sites are essential. GO's first use as a nano-carrier for drug delivery, in research by Sun et al.[72], paved the way for additional applications of graphene in biomedicine. GO

and rGO have also been identified for use as carriers in gene and protein therapy as well [73](Figure 1.10).

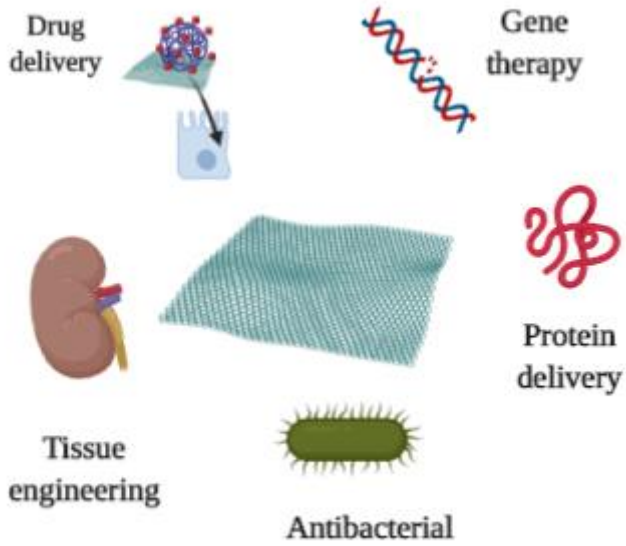


**Figure 1. 10**- The biomedical applications of GBMs, including drug and protein delivery, gene therapy, tissue engineering and antibacterial activity[73].

### 1.6.1. Graphene as a substrate for drug delivery

Graphene has a greater drug-loading capacity (i.e. up to 200% loading ratio of loaded drug weight to vehicle) than other nano-carriers for drug delivery, including single-walled CNTs[10]. Consequently, graphene has been used as a nano-carrier for drugs and several bioactive compounds, including camptothecin (CPT), doxorubicin (Dox), 5-fluorouracil, ibuprofen, heparin, rhodamine 6G, SN38, hypocrellin A, chlorin e6, paclitaxel, curcumin and ellagic acid (EA), a summary of a range of anticancer drugs loaded onto GBMs appears in Table 1.3 [74-76]. To improve its practical applications, graphene's surface chemistry needs to be altered to enhance its biocompatibility with cells and macromolecules. To that end,

functionalisation is a process that involves introducing new functional groups to the surface of nanoparticles via physical or chemical attachment[77].

Polyethylene glycol (PEG) is a hydrophilic biocompatible polymer widely used to functionalise a variety of nanomaterials in order to enhance their biocompatibility and decrease their non-specific adsorption to cells and biological molecules. Among those nanomaterials, GO and its functional oxygen groups (i.e. COOH and OH) have been described as effective carriers for drug and gene delivery. Indeed, Liu et al. [78] formed a complex with excellent aqueous stability by attaching the covalently linked GO–PEG to the water-insoluble aromatic molecule SN38, a CPT analogue,. Robinson et al. [79] confirmed similar work on rGO using covalent PEGylation with high near-infrared for a potential form of photothermal therapy. Nevertheless, traditional functionalisation agents—for instance, polyethylene glycol and poly(lactic-co-glycolic acid) — pose some disadvantages, including a time-consuming, multistep method that requires temperatures greater than 100 °C and using highly corrosive solutions, both of which raise the cost of the entire procedure [78, 80-83].

The delocalised π electron on graphene's surface aids in attaching aromatic anticancer drugs via π–π stacking or hydrophobic interaction. When loading Dox onto PEGylated nano-GO, the quinone portion of the Dox conjugated with GO by way of π–π interactions, while a hydrogen bond formed between Dox hydroxyl and/or amino groups and GO hydroxyl and/or carboxyl groups. Such results suggest that the mechanisms of drug loading and release are pH-dependent: indeed at neutral pH, drug-loading capacity peaked, while at pH 2 more than 70% of the drug was released [84].

Other polymers have also been grafted onto GO sheets through covalent methods to increase their biocompatibility. For example, the highly hydrophilic and biocompatible poly(vinyl alcohol), "PVA", was functionalised with GO, after which CPT was loaded onto GO–PVA through π–π interactions; the resulting controlled drug delivery system showed to be highly

effective on MDA-MB-231 human breast cancer cells [85]. Zhang et al. [86, 87] prepared a complex of GO conjugated with PEI on which Dox and short interfering RNA (siRNA) were loaded; these resulted in significant improvements *in vitro* anticancer efficacy. From another angle, Li et al. [88] demonstrated the high solubility and stability of GO covalently functionalised with poly(*N*-isopropylacrylamide), or "pNIPAM", in water and physiological solutions (e.g. phosphate buffered saline). Following the loading of CPT on GO-pNIPAM via π–π interactions, the resulting GO-pNIPAM complex exhibited high solubility and stability, unique amphiphilicity and the release of CPT from GO-pNIPAM-CPT showed high toxicity to A-5RT3 cancer cells.

Another study by Gao et al. [89] used GO with poly(sebacic anhydride) as a drug carrier for levofloxacin, whereas Rana et al. [90] covalently functionalised GO with chitosan and loaded ibuprofen and 5-fluorouracil onto GO–chitosan, thereby yielding a complex allowing controlled release and with high biocompatibility. Depan et al.[91] showed the excellent release of Dox from GO-Dox encapsulated with folic acid (FA) conjugated chitosan compared with its non-encapsulated nanocarrier. Hu et al. [92] prepared PG with the amphiphilic copolymer Pluronic PF127 as a solubilising agent, followed by hydrophobic interactions and π–π stacking between Dox and the PG–PF127 complex, which resulted in Dox's high pH-dependent release and loading efficiency. By contrast, Kakran et al. [93] covalently functionalised GO with Pluronic F38, Tween 80 and maltodextrin, after which poorly water-soluble EA loaded onto the complex via π–π interactions, thereby resulting in higher toxicity to human breast carcinoma cells (MCF7) and human colon adenocarcinoma cells (HT29) than EA alone. Researchers have also modified rGO's covalent surface modification with PEI, followed by covalent binding to FA, to specifically target cells and load elsinochrome A to the rGO–PEI–FA complex in order to improve elsinochrome A's water solubility and release. In such work, the conjugation rGO–PEI–FA with Dox resulted in the increased apoptosis of CBRH7919

cancer cells compared with Dox alone [94]. Last, Zhang et al. [95] prepared GO with sulphonic acid groups ($SO_3H$) to stabilise them in a physiological solution, followed by the covalent binding of FA to GO, to target MCF-7 cancer cells. The surface of the FA–GO complex was loaded with Dox and CPT via π–π stacking and hydrophobic interactions, for results indicating that GO loaded with either Dox or CPT demonstrated better therapeutic efficacy than that of either drug alone.

Amphiphilic polymers conjugated to GO could be used to enhance GO's drug-loading capacity, solubility and anti-biofouling ability. Yang et al. [96] designed a nano-supramolecular assembly using FA-modified β-cyclodextrin (GO–FA–β-CD) as a target unit and GO non-covalently linked by an adamantanyl porphyrin via π–π stacking. Once Dox was loaded to that complex via π–π interaction, the results highlighted Dox's high toxicity towards HeLa and OCT-1 cancer cells compared with that of free Dox. Likewise, Depan et al. [91] attached GO to Dox via a π–π interaction, followed by GO's encapsulation with FA attached to chitosan. The encapsulation of GO enhanced the complex's stability in an aqueous medium due to chitosan's cationic and hydrophilicity nature.

GBMs in conjugation with metal nanoparticle composites, including $MnO_2$, Pd, Ni, Ag, Au and $Fe_3O_4$, have been used in various applications for drug delivery, largely due to their exceptional optical and magnetic properties as well as ability to combine drug delivery with biosensing. The interaction between those metal nanoparticles and GBMs has been studied by multiple groups of researchers [97-100]. In another contribution to such work, Yang et al. [101] developed super-paramagnetic GO with $Fe_3O_4$ via simple chemical precipitation. Once the hybrid was loaded with Dox with a loading capacity up to 1.08 mg /mg under acidic conditions, the hybrid congregated while under basic conditions the hybrid dispersed to form a stable suspension. Beyond that, Ma et al. [102] prepared multifunctional super-paramagnetic GO with an iron oxide nanocomposite (GO–IONP), functionalised the hybrid with a biocompatible PEG

polymer to obtain a stable complex in physiological solutions and subsequently loaded it with Dox to form GO–IONP–PE– Dox. The aforementioned complex, which allowed magnetically targeting drug delivery, demonstrated strong optical absorbance from the visible to the near-infrared region and, for that reason, could be used in the localised photothermal ablation of cancer cells guided by magnetic fields. In still other research on the topic, β-lapachone loaded onto rGO–$Fe_3O_4$ showed high cytotoxicity against MCF-7 [97], while a superparamagnetic nano-carrier prepared by conjugating $Fe_3O_4$ to GO, followed by being loaded with paclitaxel, was toxic against MCF-7 cancer cells whereas, cellular toxicity assay indicated nanocarriers are biocompatible having cell viability more than 80% for L-929 fibroblast cell line [103]. However, graphene functionalised with those nanocomposites may need more accurate testing in biological environments in order to determine its proper application and biocompatibility in drug delivery.

Another approach to decorating graphene surfaces is non-covalent functionalisation with ordered supramolecular architectures. To fine-tune graphene's electronic properties and especially to modulate its doping, it is crucial to design molecular building blocks capable of undergoing controlled self-assembly on graphene and, in turn, forming ordered nano-patterns. Depositing simple molecules or layers of self-assembled species on graphene's surface—that is, species suitable for modifying interfacial electronic interactions—induces interstitial doping by charge transfer processes between supramolecular architectures and graphene, which subsequently modulates the graphene's work function[104]; however, these non-covalent methods do pose some limitations. Indeed, the adsorption of polymers onto GO's surface via non-covalent methods is less than with covalent methods, which affects the stability of drug delivery systems in biological environments. In practice, non-covalently functionalised GO could load fewer aromatic drugs due to the unavailability of areas of GO sheets conjugated with coated polymers. Zhang et al. [86] compared the drug-loading efficacy of PEI–GO

prepared non-covalently via hydrogen and electrostatic bonding with PEI–GO prepared covalently via the formation of an amide bond, and the results indicated that the latter was more stable than the former.

**Table 1. 3-** Summary of drug delivery system using GBMs.

| Drug carrier system | Drug(s) loaded | Binding approach | | Target cells studied | Ref. |
|---|---|---|---|---|---|
| | | PG/GO-functionalisation | Carrier -Drug | | |
| **PG–gelatine** | Rhodamine 6G | Non-covalent | Covalent | MCF-7 cells | [105] |
| **PG–PF127** | Dox | Non-covalent | Covalent | MCF-7 cells | [92] |
| **PG– DESs** | Dox | Non-covalent | Covalent | MCF-7 cells | [106] |
| **GO–PEG–Rituxan** | Dox | Covalent | Covalent | B-cell lymphoma cells | [72] |
| **GO–FA–chitosan** | Dox | Covalent | Covalent | MCF-7 cells | [107] |
| **GO–$Fe_3O_4$–FA** | Dox | Non-covalent | Covalent | SK3 and HeLa cells | [96] |
| **rGO–GNC** | Dox | Non-covalent | Covalent | HepG2 cells | [108] |
| **GO–PEG** | Dox | Covalent | Covalent | EMT6 cells | [109] |
| **GO–FA–β-CD** | Dox | Non-covalent | Covalent | HeLa and OCT-1 cell | [96] |
| **GO–PEG** | Dox | Non-covalent | Non-covalent | HeLa cells | [110] |
| **GO– Tf –PEG** | Dox | Covalent | Covalent | C6 glioma cells | [111] |
| **GO–PEI** | Dox | Covalent | Covalent | HeLa cells | [86] |
| **GO–PEG** | SN38 | Non-covalent | Non-covalent | HCT 116 | [78] |
| **GO–chitosan** | CPT | Covalent | Covalent | HepG2 and HeLa cell lines | [112] |

| | | | | | |
|---|---|---|---|---|---|
| **GO–PVA** | CPT | Non-covalent | Non-covalent | MDA-MB-231 cells | [85] |
| **GO–PNIPAM** | CPT | Non-covalent | Non-covalent | A-5RT3 cells | [88] |
| **GO–FA** | Dox + CPT | Covalent | Non-covalent | MCF-7 cells | [95] |
| **GO–Tween 80** | EA | Covalent | Non-covalent | MCF7 and HT29 cells | [93] |
| **GO–MDx** | EA | Covalent | Non-covalent | MCF7 and HT29 cells | [93] |
| **GO–Pluronic F38** | EA | Covalent | Non-covalent | MCF7 and HT29 cells | [93] |
| **GO** | HA | Non-covalent | Non-covalent | HeLa cells | [113] |
| **GO** | Chlorin e6 | Non-covalent | Non-covalent | MGC803 cells | [114] |
| **GO–chitosan** | 5-Fluorouracil | Covalent | Non-covalent | MCF-7 cells | [90] |
| **GO–chitosan** | Ibuprofen and 5-fluorouracil | Covalent | Non-covalent | CEM cells | [90] |
| **GO–PAA** | BCNU | Covalent | Covalent | GL261 cells | [115] |
| **GO–$Fe_3O_4$** | Paclitaxel | Covalent | Non-covalent | MCF-7 cells | [103] |
| **rGO–GNCs** | Dox | Non-covalent | Non-covalent | HepG2 cells | [116] |
| **rGO–FA** | Dox | Non-covalent | Non-covalent | MDA-MB 231 cells | [117] |
| **rGO–PEI–FA** | Dox | Covalent | Covalent | CBRH7919 cells | [94] |
| **rGO– CHA** | Dox | Covalent | Non-covalent | KB cells | [118] |
| **rGO–PEI–FA** | EA | Covalent | Non-covalent | CBRH7919 cells | [94] |
| **rGO– UFH** | Curcumin | Covalent | Covalent | MCF-7 cells | [119] |
| **rGO–chitosan** | Fluorescein sodium | Covalent | Non-covalent | 1 kN load cells | [120] |
| **rGO– BPBA** | Gallic acid | Covalent | Non-covalent | A549 cells | [121] |
| **rGO–$Fe_3O_4$** | β-Lapachone | Non-covalent | Non-covalent | MCF-7 cells | [97] |

### 1.6.2. Graphene substrates for gene and protein delivery

Gene therapy is a grafting method to treat several genetic disorders. In general, gene therapy succeeds by creating a vector that protects DNA from endonuclease and offers high-efficiency transfection.

Gene silencing in cells was achieved by delivering siRNA using GO–PEI. As a case in point, Zhang et al. [54] established GO–PEI complexes to deliver Bcl-2-targeted siRNA and Dox for improved therapeutic purposes. The complex showed greater cytotoxicity due to the synergistic effect of the drug and siRNA. Moreover, PEI showed improved transfection efficiency under moderate laser irradiation while grafted onto nGO sheets [86]. When heat produced at the irradiated site physically disrupted the endosomal membrane, the release of complexes was improved and led to enhanced transfection efficiency. Additionally, for the efficient delivery of the vascular endothelial growth factor gene, PEI-functionalised GO added to GelMA hydrogel was used to promote vasculogenesis and cardiac repair.

As graphene excels as a binding site for protein molecules as well as prevents proteolysis, GBMs can be used as intracellular nano-carriers of therapeutic proteins. For example, the local delivery of bone morphogenetic protein (BMP), an osteo-inductive protein that induces bone regeneration, was performed on a mouse model with a calvarial defect with a GO-coated Ti implant to the target site[122]. , GO coating was used to sustain BMP's release at the site, and the conjugation of substance P and BMP using a GO–Ti implant recruited mesenchymal stem cells and, in turn, facilitated bone formation. Among other work, Emadi et al. [123] conjugated GO with chitosan for a nano-carrier able to deliver protein during oral and intravascular administration. Collagenase and bovine serum albumin (BSA) were loaded onto the chitosan-modified GO, such that chitosan functionalised GO, prevented BSA from proteolytic cleavage and maintained the collagenase's enzymatic activity. In general, BSA removes functional groups containing oxygen from GO, thus leaving reduced GO-created aggregates and wraps

around trypsin that prevents its interaction with BSA. Chitosan-functionalised GO's protection of BSA from trypsin digestion stemmed from both GO's steric hindrance and the reduction of BSA's effect Altogether, their results show promise for using GO nano-carriers to improve protein delivery and lower the overall cost of therapy by enhancing its efficiency and reducing the need for frequent, repeated use [123].

### 1.6.3. Graphene derivatives as antimicrobial agents

Although GO and rGO both exhibit antibacterial activity against a host of bacteria, Gram-negative bacteria (e.g. *Escherichia coli*) have shown less sensitivity to graphene than Gram-positive bacteria such as *Staphylococcus aureus* [124]. In general, graphene exerts its antibacterial activity while directly interacting with the cell membrane. To explain graphene's antibacterial action, Liu et al. [125] have suggested a three-step process: bacterial binding to graphene's surface, membrane damage that causes intracellular leakage and the oxidisation of the membrane's proteins and lipids.

Studies suggest overall that rGO is more toxic to bacteria than GO due to its sharp edges, which damage the membrane and cause intracellular leakage, as well as better charge transfer with bacterial cells than GO [126]. Graphene also excels as an electron acceptor and inhibits the transfer of electrons in the electron transport chain, which prompts the depletion of ATP and ends in cell death. The minimum inhibitory concentrations for Gram-negative and for Gram-positive bacteria were 1 μg/ mL and between 4–8 μg/ mL respectively [127].

Within cells, graphene induces the formation of reactive oxygen species (ROS) that damage cellular components, including proteins, DNA and lipids. Lipid peroxides are produced by the oxidation of fatty acids, which disintegrates the cell membrane and ultimately results in cell death. Contact between the bacterial membrane and semimetal graphene has also been suggested to promote the charging of electrons from the membrane to graphene[128]. The

disturbance of electron transfer in respiratory chains causes the depletion of intracellular ATP, and graphene gradually removes electrons until the bacteria lose their viability. Numerous graphene composites containing polymers (e.g. chitosan, PLL, polyvinyl-*N*-carbazole and lactoferrin) have been created to provide antibacterial surfaces for biomedical applications. Recently, the anti-biofilm and antimicrobial activity of both Gram-negative and Gram-positive bacteria of organic compounds containing amines conjugated GO were studied [129]. Amine containing GO hybrids exhibited an enhanced inhibitory activity against bacteria compared with amines alone. More recently, Hou et al. examined the antibacterial activity of GO photolysed under simulated sunlight [130]. To induce GO's photo transformation, their sample was irradiated under sunlight for different lengths of time and subjected to photo transformation via either direct photolysis (i.e. under sunlight) or indirect photolysis (i.e. with GO containing $H_2O_2$). Those subjected to direct photolysis were more efficient at preventing the growth of *E. coli* K12 bacteria than the others, possibly due to the size of GO after photolysis. Moreover, indirect photolysis involving the addition of $H_2O_2$ resulted in smaller GO sheets than those produced by direct photolysis. The larger GO flakes resulting from direct photolysis could interact effectively with cell, cover the cells and induce membrane deformation, and, they had a greater capacity for oxidation against GSH, which decreased the amount of cellular antioxidants.

Contrary to those findings, other researchers have observed increased bacterial growth on GO's surface, even up to 3 times greater than that on the surface with high particle density. [131]. GO oxygen groups are thought to confer sufficient wettability for bacterial proliferation and adhesion. Even despite those conflicting results, the antimicrobial properties of GBMs can be used in coatings on the surfaces of nanocomposites, in wound dressings [132], on the surfaces of medical devices and as smart antibiotics [133].

### 1.6.4. Graphene substrates for tissue engineering

Effective tissue engineering depends upon the biocompatible substratum that supplies cells needed for attachment, growth and proliferation. Owing to their differentiation into cells of specific lineage, stem cells are highly promising candidates for tissue regeneration, ones whose attachment and proliferation, particularly with MSCs and neuronal cells, have recently been facilitated by graphene acting as a reliable scaffold. On the surface of graphene-coated substrata, researchers have cultured several cell lines, including NIH 3T3 cells [134], osteoblasts [135], MCF-7 cells[136] and MSCs. Of them, MSCs grown on graphene's surface or 3D graphene foam and created a spindle shape with extraordinary potential for cell proliferation and differentiation towards osteogenic lineages without the addition of any external biochemical cues.

The concentration of graphene should not be ignored while being developed as a scaffold for cell cultures, largely because it determines the viability of the cells therein. A lower concentration of GO is thought to promote cell adhesion and to be biodegradable, whereas a higher concentration is thought to reduce cell attachment and induce oxidative stress-mediated cytotoxicity[137]. Graphene has thus been considered to act as a bridge that binds differentiation-inducing factors. It suppresses adipogenic differentiation as insulin, a primary inducer of adipogenesis, is denatured when attached to it via π–π interactions. Although GO does not alter adipogenesis due to the electrostatic binding of insulin, graphene does improve osteogenesis by pre-concentrating osteogenic factors [138].

Graphene's significant electrical conductivity allows it to modulate the activity of neural stem cells, and graphene differentiates human neural stem cells into neurons[137]. Graphene readily binds with neural stem cells, which facilitates their differentiation into neurons instead of glial cells, as well as encourages neurite sprouting in the hippocampal neural cells of mice and increases the expression of growth associated protein–43 [139]. Compared with tissue cultures

using polystyrene substrates, those using PG substrates have accommodated more neurites of longer average length. Several GBMs have been developed and assessed for their biocompatibility, including graphene conjugated with chitosan[140], poly-ε-caprolactone [141], hydrogel scaffolds [142] and GO–polypropylene carbonate nano-foams [143]. Electron-spun poly-ε-caprolactone nanofibers coated with GO have additionally been created to distinguish neural stem cells from oligodendrocytes exhibiting the high expression of myelin basic protein, Olig2, O4 and GalC. Polymeric scaffolds with graphene also promoted the differentiation of oligodendrocytes by controlling the downstream signalling pathway of an integrin receptor and the associated cytoskeletal remodelling [144].

Cardiac patches, used to replace damaged portions of cardiac tissue, can provide enough mechanical strength for myocardial regeneration to occur and to supply growth factors to cells that improve cardiac function. In numerous studies, researchers have included GBMs in polymeric scaffolds to enhance their mechanical properties and electrical conductivity when used in cardiac patches. Other cardiovascular applications have included a GO–gold nanosheet-conjugated chitosan scaffold [145], RGO–nanofibrous silk fibroin matrices [146], RGO–GelMA hybrid hydrogels [147], a GO-incorporated collagen scaffold [148] and a graphene–polycaprolactone scaffold [149]. Among GBMs, rGO demonstrated more suitable material for cardiac tissue engineering due to its outstanding mechanical properties, electrical conductivity and biocompatibility.

Along with those mechanical properties, graphene also has remarkable physical properties and an ability to induce the differentiation of stem cells, all of which have shown promise in dental applications. For nearly all dental materials, high mechanical strength, durability and biocompatibility are prerequisites. Introducing GBMs in dental composites would thus improve their mechanical properties, including their compressive [150]. Rosa et al. recently identified the GO-induced upregulation of odontogenic genes such as dentin matrix acid

phosphoprotein 1 and dentin sialophosphoprotein in stem cells isolated from dental pulp [151]. In turn, dental pulp stem cells can bind and proliferate on the rough GO substrate.

Other sources of cells with significant potential for tissue engineering and regenerative medicine are induced pluripotent stem cells (iPSCs). Both graphene and GO have been shown to enhance the spontaneous differentiation of iPSCs into ectodermal and mesodermal lineages [152] and thus to promote distinct pathways for cell differentiation. iPSCs bound and proliferated rapidly in GO, which promoted endodermal differentiation, while PG inhibited the cell differentiation of endodermal lineages. That dynamic could be due to the difference in surface groups that activate several receptors of iPSCs. Such findings indicate that graphene materials can be used as a substrate for culturing and expanding iPSCs, thereby eliminating the need for feeder layer cells. Moreover, they suggest the possibility of using graphene scaffolds for cell replacement therapy following acute liver failure or type I diabetes, because graphene increases cell differentiation into hepatocytes and insulin-producing β cells [152]. On the whole, all of the results above demonstrate the promise of graphene's application, at least in safe dosages, in stem cell therapy and regenerative medicine.

## 1.7. Biocompatibility and toxicity of GBMs

GBMs represent a promising class of drug carriers whose toxicity and biocompatibility have sustained the attention of researchers. Among them, Chang et al. [153] examined GO's toxicity by using various cytotoxic methods of determining GO's effect on the viability, morphology of membrane integrity and mortality of a cell line widely used in nano-toxicological studies—that is, A549, a human lung carcinoma epithelial cell line—and tested GO's generation of ROS in different concentrations (10, 25, 50, 100 and 200 μg/mL) of culture medium. Although GO seemed to hardly enter A549 cells and exerted no cytotoxic effect upon them, it did create cellular ROS at the lowest and highest concentrations examined. Such results suggest that GO

may slightly decrease cell viability and dose-dependent oxidative stress in A549 cells. Another study on the biocompatibility of NIH 3T3 fibroblast cells grown on the surface of GO, rGO and CNT demonstrated the improvement of the gene transfection efficiency, even up to 250%, of cells grown on a cover glass, which additionally exhibited high biocompatibility as surface-coating materials [134]. According to this study, enhancing the biocompatibility of GBMs requires increasing their solubility and dispersibility by functionalising their surfaces.

Liao et al. [154] examined PG's and GO's blood compatibility and cytotoxicity in suspended human red blood cells (RBCs) and adherent skin fibroblasts using the efflux of haemoglobin from suspended RBCs and an *in vitro* methylthiazolyldiphenyl–tetrazolium bromide (MTT) assay, a toxicity assay and a water-soluble tetrazolium salt (WST-8) assay. Regarding the effect of sonication and of coating GO with chitosan, both PG and GO showed dose-dependent haemolytic activity on RBCs, whereas untreated GO showed less haemolytic activity on RBCs than sonicated GO. Likewise, PG showed lower haemolytic activity than GO with higher oxygen content on its surface, activity which was eliminated by coating GO with chitosan. The cytotoxicity of both PG and GO was evaluated by measuring mitochondrial activity in adherent human skin fibroblasts using two assays. On the one hand, the MTT assay failed to predict PG's and GO's toxicity due to their spontaneous reduction of MTT, which resulted in a false positive signal. On the other, the WST-8 assay revealed that aggregated PG was more damaging to mammalian fibroblasts than the reversibly aggregated GO. Thus, the toxicity of PG and GO depends upon the mode of interaction of GBMs with cells (i.e. suspension vs. adherent cell types) and the environment to which they are exposed (i.e. whether aggregation occurs).

GO's biocompatible effects on human fibroblast cells have also been investigated by culturing human fibroblast cells with different GO doses ( 0 - 125 μg/ml) for 5 d. The *in vivo* study three test groups containing 10 mice were injected using a single tail vein injection with 0.1, 0.25

and 0.4 mg of GO, respectively, for 1, 7, and 30 d. The *in vitro* results showed that doses exceeding 50 μg/mL induced obvious forms of cytotoxicity, including cell apoptosis and decreased cell adhesion while entering the endoplasm, mitochondria, lysosomes and nuclei, whereas doses less than 20 μg/mL showed no signs of toxicity to human fibroblasts. Regarding the *in vivo* results, the GO dose under 0.1 and 0.25 mg did not show obvious toxicity to mice whereas at 0.4 mg the mice exhibited chronic toxicity, 4/9 mice death as a result of the formation of granuloma mainly found in lung, liver, spleen and kidney almost could not be cleaned by the kidney. According to those results, GO exerts dose-dependent toxicity upon cells[155]. Another group studied the cytotoxicity of GO after purification in comparison with conventional GO. It was found that GO does not have a significant cytotoxic response up to 100 μg/ml and no granuloma formation and inflammation response up to 50 μg/ animal dose exposure [156].

Zhang et al. [157] used radio-tracing to determine the distribution and biocompatibility of GO in mice and found high GO uptake and long-term retention in the lungs. At 1 mg /kg of GO for 14 d, no sign of pathological change in mice organs was apparent, which implies that GO may be a promising carrier in targeted drug delivery. At 10 mg /kg body weight of GO for 14 d, mice exhibited significant pathological changes, including pulmonary oedema, inflammatory cell infiltration and the formation of granuloma in the lungs of mice. In other work, Hu et al. [158] studied the antibacterial activity of GO and rGO in inhibiting the growth of *E. coli* by way of slight cytotoxicity. Among the results, rGO showed less antibacterial activity than GO, whereas rGO's cytotoxicity was significantly greater than GO's due to their different surface charges and functional groups.

Liu et al. [105] functionalised PG with gelatine and loaded it with Dox for an ideal drug-carrying PG–gelatine complex that demonstrated high solubility and stability in various physiological fluids, a high drug-loading capacity and excellent therapeutic efficacy. When

administered directly into the lungs of mice, GO can cause lung injury, thereby activating inflammatory and apoptotic pathways. It is possible to overcome that problem, however, by using the block copolymer Pluronic. Duch et al. [159] studied that approach using PG after liquid phase exfoliation, which was further minimised when the unoxidised graphene was sufficiently dispersed with Pluronic as graphene's covalent oxidation is a chief source of its pulmonary toxicity.

PEG modifications have also been applied to PG and GO in order to enhance their biocompatibility and tumour targeting as well as reduce their non-specific binding to biological molecules and cells. Several studies demonstrated that GO's functionalisation with PEG showed insignificant *in vitro* toxicity to many cell lines, including lymphoblastoid cells (Raji cells) with GO–PEG– Dox at concentrations greater than 100 mg/L and a human colon cancer cell line, HCT 116, with GO–PEG–SN38–CPT [72, 78]. By extension, Yang et al. [160] functionalised PG with PEG coating using a fluorescent labelling method that showed insignificant signs of toxicity for the complex. In another study, long-term *in vivo* bio-distribution using $^{125}$I radionuclide-labelled PG functionalised with PEG was systematically explored in relation to the potential toxicity of PG over time. Its results indicated that PEGylated PG mostly accumulated in the reticuloendothelial system (e.g. spleen and liver) after intravenous administration and may be gradually cleared via faecal and renal excretion. At the dose of 20 mg/kg of $^{125}$I radionuclide-labelled PG functionalised with PEG, haematological analysis, blood biochemistry and histological examinations on the mice showed no obvious signs of toxicity over 3 months [161].

GO may cause thrombogenicity in mice and initiate a strong aggregatory response in human platelets [162] thus its biomedical applications are severely limited. When amine-modified graphene (G-NH2) was derived from GO sheets by replacing carboxyl groups with cytoprotective amines, it appeared to be the safest graphene derivative with no stimulatory

effect on human platelets. Moreover, unlike other graphene derivatives (e.g. GO and rGO), it did not enhance pulmonary thromboembolism in mice when introduced intravenously. Thus, G-NH2 may be safe for biomedical applications.

In sum, studies on biocompatibility have shown that functionalising the surfaces of GBMs contribute to their toxicity, for GBMs with functionalised surfaces have been significantly less toxic than their counterparts with non-functionalised ones.

## 1.8. Computational approaches to studying graphene

Bio-conjugated systems have recently attracted considerable attention for their potential use in biomedical applications. In multiple studies, several biomolecules, including peptides and proteins, were used to functionalise those nanostructures to make them applicable in composite materials, gas sensors, transparent electrodes and transistors[163-166]. In particular, single-layer PG appears to be a promising candidate owing to its outstanding properties[167]. In fact, due to its characteristic structures, graphene can interact with a wide variety of organic molecules by either covalent or non-covalent forces, including via hydrogen bonding, π–π stacking, electrostatic forces, van der Waals forces and hydrophobic interactions [7, 167-169]. However, an excess of π–π stacking and van der Waals forces as a result of attraction between adjacent layers of graphite layers to facilitates the formation of graphene, the irreversible aggregation of graphene or even its restacking to graphite, which greatly limits graphene's applications in biomedical applications.

### 1.8.1. Molecular dynamics (MD)

As a powerful tool that can help to answer several questions about graphene interaction with several biomolecules. The method involves simulating a set of particles that move under intermolecular forces following the equations of motion according to classical mechanics. The classical

approach to the method is based on the Born–Oppenheimer approximation[170], which considers only nuclear displacements. This sections provides a brief outline of the application and implementation of the concept of MD simulation.

The net force acting on an atom, *i*, in a system can be calculated from the derivative of the force field potential, *V(r)*, with respect to *r*, as in the following equation:

$$\boldsymbol{F_i} = -\frac{dV\ (r)}{dr_i} \qquad \textbf{Equation 1.9}$$

The motion of atoms over time is controlled by the total force according to Newton's second law of motion, as given in the next equation:

$$\boldsymbol{F} = m_i a_{\ i} \qquad \textbf{Equation 1.10}$$

in which *F* is the force that acts on atom *i* with mass *m* and acceleration *a*. The second-order differential equation can be written as follows, in which *x* is the atomic position and *t* is time:

$$\boldsymbol{F_i} = \ m_i\ \frac{d^2 x_i}{dt^2} \qquad \textbf{Equation 1.11}$$

The second-order Equation 1.11 is equivalent to the first-order Equations 1.12 and 1.13:

$$\boldsymbol{F_i} = \ m_i\ \frac{dv_i}{dt} \qquad \textbf{Equation 1.12}$$

$$\boldsymbol{v_i} = \frac{d\ x_i}{dt} \qquad \textbf{Equation 1.13}$$

In Equation 1.14, the velocity at time *t* is calculated, while the displacement of the position is calculated in Equation 1.15:

$$\frac{\boldsymbol{dx_i}}{\boldsymbol{dt}} = \ v_i + at \qquad \textbf{Equation 1.14}$$

$$\boldsymbol{x_i} = \ v_i\ t + \frac{1}{2}\ a_i\ t^2 + c \qquad \textbf{Equation 1.15}$$

A Taylor series can be used to determine the position in the future after a step involving $\Delta t$. Calculating atomic trajectories requires the initial velocities, positions and accelerations. The acceleration obtained from the potential energy function is given in Equation 1.16:

$$\boldsymbol{x_i}\,(\boldsymbol{t}+\Delta\boldsymbol{t}) = x_i(t) + \frac{dx_i}{dt}\Delta t + \frac{d^2x_i}{dt^2}\,\Delta\frac{t^2}{2} + ..$$ **Equation 1.16**

That equation is solved numerically in order to determine the position at future time $t + \Delta t$, which, if done repeatedly, generates a MD trajectory.

### 1.8.2. Solvation models

Water can be modelled either as individual solvent molecules, termed *explicit solvents*, or as continuous media, termed *implicit solvents*.

#### 1.8.2.1. Explicit solvent models

In explicit solvent models, solutes are surrounded completely by water molecules, meaning that several interactions have to be considered in analysing the system. For that reason, a simple model of water is desirable for the sake of computational costs and ease of analysis. The water models generally used are TIP3P[171] and SPC[172] models, in which hydrogen atoms have positive charges and oxygen atoms have negative ones. Each model is represented by a single set of van der Waals parameters, in which oxygen atoms are considered to be the site of interaction and the O–H bond of water is considered to be rigid.

#### 1.8.2.2. Implicit solvent models

In implicit solvent models, or *continuum models*[173], water is represented as a uniformly polarisable medium with a defined dielectric constant, ε. The simulation's computational cost is decreased by the model's low number of non-bonded interactions.

### 1.8.3. Periodic boundary conditions

The conditions in which the simulations are performed with few particles subjected to forces of bulk solvent are termed *periodic boundary conditions*. Because a simulation system is

surrounded by its own periodic image, the particles that move away from the simulation box from one end are forced to enter the box again from the other side. The interaction of a particle can occur only with the image of the particle nearest to it, because the boundary conditions are such that minimum image convention can occur for forces in short range. The consideration of long-range forces, by comparison, makes the state of particle highly complex, because the unit cell and all of its periodic images have to be considered, usually with the particle mesh Ewald method [174], an application of the Ewald summation, which itself is based on the concept that the direct summation of the interaction energies between particles is broken into two summations. The first summation, representing interactions in the short range, is the sum of the real space, which can be analysed in light of particle–particle interactions using a modified Coulomb's law. The second summation, representing interactions in the long range, is the reciprocal of the real space's sum [175], which can be analysed by using a Fourier transform to build a mesh of charges interpolated to form a grid.

### 1.8.4. Regulation of temperature and pressure

A MD simulation can simulate data under controlled conditions when the system has a fixed number of particles in a box of fixed size. That system, with a constant volume, energy and number of atoms, is compatible with the micro-canonical ensemble. By contrast, other ensembles, including the isothermal–isobaric ensemble or canonical ensemble, are simulated by thermostats and barostats that help to regulate the system's temperature and pressure. The total kinetic energy of the system yields the temperature of the system, as represented by the following equation:

$$\sum_{i=1}^{N_{df}} \frac{\boldsymbol{m_i v_i^2}}{\mathbf{2}} = \frac{N_{df} K_b T}{2} \qquad \textbf{Equation 1.17}$$

in which $N_{df}$ is the number of degrees of freedom, $K_b$ is the Boltzmann constant, and $T$ is the temperature. The equation indicates that the temperature can be controlled by altering the velocities of the particles in the system. The motion of particles has been ordered to maintain a constant temperature in the system by different thermostats, including Berendsen's [176], Nosé–Hoover's [177], Andersen's [178] and Langevin's [179].

The system is connected to an external heat bath with a fixed temperature according to Berendsen's thermostat, in which the velocities of the particles are scaled by a coupling parameter proportional to the temperature difference between the heat bath and the system in each step. The heat bath and the system are coupled by stochastic collisions in Andersen's thermostat that alter the system's kinetic energy. The new momentum is predicted based on the collision frequency following Boltzmann's distribution and Poisson's distribution of temperature. In the case of Nosé–Hoover's thermostat, an artificial variable is used in the Lagrangian, and the system is coupled by the artificial variable with a heat bath to regulate the temperature, which in turn regulates the velocity by which energy is transferred. Last, the Langevin thermostat is given by the Langevin equation of motion, a type of Newtonian equation of motion encompassing collision effects as well as frictional effects. The coupling of the heat bath to the system imparts a random force and frictional coefficient to each particle, and the temperature constant is maintained due to the balance between those factors.

### 1.8.5. Applying MD in studying biomolecular phenomena

Dynamic properties in fields of biophysics, pharmaceutical chemistry, enzymology, molecular biology, biotechnology and structural biochemistry have been studied with the help of MD. Time-dependent phenomena as well as thermodynamic properties can be studied with the aid of MD simulation, which affords insights into the dynamic aspects of structural recognition

and function. The evolution of the simulated structure is termed a *MD trajectory*, which generates data about energies, velocities and atomic positions.

The mechanism of the conformational change in a particular protein or the change in the binding energy of a specific drug candidate can be analysed with numerous MD packages. Molecular dynamics can also be used to explore various kinetic, thermodynamic and biomolecular structures involved in protein hydration [180], ion and small molecule transport [181, 182], macromolecular stability [183], enzyme activity [184, 185], protein folding [186, 187], conformational and allosteric processes [188] and protein association [189]. Thus, molecular drug design [190] and protein design [191], as well as structural determination by X-ray [192], nuclear magnetic resonance (NMR) [193] and modelling [194], can be studied with the aid of MD.

### 1.8.6. Recent advances in the theoretical aspects of MD

#### 1.8.6.1. Force fields

The stability and validity of the MD simulation of graphene, proteins and all macromolecules depend strongly on the accuracy of the potential energy function [195, 196]. At base, computations with simple forms of energy functions are easier than ones with complex forms, and the minimisation and integrators of motion can be made effective by using easily accessible derivatives. The force fields used during the molecular simulation of proteins are mostly similar; torsions are represented by Fourier series, bond angles and bond lengths are represented in harmonic terms, and atomic interactions are described by a combination of the Coulombic and Lennard–Jones functions.

The parameters for the protein system are obtained first, followed by ones for lipids, nucleic acids and other biological molecules in a manner consistent with the protein set. Different approaches to deriving individual parameters cause the chief differences in the various force

fields. The final results of the simulation generate desirable experimental observations because the parameters have compensatory components and interrelations among themselves. The treatment of interactions between atoms bonded by a few intermediate atoms and the treatment of long-range electrostatic interactions make different energies with an alternative energy function possible.

For that reason, different force fields cannot be used to compare the parameters of certain types of atoms, and the parameters cannot be directly transferred within the various fields. Among them, the consistent valence force field [197] possesses a highly complex functional form that distinguishes it from other fields due to minor factors such as types of scaling factors used for non-bonding interactions, various treatments of improper torsions or explicit or implicit types of hydrogen bonding. If van der Waals parameters for all force fields are generated for both liquid and solid phases by being empirically fitted with models with small molecule systems, the densities of the solvated protein system become similar to the real system. Although a mixture of quantum mechanical and empirical data can be used to easily adjust the torsional parameters, it is quite difficult to determine parameters for the template's partial charges regarding the atoms in the residue where resultant electrostatic interactions should be balanced with definite models of water.

In one approach, partial changes in the gas phase are analysed with the help of quantum mechanical calculations of a model compound. In turn, the calculated charges can be measured with the aid of a standard multiplicative factor. A study of 20 protein force fields based on an alanine tetrapeptide model using *ab initio* quantum mechanical calculations revealed inconsistent results among the fields [198].

The restrained electrostatic potential method[198, 199] has been used to calculate partial charges in the AMBER force field, where electrostatic potential obtained after quantum mechanical calculations is placed on the molecular surfaces with the help of an atom-centred

point charge model. Different studies have shown that the model was more successful in calculating conformational energies in the AMBER force field than in others [198]. The restrained electrostatic potential charges have been analysed for molecules with atom-centred polarisation and lone pair donor sites[200].

Another model, the general AMBER force field [201], for organic molecules has been developed to be compatible with existing AMBER force fields. In such work, an automated technique generates the parameters (e.g. for a range of pharmaceutically significant molecules), such that protein–ligand simulations can be used to design drugs, which overcomes the challenge of manually assigning parameters to different ligands.

Techniques of covalent and non-covalent modification have provided researchers with an array of applications for graphene [167]. On the one hand, covalent modification creates chemical bonds between materials and graphene, thereby modifying the graphene carbon atoms' hybridisation and structure and consequently changing the physico-chemical properties of the materials. On the other, non-covalent modification allows the graphene's surface to adsorb materials due to weak non-covalent forces; however, such adsorption has less profound effects on the physico-chemical properties of the materials than covalent modification [82, 167].

Computational chemistry, discussed in greater detail in Chapter 2, establishes a clear understanding of the strength and nature of graphene's interactions with amino acids. The effects of graphene's modifications with such materials have also been obtained by modelling with either electronic structural approaches derived from quantum mechanics or molecular mechanical approaches that significantly simplify the calculations of molecular systems[202]. MD is a technique that can be performed using various widely available software packages, including AMBER[203], GROMACS[204], CHARMM[205], large-scale atomic/molecular massively parallel simulator (LAMMPS)[206] and NAMD[207]. The chief limitations of MD

simulations are the cost of the computational calculations, the time scale's being limited to microseconds and the length scale's being limited to approximately 10 nm per dimension[202]. In certain applications, modified graphene derivatives are highly attractive due to their unique properties, and in particular, GO is useful due to its high number of oxygenated groups. Considering that condition, Lerf and Klinowski (Figure 1.3) [35] developed a new structural model for GO with two types of regions: aliphatic regions with six membered rings and aromatic regions with unoxidised benzene rings. The degree of oxidation affects the size of both types, and a flat carbon lattice is the result of double bonds, epoxide groups and an aromatic structure. In a tetrahedral configuration, distorted OH groups attached to carbon atoms cause layers of the lattice to wrinkle, while below and above the lattice are oxygen functional groups in different concentrations. Such negatively charged arrangements of oxygen atoms protect the carbon atoms from nucleophilic attack, thereby rendering the GO epoxide groups chemically inactive [35, 208].

In a series of experiments and MD simulations, Shih et al. [209] found that GO behaved differently in aqueous solutions at different pH levels. The OPLS–AA potential was the force field used in that study, implemented with the GROMACS 4.020 software package. At low pH levels, GO's hydrophilicity decreased, and GO sheets became aggregated due to the protonation of carboxyl groups. MD simulations attributed that aggregation to the formation of sandwich-like aggregates of GO–water–GO that were stable in water.

Conversely, at high pH levels, the GO sheets dissolved in water due to the hydrophilicity of the deprotonated carboxyl groups [209]. The effect of reducing atmospheric pressure during GO reduction has also been studied, particularly with MD simulations using the reactive force field and Car–Parrinello MD with density functional theory (DFT) [210]. While examining the GO reduction process in an active chemical atmosphere enriched with hydrogen, those authors also investigated the pressure and concentration of hydrogen gas as a function of temperature.

Among their results, GO at low temperatures prevented its structural damage. The $sp^2$ bond's protective mechanism resulting from the migration of the epoxide group also protected the integrity of the GO lattice structure and prevented the formation of carbonyl pairs. Although the presence of hydrogen removed the oxygen, it did not suppress the breaking of C–C bonds, which resulted in decreased C–O bonding in the GO.

In another study [211], researchers examined how carbon monoxide, CO, induces the reduction of oxygen groups in GO's basal plane by using MD simulations with a reactive force field and DFT calculations. The results showed that oxygen from GO was removed by CO's reducing action; at low temperatures, the energy barriers were easily overcome and exceptionally small. rGO with excellent properties can also be gained by reducing GO in a CO atmosphere.

In still other research, MD simulations using the LAMMPS package were created to study the wetting properties of GO with different concentrations of oxygen-containing functional groups, morphological corrugation and textural patterns. The oxygen-containing groups in GO became hydrophilic, thereby decreasing the contact angle of water with its concentration ($c$) and prompting a transition at $c \approx 11\%$ that controlled the spread of water droplets in lateral spans. That technique can therefore be used to control the performance of water on the GO surface [212]. According to the literature, the suggested contact angle of water on a graphene surface is 127°, which is compatible with the accepted value on a graphite surface—that is, 90−95°. MD simulations performed with GROMACS have been used to predict the contact angle of water on graphene, and both Taherian et al. and Shih et al. estimated that angle on graphene's monolayer to be approximately 95−100° [213, 214].

### 1.8.6.2 Graphene's interaction with small molecules

After its discovery, graphene was quickly found to be a powerful adsorbent that interacts with a range of molecules and causes specific physico-chemical responses that can be used in new types of sensors [215]. As a consequence, several experimental and computational studies on

graphene's interactions with small molecules have focused on the nature and strength of those interactions. In one, Lazar et al. [216] studied the adsorption of seven small organic molecules (i.e. acetonitrile, ethanol, acetone, dichloromethane, toluene, hexane and ethyl acetate) on graphene to identify the nature and magnitude of the interactions. The strength of the interactions was estimated using DFT and empirical calculations on infinite and coronene-based models of graphene. Calculations following symmetry-adapted perturbation theory (SAPT) indicated that the interactions were driven by London dispersive forces[216].

In another, Jenness and Jordan [217] studied the adsorption of water molecules with graphene by using density-fitting DFT SAPT (DF–DFT–SAPT) and found an interaction energy of -2.2 kcal/mol. By contrast, Bludsky et al. [218], using DFT and coupled cluster theory, obtained an interaction energy of -2.8 kcal/mol.

Schlierf et al.[219] studied four pyrenes functionalised with sulphonic groups using modelling in the OPLS–AA force field, as implemented in the GROMACS software package. Results of MD showed that the molecular dipole aided the sliding of the molecule into the solvent layer and consequently the lateral displacement of the water molecules between PG and the aromatic cores of the dye, particularly when molecules adsorbed on PG's surface yield stable suspensions in water. The stability of such suspensions was highly pH-responsive for all four derivatives, while the solubility with fluctuating pH was the same for the various functionalisations of the pyrene core. In that graphene organic complex, colloidal stability was achieved via electrostatic repulsion between charges introduced by the surfactant, sodium SDBS, solved by adding salts or changing the pH. Added to that, Zhou et al. [220] recently studied benzene and benzene derivatives adsorbed on graphene by using a density-functional tight-binding method. As a result, they reported that the benzene derivatives showed higher adsorption energies than pure benzene, regardless of benzene substituents and electronic properties.

Large molecules such as tetracyanoethylene, an electron-acceptor molecule, may contain high number of sites of symmetry. Lu et al.'s [221] calculations identified tetracyanoethylene's adsorption energies at five individual sites based on DFT, for results indicating that graphene's electronic structure could be controlled by organic molecules in order to build graphene-based electronic devices without graphene etching or cutting.

Characterisations of the potential energy of the surfaces of adsorbates sliding on graphene have increased scholarly focus on the possible frictional force generated. In such research, MD simulations were performed with different degrees of fluorination sliding over PG using LAMMPS and the Prandtl–Tomlinson model. As a result, friction was found to increase monotonically with fluorination [222].

The strength of adsorption depends on the topology and concentration of adsorbates, thereby allowing the adsorbates to significantly modify graphene's electronic structure and bond covalently. Boukhvalov and Katsnelson [18] studied the covalent functionalisation of graphene using oxygen and hydrofluoric acid, with calculations performed using DFT with the generalised gradient approximation to generate sound results for layer-related materials due to error cancellation and Troullier–Martins pseudopotentials. Their results indicated that the dissociation energy of fluorine atoms in the bonds at low concentrations was approximately 50 kcal /mol, while the dissociation energy of fully fluorinated graphene was 112 kcal /mol, thus resulting in the transformation of a carbon atom from $sp^2$ to $sp^3$ as fluorine atoms became attached to the graphene[18].

### 1.8.6.3. Graphene's interaction with proteins

In nanomedicine, it is important to understand biomolecules' interactions with graphene, because graphene and its derivatives can act as enzymatic inhibitors. Sun et al. investigated interactions between α-chymotrypsin (ChT) and PG as well as ChT and GO via MD simulation using NAMD with a CHARMM force field [223]. ChT was adsorbed onto the surface of GO

and graphene, which strongly inhibited enzymatic activity depending upon ChT's position and formation on graphene's surface.

In other work, the translocation of DNA strands via graphene nanopores was examined with different film thicknesses using the particle mesh Ewald method to evaluate electrostatic interactions. The AMBER-94 force field was applied to model the atomic interactions in DNA oligonucleotides and the interactions between DNA oligonucleotides and water molecules or ions. The study revealed that along with the base volume of DNA, the change in the the ion distribution adjacent to the nanopore participated in blocking the ionic current. The cations controlled that current via the graphene's nanopore because the DNA strands with negative charges attracted cations that concentrated near graphene's surface and formed an electric double layer. The high concentration of cations in that layer inhibited DNA's physical blockage effects on the ionic current. The decreased current mainly stemmed from the reduction of $Cl^-$ ions, which were repelled when the DNA strand entered the nanopore. Calculations indicated that increasing the graphene membrane's thickness could also increase the DNA's physical blockage effect on the ionic current and improve the nanopore's sensitivity to the four DNA bases [163].

The entire sequence of a single-stranded DNA (ssDNA) interaction's with a graphene nanoribbon has also been studied, namely by using DFT–NEGF transport calculations. The overall aim was to produce an ultrasensitive, graphene-embedded, nano-channel device that effectively controls the motion of nucleobases via π–π interactions and deciphers ultrasensitive characteristics. Results indicated the theoretical feasibility of constructing highly sensitive graphene devices for ssDNA sequencing as a rapid, cost-effective alternative to current techniques [85].

The interaction between graphene's surface and peptides was investigated using MD by computing graphene's binding enthalpies with a series of tripeptides and water molecules to

study the solvent's effect. Trajectories indicated that graphene indeed affected the conformation of peptides, while the presence of water at the graphene–peptide interface strongly influenced the conformation and binding of peptides. In addition, the binding of the hydrophobic residues was weaker than that of hydrophilic residues, thereby suggesting that including explicit solvent atoms is important to accurately simulate experimental conditions [224].

Amino acids are naturally occurring, safe and environmentally friendly substances with the potential to make graphene a promising material for drug delivery. The ability of amino acids to interact with graphene surfaces in aqueous solutions has been studied theoretically and, to a lesser degree, experimentally. The interaction of PG or GO with the aromatic amino acids tryptophan (Trp), histidine (His), phenylalanine (Phe) and tyrosine (Tyr), for example, was examined using DFT-based methods. The results indicated that hydrogen bonding interactions stabilised GO complexes, while π–π interactions stabilised PG complexes, thus making the binding energies of GO complexes greater than those of PG complexes. The intermolecular hydrogen bonding between GO–Phe did not occur due to a lack of any heteroatoms other than carbon and hydrogen in Phe[225]. The presence of a double hydrogen bond with His afforded the highest binding energy with GO, whereas Phe showed the least interaction. For PG, the binding energy was highest with Trp, and similar to GO, Phe had the lowest binding energy.

Another study [226] used DFT and MD approaches to examine the energies, geometries, isotherms, energies of adsorption and electronic band structures of L-leucine molecules on graphene. The adsorption direction of L-leucine controlled graphene's electronic structure and the energetic stability of L-leucine on graphene, whereas MD simulations indicated that the van der Waals interaction between the graphene and L-leucine controlled the adsorption process under different temperature and pressure conditions, as well as that L-leucine adsorbed onto graphene in aqueous solution [226].

Four amino acid molecules, namely Tyr, Phe, Trp and His, have been studied in combination with CNTs and PG to determine the effect of curvature on non-covalent interaction. That research involved using DFT and Møller–Plesset second-order perturbation theory. Among the findings, configurations of complexes with similar equilibrium and π–π interactions were weak, thereby making the aromatic rings of the amino acids orient themselves in parallel structures over PG and CNT. The amino acid with the highest binding strength was Trp, while His was the lowest, because the interaction energy between graphene–CNT and His was 0.55/0.40 eV and for Trp was 0.84/0.72 eV. The binding strength of the amino acids was weaker with CNT than with PG [227].

Another theoretical study on the binding of the amino acids proline, glycine and hydroxyproline to PG and calcium-doped graphene by DFT as well as *ab initio* MD simulations showed adsorption energies ranging from -90 meV to 20 meV. Among its other results, the binding of amino acids to graphene was enhanced by doping the carbon's surface with calcium atoms [228].

The interaction between graphene and amino acids can occur either by hydrogen bonding or π–π interactions. In research on the topic, it was observed that aromatic side chains of amino acid interact with graphene benzene rings via π–π interaction with Trp, Tyr and Phe[225]. It was thus proposed that the valine isopropyl group interacted with the graphene benzene group via hydrogen bonding[229]. PG has weak hydrogen bonding and van der Waals interactions, poorly disperses in water and tends to aggregate.

## 2. Aims and Objectives

The use of GBMs in biomedical applications has been shown in Chapter 1 to be a growing area of research with considerable potential. However, it remains a very new area. The 2D geometry of GBMs is used as a drug delivery carrier that can directly target disease cells. Yet major effort remains to enhance the uniformity of the samples. A carefully designed drug delivery carrier may produce these results by adjusting the size, shape and surface chemistry. However, the design of a drug delivery system for GBMs to achieve these objectives faces significant challenges. Before additional functionalisation can occur to organize the GBMs for their particular use and before the material may proceed to a place in the clinic, it is essential to be very well characterised. From this context, it was hypothesised that graphene and related materials can be adequately prepared for targeting certain cells by using controlled formulations and characterisation methods, using a combination of traditional and novel methods. The ideal nanocarrier is inert and stable as it passes through the body, while being able to cross the essential physiological barriers and carry its load to both the target cell and frequently the specific intracellular region essential for therapeutic effect.

Thus the aims of this thesis are:

- To evaluate the stability of pristine graphene with amino acids known to be biologically benign (GRAS, by the FDA) and determine appropriate formulations to minimise aggregation.
- To understand the role of amino acids in the stability of graphene suspensions by comparing computer modelling and experimental data.
- To evaluate the ability of pristine graphene in the presence of the aforementioned peptides to serve as a drug delivery system using doxorubicin as a model drug: this was determined by experiments using fluorescence and computer modelling.

- To determine the cell viability of the different suspensions using mda-mb-231cell lines.
- To evaluate the stability of graphene oxide suspensions using its natural fluorescence properties.

To meet the aforementioned aims, the objectives of this thesis are to

- ***To examine the use of amino acids in pristine graphene as biocompatible exfoliating and suspending agents***- First focused on molecular dynamics (MD) simulations to obtain insights into the interactions of a model single-layer graphene flake in water with increasing numbers of L-Trp, L-Tyr and L-Val molecules present. In addition, using experimental study to assess the ability of these three amino acids to assist graphene exfoliation using sonication and stabilize the suspensions. Last, quantify the results using UV-vis absorption spectroscopy and atomic force microscopy (AFM).
- ***To design a drug carrier using pristine graphene and peptides that could be conjugated to Dox to provide targeted delivery to the mda-mb-231cells-*** Initially, a Study show that short tryptophan peptides (i.e. monopeptide, dipeptides and tripeptides) can functionalise PG to form stable suspensions using MD, UV-vis absorption spectroscopy, AFM, Raman spectroscopy, DLS, zeta potential and FTIR spectroscopy. The resulting suspensions may also be employed as vehicles for drug delivery by using Dox as a model drug. Fluorescence spectroscopy have been utilised in determining the entrapment efficiency (EE), loading efficiency (LE) and the Dox release from PG-$Trp_x$ . The *in vitro* cytotoxicity and intracellular distribution of free Dox, PG–Dox and PG–$Trp_x$–Dox systems was tested with a MTS assay and fluorescence microscopy using MDA-MB-231 cells.
- ***To formulate and characterise washed, unwashed and functionalised GO designed for use in drug delivery-*** Samples of GO and GO-PEG were characterised, first by using the traditional techniques of optical microscopy, AFM and DLS, and, once their

limitations were demonstrated, by using RICS for comparison. The current GO characterisation techniques were limited, both in terms of the size range that could be applied, and the often prolonged timescales needed. Additionally, to study their stability in biologically relevant media. Among the results, RICS allowed us to capture the full range of flake sizes and the interactions of flakes with relevant biological media.

# 3. Solvation of Pristine Graphene using Amino Acids: a Molecular Simulation and Experimental Analysis

Fai A. Alkathiri[a], Catriona McCallion[a], Alexander P. Golovanov[b], John Burthem[c], Alain Pluen[a,*] and Richard A. Bryce[a,*]

[a] *Division of Pharmacy and Optometry, School of Health Sciences, University of Manchester, Manchester, UK*

[b] *Manchester Institute of Biotechnology, and School of Chemistry, Faculty of Science and Engineering, University of Manchester, Manchester, UK*

[c] *Division of Cancer Sciences, University of Manchester, Manchester, UK*

Corresponding Authors

*Richard Bryce, Division of Pharmacy and Optometry, School of Health Sciences, University of Manchester, Manchester, M13 9PT, U.K. Email: Richard.Bryce@manchester.ac.uk, Tel: (0)161-275-8345

*Alain Pluen, Division of Pharmacy and Optometry, School of Health Sciences, University of Manchester, Manchester, M13 9PT, U.K. Email: Alain.Pluen@manchester.ac.uk, Tel: (0)161-275-1792

## 3.1. Abstract

We explore the ability of amino acid solutions, of L-Trp, L-Tyr or L-Val, to solvate pristine graphene flakes in an aqueous environment, via atomistic molecular dynamics simulations and experimental characterization. In accord with previous theoretical work, simulations of single amino acid adsorption on graphene predict that L-Trp is most strongly bound, followed by L-Tyr then L-Val. As the number of amino acids is increased in the simulations, steric hindrance at the graphene interface and amino acid clustering (most pronounced for L-Tyr) reduces the efficiency of interaction with graphene. Using atomic force microscopy and UV-vis absorption spectroscopy, we determine that all three amino acid solutions can exfoliate and suspend pristine graphene flakes in water. However, L-Trp and L-Tyr solutions are considerably more effective than L-Val: L-Trp produces the most stable suspensions and thinnest graphene flakes compared to L-Tyr, with a mean thickness of 6.4 nm, and a narrow distribution of diameter with a mean value of 16 nm, commensurate with the width of cell membranes. At high concentration of L-Trp and L-Tyr, there was severe instability of the suspensions, along with agglomeration and precipitation; this reflects clustering of amino acid molecules observed in molecular dynamics simulations. This study indicates the potential of amino acids to exfoliate and suspend pristine graphene as a step towards developing non-toxic graphene-based vehicles for drug delivery and other in vivo applications.

## 3.2. Introduction

Graphene is a two-dimensional allotrope of carbon, comprising a single layer of $sp^2$ hybridized carbon atoms arranged in a hexagonal lattice.[1] Its exceptional mechanical strength,[230] large specific surface area[2], high absorbance capacity[231] and high thermal and electrical conductivity[3] make graphene an ideal material for a range of applications, including sensing,[232] nano-electronics,[233] catalysis[234] and as a potential vehicle for delivering therapeutic agents such as small molecule drugs,[84, 88, 90, 91, 95] proteins[235, 236] and DNA[237] including entire genes.[87, 238]

While interest in using graphene for drug delivery has grown rapidly in recent years, much initial work has focused on graphene oxide (GO), due to its inherent solubility and ease of functionalization:[19] for example, Jie et al.[89] prepared GO with poly(sebacic anhydride) as a drug carrier for the antibiotic, levofloxacin. Rana et al.[90] covalently functionalised GO with chitosan; ibuprofen and 5-fluorouracil were then loaded on to the GO-chitosan complex to achieve controlled release. Although the use of pristine graphene as a platform for small molecule adhesion is less well developed,[17] its outstanding properties make it a promising candidate for drug delivery.[167] Pristine graphene offers a defect-free plane that can interact with a variety of organic molecules by noncovalent forces such as ion-π, CH-π and π–π interactions.[239-242]

However, the intrinsically hydrophobic nature of graphene leads to its poor solubility in polar solvents, forming irreversible aggregates in water. To improve its aqueous solubility, graphene requires surfactants or surface modification.[18] Efforts have included functionalization with gelatine[105] and coating by polyethylene glycol.[160] For pharmaceutical applications of graphene, a biologically benign excipient is needed.[243] In this regard, amino acids are promising candidates; these non-toxic reagents have been used successfully to coat other nanoparticles, improving their stability in a biological environment.[244, 245] Amino acids in

their native L-isomer form have also been used to stabilize suspensions of GO[246] and reduced GO (rGO);[247] for example it was found that a rGO dispersion was stabilized by the presence of L-Trp.[248] Covalent modification of the carboxylic acid and epoxy groups on the surface of GO[249] by amino acids such as L-Phe, L-Tyr, L-Leu, L-Met and L-Val led to increased stability of the resulting suspensions.

Nevertheless, the ability of amino acids to solvate pristine graphene, a fundamentally different and more hydrophobic material than GO or rGO, remains largely unexplored. In this work, we employ molecular dynamics (MD) simulations to obtain insights into the interactions of a model single layer graphene flake in water with increasing numbers of L-Trp, L-Tyr and L-Val molecules present. We also experimentally assess the ability of these three amino acids to assist graphene exfoliation using sonication, and stabilize the suspensions; we quantify the results using UV-vis absorption spectroscopy and atomic force microscopy (AFM).

## 3.3. Materials and methods

### 3.3.1 Molecular dynamics simulations

A model single layer graphene flake in a hexagonal arrangement of size $C_{96}H_{24}$ was constructed using *carbon nanotube builder* in VMD.[250] We denote the systems as $G(Trp)_n$, $G(Tyr)_n$ and $G(Val)_n$ where Trp, Tyr and Val are the amino acid types and *n* is the number of amino acids used in addition to the graphene flake. Four graphene systems were constructed, comprising *n* = 1, 6, 12 or 24 amino acids placed around the flake. This combination of amino acids and $C_{96}H_{24}$ flake provides a suitable basis for studying direct graphene-amino acids interactions under dilute and more concentrated conditions; in the latter situation, potentially indirect interactions can also be sampled, e.g. second solvation shell effects. The graphene-amino acid systems were then solvated octahedrally with explicit water molecules. Further details of the twelve simulation systems are given in Appendix Table 8.1. The flake was modelled as neutral,

with aromatic atom types *ca* and *ha* from the GAFF force field.[251] L-isomers of Trp, Tyr and Val amino acids were modelled in zwitterionic form, using the ff14SB force field.[252] Water was represented via the TIP3P model.[171]

Molecular dynamics simulations of these systems used the AMBER16 simulation software package.[253] The SHAKE algorithm[254] was applied to constrain lengths of covalent bonds involving hydrogen atoms. A 2 fs time step was employed. Temperature was regulated via a Langevin thermostat[255] which used a collision frequency of 1 $ps^{-1}$. A nonbonded cutoff of 10 Å was used for nonelectrostatic interactions and the particle mesh Ewald method for long range electrostatic interactions.[174] After initial energy minimisation, for the $n$ = 6, 12 and 24 amino acid systems, the locations of the amino acids around the graphene were randomized using simulated annealing to 600 K via molecular dynamics for 20 ns, with strong constraints on graphene atoms relative to their initial positions (500 kcal $mol^{-1}$ $Å^{-2}$); this was followed by cooling with these restraints to 298 K over 20 ns. After re-minimization, the systems were equilibrated to 298 K using rounds of NVT and NPT dynamics over 2 ns, with gradual removal of restraints on graphene atoms from 10 kcal $mol^{-1}$ $Å^{-2}$ to zero. Finally, NVT production dynamics without atomic restraints was performed for 500 ns.

For geometric analyses of the simulations, the *cpptraj* module of AmberTools16[256] was employed. Adsorption of an amino acid on graphene was defined as a distance of ≤ 5.5 Å between the centres of mass of the amino acid and the closest graphene aromatic ring. To evaluate the orientation of the side-chain with respect to the graphene surface, the angle $\theta$ between the normal to the graphene surface and a vector defined within the amino acid side-chain was computed: for L-Trp, this vector was from atom $C_{\delta 1}$ to $C_{\eta 2}$; for L-Tyr, from $C_{\zeta}$ to $C_{\nu}$; ; and for L-Val, from $C_{\alpha}$ to $C_{\beta}$. .

Computation of amino acid-graphene interaction energies was performed for five equispaced configurations over the 500 ns production trajectory, using the PM7 semi-empirical quantum mechanical (QM) Hamiltonian as implemented in the Gaussian 16 software package.[257] This model includes a correction for dispersion[258] and hydrogen bonding.[259] Specifically, we note that in a study of desorption of four aromatic hydrocarbons from graphene, the PM7 Hamiltonian gave predicted interaction energies with a mean signed error of 5.7 kcal/mol from values obtained from temperature-programmed desorption experiments.[260] For further validation, we calculate gas-phase interaction energies at the PM7 and ω B97X-D/def2-SVP density functional theory (DFT) levels,[261] for a set of five geometries obtained from MD simulations in water of $G(Trp)_n$, $G(Tyr)_n$ and $G(Val)_n$ for $n = 1$ and $n = 6$ (Table 8.2, Appendix); we find the PM7 method systematically overpredicts the graphene-amino acid energy $\Delta E_g$ relative to DFT, by 2.7 kcal/mol on average; there is a smaller relative error $\Delta\Delta E_g$ of 1.3 kcal/mol between $n = 1$ and $n = 6$, with a relative error in the corresponding dispersion energy component of 1.2 kcal/mol. This suggests PM7 is capable of providing insight into trends in graphene binding across amino acid type and for differing numbers of amino acids.

### 3.3.2. Materials

Acid-washed stacked graphene platelet nanofibers (SGNFs), of mean diameter 40 - 50 nm, were purchased from Strem Chemicals, Inc. (United Kingdom). Graphite powder (diameter <45.0 μm, purity ≥ 99.99%), L-valine, L-tyrosine and L-tryptophan from non-animal sources were purchased from Sigma Aldrich (UK). All of the solutions were prepared in Milli-Q water.

## 3.4. Graphene suspension preparation

L-amino acids and graphitic material (either graphite powder or SGNFs) were weighted directly into an RBF for bath sonication. The graphitic material and amino acid powder were

ground together using a tissue grinder and a small amount of water (2 mL) for the maximum concentrations of L-valine, then the paste was topped up to the final volume with fresh Milli-Q water. The full amount of water was added directly to the lower final concentrations of L-amino acid (40 mL). Bath sonication was regularly cooled using ice water, in order to prevent the temperature from rising above 35 °C. Sonication was performed at 59 kHz, 100% power and sonicated between 1-10 h.

## 3.5. Characterisation of graphene/amino acid suspensions

UV-vis absorption spectroscopy was recorded using a Cary 60 UV-vis spectrophotometer (Agilent, USA). This technique was used both to monitor the concentration of the suspensions and to assess their quality. Atomic force microscopy was performed using a Bruker MultiMode8 (Bruker, UK) with a Scanasyst-air probe. Bath sonication was performed using a Falc Labsonic LBS 1 sonication bath (Falc Instruments, Italy).

### 3.5.1. UV-vis absorption spectroscopy

Absorption spectra of the suspensions were recorded between 200 and 800 nm in a quartz cuvette with a path length of 1.0 cm. Amino acid solution was used as a blank, which was subtracted prior to measurement. Stability measurements were performed after the suspensions were left in borosilicate glass vials at 4.0°C undisturbed for four weeks. Graphene concentrations were determined using the Beer-Lambert law, where absorbance $A = \alpha_\lambda Cl$ where $\alpha_\lambda$ is the extinction coefficient ($\alpha_\lambda$= 4861 $Lg^{-1}m^{-1}$ at $\lambda$ = 750 nm),[262] $C$ is the concentration ($gL^{-1}$) and $l$ is the path length (cm). The average number of graphene layers per flake was estimated from the shape of the suspension's absorption spectrum using an empirical formula derived by Backes et al.,[262] as $< N > = (35.7 \cdot (A_{550}/A_{325}) - 14.8)$, where $A_\lambda$ is

absorption at the wavelength λ and <N> is the average number of layers found in the suspended flakes.

### 3.5.2. Atomic force microscopy

Graphene suspensions in amino acid solutions were filtered on to Nuclepore Track Etched Membrane filters using vacuum filtration. Next, the deposited flakes were washed with Milli-Q water and transferred onto silicon wafers with a 290.0 nm oxide layer using GelPak film. Images were obtained using both contact mode and Bruker® ScanAsyst™ mode, which performs a very fast extension-retraction force curve at each measurement point and alters the position of the tip to compensate for any change in topography. In addition, ScanAsyst™ mode will automatically change parameters such as gain while the image is being recorded.

### 3.5.3. Preparation of graphene suspensions

The experiments utilised pristine graphite powder, which was exfoliated using bath sonication in aqueous L-Val solutions over a concentration range of 0.022 – 474 mM. It includes saturated solutions of L-Val; the solubility limit of L-Val in Milli-Q water is 474 mM.[263] Stacked graphene nanofibers were probe sonicated in aromatic amino acid solutions with concentrations ranging from 0 – 2200 μM. The concentration range of the aromatic amino acids was kept consistent; the upper limit was determined by the amino acid with the lowest solubility limit, i.e. L-Tyr, which has a solubility limit of 2.5 mM in pure water;[264] this compares with a value of 55 mM for L-Trp in pure water[264].

## 3.6. **Results**

### 3.6.1. Molecular dynamics simulations at infinite dilution

We first consider the interaction of a single L-Trp, L-Tyr or L-Val amino acid with a $C_{96}H_{24}$ graphene flake, over the course of 500 ns MD simulation in explicit aqueous solvent, for convenience referring to these systems as $G(Trp)_1$, $G(Tyr)_1$ and $G(Val)_1$, respectively. Over the duration of the simulations, the L-Trp and L-Tyr molecules remain bound to the graphene surface (Figure 3.1a,b), with average distances between the molecule's center of mass and the graphene surface of 4.1 and 4.2 Å respectively. Inspection of these trajectories indicate persistent parallel π–π interactions between the amino acid rings and the graphene surface (Figure 3.2a,b). This is also evidenced by a shorter average sidechain-graphene distances, of 4.6 and 4.5 Å for L-Trp and L-Tyr respectively; this compares with backbone amino and carboxylate-graphene distances to graphene of 6.5 – 6.8 Å for L-Trp and L-Tyr. A representative structure from the MD simulations indicates projection of these charged amino and carboxyl groups towards aqueous solvent (Figures 3.2a,b and 3a,b), while the side-chains stack with the graphene surface. For only when the amino acid is graphene-bound, we also compute the MD average of angle $\theta$ between the normal to the graphene plane and side-chain vector of amino acid (see Methods for definition). From this, we obtain average $\theta$ values of 89.9 ± 0.2° and 123.9 ± 2.8° for L-Trp and L-Tyr respectively, suggesting parallel stacking is more strictly preserved for L-Trp than L-Tyr over the trajectory. In both cases, while maintaining a stacked geometry during the MD simulation, the sidechains are observed to translate quite freely on the hydrophobic face of the flake.

The potential energy of interaction ($\Delta E_g$) between the L-Trp sidechain, averaged over equispaced trajectory snapshots, was calculated at the PM7 level of semiempirical quantum mechanics as -30.5 kcal/mol (Table 3.1). As expected, of this $\Delta E_g$, the majority (-27.6

kcal/mol) is computed to arise from dispersive interactions (Table 3.1). The L-Tyr molecule is predicted to bind to graphene with 6 kcal/mol lower affinity than L-Trp (Table 3.1). This might be expected given the larger surface of the bicyclic indole ring of L-Trp compared to the phenol ring of L-Tyr. Indeed, of this 6 kcal/mol difference, 5 kcal/mol arises from the dispersion component of the computed energy. The greater π−π stacking ability of L-Trp side-chains compared to L-Tyr has been well documented[227].

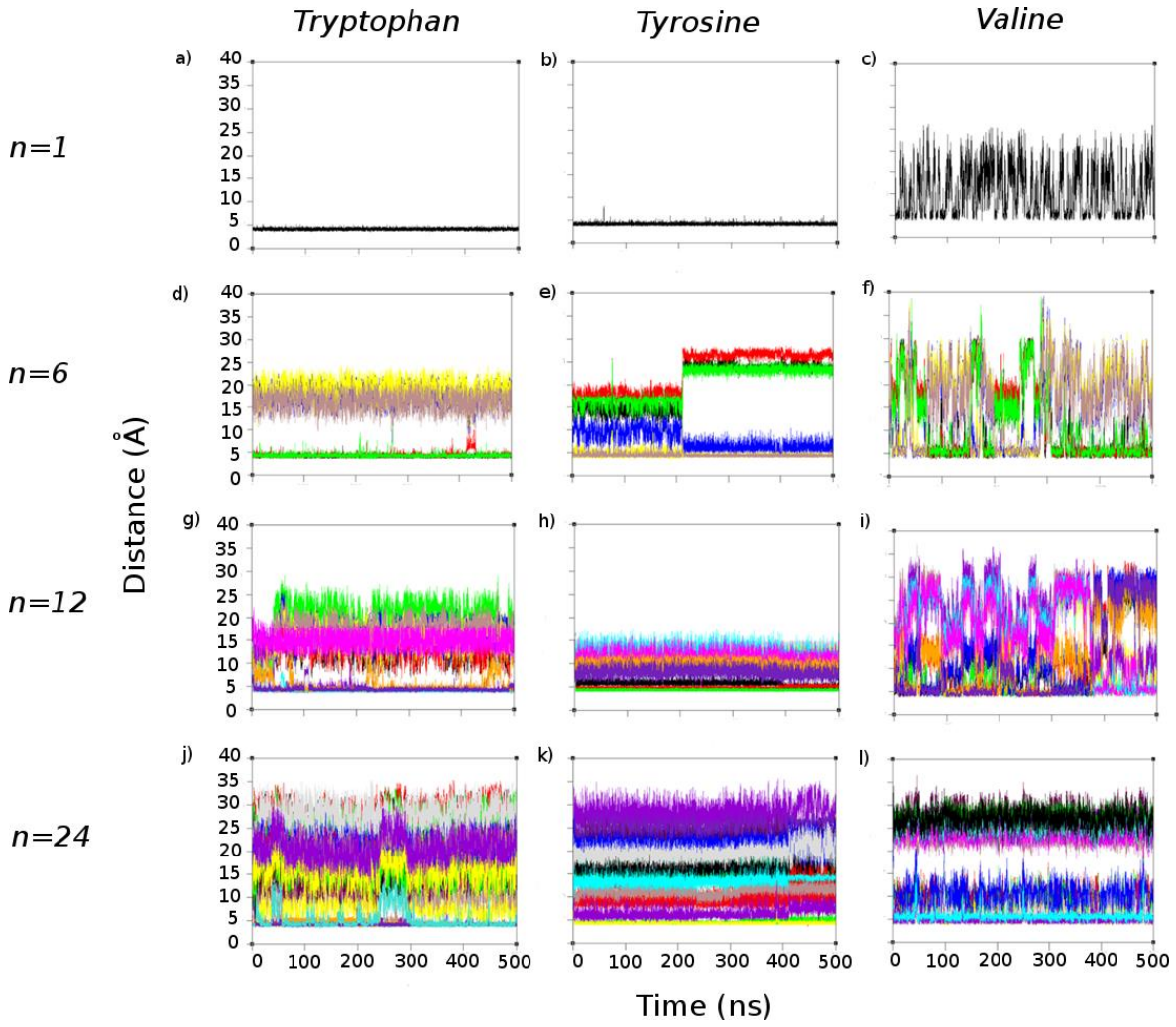


**Figure 3. 1-** Time series of distance (in Å) between surface of graphene and center of mass of each amino acid molecule in the system (colored distinctly), for MD simulations of (a) G(Trp)1, (b) G(Tyr)1, (c) G(Val)1, (d) G(Trp)6, (e) G(Tyr)6, (f) G(Val)6, (g) G(Trp)12, (h) G(Tyr)12, (i) G(Val)12, (j) G(Trp)24, (k) G(Tyr)24, and (l) G(Val)24.

For the $G(Val)_1$ system, however, quite different behaviour is predicted from MD simulation. Frequent transitions of L-Val molecule between graphene-bound and unbound states are observed (Figure 3.1c). The L-Val is bound for only 33% of the 500 ns simulation; when bound, its mean centre of mass distance from the graphene surface is 4.2 Å. Closer inspection indicates that the hydrophobic isopropyl sidechain of L-Val generally orients towards to the surface, with an average distance of 4.6 Å. The N- and C-terminal groups form average distances to graphene of 6.1 and 5.8 Å respectively but also are able to frequently interact with the graphene interface (Figures 3.2c and 3c). The $C_\alpha$-$C_\beta$ vector of valine forms an average angle $\theta$ of 94.0 ± 8.7° with the graphene surface normal (Table 8.3, Appendix), implying the bond lies along the flake surface when the molecule is bound (as in Figure 3.2c), although with considerable fluctuation in geometry.

In accord with the lower residence time at the interface, the L-Val CH-π interactions with graphene are considerably weaker than for the π−π stacking of the aromatic amino acids, with a computed $\Delta E_g$ of -11.0 kcal/mol for $G(Val)_1$ compared to -30.5 and -24.5 kcal/mol for $G(Trp)_1$ and $G(Tyr)_1$ respectively (Table 3.1). We may also compute the energetic effect of water on binding, at the PM7 level of semiempirical QM using the SMD implicit solvent model, where SMD denotes "solvation model based on density".[265] Here, we find solvation reduces the *in vacuo* interaction energies, $\Delta E_g$, of L-Trp, L-Tyr and L-Val by 2.0, 5.1 and 5.1 kcal/mol respectively (Table 3.1). This corresponds to 7%, 21% and 46% of the total interaction energy for L-Trp, L-Tyr and L-Val respectively, reflecting somewhat the relative magnitudes of their corresponding experimental solubility limits, of 55 mM, 2.5 mM and 474 mM. This greater balance in computed affinity of L-Val for water and graphene, relative to the aromatic amino

acids, explains its transient residence on the graphene surface in the MD simulation (Figure 3.1c).

**Table 3. 1**- Average per amino acid interaction energy, ΔEg, and its dispersion energy component, ΔEg,disp, of pristine graphene, computed via the PM7 model in vacuo; and corresponding energies ΔEaq and ΔEaq,disp in aqueous solution computed via the SMD solvent model. Number of bound amino acids, $N_{aa}$, within a certain cutoff distance from the graphene surface. All energies in kcal/mol.

| **System** | **$\Delta E_g$** | **$\Delta E_{g,disp}$** | **$\Delta E_{aq}$** | **$N_{aa}$ < 5.5 Å** | **$N_{aa}$ < 10 Å** |
|---|---|---|---|---|---|
| $G(Trp)_1$ | -30.5 ± 1.3 | -27.6 ±0.9 | -28.5 ± 1.2 | 1.0 | 1.0 |
| $G(Trp)_6$ | -24.5 ± 1.4 | -23.4 ± 1.1 | -12.4 ± 2.5 | 2.9 | 3.2 |
| $G(Trp)_{12}$ | -23.8 ± 0.8 | -19.6 ± 1.6 | -10.1± 1.3 | 5.2 | 7.4 |
| $G(Trp)_{24}$ | -22.0 ± 1.7 | -16.7 ± 0.6 | -5.6 ± 1.2 | 6.4 | 9.5 |
| $G(Tyr)_1$ | -24.5 ± 2.8 | -22.5 ± 1.6 | -19.4 ± 2.2 | 1.0 | 1.0 |
| $G(Tyr)_6$ | -17.1 ± 1.9 | -16.8 ± 2.1 | -8.5 ± 1.4 | 2.6 | 2.9 |
| $G(Tyr)_{12}$ | -14.8 ± 1.2 | -12.1 ± 0.8 | -4.9± 1.5 | 3.4 | 8.2 |
| $G(Tyr)_{24}$ | -10.5 ± 3.2 | -9.8 ± 7.9 | -2.4± 5.1 | 4.2 | 6.4 |
| $G(Val)_1$ | -11.0 ± 1.3 | -8.7 ± 4.1 | -5.9 ± 2.9 | 1.0 | 1.0 |
| $G(Val)_6$ | -9.4 ± 2.0 | -7.6 ± 1.5 | -4.7 ± 2.6 | 2.5 | 3.2 |
| $G(Val)_{12}$ | -7.5 ± 1.0 | -5.2 ± 0.7 | -3.6 ± 1.3 | 4.7 | 5.5 |
| $G(Val)_{24}$ | -5.9 ± 0.7 | -4.8 ± 2.2 | -1.7 ± 0.5 | 5.4 | 8.2 |

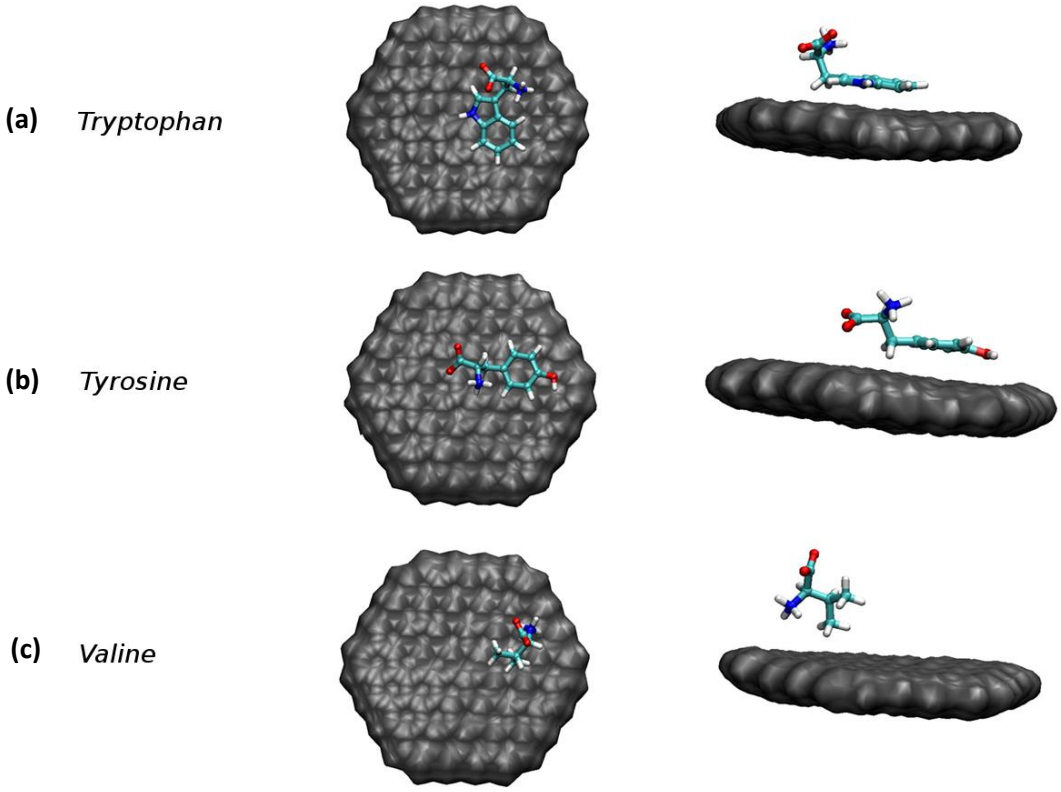


**Figure 3. 2-** Top and side views of representative amino acid-C96H24 orientations from (a) G(Trp)1, (b) G(Tyr)1, (c) G(Val)1 molecular dynamics simulations in explicit aqueous solvent.

### 3.6.2. Molecular dynamics simulations: increasing amino acid concentration

We next consider the effect of increasing the number of amino acids *n* in the graphene-water MD simulations, referring to these as $G(Trp)_n$, $G(Tyr)_n$ and $G(Val)_n$ systems, extending from *n* = 1 to 6, 12 and 24 amino acids. Initial simulation boxes were prepared using high temperature annealing to ensure a random distribution of the amino acids around the graphene. For the 500 ns MD simulation of $G(Trp)_6$, during equilibration, three of the six amino acid molecules adsorb on the graphene surface; as for $G(Trp)_1$, these amino acids form stacking interactions, with their charged groups oriented towards bulk water; L-Trp molecules remain adsorbed for the duration of the trajectory (Figure 3.1d), making only brief excursions from the immediate

surface. The remaining three L-Trp molecules form a small persistent cluster in solution (Figures 3.1d and 3d).

Increasing the number of amino acids from 6 to 12 leads to a modest increase in the number of L-Trp adsorbed on the surface, from 2.9 to 5.2 on average (Table 3.1). A further 2.2 amino acids on average lie within 10 Å of the graphene flake (Table 3.1), with some dynamical transitions between bound and unbound states (Figure 3.1g). The unbound L-Trp molecules form small clusters in solution (Figure 3.3g). Finally, for the $n = 24$ simulation, L-Trp molecules saturate the graphene surfaces (Figure 3.3j), with 6.4 molecules directly adsorbed and a further 3.1 in proximity (Table 3.1). Interestingly, a separate, large cluster of ten L-Trp molecules form at an average distance of 23.3 Å (Figure 3.3j). Exchange between graphene-bound and unbound locations is observed on the nanosecond timescale (Figure 3.1j). However, whenever the amino acids are bound to graphene, they form a tight stacking arrangement, with an average $\theta$ angle of $89.8 \pm 0.4°$ across the $n = 1$ to $n = 24$ simulations (Table 8.3, Appendix).

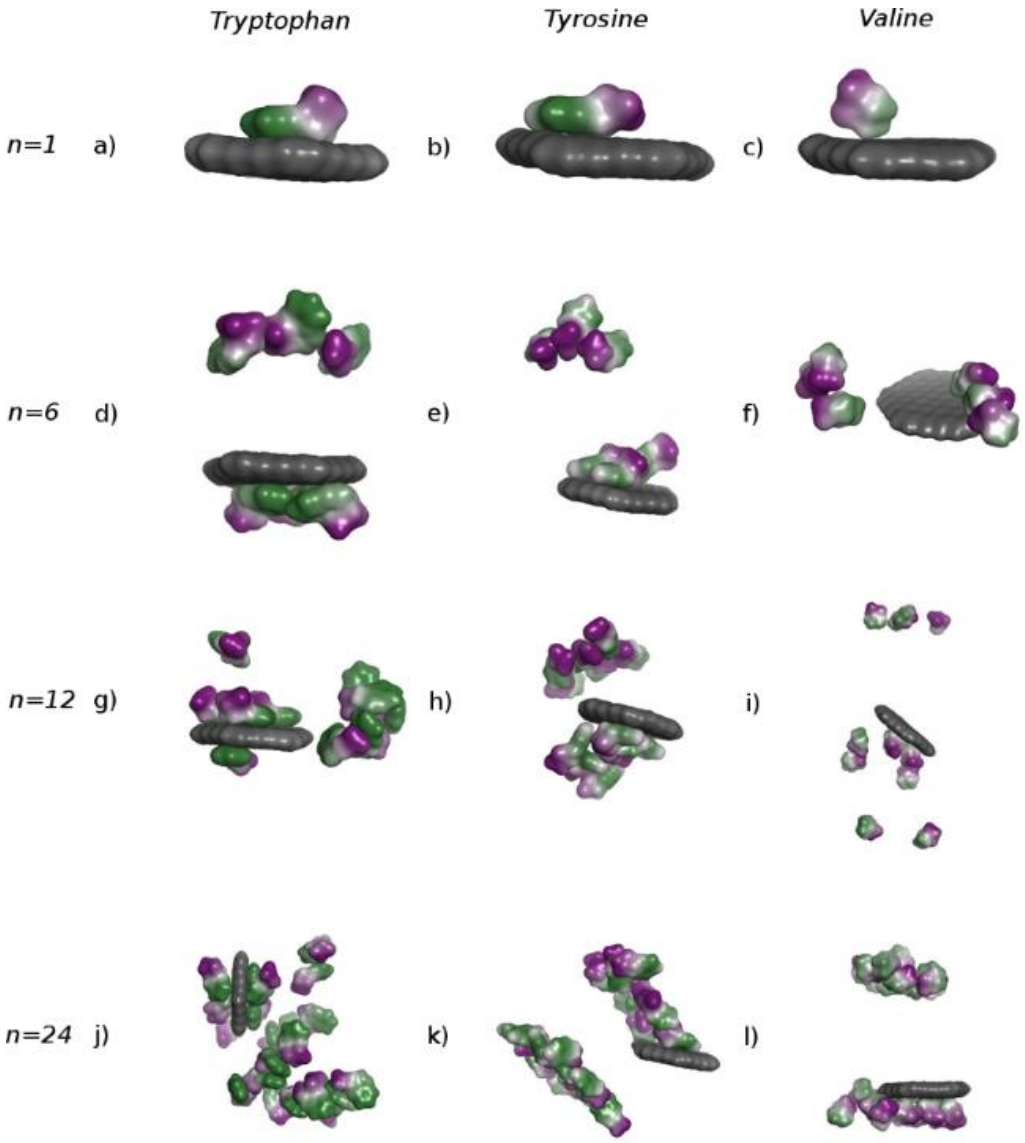


**Figure 3. 3**- Representative geometries of graphene (grey) and amino acids from molecular dynamics simulations in explicit aqueous solvent (water omitted for clarity); for the amino acids, the hydrophobic regions are in green and hydrophilic regions in purple: for (a) $G(Trp)_1$, (b) $G(Tyr)_1$, (c) $G(Val)_1$, (d) $G(Trp)_6$, (e) $G(Tyr)_6$, (f) $G(Val)_6$, (g) $G(Trp)_{12}$, (h) $G(Tyr)_{12}$, (i) $G(Val)_{12}$, (j) $G(Trp)_{24}$, (k) $G(Tyr)_{24}$ and (l) $G(Val)_{24}$.

Secondly, we consider MD simulation of $G(Tyr)_n$ systems, for $n = 6$, 12 and 24. For the duration of the $n = 6$ MD simulation, only two amino acids associate with the graphene, with a third adsorbing at 205 ns (Figure 3.1e). This coincides with separation of the remaining amino acids into a distinct cluster remote from the graphene (Figure 3.3e). The mean number of associated

L-Tyr molecules over the trajectory is 2.6 (Table 3.1). Interestingly, in contrast to the L-Trp simulations, as the number of L-Tyr molecules increases from 6 to 12 and 24, the number of associated amino acids remains around 3-4 (Table 3.1). For the $n$ = 12 simulation, there is a significant presence of 4.8 molecules within 10 Å of the graphene (Table 3.1); for G(Tyr)$_{24}$ however, this second shell reduces to 2.2 molecules, the remaining L-Tyr molecules forming a large cluster at a mean distance of 22 Å from graphene (Figures 3.1k and 3.3k). When bound to graphene, the L-Tyr residues show considerably higher fluctuation in ring stacking orientation relative to L-Trp, with an average $\theta$ angle of 108.7 ± 32.1° across the $n$ = 1 to $n$ = 24 simulations (Table 8.3, Appendix). This reflects the dual hydrophobic (phenyl) and hydrophilic (hydroxyl group) nature of its phenol sidechain, which competes for interaction with water, graphene and neighbouring L-Tyr residues.

Finally, we examine the MD trajectories of the G(Val)$_n$ systems. The highly dynamic profile of the G(Val)$_1$ simulation (Figure 3.1c) is similarly found for the G(Val)$_6$ and G(Val)$_{12}$ trajectories (Figure 3.1f,i), with very labile L-Val/graphene interactions in competition with water. For G(Val)$_6$ and G(Val)$_{12}$, on average there are 2.5 and 4.7 molecules at the graphene interface, with only 0.7 and 0.8 molecules in the second solvation shell respectively (Table 3.1). Small clusters are observed in bulk solution for both systems (Figure 3.3f,i). However, when a further 12 amino acids are added to the system, the stability of both the graphene-associated molecules and the free L-Val cluster increases (Figure 3.3l), with relatively few transitions between them (Figure 3.1l). The number of amino acids directly bound to the flake increases by only 0.7 compared to the $n$ = 12 system; and the second shell increases by 2.7 L-Val molecules. When bound to graphene, these L–Val molecules show an average $\theta$ angle of 86.4 ± 10.2° across L-Val simulations (Table 8.3, Appendix). Thus, their $C_\alpha$-$C_\beta$ vector on average lies along the face of the graphene surface, but with considerable variation in this orientation.

For these $G(Trp)_n$, $G(Tyr)_n$ and $G(Val)_n$ trajectories, we again compute graphene-amino acid interaction energies at the PM7 level of semiempirical quantum mechanics. For the $G(Trp)_6$ simulation, the total interaction energy between graphene and the 2.9 bound Trp molecules is -71.1 kcal/mol (Table 3.1). We normalise for the number of interacting amino acids, calculating the per amino acid molecule interaction energy, $\Delta E_g$. Thus, for the 2.9 interacting amino acids, $\Delta E_g$ is -24.5 kcal/mol (Figure 3.4, Table 3.1). Comparing the $G(Trp)_6$ and $G(Trp)_1$ systems, increasing *n* leads to a drop in per molecule interaction energy, $\Delta E_g$, by 6 kcal/mol; this loss in graphene binding affinity of a given amino acid may arise from steric crowding effects due to three neighbouring indole rings occupying the majority of the graphene surface. However, while the number of L-Trp molecules in the system increases to 12 and 24, the interaction energy per molecule only drops slightly, by 0.7 and 1.8 kcal/mol respectively (Figure 3.4, Table 3.1); this appears in part due to complete coverage of both sides of the flake by amino acid, with approximately three L-Trp molecules on either side, alleviating steric congestion.

For the Tyr-graphene systems, a similar loss of affinity per amino acid is found as *n* increases (Figure 3.4), with an initial large drop by 7.4 kcal/mol for $n = 6$, and smaller reductions of 2.3 and 4.3 kcal/mol for $n = 12$ and $n = 24$. Nevertheless, for the $n = 12$ and $n = 24$ simulations, fewer L-Tyr are interacting directly with the graphene surface and interact more weakly. The average total interaction energies for $G(Trp)_{12}$ and $G(Trp)_{24}$ are -119.2 and -132.1 kcal/mol, respectively; this compares with interaction energy values of only -50.2 and -44.2 kcal/mol for $G(Tyr)_{12}$ and $G(Tyr)_{24}$ respectively. This represents a factor of four more effective interaction with graphene by L-Trp compared to L-Tyr, as determined from these $n = 24$ interaction energies.

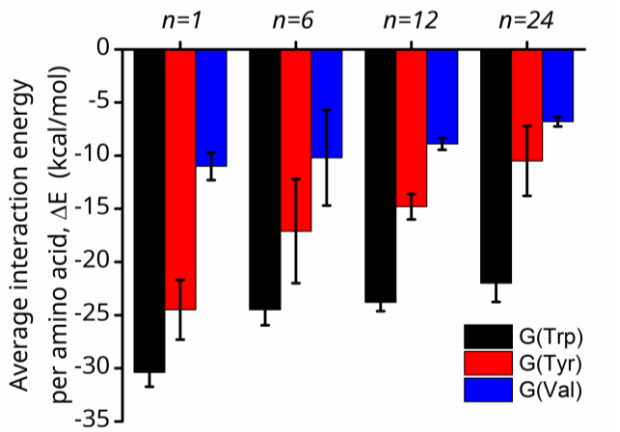


**Figure 3. 4**- Average interaction energies per molecule, ΔE, between pristine graphene and (a) L-Trp, (b) L-Tyr and (c) L-Val computed from MD simulations of G(Trp)n, G(Tyr)n and G(Val)n in water via the PM7 model.

For the 500 ns trajectories of the $n$ = 6, 12 and 24 amino acid G(Val)$_n$ systems, the number of L-Val molecules adsorbed on the graphene increases, from 1.0 to 2.5, 4.7 and finally 5.4 (Table 1). The corresponding interaction energy per amino acid, $\Delta E_g$, steadily drops, from an initial energy of -11.0 kcal/mol to a final value of -5.9 kcal/mol per molecule for G(Val)$_{24}$ (Figure3. 4, Table 3.1); this equates to a total interaction energy of -31.9 kcal/mol for the G(Val)$_{24}$ system, similar to the value of -44.2 kcal/mol for G(Tyr)$_{24}$ and much less favourable than the value of -132.1 kcal/mol for G(Trp)$_{24}$ (Table 3.1). Despite this variation in interaction energy, for all L–Tyr-, L-Tyr and L-Val systems, the dispersive contribution is predicted as the dominant interaction type (Table 3.1).

We also consider the environmental effect of aqueous solvent on amino acid-graphene energetics. On incorporating the effects of water via the SMD model, the interaction energy $\Delta E_{aq}$ drops substantially compared to $\Delta E_g$ for the G(Trp)$_n$, G(Tyr)$_n$ and G(Val)$_n$ systems (Table 3.1). For G(Trp)$_{24}$, G(Tyr)$_{24}$ and G(Val)$_{24}$, the total interaction energies between the amino acids and graphene in solution are -35.6, -10.1 and -9.5kcal/mol. Therefore, for these simulations,

the large L-Trp molecule (MW 204.2 g/mol) interacts with an affinity over three times higher for graphene ($\Delta E_{aq}$, Table 3.1), compared to the smaller L-Val (MW 117.2 g/mol) and L-Tyr (MW 181.2 g/mol) molecules; this again reflects the larger and more hydrophobic nature of the L-Trp molecule, with its lower solvation penalty on association with the lipophilic graphene surface.

In summary, the simulations indicate that a single amino acid molecule adheres to graphene with the preference of L-Trp > L-Tyr > L-Val, both in gas-phase and in solution. This concurs with previous studies for $n = 1$ graphene systems by Sanyal et al.[225] and Goel et al.[266] and appears to reflect the size and hydrophobicity of the amino acids. However, for more concentrated amino acid solutions, there is a predicted propensity for amino acid clustering as well as intermolecular steric effects that appear to hinder interaction with the graphene flake as its surface saturates with amino acid; the preference for interaction becomes L-Trp > L-Val > L-Tyr in gas-phase and solution. To further explore these conclusions, we next evaluate experimentally the ability of these three amino acids to suspend and exfoliate pristine graphene.

### 3.6.3. Concentration and stability of graphene suspended in amino acid solutions

The ability of L-Val to exfoliate and suspend pristine graphene in aqueous solution following sonication of graphite flake powder was studied, as moderate interaction energy between L-Val and graphene was found by quantum chemical calculations (Figure 3.4). We did find that the concentration of graphene suspended increased as the L-Val concentration increased up to 340 mM, to reach a suspended graphene concentration of 22.5 ± 5.0 μg/ml; this then plateaued and subsequently decreased (Figure 8.1, Appendix). As the optimum concentration

of L-Val (340 mM) was very close to its known maximum solubility limit (474 mM)[263] and may be considered too high for biological applications of suspended graphene, we focused our further studies on the aromatic amino acids L-Tyr and L-Trp as suspending agents, which we find here work at lower concentrations.

For the aforementioned aromatic amino acids, we choose to exfoliate stacked graphene platelet nanofibers rather than graphite powder. Whereas graphite powder yields a wide range of lateral sizes of flakes, the selected SGNFs were formed by stacked graphene sheets of consistent 40 - 50 nm diameter; hence, these fibrils are expected to exfoliate into nanoflakes with relatively monodisperse lateral sizes, small compared to the size of the typical human cell. The graphene concentrations of the suspensions produced from SGNFs were measured immediately after preparation and then again four weeks after preparation to assess the stability of the suspensions (Figure 3.5). In these experiments, *stability* was defined as the propensity of flakes to remain in suspension and the likelihood of flakes settling to the bottom of the container to be redispersed when agitated. The concentration of suspended graphene for different concentrations of L-Trp and L-Tyr was measured using UV-vis absorption spectroscopy (Figure 3.5).

We find that the aromatic amino acids are able to suspend graphene at much lower concentrations than Val, and therefore may be more appropriate for biological applications. We reach concentrations of 11.2 ± 1.0 and 14.7 ± 2.0 μg/ml at amino acid concentrations of 1.1 and 0.55 μM for L-Trp and L-Tyr respectively. However, as the concentration of L-Trp and L-Tyr amino acid increases, we observe an unexpected decrease in initial suspension and stability over time (Figure 3.5). Indeed, for the higher concentrations of L-Trp or L-Tyr amino acids (22 - 2200 μM and 2.2 - 2200 μM respectively), the concentrations of graphene present in suspension after four weeks remained close to 0.0 μg/mL (Figure 3.5).

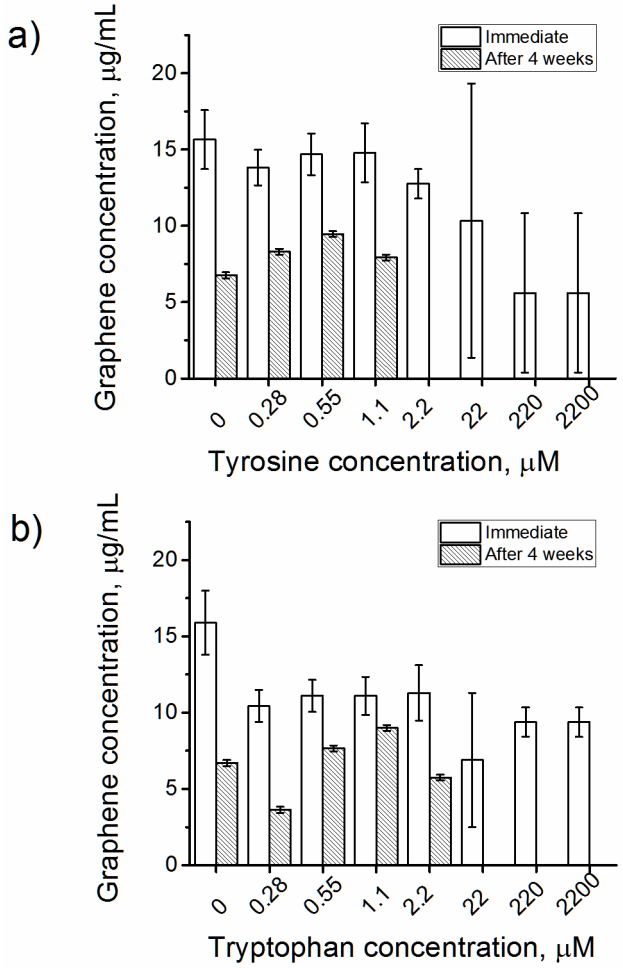


**Figure 3. 5**- Concentrations of graphene prepared from SGNFs exfoliated in (a) L-Tyr and (b) L-Trp solutions in water; all concentrations were determined using UV-vis absorption spectroscopy at a wavelength of 750 nm. Each graph shows the initial graphene concentration and the concentration after 4 weeks for a range of concentrations of amino acids. Errors were calculated as the standard deviation of the measurements from three samples.

For the lower concentration range of L-Trp or L-Tyr, although suspended graphene was observed, after four weeks the concentration in various suspensions decreased by 6 – 65%, as compared to initial concentration. The most stable suspensions for L-Tyr and L-Trp were

at concentrations of 0.55 and 1.1 μM, respectively (Figure 3.5). Over a similar time frame, Lotya et al.[267] found that samples of graphene suspended with the detergent sodium dodecylbenzene sulfonate (SDBS) decreased in concentration by 65%. Although Wang et al.[268] observed that 80% of graphene flakes prepared with Tween-80 or Triton-X 100 remained in suspension after 20 days, Lee et al.[269] found visible agglomerates and sedimentation of suspended graphene prepared with Triton-X 100.

### 3.6.4. Morphology of graphene flakes suspended in amino acid solution

To further characterise the effectiveness of aromatic amino acids in suspending graphene, we assessed flake size, thickness and geometry. Indeed, for biological applications such as drug delivery, not only are stable suspensions required, but to minimise cellular toxicity,[270, 271] the graphene flakes should ideally be thin, with only a small number of layers, <N>; their lateral dimensions should also be relatively monodispersed[272].

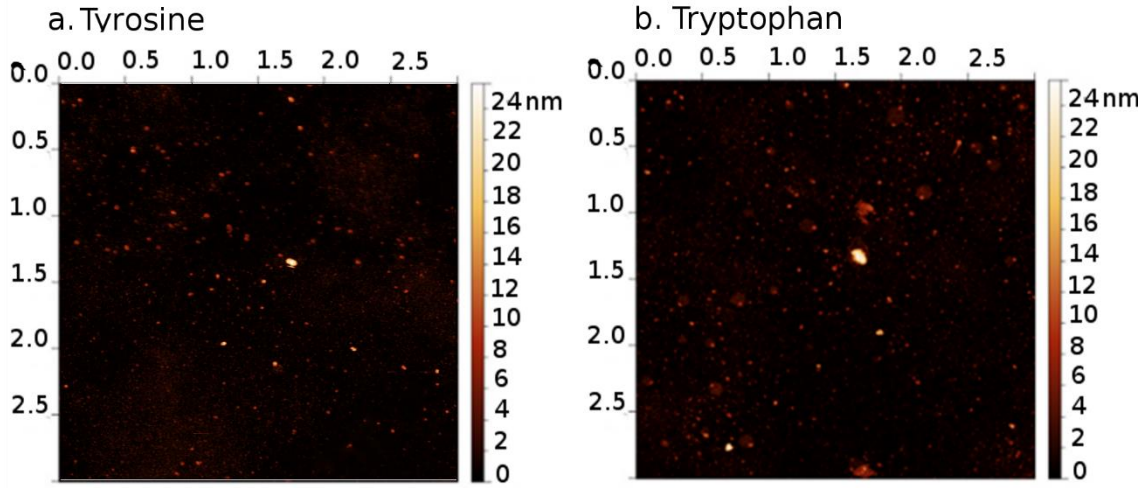


**Figure 3. 6-** Representative AFM images of graphene flakes exfoliated from SGNF and suspended in (a) a 0.55 μM L-Tyr solution and (b) in a 0.55 μM L-Trp solution. Abscissa and ordinate distances are expressed in μm.

Using AFM, we therefore examine the morphology of flakes found in the most stable graphene suspensions, prepared in a 0.55 μM solution of L-Tyr and 0.55 μM solution of L-Trp. Representative AFM images for graphene/L-Tyr and graphene/L-Trp suspensions (Figure 3.6) confirm that both L-Tyr and L-Trp are able to exfoliate graphene. Using height thresholding of the AFM images obtained, the distribution of flake thicknesses was determined for each amino acid (Figure 3.7).

While a single layer of graphene is calculated as having a thickness of 0.34 nm, equal to the out-of-plane extension of the π orbitals,[273] graphene and graphitic layer thicknesses have been measured by different groups to be between 0.5 - 1 nm using AFM;[274, 275] the variation in measured thickness depends upon the interaction between the AFM tip and the flake surface, including the presence of any adsorbed molecules, particularly water molecules. Therefore, the thinnest flakes would be expected to be at least three layers thick, with the mean thickness between 8 - 16 layers. Both of the aromatic amino acid preparations examined produced a relatively narrow distribution of flake thickness (Figure 3.7a, b). The mean thickness of the L-Trp and L-Tyr flakes were 6.4 and 7.5 nm respectively (Table 3.2).

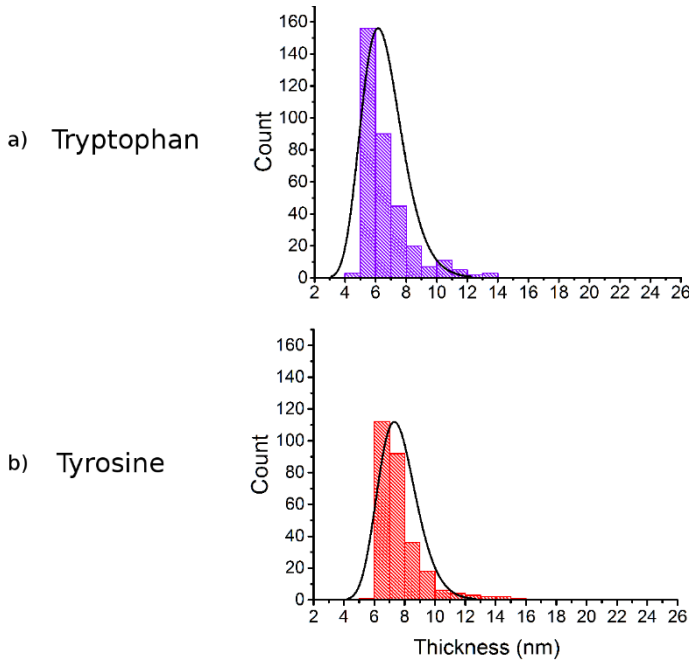


**Figure 3. 7-** Distribution of flake thicknesses calculated from the AFM images taken of graphene suspensions in a) Trp and b) Tyr. The amino acid concentration for Trp and Tyr was 0.55 μM.

**Table 3. 2-** Flake thicknesses found using AFM, <N>AFM, compared with predicted thicknesses estimated from the UV-vis spectra, <N>UV-vis.The predicted thickness range was calculated by multiplying the predicted <N> by the layer thicknesses reported in previous AFM studies.[274, 275] The amino acid concentration was 0.55 μM for L-Trp and Tyr. Mean diameter measured by AFM.

| **Amino acid** | **Mean thickness (nm)** | **Mean diameter (nm)** | **Estimated $\langle N \rangle_{AFM}$** | **Predicted thickness (nm)** | **Estimated $\langle N \rangle_{UV\text{-}vis}$** |
|---|---|---|---|---|---|
| **Trp** | 6.4 | 16.0 | 6.0 – 12.0 | 4.3 – 8.6 | 9.0 |
| **Tyr** | 7.5 | 13.9 | 8.0 – 15.0 | 5.0 – 10.0 | 10.0 |

The mean flake diameters for L-Trp and L-Tyr preparations were measured by AFM and found to be 16.0 and 13.9 nm (Table 3.2, Figure 3.8). The observed lateral size of the flakes is smaller than the expected 40 - 50 nm diameter, suggesting that flakes have mostly fragmented during sonication. However, virtually no flakes with a diameter larger than 50 nm were observed, confirming that the chosen starting SGNF material produces flakes consistently smaller than the typical size of a living cell, with actual flake diameters comparable to the thickness of a cell membrane.

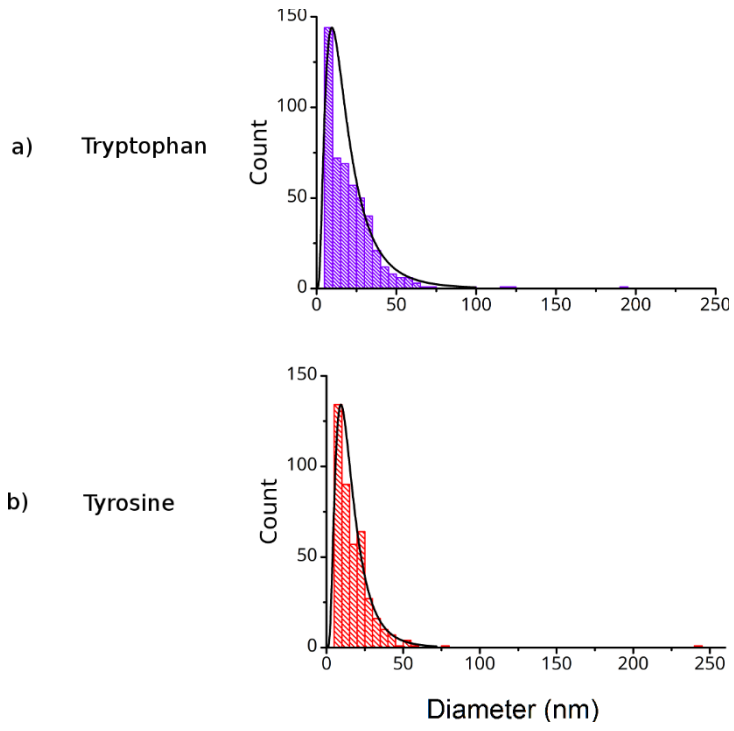


**Figure 3. 8-** Flake diameters (in nm) calculated from AFM images taken of graphene suspensions in a) L-Trp and b) L-Tyr solutions at an amino acid concentration of 0.55 μM. A log (normal) distribution was fitted in each case.

## 3.7. Discussion

In this work, we observe from experiment that L-Trp and L-Tyr amino acids are good graphene exfoliators and suspend graphitic material as effectively as surfactants e.g. SDBS. Suspended graphene concentrations following centrifugation were within the ranges obtained by other research groups when performing exfoliation using graphite powder.[267, 276] By contrast, the required concentration of a third amino acid, L-Val, for exfoliation and suspension was very high (340 mM); we can relate this to the rather weak computed interaction energy between L-Val and graphene (Table 3.1) and its consequently highly labile adsorbed first layer on the graphene surface (Figure 3.1f,i), although slightly more stable at high concentration (Figure 3.1l).

For exfoliation and suspension of graphene, the low concentrations (micromolar) of L-Trp and L-Tyr required were found to be in line with the more favourable calculated energies for the per molecule interaction of graphene with L-Trp and L-Tyr than for L-Val (Figure 4). The two aromatic amino acids were able to form stable suspensions of graphene over 4 weeks at 0.55 - 1 μM (Figure 3.6) and yield a high proportion of thin, small diameter flakes (Figures 7 and 8). Nevertheless, at higher concentrations of L-Trp and L-Tyr amino acids, there was a decrease in exfoliation and suspension (Figure 3.6); this would appear to reflect the suggestion from the MD simulations here that, within the sampling limits of the trajectories, there is an increased propensity for L-Trp and L-Tyr to self-aggregate rather than solvate graphene as amino acid concentration increases (Figure 3.3). This appears particularly to be the case for the G(Tyr)$_n$ simulations, where the number of directly bound molecules remained rather constant as L-Tyr concentration increased (Table 3.1). For both L-Tyr and L-Trp systems, there was a weakening of binding efficiency of the amino acid to graphene, due most likely to steric congestion at the flake surface (Figure 3.4).

When considering the stability of the L-Trp and L-Tyr suspensions in experiments, we observed a sharp drop-off in suspended graphene concentration at four weeks for solutions exceeding 22 μM for L-Trp and 2.2 μM for L-Tyr. This trend was accompanied by visible aggregates of graphitic material observed at the bottom of the vials. In a similar vein, we note that it has previously been reported that L-Tyr spontaneously forms fibrils at concentrations as low as 1 mM in both dd$H_2O$ and human serum[275, 276]. These micromolar thresholds for L-Trp and L-Tyr are significantly below the solubility limits of the amino acids, namely 55 mM for L-Trp and 2.5 mM for L-Tyr.[264] The lower solubility limit of L-Tyr compared to L-Trp would appear reflected by its higher predicted propensity for self-aggregation than L-Trp from the MD simulations (Table 3.2); from these simulations, it is evident that L-Tyr aggregation features intermolecular hydrogen bonding via the phenol OH group of its sidechain (Figure 8.2, Appendix); this is not possible for the indole ring of L-Trp. It therefore follows that the decreased stability of the graphene suspensions and the increased thickness of the flakes should occur at lower concentrations of L-Tyr than L-Trp. In fact, of the three amino acids, L-Trp continued to produce the most stable suspensions, even at high concentrations, and the thinnest flakes at 0.55 μM, as measured by AFM. The bicyclic indole ring is the most lipophilic of the three sidechains and makes the strongest computed interaction energy with graphene. In choosing an exfoliating and suspending agent for graphene, we find that its lipophilicity and solubility limit are key in proposing such an agent: L-Tyr had the lowest solubility limit of the three amino acids considered, producing less stable suspensions and thicker flakes than L-Trp.

## 3.8. Conclusions

We have determined that L-Trp, L-Tyr and L-Val amino acid solutions are able to exfoliate and suspend pristine few-layer graphene flakes in water. However, the aromatic amino acids are

considerably more effective on a per molar basis than L-Val. L-Trp produces slightly thinner flakes than L-Tyr, with a mean thickness of 6.4 nm, and the most stable suspensions after four weeks. At high aromatic amino acid concentration, the suspensions become increasingly unstable and exhibit visible signs of precipitation at the bottom of the vessels. This is in line with graphene-water MD simulations of increasing aromatic amino acid concentration, where self-aggregation and reduced graphene binding efficiency was observed. Exfoliation of SGNF using these aromatic amino acids produced nanoflakes with diameters smaller than 50 nm, and hence, much smaller than the typical size of living cells; indeed, the fairly consistent diameter distributions are comparable with the thickness of cellular membranes. This study indicates the potential of amino acids to exfoliate and suspend pristine graphene as a step towards developing nontoxic graphene-based vehicles for drug delivery and other in vivo applications.

*Research Article*

# 4. Preparation and characterisation of pristine graphene using peptides by loading doxorubicin for therapeutics delivery

Fai A. Alkathiri[a], Alexander P. Golovanov[b], , Richard A. Bryce[a, *] and Alain Pluen[a *]

[a] *Division of Pharmacy and Optometry, School of Health Sciences, University of Manchester, Manchester, UK*

[b] *Manchester Institute of Biotechnology, and School of Chemistry, Faculty of Science and Engineering, University of Manchester, Manchester, UK*

Corresponding Authors

*Alain Pluen, Division of Pharmacy and Optometry, School of Health Sciences, University of Manchester, Manchester, M13 9PT, U.K. Email: Alain.Pluen@manchester.ac.uk, Tel: (0)161-275-1792

*Richard Bryce, Division of Pharmacy and Optometry, School of Health Sciences, University of Manchester, Manchester, M13 9PT, U.K. Email: Richard.Bryce@manchester.ac.uk, Tel: (0)161-275-8345

## 4.1. Abstract

Pristine graphene (PG) was modified by attachment into different Trp residues ($Trp_x$), where x= 1, 2 and 3 is the number of tryptophan of the peptide via non-covalent functionalisation for the efficient loading and release of the aromatic anticancer drug, doxorubicin (Dox). Dox's loading onto PG is likely due to simple π–π, interactions of the aromatic rings of PG with the quinine Dox component. Dox's amine (-NH2) and hydroxyl (-OH) groups can produce strong hydrogen-bonding interactions with COOH and NH2 groups on peptides. The attachment of $Trp_x$ to PG was examined using molecular dynamics simulations. Results not only confirmed that PG attached with $Trp_x$ via *π–π* interactions but also revealed that $Trp_3$ may cover PG's surface more thoroughly than Trp and $Trp_2$, largely because its aromatic ring resulted in strong *π–π* interactions and functionalised PG's surface better than Trp and $Trp_2$. The experiment additionally showed that increasing Trp residues to $Trp_3$ allowed Trp to exfoliate and suspend PG in an aqueous solution and had thinner flakes, as later confirmed by both atomic force microscopy and Raman spectroscopy. Stability studies demonstrated that PG–$Trp_3$ had the smallest apparent hydrodynamic radius both immediately and after 4 weeks, while zeta potential analysis confirmed that $Trp_3$ produced a highly stable suspension both immediately and after 4 weeks and that 75% of flakes remained in the PG–$Trp_3$ suspension. The drug's release from PG–$Trp_x$ was analysed in different media with pH 7.4 and pH 5.4. Results indicated that its release from PG and PG–$Trp_x$ was pH-dependent, for it appeared to be more limited at pH 7.4 than at pH 5.4. The *in vitro* cytotoxicity and intracellular distribution of the samples were studied using MTS assay and fluorescence microscopy on MDA-MB-231cells. In sum, PG–$Trp_3$, especially with Dox, can be used as promising material for drug delivery and other biological applications.

## 4.2. Introduction

Pristine graphene (PG) is an atomically flat sheet material with a van der Waals thickness of 0.34 nm [17]. Hydrophobic and incompatible with organic polymers, PG fails to form homogeneous composites [3, 277] owing to its defect-free plane and lack of oxygen groups. It is also poorly soluble in aqueous environments, requires surfactants or surface modification to be used in drug delivery and makes irreversible aggregates in aqueous media due to its hydrophobicity [277]. Given those drawbacks, PG has received less attention than graphene oxide (GO) as a candidate for biomedical applications, cell imaging, photothermal therapy and tissue engineering [278, 279]. Although GO's and PG's vast surface areas would both benefit drug delivery systems, PG requires far more effort before allowing a stable, uniform suspension of graphene. Thus, numerous approaches have been considered to limit PG agglomeration, which results from its hydrophobicity and the strong van der Waals forces between its layers.

Graphite powder and GO are precursors of graphene's dispersion, a process achieved by either a physical approach (e.g. ball-milling, mechanical stirring and ultrasonic treatment) or a chemical approach (e.g. covalent and non-covalent modification). To create the final suspension, however, both approaches are typically combined. For example, as sonication creates cavitation and shear stresses in the solvent [28], the graphene sheets exfoliate into graphene flakes - the dispersion's concentration being affected by both the power and duration of sonication [280] –, and stable dispersion may be achieved using specific solvents such as the widely used solvent is *N*-methyl-2-pyrrolidone (NMP), an organic solvent that can yield stable dispersions of graphene ranging from 0.01 to 2.0 mg/mL [32, 280]. However, using organic solvents such as, NMP, dimethylformamide, and cyclohexanone to exfoliate and suspend PG can be problematic in biological applications due to the toxicity and extremely high boiling points of the organic solvents [281]. By contrast, in solvents with low boiling points (e.g. cyclohexanone, acetone and chloroform), the intensity of conditions created by

sonication allows graphene to disperse, such that its concentration increases with the square root of the duration of sonication [33, 281]. long sonication time affects the quality and size of the graphene sheet, which can consequently introduce defects into the sheet [33, 35, 36]. When Bracamonte *et al.* [282] investigated the effect of sonication's duration on graphene's dispersion, sonication lasting less than 2 h caused defects to develop on the graphene's edge, whereas sonication lasting more than 2 h caused defects on the graphene's basal plane. Another study suggested high sonication power lead to yield high concentrations of graphene [283].

Although PG could be a promising class of drug carrier, attention needs to be paid to the resulting suspension's toxicity—most solvents used are toxic—as well as its biocompatibility profile. For that reason, covalent as well as non-covalent strategies to modify PG's surface chemistry have been utilised to functionalise PG and, thereby, overcome its aggregation. For example, Liu *et al.* [105] functionalised PG with gelatine, which demonstrated high stability in water and various physiological media, including serum and cellular growth media. Their cellular toxicity study also revealed that, although the PG–gelatine complex by itself was not toxic to MCF-7 cells, when loaded with doxorubicin (Dox) it prompted the sustained release of Dox *in vitro* with obvious toxicity to MCF-7 cells and displayed excellent therapeutic efficacy. The high drug-loading capacity (LC) observed was thought to be related to graphene's large surface area, π–π interactions and hydrogen-bonding interactions. Such findings are important for drug delivery applications, because the resulting suspensions should have the lowest toxicity, and excipients should be "generally recognised as safe" (GRAS). Using water to disperse graphene while preserving its quality offered several benefits, including lack of toxicity, low cost, low boiling points, no need for stabilisers, easy handling and better biocompatibility than other graphene dispersion in organic solvents[40].

In a previous study [284], we combined modelling and experiments to highlight the potential of amino acids (i.e. L-Val, L-Tyr and, in particular, L-Trp) to exfoliate and suspend PG, which

may facilitate the development of non-toxic, graphene-based vehicles for drug delivery and other *in vivo* applications. The study demonstrated the ability of all three amino acid solutions to exfoliate and suspend PG flakes in water, although the L-Trp and L-Tyr solutions were considerably more effective than the L-Val solution. Of them all, L-Trp produced the most stable suspensions and the thinnest graphene flakes, with a mean thickness of 6.4 nm and a narrow mean diameter of 16 nm. With high concentrations of L-Trp and L-Tyr, the suspensions became increasingly unstable, which resulted in visible signs of aggregation and sedimentation. Those results corroborated the outcomes of graphene–water molecular dynamics simulations, in which self-aggregation and reduced graphene binding was observed with higher concentrations of amino acids.

Having demonstrated L-Trp's ability to suspend PG, we sought to take the obvious next step: determining the potential of short peptides as suspending agents for PG. Peptides often play important roles as diagnostic and therapeutic agents in biomedical applications due to their various advantages, including low cost, specific targeting ability, bioactivity and biocompatibility. Furthermore, they are easily manufactured, for instance, by using peptide solid-phase methods in which amino acid sequences can be precisely chosen at the molecular level by changing the basic units [285]. The amino acids in peptides may result in π–π interactions with graphene that could in turn stabilise PG, and adding a new functional group to PG's surface could prompt hydrogen-bonding interactions with drug molecules [284].

To demonstrate the ability of the non−covalent complex PG–$Trp_x$ ; where x is the number of tryptophan of the peptide, this complex serve as vehicles for drug delivery, we chose Dox, an anticancer chemotherapy drug commonly used to treat breast cancer, acute lymphocytic leukaemia, Kaposi's sarcoma, osteogenic sarcomas, bladder cancer and lymphoma [286-290]. The resulting complex, PG–$Trp_x$–Dox, was expected to improve the delivery of Dox, which lacks efficiency and selectivity against cancerous cells [291], by passive targeting or enhanced

permeability retention effect [292], which is exploited by drug carriers such as liposomes (e.g. Myocet liposomal). A final fundamental advantage of Dox as a drug for modelling is its intrinsic fluorescence, which allows characterising the loading and release of carriers and delivery to cells [293].

Herein, we show that short tryptophan peptides (i.e. monopeptide, dipeptides and tripeptides) can functionalise PG to form stable suspensions with reduced toxicity. The resulting suspensions may also be employed as vehicles for drug delivery, as we demonstrated by using Dox as a model drug.

## 4.3. Experiment

### 4.3.1. Molecular dynamics simulations

The molecular dynamics simulations as described in section 2.1. used a computational model of a single graphene layer (area: $17.24 \times 15.59$ Å$^2$) consisting of 96 carbon atoms in a hexagonal arrangement was created with a carbon nanotube builder in Visual Molecular Dynamics (VMD). Once the edges of the sheet were terminated by hydrogen atoms, molecular dynamics simulations were performed in the AMBER 16 package [294], with the parameters of the general AMBER force field (GAFF) [201] used for PG–$Trp_x$. The systems were solvated using the TIP3P water model for the simulations, with cut-off values 10 Å away from each side of the solute. Thus, the graphene sheet was modelled using the GAFF definition of aromatic carbon for the parameters of van der Waals interactions. Solvent molecules were distributed across the volume of the box of simulations.

We created six systems using either one or six molecules of $Trp_1$, $Trp_2$ and $Trp_3$: graphene–tryptophan–water (PG–Trp–water), graphene–$Trp_2$–water (PG–$Trp_2$–water) and graphene–$Trp_3$–water (PG–$Trp_3$–water). Amino acids were mostly zwitterions in aqueous solution—that is, contained a negative α-carboxylate group and a positive α-ammonium group. After the

systems were minimised using a restraint force constant of 500 kcal $mol^{-1}$ $Å^{-2}$ on both amino acids and graphene atoms, they were minimised without restraints. The systems were subsequently heated to 5000 K for 25 ns while using restraints on graphene with a force constant of 100 kcal $mol^{-1}$ $Å^{-2}$, followed by cooling with restraints to 2000 K for 2.5 ns. Again, the systems minimised as in the previous steps. Once the systems were heated to 298 K for 0.5 ns, restraints were used on graphene with a force constant of 10 kcal $mol^{-1}$ $Å^{-2}$ , and the systems were controlled by applying a Langevin thermostat [295] with a collision frequency of 1 $ps^{-1}$. The SHAKE algorithm [254], with a 2-fs time step for dynamics, was applied to limit covalent bond lengths to hydrogen.

Equilibration began with NPT dynamics with restraints exceeding 1 ns and their steady reduction on amino acids to 0 and on the graphene sheet to 10 kcal $mol^{-1}$ $Å^{-2}$, followed by 0.5 ns of NPT without restraints. After that, NVT production was attempted without restraints on graphene and amino acids. Simulations of 0.1 ns were acquired, and NVT production sampling without restraints was performed for 500 ns.

We used VMD as the graphical interface in molecular dynamics (MD) simulations. The program Molecular Operating Environment (MOE) was used to identify lipophilic and hydrophilic regions, and all geometric analyses were performed in the CPPTRAJ module in AMBER.

### 4.3.2. Materials

Graphite powder (diameter: <45 μm, purity: ≥ 99.99%) and doxorubicin hydrochloride (Dox) were purchased from Sigma Aldrich (UK). L-Tryptophan (L-Trp), di-tryptophan (Trp–Trp), and tri-tryptophan (Trp–Trp–Trp), hereafter referred to as Trp, $Trp_2$ and $Trp_3$, respectively, were purchased from Cambridge Bioscience (UK). Phosphate-buffered saline (PBS) was purchased as tablets from Sigma Aldrich and dissolved in $H_2O$ as recommended by the

manufacturer. All solutions were prepared in Milli-Q water. Bath sonication was performed in borosilicate round-bottom glass flasks (Sigma Aldrich), and all suspensions were stored in Wheaton snap-cap borosilicate glass vials (Thomas Scientific, UK).

#### 4.3.2.1. Cell culture materials

Dulbecco's modified Eagle's medium without L-glutamine, L-glutamine, penicillin-streptomycin and foetal bovine serum were purchased from Sigma Aldrich (UK), along with a supply of Corning multi-well plates.

### 4.3.3. Chemical methods

#### 4.3.3.1. Graphene suspension preparation

Graphite powder from Sigma Aldrich (UK) and 0.55-μM solutions of Trp, $Trp_2$ and $Trp_3$ were prepared in Milli-Q water. Graphite was sonicated in the presence of Trp, $Trp_2$ and $Trp_3$ in an Elmasonic X-tra sonication bath (Tovatech, US) for 6 h, during which time the bath's water was regularly cooled using ice to prevent temperatures greater than 35 °C. Sonication was performed at 59 kHz and at 100% power. Once prepared, all suspensions were stored in borosilicate glass vials.

#### 4.3.3.2. Preparation of doxorubicin loaded PG– $Trp_x$

The anticancer drug Dox was loaded onto particles at a final concentration of 1 mg/mL, determined by using the drug's standard calibration curve (Figure 8.3 and 8.4 Appendix). The Dox–particle mixture was sonicated for 1 h, followed by overnight stirring at room temperature in the dark. After 24 h, the samples were centrifuged twice at 13,000 rpm for 15 min using the Avanti® J-30I high-performance centrifuge (Beckman Coulter, US) to remove any unbound Dox. The product, PG–$Trp_x$–Dox, was redispersed in PBS with pH values of 7.4 and 5.4.

## 4.4. Methods of characterisation

### 4.4.1. UV-visible absorption spectroscopy

UV– visible (UV-vis) absorption spectroscopy was used both to monitor the concentration of the PG suspensions and to assess their quality. Absorption spectra of the suspensions were recorded from 200 nm to 800 nm using a microplate reader (Synergy-HT, BioTek, US), and aqueous peptide solutions were used as a blank. To assess the stability of the suspensions, the absorbance of the suspensions left undisturbed in borosilicate glass vials at 4 °C was measured after 4 weeks. Already prepared particle suspensions of 100 µL were aliquoted into Corning 96-well plates, and the absorbance was read at 265 nm [262].

### 4.4.2. Fluorescence spectroscopy

Fluorescence measurements were taken with a Cary Eclipse fluorescence spectrophotometer (Agilent, US) at excitation and emission wavelengths of 470 nm and 600 nm for Dox [296] and of 280 nm and 350 nm for tryptophan, respectively [297]. For Dox, the standard calibration curve was determined using concentrations of the drug up to 100 µg/mL; at higher concentrations, self-quenching was liable to occur [298, 299]. PG–Dox and PG–$Trp_x$ were used as blanks to correct the background fluorescence for $Trp_x$ and Dox, respectively. All samples were measured in triplicate in quartz cuvettes.

### 4.4.3. Atomic force microscopy

Atomic force microscopy (AFM) was performed using a Bruker Multimode in ScanAsyst mode (Bruker, UK) with the following dimensions: cantilever, 450 µm × 50 µm × 2 µm; tip height, 17 µm; tip radius, <10 nm; cantilever, 115 µm × 25 µm × 0.65 µm; tip height, 2.5–8.0 µm; tip radius, approximately 2 nm. Images were evaluated using Gwyddion analysis software (Czech

Metrology Institute, CZ) for scanning probe microscopy and automatic thresholding techniques for particle analysis.

### 4.4.4. Dynamic light scattering

Dynamic light scattering (DLS) was performed using a Wyatt DynaPro Plate Reader II (Wyatt Technology Corporation, US). Particle suspensions were diluted to approximately 50 μg/mL, and 100 μL was aliquoted into a 384-well microtitre plate transparent to U/V light. All samples were measured in triplicate following an event schedule set on the DynaPro plate reader using Dynamics software. The laser was auto-attenuated for each reading, and all acquisitions were performed over the course of 10 s; 10 acquisitions were performed on each well, and the temperature was maintained at 25 °C. As the software enabled real-time data filtering, correlation function cut-off values were set at $0.93 \times 10^6$ and $1.33 \times 10^6$ as the low and high passes, respectively, whereas the peak radius cut-off values were set at 0.5 nm and 10 μm. Diffusion coefficients were obtained from cumulative fits to the correlation function over the time delays using Dynamics. An infinite dilution hydrodynamic radius ($R_h$) was calculated from the extrapolated value for $D$ using the Stokes–Einstein equation:

$$\boldsymbol{R_h} = \frac{k_B T}{6\pi\, \eta_0\, D} \qquad \textbf{Equation 4.1}$$

Where $k_B$ is the Boltzmann constant (i.e. $1.38 \times 10^{-23}$ $m^2\,kg\,s^{-2}\,K^{-1}$), $T$ the absolute temperature (K), and $\eta_0$ the solvent viscosity ($kg \times m^{-1} \times s^{-1}$).

### 4.4.5. Raman spectroscopy

Raman spectra were determined with a confocal Raman spectrometer using a Leica DM2500 with a Renishaw VIS Confocal Micro-Raman and Bruker AFM System (Bruker, UK). To avoid the potential effects of laser heating on the samples, the laser power for excitation was kept

below 5 mW, and spectra were recorded by a spectrometer under a wavelength of 514 nm. A 50× objective lens was used both to focus the laser beam to approximately a 1-μm spot on the sample and to save the backscattered Raman signal [300, 301].

### 4.4.6. FTIR spectroscopy

The surface chemistry of PG and PG-$Trp_x$ were assessed using Fourier transform infrared (FTIR) spectroscopy. FTIR spectra recorded using a Bruker tensor 37 instrument (Bruker, UK) were scanned from 4000 to 400 $cm^{-1}$, and the average of 24 scans at a resolution of 4 $cm^{-1}$ was recorded, with air as the reference background [302]. For each sample, three replicates were recorded.

### 4.4.7. Zeta potential

The surface charge of PG and PG-$Trp_x$ were determined using the zeta potential analyser, Zetasizer Nano-ZS (Malvern, UK), at 25 °C. All samples were diluted using deionised water and measured in triplicate.

### 4.4.8. Efficiency of drug attachment

The efficiency of drug attachment was calculated with a direct method using Dox's fluorescence at an excitation wavelength of 470 nm and an emission wavelength of 600 nm [296]. Explained briefly, the unbound Dox amount in the supernatant was calculated using fluorescence spectrophotometer at an emission wavelength of 600 nm then the unknown drug concentration of the carrier system was determined using a calibration curve based on a series of known concentrations of Dox. The percentage of entrapment efficiency (EE) and loading efficiency (LE) were ascertained by measuring the unbound drug in the supernatant using two equations adapted from Abidin *et al.* [106]:

$$\boldsymbol{Entrapment\ efficiency\ (EE\%)} = \frac{W_i - W_s}{W_i} \times 100 \qquad \textbf{Equation 4.2}$$

$$\boldsymbol{Loading\ efficiency\ (LE\ \%)} = \frac{W_i - W_s}{W_G} \times 100 \qquad \textbf{Equation 4.3}$$

in which *EE* is the entrapment efficiency, $W_i$ is Dox's initial weight, $W_s$ is Dox's total weight in the supernatant after centrifugation, and $W_G$ is PG's weight used for attachment.

### 4.4.9. Drug release from the PG–Dox complex

The release of Dox was achieved using dialysis bags with a molecular weight cut-off value of 12,000 Da obtained from Sigma Aldrich® (UK). The bags were placed in 50 mL aqueous solutions of either PBS with a physiological pH (7.4) or endosomal cancer cell pH (5.4) at 37 °C with continuous stirring at 400 rpm in the dark. The drug's release from the PG–Dox and PG–$Trp_x$–Dox complexes was accomplished by withdrawing 0.5-mL samples every 1 h for 6 h and then at 12 h, 24 h and 48 h. The concentration of Dox released from PG and PG–$Trp_x$ was derived from fluorescence measurements at 600 nm using a calibration curve prepared under the same conditions (Figure 8.3 and 8.4, Appendix).

$$\boldsymbol{\%Cumulative\ Dox\ Released} = \frac{Amount\ of\ drug\ release}{Initial\ amount\ of\ drug} \times 100 \qquad \textbf{Equation 4.4}$$

### 4.4.10. Statistical analysis

Statistical analysis was performed in GraphPad Prism (GraphPad Software Inc., US) and Origin Pro (OriginLab Corporation, US). Because most populations of PG flake sizes were abnormal (i.e. skewed) and in a range of sample sizes, non-parametric tests were administered with few exceptions. The Mann–Whitney *U* test was used to compare two samples at a time, whereas the Kruskal–Wallis test was used for multiple comparisons. Those tests can be interpreted as non-parametric extensions of the *t* test and ANOVA, respectively.

### 4.4.11. Cell culture and toxicity

#### 4.4.11.1. Cell culture

Breast adenocarcinoma (MDA-MB-231) cells were kindly donated by Dr A. Tirella's team (University of Manchester), while Dulbecco's modified Eagle's medium was purchased from Sigma Aldrich® (UK). MDA-MB-231 cells were cultured with 10% v/v foetal bovine serum, 1% v/v penicillin–streptomycin and 1% v/v L-glutamine (i.e. complete medium), all purchased from Invitrogen™ (Thermo Fisher, UK). The cells were incubated in a humidified 5% $CO_2$ incubator at 37 °C and initially sub-cultured 3 times a week to a 1:3 dilution with a fresh culture medium for detachment using a trypsin–ethylene diamine tetra acetic acid solution obtained from Invitrogen™ (Thermo Fisher, UK).

#### 4.4.11.2. Cell proliferation assay

For a cell proliferation assay, we used a tetrazolium compound [3-(4,5-dimethylthiazol-2-yl)-5-(3-carboxymethoxyphenyl)-2-(4-sulfophenyl)-2H-tetrazolium, inner salt] (MTS) assay [303], in which the amount of formazan yielded was directly proportional to the number of viable cells. For the assay, the seeding density of cells was 5000 per well (100 µL) in 96-well plates, which allowed them to attach in the incubator overnight at 37 °C and 5% $CO_2$ with fresh media. After 24 h, the media were replaced and treated with free Dox and Dox–PG–$Trp_x$; the amount of free Dox used was 50 µg/mL, which equalled the amount present in Dox-loaded PG–$Trp_x$. The cells were incubated for 24 h and 48 h and treated with 20 µL of cell titre 96 aqueous MTS solution (Promega, US), followed by incubation at 37 °C and 5% $CO_2$ for 4 h. The absorbance of the formazan product resulting from the reduction of the MTS tetrazolium compound was recorded using a microplate reader at 490 nm. MDA-MB-231 cells with no treatment used as a negative control. All experiments were performed in triplicate.

#### 4.4.11.3. Fluorescence imaging

The intracellular distribution of free Dox, PG–Dox and PG–$Trp_x$–Dox systems was visualised with a Zeiss Axio Observer fluorescence microscope (Zeiss, Germany). MDA-MB-231 cells were seeded at $5 \times 10^3$ cells per well in six-well chamber slides for cell culturing (Thistle Scientific, UK). After being cultured for 24 h, in each well, cells were treated with free Dox and Dox derived from PG and the PG–$Trp_x$ systems, after which they were washed with PBS (pH 7.4) and fixed with paraformaldehyde for 5 min at 25 °C. Their nuclei were counterstained with 4,6-diamidino-2-phenylindole (DAPI) nucleic acid stain (Thermo Fisher, UK). Next, the cells were again washed with PBS, mounted and observed with the Zeiss fluorescence microscope. Following a standard procedure[304], DAPI nuclear stains and Dox were excited at 395 nm and 570 nm while their emissions were 445 nm and 605 nm, before being imaged with fluorescence microscopy.

## 4.5. Results and discussion

### 4.5.1. Molecular dynamics simulations

We first considered the interaction of Trp, $Trp_2$ and $Trp_3$ amino acids with a $C_{96}H_{24}$ graphene flake during a 500-ns MD simulation in explicit aqueous solvent, which we refer to as PG–Trp, PG–$Trp_2$ and PG–$Trp_3$, respectively. An inspection of those trajectories revealed persistent parallel π–π interactions between the indole ring of the amino acids and PG, which increased the number of Trp residues, to $Trp_2$ and $Trp_3$ resulted in more indole rings that interacted with PG (Figure 4.1). Those trends were also evidenced by short average side chain–graphene distances of 4.6 Å, 3.64 Å and 3.32 Å, respectively, compared with the backbone amino and carboxylate–graphene distances to graphene of 6.5 Å, 5.7 Å and 5.2 Å for Trp and $Trp_3$. A representative structure from the MD simulations furnished a projection of those charged amino and carboxyl groups towards the aqueous solvent (Figure 4.2), while the side chains

were stacked on the graphene's surface. In both cases, while maintaining a stacked geometry during MD simulation, the side chains were observed to translate quite freely on the hydrophobic face of the flake. Figure 4.2 shows the increased amount of peptide residue that attached to PG's surface revealed that $Trp_3$ stacked to PG's surface more than the single Trp. Raising the number of peptides to 12 also revealed that $Trp_3$ covered PG more thoroughly than Trp and $Trp_2$. Over the course of the simulations, the Trp, $Trp_2$ and $Trp_3$ molecules remained bound to the graphene's surface (Figure 4.3), with average distances between the molecular centres of mass and graphene's surface of 4.1 Å, 3.4 Å and 3.1 Å, respectively.

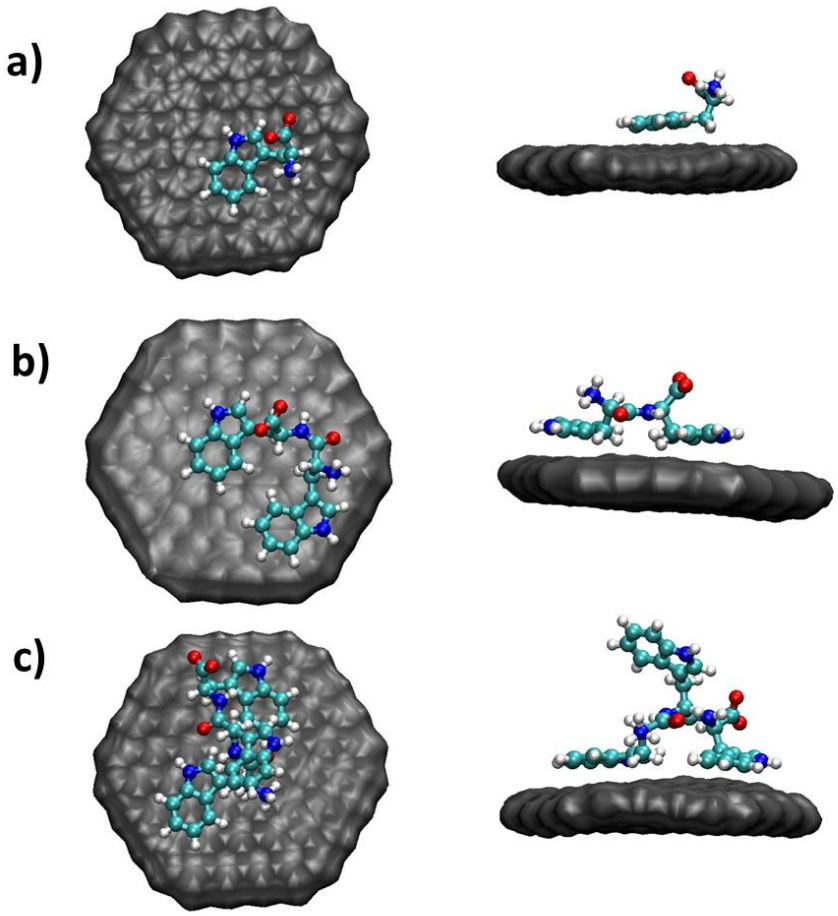


**Figure 4. 1-** Top and side views of representative Trpx–C96H24 orientations from (a) PG–Trp1, (b) PG–Trp2 and (c) PG–Trp3 MD simulations in explicit aqueous solvent.

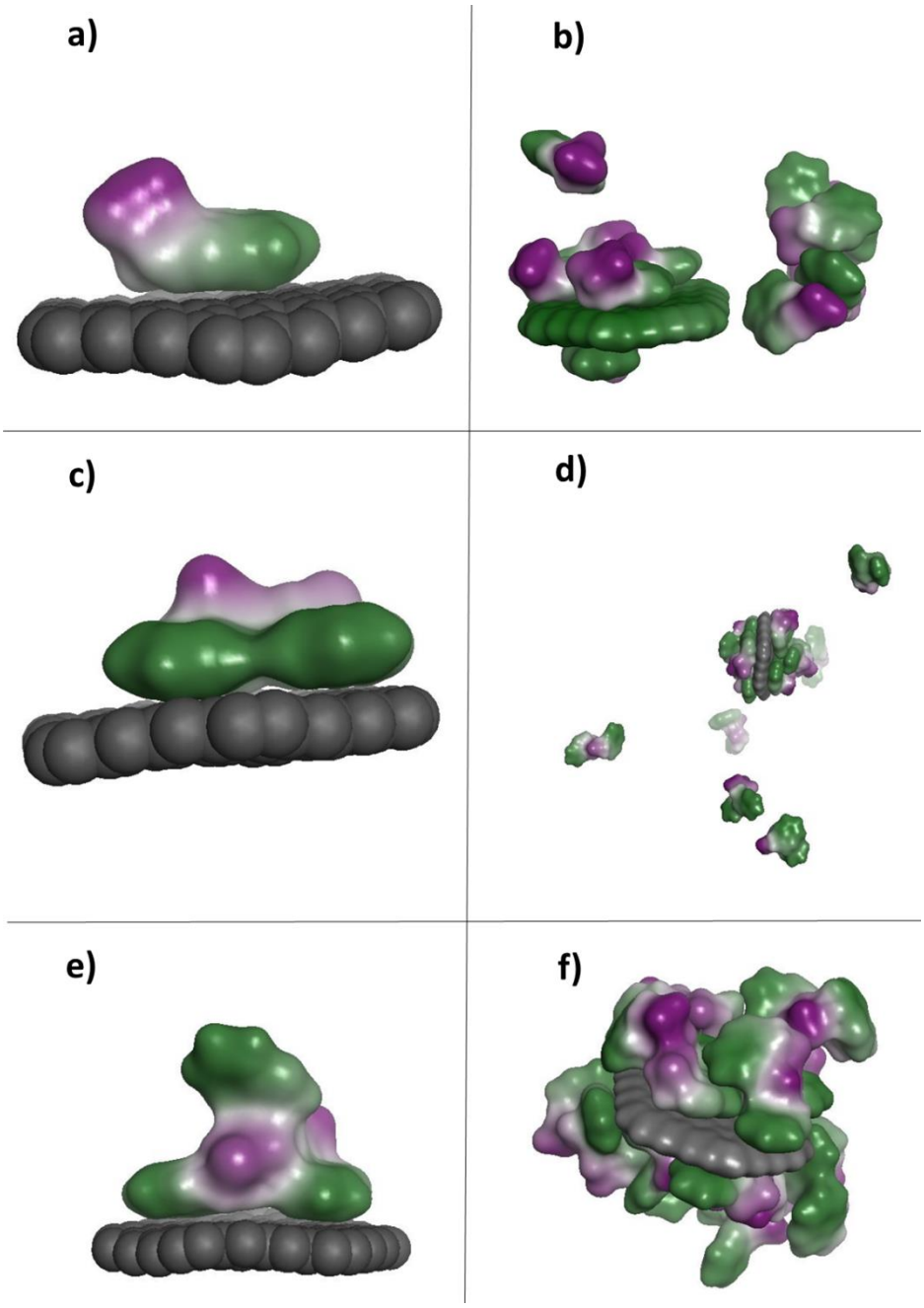


**Figure 4. 2**- Representative geometries of graphene (grey) and peptides from MD simulations in explicit aqueous solvent (water omitted for clarity). For the peptides, the hydrophobic regions appear in green and the hydrophilic regions in purple: (a) PG–$(Trp_1)_1$, (b) PG–$(Trp_1)_{12}$, (c) PG–$(Trp_2)_1$, (d) PG–$(Trp_2)_{12}$, (e) PG–$(Trp_3)_1$ and (f) PG–$(Trp_3)_{12}$.

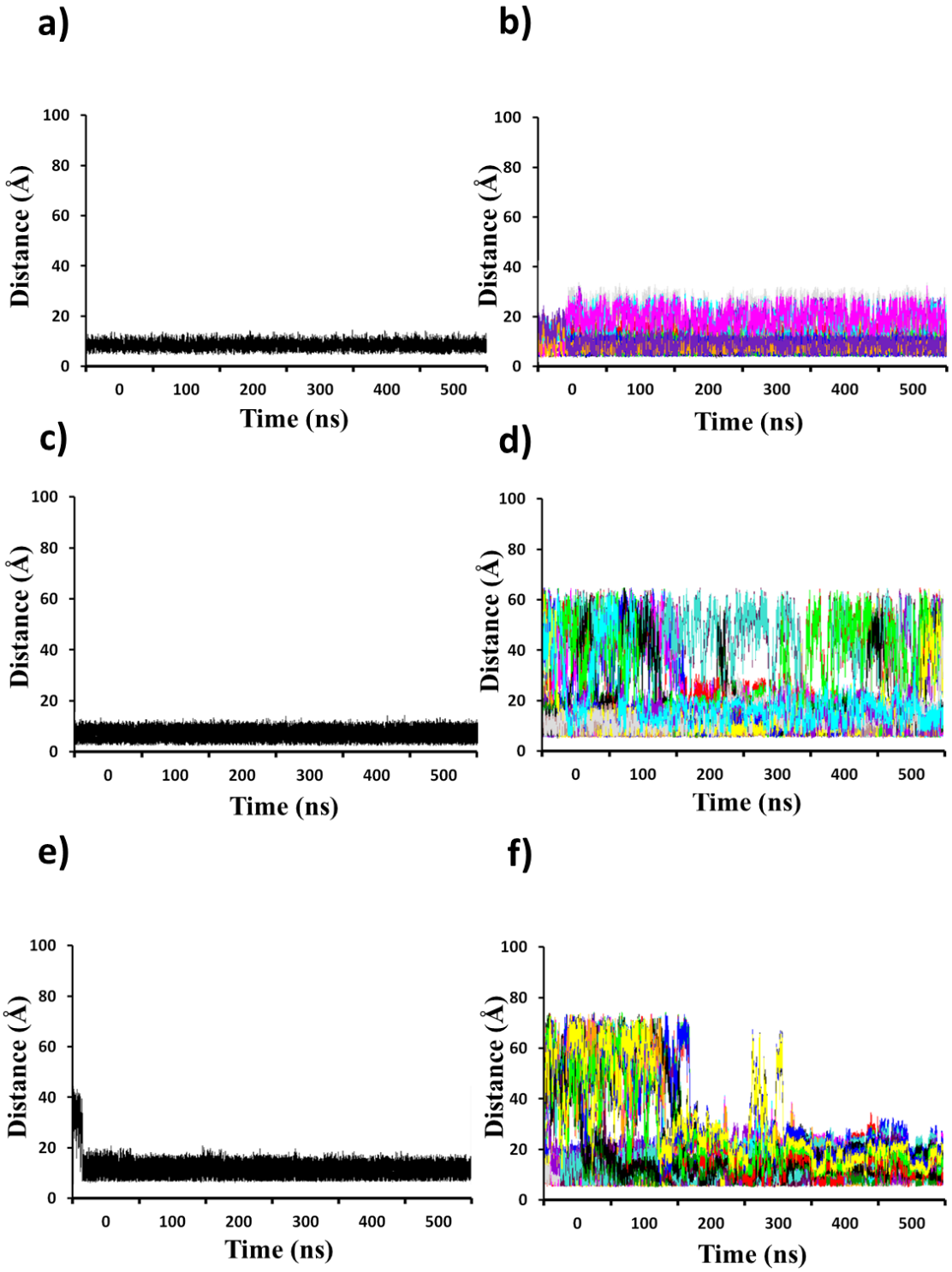


**Figure 4. 3**- Time series of distance (in Å) between the graphene's surface and the centre of mass of each peptide molecule in the system (coloured differently) for MD simulations of (a) PG–Trp, (b) PG–$(Trp_1)_{12}$, (c) PG–$(Trp_2)_1$, (d) PG–$(Trp_2)_{12}$, (e) PG–$(Trp_3)_1$ and (f) PG–$(Trp_3)_{12}$.

### 4.5.2. Characterisation of PG–Trp$_x$ particles

Assessing flake morphology is particularly important in characterising PG flakes, because the size, thickness and geometry of flakes are all significant determinants of how graphene may interact with a biological system. Thus, we employed various techniques to characterise PG and PG–Trp$_x$.

The morphology and thickness of the PG and PG–peptide samples were characterised by AFM, typical images of which and cross-sectional analyses of PG and PG–Trp$_x$ appear in Figure 4.4. Once the flakes were marked using height thresholding, the distribution of their thicknesses was determined. The topographic image in Figures 4.4(b) and 4.4(d) reveals a multilayer flakes with thicknesses of 1.70 ± 0.16 nm and 0.81 ± 0.36 nm, respectively, corresponding to, assuming that a single layer of graphene is 0.34 nm thick, approximately five and three layers, also respectively; such thickness equalled the extension of the π orbitals beyond the plane [273]. Figure 4.4(f) shows a bilayer flakes with a thickness of 0.628 nm, while Figure 4. 4(h) shows a monolayer with a thickness of 0.52 nm. Taken together, the distribution of flake thickness shown in Figure 4. 4 indicates that tripeptides were most likely able to produce single-layer of PG flake. An AFM study on the drug carrier was performed to provide information on the morphology and thickness of PG in Figure 4.4. While the conjugation of the Dox to the carrier was determined using FTIR shown in Section 4.5.4.

For each sample, the mean flake thickness measured using AFM was within the predicted range, based on graphene layer thicknesses reported in other research involving AFM [305, 306], thereby suggesting that the method is a reliable predictor of flake thickness in the system tested. In the three types of peptides, flakes in the monopeptide preparation were the thickest, whereas those in the tripeptide preparation were the thinnest. Those data were compared with other thicknesses derived from Raman spectroscopy.

Not only could Trp and $Trp_2$ exfoliate and suspend PG in an aqueous solution, but the nature of their interactions was highly dependent upon hydrophobicity and hydrogen-bonding interactions. When the efficacy of the exfoliating and suspending agents was assessed in terms of the graphene suspension's concentration and stability, $Trp_3$ was found to produce suspensions of a higher concentration, composed of thinner flakes ($0.52 \pm 0.33$ nm), than those produced by Trp and $Trp_2$, all observed using AFM. Flakes in $Trp_3$ were thinner than those achieved with graphene when gelatine was the reducing reagent (3.0 nm), precisely due to the attachment of gelatine [105]. $Trp_3$ still produced the most stable suspensions and the thinnest flakes. In other studies, the thicknesses of graphene layers have ranged from 0.5 nm and 1.0 nm as measured using AFM [274, 275], with measured thickness varying upon the interaction of the microscope's tip and the surface of the flakes, including the presence of any adsorbed molecules, particularly water molecules. Such thickness was confirmed using Raman spectroscopy in attachment with AFM; the single layer observed in the $Trp_3$ sample had a far more intense and sharper 2D band than one in multilayer graphene [307].

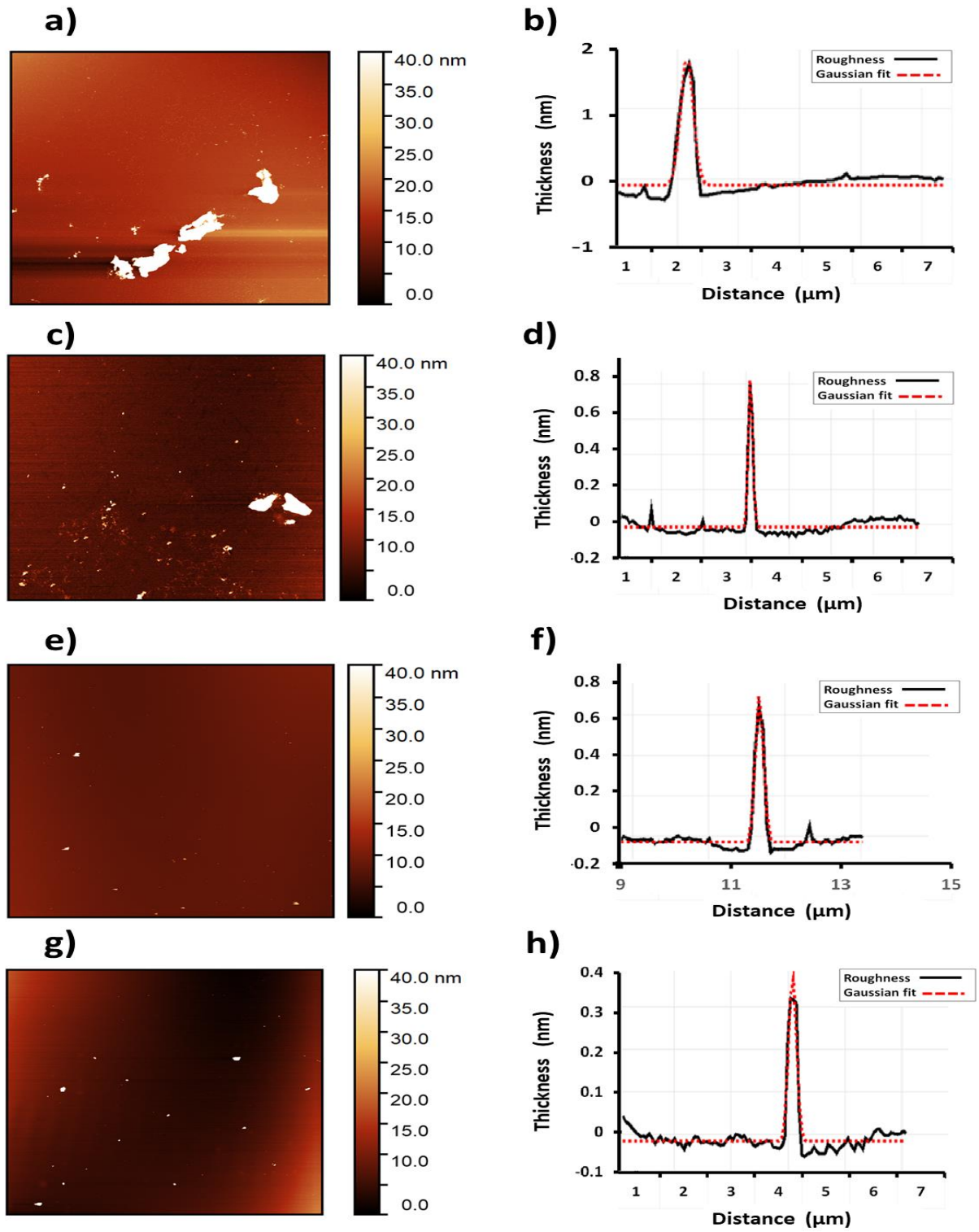


**Figure 4. 4**- Representative AFM images of PG flakes exfoliated and suspended in (a) PG only no Trp, (c) PG-Trp, (e) PG-$Trp_2$ and (g) PG-$Trp_3$, along with their thickness profiles (in nm) calculated from AFM images. Gaussian distribution was fitted in each case.

In addition to AFM, Raman spectroscopy revealed spectra of the different samples. Figure 4.5 presents characteristics of those spectra with unique G, D and 2D bands utilised to determine the number of different thin graphite films.

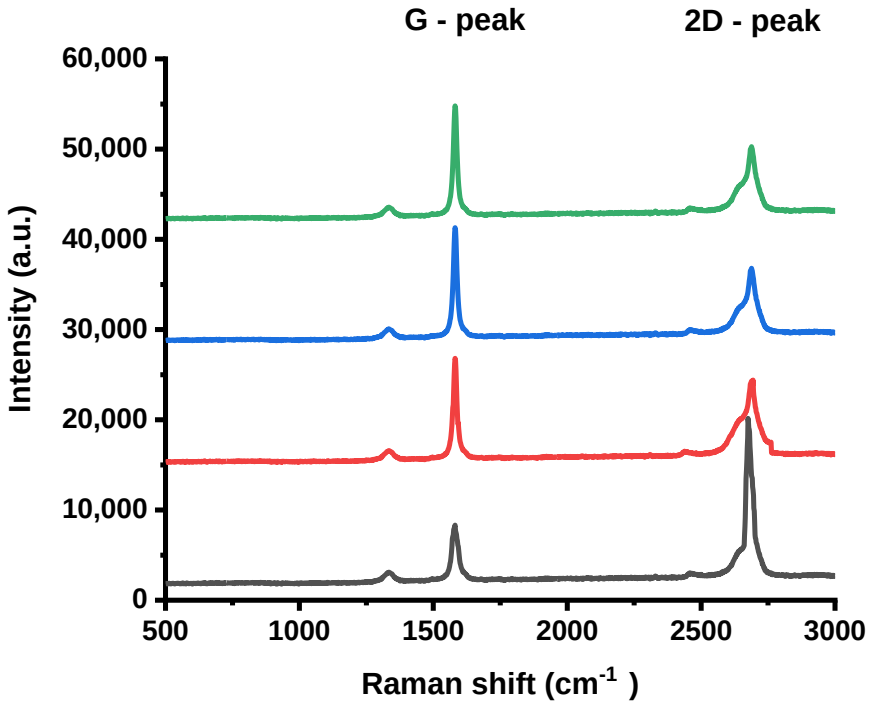


**Figure 4. 5-** Raman spectra for PG (green), PG–Trp (blue), PG–Trp2 (red) and PG–Trp3 (black) determined using Raman spectrometry at an excitation of 514.5 nm[307]. The measurements were taken as backscattering geometry at room temperature.

As the single-layer, bilayer and multilayer graphene have their own unique Raman fingerprints, the intensity of the D peak decreased as thickness increased, and the ratio of $I_{2D}$ *to* $I_G$ decreased especially sharply as thickness increased [308]. The Raman spectrum for PG revealed three important characteristics: a G peak of approximately 1580 $cm^{-1}$ [309], a 2D peak of approximately 2688 $cm^{-1}$ and a D peak of approximately 1333 $cm^{-1}$ [38]. The G band has been primarily associated with the formation of $sp^2$-bonded hybridised carbon, whereas the 2D band has been generally correlated to the $sp^3$ hybridisation of the graphitic structure [307, 310]. As

shown in Figure 4.5, monolayer graphene had an extremely sharp 2D bond (approx. 2678 $cm^{-1}$), one greater than the G band in $Trp_3$, as observed by AFM, with thickness of 0.52 nm. For bilayer graphene, the 2D peak was smaller than that of $Trp_3$, while the G band was greater than a single layer, as in $Trp_2$. The further increase in the number of layers prompted a significant decrease in the intensity of the 2D peak and an increase in the G peak. The Raman spectra could be used to distinguish single-layer and bilayer graphene from multilayer graphene (≥3 layers), and bulk graphite could be distinguished by the Raman fingerprints of the 2D bond [311]. The ratio of intensities of $I_{2D}$ to $I_G$ (Table 8.4 in Appendix) increased from PG to PG–$Trp_3$, thereby indicating a significant increase in the intensity of the 2D peak and a decrease in the G peak, both owing to an increased number of PG layers. After PG's functionalisation with Trp, the $I_{2D}$-to-$I_G$ ratio increased due to the increased intensity of the 2D band (Figure 4.5). Such outcomes suggest that adding the functional groups of $Trp_2$ and $Trp_3$ by functionalising PG restores the $sp^2$ hybridisation on the structure of PG.

### 4.5.3. Stability of PG–$Trp_x$ suspensions

After characterising the graphene flakes, it was important to determine the stability of the suspensions. The suspensions were left in glass vials undisturbed over the course of 4 weeks. In experiments that involved assessing the size, zeta potential and concentration of the suspended particles. With respect to these experiments, *stability* was defined as the propensity of the flakes to remain in suspension and for ones that had settled to the bottom of the container to redisperse when agitated.

### 4.5.3.1. Characterisation of flake size and behaviour in suspension using DLS

As illustrated in Figure 4.6(a), the median apparent $R_h$ values of the flakes after immediate preparation were 189.0, 96.5, 66.0, and 43.0 nm for PG, Trp, $Trp_2$, and $Trp_3$, respectively. By comparison, after 4 weeks of storage, those values were 139, 94, 56 and 32 nm for PG, Trp, $Trp_2$ and $Trp_3$, also respectively. The vast majority of the flakes in PG and Trp had aggregated into dark precipitates that sat at the bottom of their glass vessels, whereas those prepared using $Trp_2$ and $Trp_3$ had fewer precipitates and more PG flakes in suspension, as shown in Figure 4.7. For the majority of PG-only samples, the solution was entirely transparent, meaning that few particles remained in suspension. By contrast, in the presence of Trp, $Trp_2$ and $Trp_3$, the flakes remained in suspension, these results all agree with the findings from MD. Not only did apparent $R_h$ values in water suggest a significant difference between PG–$Trp_x$ samples and no Trp samples (Kruskal–Wallis, $p < .05$), but their apparent $R_h$ values after 1 month differed significantly as well (Kruskal–Wallis, $p < .05$).

DLS confirmed the instability of the PG flakes samples in the no Trp samples, and the difficulty of redispersing the flakes after aggregation suggested that aggregation was irreversible. Even immediately after preparation, the apparent $R_h$ of the flakes were far greater than those in $Trp_3$. It should be mentioned, however, that DLS depends upon observed diffusion times, which are necessarily affected by any molecules surrounding the surface, including multiple layers of peptides in the solution. Therefore, like all techniques relying on the assumption the particle is a sphere, DLS is likely to provide incorrect information for flakes. DlS results need to be compared to those given by a direct imaging method such as AFM [66].

### 4.5.3.2. Analysis of suspension stability and concentrations using zeta potential and UV-Visible absorption spectroscopy

Zeta potential were dropped from - 32.0 ± 2.6 to - 51.0 ± 0.4 mV in PG to PG–$Trp_3$, respectively, the apparent charge (Figure 4.6b) of the particles became more negative with Trp. After 4 weeks, the charge of the suspended particles remained between - 12.0 ± 3.1 and - 43.0 ± 0.8 mV, also in PG to PG–$Trp_3$, respectively. Zeta potential analysis also confirmed that $Trp_3$ produced a very stable suspension immediately after preparation and after 4 weeks.

Concentrations of PG in suspensions immediately after preparation did not demonstrate any major trends concerning type of peptides, whereas the $Trp_3$ sample had more PG flakes remaining in suspension after 4 weeks. Also after 4 weeks, concentrations in suspensions declined significantly in the PG sample, even beneath concentrations immediately after preparation, and was accompanied by visible aggregates of PG at the bottom of the vial (Figure 4.7). In Trp sample, more flakes had precipitated at the bottom than with $Trp_2$ and $Trp_3$, which aligns with the UV-vis absorbance measurements presented in Figure 4.6c. After 4 weeks, the concentration of particles decreased in all cases. That outcome was far more important for PG particles, however, because the concentration of PG–$Trp_3$ particles remained approximately 75% of the initial value compared with only 30% for PG particles [312].

The Mann–Whitney *U* test performed to assess whether each preparation's concentration of PG varied significantly over time revealed a significant difference ($p \geq .05$) for PG, PG-Trp and PG-$Trp_2$. No significant difference occurred for $Trp_3$.

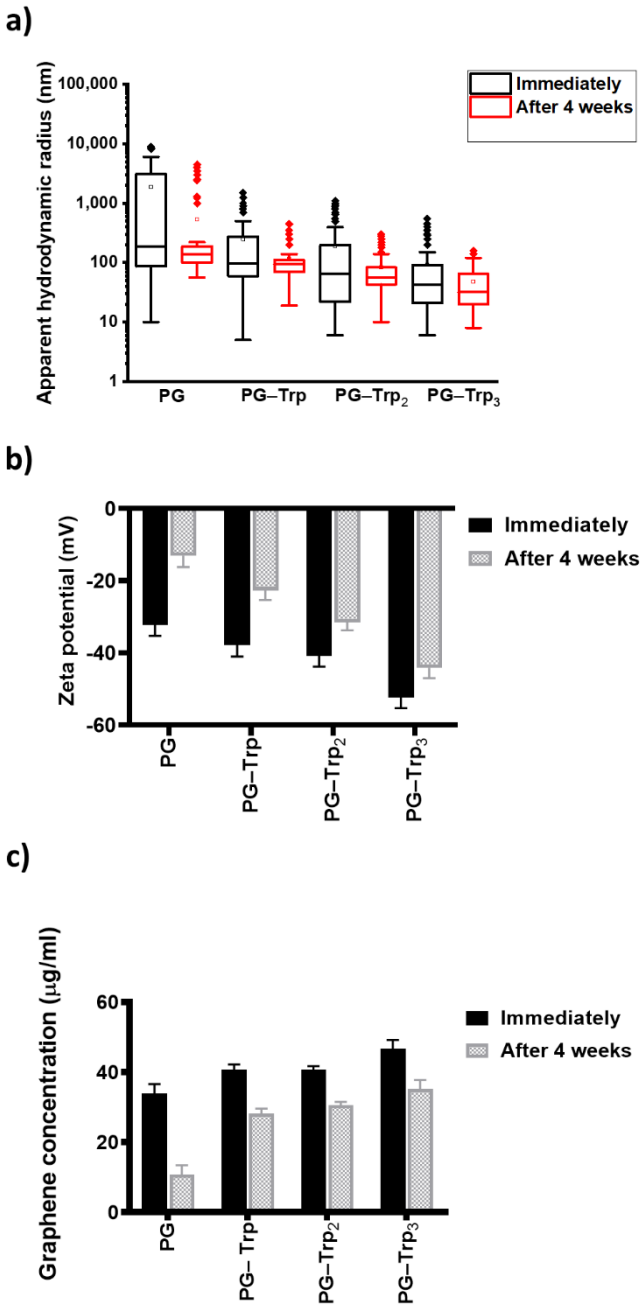


**Figure 4. 6-** Variation in the (a) size, (b) zeta potential and (c) concentration of PG, PG–Trp, PG–Trp2 and PG–Trp3 samples immediately after preparation and after 4 weeks**.** Data are expressed as mean ± SD (n = 3). Extended bars represent the 1st and 4th quartiles of the distribution, whereas box edges represent the 2nd and 3rd; the horizontal line in the body of the box is the median, the hollow squares represent the mean, and solid diamonds represent outliers. Errors were calculated as the standard deviation between the three samples taken.

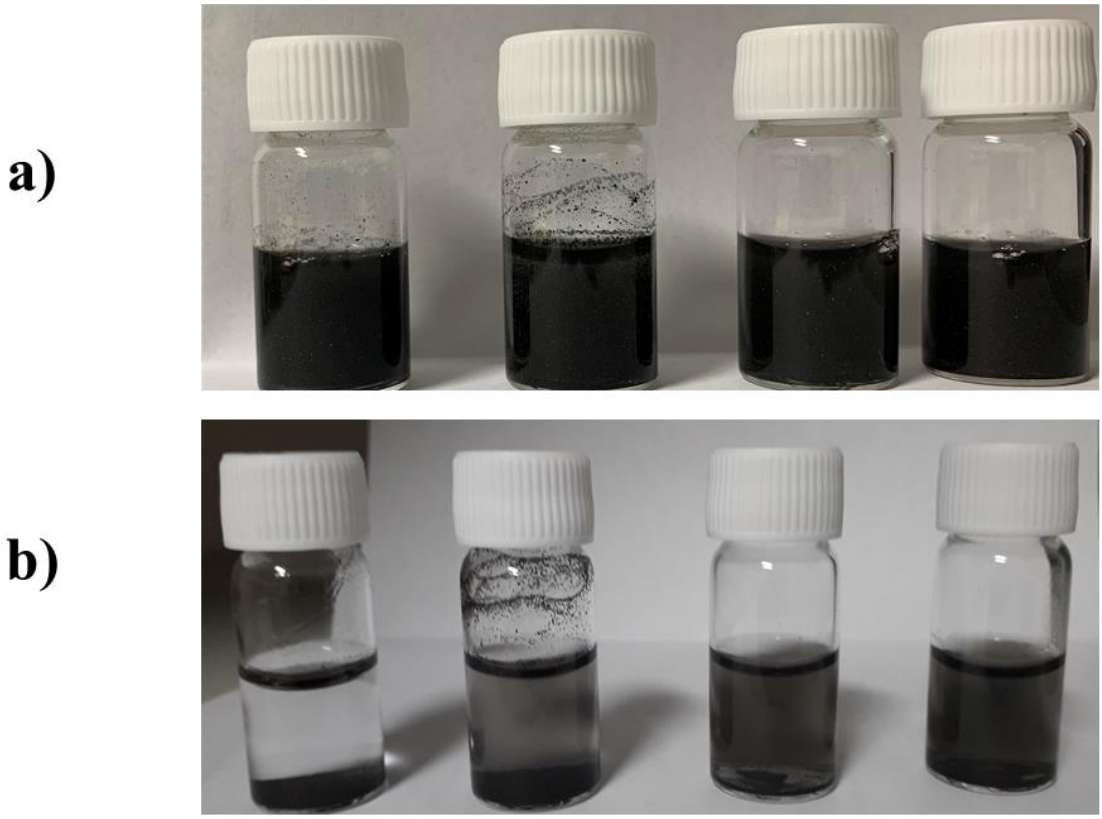


**Figure 4. 7-** Suspensions of PG at a) day 1 and b) 4 weeks after preparation. From left to right: PG, PG–Trp, PG–$Trp_2$ and PG–$Trp_3$.

### 4.5.4. Loading doxorubicin on pristine graphene attached with peptides

Once PG–$Trp_x$ particles were characterised, their abilities to load and release Dox were assessed. Figure 4.8 shows the drug-loading performance of PG for different initial mass ratios ($M$ ) of PG/Dox. The mass of Dox loaded rose as the initial PG/Dox mass ratios (i.e. black line in the figure) increased, meaning that PG's loading capacity may be as high as 3.9 mg of Dox per milligram of PG. However, the percentage of Dox loaded onto PG decreased (i.e. red line in the figure) as a function of the PG/Dox mass ratio; Dox's loading percentage fell as the amount of Dox rose and fell further from 85.5% to 55.0% when the amount increased from 1

mg to 2 mg. A possible explanation is that the first layer of Dox deposited onto PG's surface may be more densely adsorbed due to stronger non-covalent interactions [313].

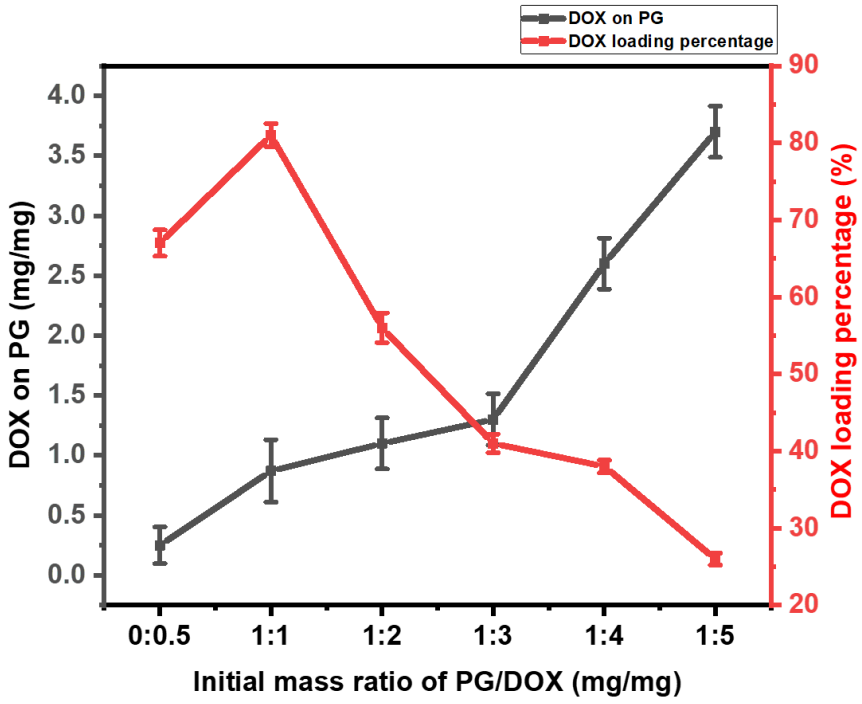


**Figure 4. 8-** Dox's loading percentage onto PG depending upon its different mass ratios. Data are expressed as mean ± SD (n = 3). The black line represents the amount of Dox loaded onto PG, while the red line corresponds to Dox's loading percentage, with errors calculated as the standard deviation of measurements from three samples.

Dox's loading onto PG is likely due to simple π–π, similar to that with carbon nanotubes. However, compared with single-walled carbon nanotubes for drug loading via π–π stacking, PG is not only inexpensive but also beneficial for scalability [17]. The hybridised π attached structure of PG's $sp^2$ may thus involve π–π stacking interactions with the quinine Dox component. At the same time, Dox's amine ($-NH_2$) and hydroxyl (-OH) groups can produce stacking strong hydrogen-bonding interactions with COOH and $NH_2$ groups on peptides; Dox can be loaded non-covalently onto PG, and its loose binding may rely on weak Dox–Dox

interactions [314]. Given all of the above, the mass ratio 1:1 was used for the remainder of the experiments in order to achieve effective Dox loading and lessen Dox waste.

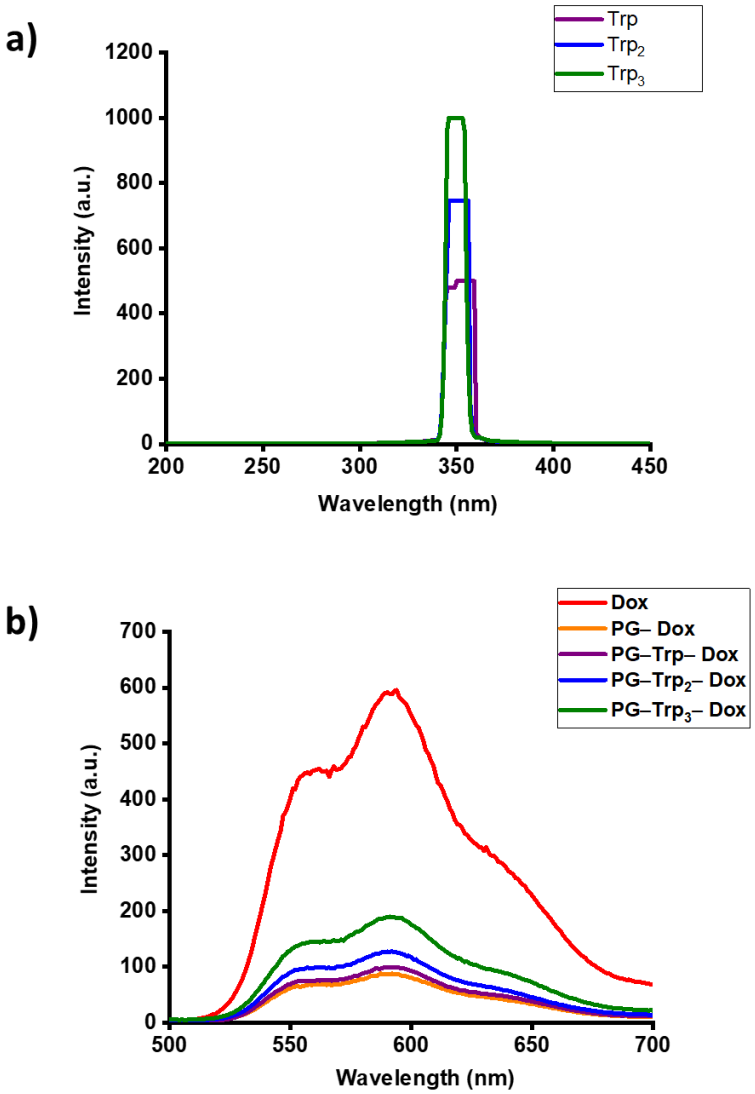


**Figure 4. 9**- Fluorescent intensity spectra for a) Trp1 (purple), Trp2 (blue),Trp3 (green) and b)Dox (red), PG–Dox (orange), PG–Trp–Dox (purple), PG–Trp2–Dox (blue) and PG–Trp3–Dox (green) produced with a fluorometer with emission wavelengths of 350 nm and 600 nm. The peptides and Dox concentration were 0.55µM.

To determine the LE of Dox molecules onto PG–$Trp_x$, Dox fluorescence quenching was monitored (Figure 4.9). Emission spectra of PG–$Trp_x$–Dox revealed the presence of two shoulders for peptides and Dox at two wavelengths: 350nm for tryptophan (Figure 4. 9a) and 600 nm for Dox (Figure 4.9b). For Dox PG-Trp, the fluorescence emission spectrum showed no obvious difference compared with that of PG–Dox only. However, when increasing the residue to $Trp_2$, the fluorescence intensity was higher than that of PG–Dox and PG–Trp–Dox. Added to that, $Trp_3$ demonstrated greater fluorescence intensity when attached with Dox. Those results suggest that the LE of $Trp_3$—that is, 40.2 (Table 4.1)—exceeded that of Trp and $Trp_2$. The fluorescence intensity increased as peptide residues to tripeptides increased at λ 350 nm, and, in turn, Dox loaded more intensely onto PG–$Trp_3$ than onto PG–Trp (Figure 4.9).

**Table 4. 1-** Effect of Dox's loading on the EE and LE in the PG and PG–Trpx samples.

| **Sample** | **EE%** | **LE%** |
|---|---|---|
| **PG–Dox** | 29.0 ± 5.9 | 13.9 ± 2.7 |
| **PG–Trp–Dox** | 31.5 ± 2.4 | 16.3 ± 3.9 |
| **PG–$Trp_2$–Dox** | 72.5 ± 2.7 | 37.1 ± 5.2 |
| **PG–$Trp_3$–Dox** | 81.3 ± 1.3 | 40.2 ±0.74 |

Listed in Table 4.1, the EE and LE using PG and PG–peptide carriers revealed that, for both measures, PG–Trp–Dox did not differ significantly from PG–Dox. However, PG's functionalisation using $Trp_2$ and $Trp_3$ increased the amount of Dox that loaded compared with non-functionalised PG and PG functionalised using Trp. As a Dox carrier and at this PG/Dox ratio (1mg/1mg), PG–$Trp_3$ achieved the highest EE (81.3% ± 1.3%) and the highest LE (40.2% ± 0.74%), followed by PG–$Trp_2$ (EE: 72.5% ± 2.7%, LE: 37.1% ± 5.2%).

Drug-loading and drug-releasing behaviour are essential characteristics to evaluate in every drug delivery system. Figure 4.8 shows the drug-loading performance of PG–$Trp_x$; PG's attach structure and high surface area facilitated strong π–π interactions with Dox and, in turn, contributed to high Dox loadings [42]. By increasing the amount of Dox used during drug loading, Dox's loading content (i.e. the weight of Dox to the weight of PG) rose sharply to peak at 5 mg Dox per 1 mg PG. Conversely, Dox's LE (i.e. the weight percentage of initial Dox bound to PG–$Trp_x$) decreased with rising amounts of Dox used and fell from 85.5% to 25.3% when 5 mg Dox was used.

A particularly interesting result was that the EE of the aforementioned particles was greater than that of chitosan nanoparticle formulations, namely polyphosphoric acid (EE: 12.2%), type B gelatine (EE: 8.4%), glucomannan (EE: 9.3%) and dextran sulphate with chitosan nanoparticles (EE: 21.9%) [315]. Beyond that, the LE for $Trp_2$ and $Trp_3$ was significantly greater than that in the polymer micelle carrier systems—for example, LE ranged from 15% to 20% for poly(ethylene glycol)–poly(β-benzyl-L-aspartate) copolymer micelles [316]. Those peptide-functionalised PG systems also demonstrated higher LE values than glyceryl caprate–curdlan solid lipid nanoparticles (2.8%) [317].

Graphene is potentially a superior drug carrier, because both sides of its flakes are available for drug loading and binding by way of physical adsorption [318, 319]. The presence of π electrons on graphitic domains facilitates the formation of non-covalent binding via π–π stacking interactions with several materials, including Dox [75, 320]. In our experiment, those π electrons on the plane immobilised Dox by non-covalent physical adsorption [10]. Along with π–π stacking interactions, peptide-functionalised PG formed strong hydrogen bonds with Dox, because the presence of peptide functional groups on PG's surface can promote hydrogen-bonding between peptides functionalised with PG and Dox [321, 322]. The combined effect of those two interactions (i.e. π–π stacking and hydrogen bonding) may have exposed PG–$Trp_2$

and PG-$Trp_3$ to a higher LE than with non-functionalised PG. As shown by the results of MD (Figure 4.2f), the ability of $Trp_3$ to functionalise PG resulted in more PG flakes being suspended thus may also explain more Dox being loaded in the experiment.

The apparent charge of the particles (Figure 4.10) presented a trend similar to that observed in Figure 4.6(b). However, adding Dox reduced that charge from PG to PG–$Trp_3$ in measurements taken immediately after preparation and after 4 weeks. Moreover, the increased zeta potential might be due to the addition of amino groups in Dox after the binding of Dox to PG particles[323].

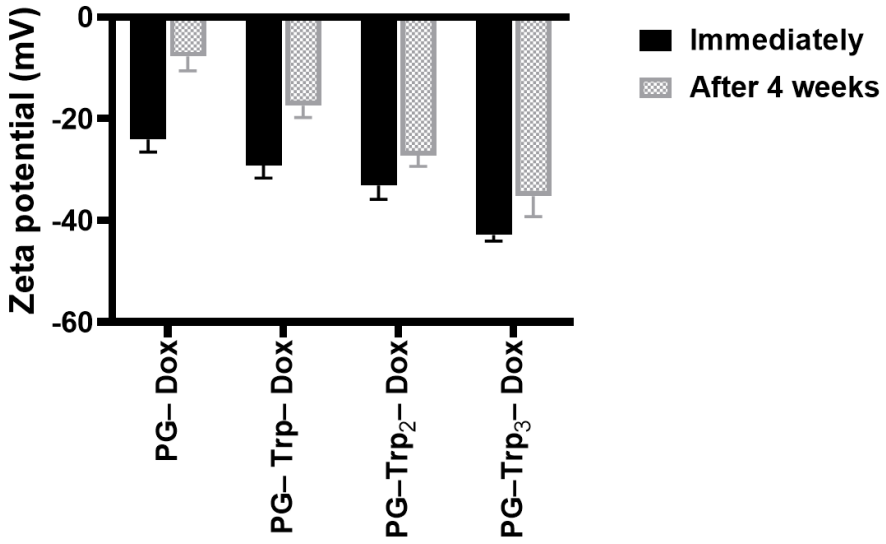


**Figure 4. 10**- Zeta potential values of Dox with PG, PG–Trp, PG–Trp2 and PG–Trp3 in aqueous solutions. Each graph shows the immediate zeta potential value and that after 4 weeks. The errors were calculated as the standard deviation of measurements from three different samples.

Furthermore, FTIR spectra, generated to investigate PG's functionalisation and detect non-covalent binding on PG (Figure 4.11), revealed no significant peaks for PG, despite strong

absorption peaks for Trp at 3402, 3037, 2561, 1589, 1411, 1357, 1059 and 744 $cm^{-1}$, respectively assigned to N–H stretching in amines, C–H stretching in alkenes, O–H stretching in carboxylic acids, N–H bending in amines, C–H bending in alkanes, C–N stretching in aryl amines and C–H bending in the aromatic ring [324]. In PG–$Trp_x$–Dox, a drop in Trp peak intensity at 3037 $cm^{-1}$ suggested π–π stacking, and intensity at 3403 $cm^{-1}$ fell as the amount of peptide residues attached to PG rose [325]. Finally, an additional peak for PG–$Trp_3$–Dox emerged at 3000 $cm^{-1}$, possibly owing to Trp's covering of PG's surface via π–π interactions, which would also explain the increased amount of Dox loaded on PG's surface (Table 4.2).

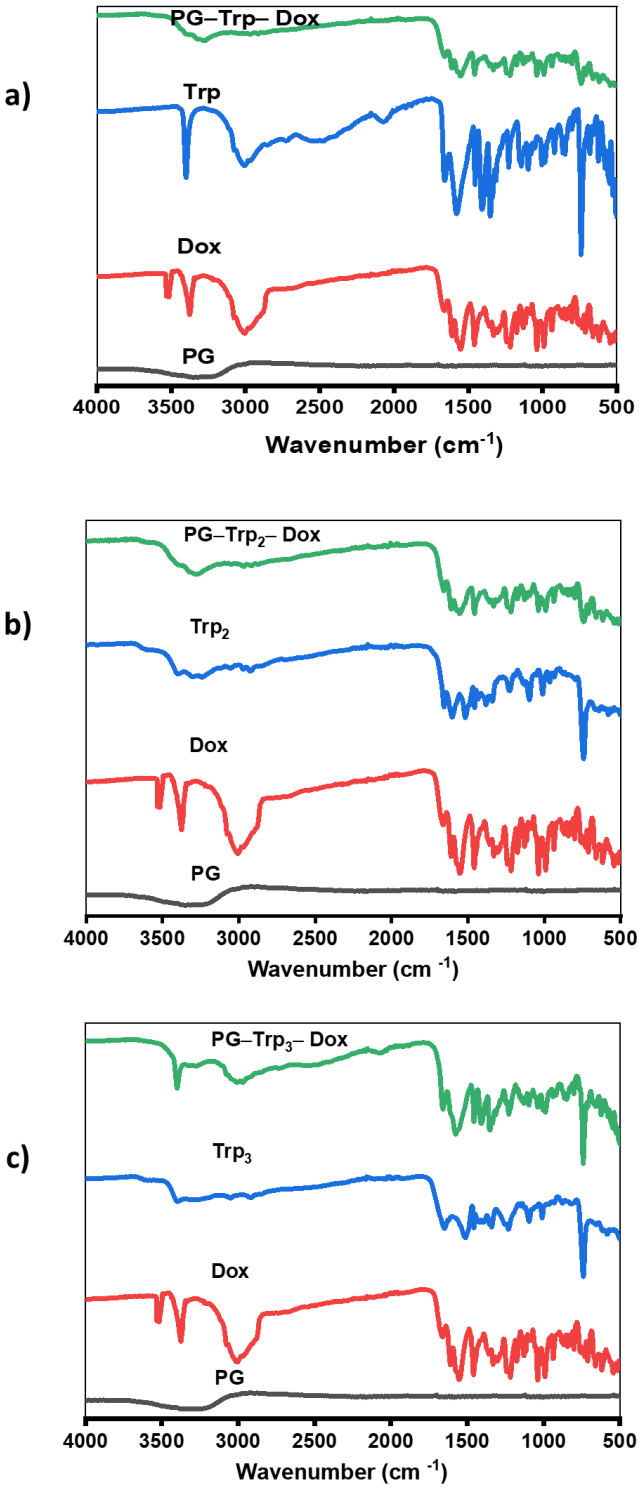


**Figure 4. 11-** FTIR spectra of (a) PG–Trp–Dox, (b) PG–Trp2–Dox and (c) PG–Trp3–Dox, produced using an FTIR spectrometer scanning from 4000 to 400 $cm^{-1}$**.** PG (black), Dox (red), $Trp_x$ (blue) and PG-$Trp_x$-Dox (green). The average of 24 scans at a resolution of 4 $cm^{-1}$ was recorded, with air as the reference background. For each sample, three replicates were recorded.

### 4.5.5. *In vitro* studies

#### 4.5.5.1. Drug release response

A drug's *in vitro* release from a drug carrier depends upon several experimental factors, including particle size, pH, degradation rate, drug–surface interaction and the behaviour of the carrier in solvent [326]. As shown in Figure 4.8, Dox's content on the PG–$Trp_x$ carrier hovered around 1 mg/mg and thus potentially above the content of common drug carriers such as carbon nano-horns [327] and polymer vesicles [328], whose values usually fall below 1 mg/mg at saturated carrying concentrations. Although Dox may have loaded efficiently onto those PG-based particles, another important aspect to assess in the drug delivery systems was their ability to release Dox. Thus, Figure 4.12 shows the release of Dox from PG and PG–$Trp_x$ at pH 7.4 (i.e. physiological pH) and pH 5.0 (i.e. endosomal pH of cancer cells).

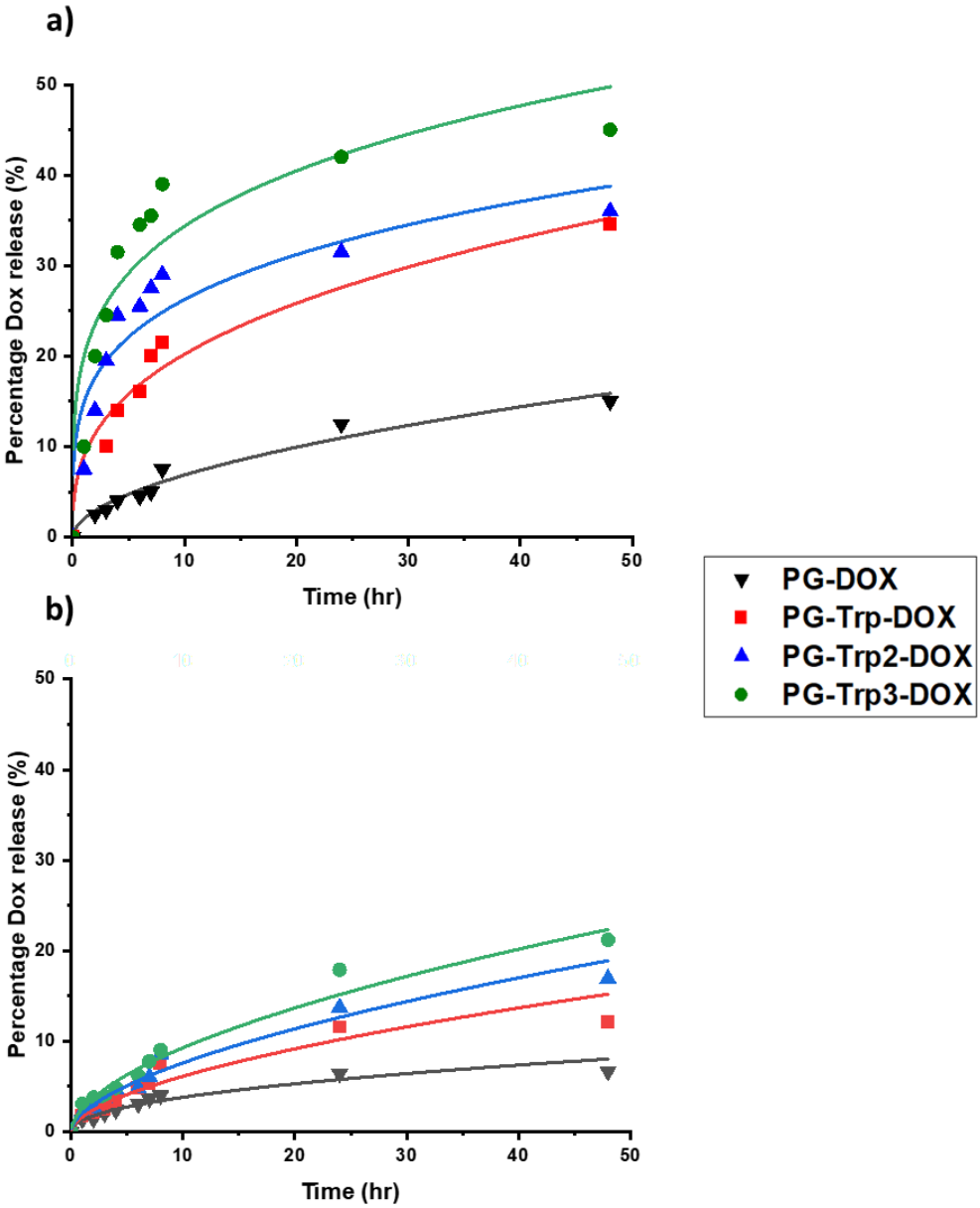


**Figure 4. 12-** Release of Dox in the PG–Dox (black), PG–Trp–Dox (red), PG–$Trp_2$–Dox (blue) and PG–$Trp_3$–Dox (green) complexes in PBS at a) pH 5.4 and b) pH 7.4, over 48 h. Symbols represent experimental data and lines represent best fits using Equation 4.5.

Dox's release from PG and PG–$Trp_x$ was clearly pH-dependent (Figure 4.12), for it appeared to be more limited at pH 7.4 than at pH 5.4. After 48 h, approximately 10%, 30%, 34% and 48% of Dox loaded onto PG, PG–Trp, PG–$Trp_2$ and PG–$Trp_3$, respectively, were released at pH 5.4. At pH 7.4, by contrast, those percentages dropped to approximately 6%, 12%, 16%

and 21%, also respectively. As calculated in past studies [329, 330], drug release can be represented as:

$$\frac{M_i}{M_\infty} = kt^n \qquad \textbf{Equation 4.5}$$

in which Mi/M∞ represents drug released at time *t*, and *k* and *n* are constants. Equation 4.5 can also be applied to our experimental data to determine the constant *n*. The *k*, n and correlation coefficient ($R^2$) were shown in Table 4.2. For drug release at pH 5.4, $n < 0.5$ a Fickian diffusion is suggested, which was related to the fast drug release as *n* changed from 0.53 to 0.34 for PG and PG–$Trp_3$. As shown in Table 4.2, the *k* value was increased from 1.5 to 15.3, which clearly showed more drug released in the PG-$Trp_3$ sample. Whereas, at pH 7.4 PBS, $n > 0.5$ is non-Fickian with a value of *n* ranging from 0.57 and 0.60 for PG and PG–$Trp_x$ [331]. The *k* value increased slightly from 1.2 to 2.5 at pH 7.4, which is lower than pH 5.4, thus indicated less Dox released at pH 7.4.

**Table 4. 2**- Parameters n, k and R2 determined by equation (4.5) for the Dox release of samples with PG and PG-$Trp_x$.

| Samples | Release condition | *k* | *n* | $R^2$ |
|---|---|---|---|---|
| **PG-Dox** | pH 5.4 | 1.5 ± 0.3 | 0.55 ± 0.05 | 0.90 |
| **PG-Trp. Dox** | | 5.5 ± 1.2 | 0.53 ± 0.05 | 0.83 |
| **PG-$Trp_2$-Dox** | | 11.6 ± 0.7 | 0.35 ± 0.04 | 0.64 |
| **PG-$Trp_3$-Dox** | | 15.3 ± 0.4 | 0.34 ± 0.05 | 0.65 |
| **PG-Dox** | pH 7.4 | 1.2 ± 2.8 | 0.57 ± 0.02 | 0.86 |
| **PG-Trp. Dox** | | 1.6 ± 1.3 | 0.58±0.03 | 0.88 |
| **PG-$Trp_2$-Dox** | | 1.9 ± 0.8 | 0.59± 0.03 | 0.93 |
| **PG-$Trp_3$-Dox** | | 2.5± 0.6 | 0.60± 0.02 | 0.94 |

At pH 5.4, the differences appeared to be significant (Kruskal–Wallis, $p < .05$) between PG–$Trp_x$ release profiles. Such divergence may be due to reduced hydrogen-bonding interaction between Dox and peptides in acidic conditions. In those conditions, because the amine ($-NH_2$) groups in Dox protonated and resulted in the partial dissociation of hydrogen bond, the amount of Dox released from PG–$Trp_x$ was greater than in neutral conditions. Nevertheless, those differences did not appear to be significant (Kruskal–Wallis, $p < .05$) between PG–$Trp_x$ at pH 7.4, possibly due to the hydrogen-bonding interactions between Dox and peptides, which occurred more prominently in the neutral conditions and resulted in a controlled release. Overall, the pH-dependent release of Dox from PG–$Trp_x$ is important knowledge for drug delivery, given the acidic micro-environments in the extracellular tissue around tumours, intracellular lysosomes and endosomes [332].

#### 4.5.5.2. *In vitro* cytotoxicity

The *in vitro* cytotoxicity was tested with a MTS assay. In particular, the *in vitro* cell viability of free Dox, PG, PG–$Trp_x$ , PG–Dox and PG–$Trp_x$–Dox was tested against the breast cancer cell line MDA-MB-231. Cell viability remained above 95% after 24 h and 48 h following treatment with PG, PG–Trp, PG–$Trp_2$ and PG–$Trp_3$, thereby indicating that PG–$Trp_x$ particles are not toxic to those cells (Figure 4.13).

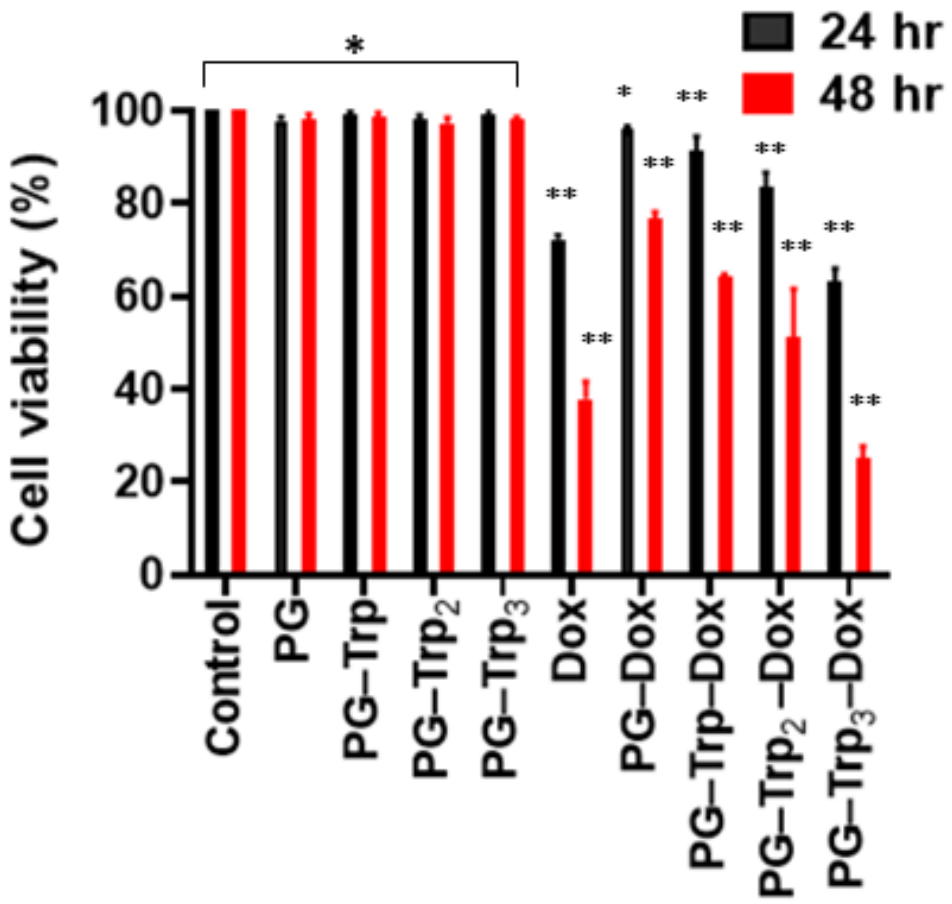


**Figure 4. 13-** Cytotoxicity of PG, PG– Trpx , Dox, PG–Dox and PG–Trpx– Dox against MDA-MB-231 cancer cells by MTS assay using 50 µg/mL of Dox-equivalent concentrations after 24 h and 48 h. Data are expressed as mean ± SD (n = 5). * $p > .05$ and ** $p < .05$ are no statistical significant difference and the statistical difference. Two way ANOVA was performed using Sidak's multiple comparisons test and the significance level is indicted. Bars indicate standard deviation.

For that MTS assay, the concentration of Dox loaded onto PG and PG–$Trp_x$ was kept the same as that of free Dox (50 µg/mL). Following incubation with free Dox and Dox loaded onto PG and PG–$Trp_x$, an inhibition of the growth of MDA-MB-231 cell lines was observed after 24 h and 48 h. After 24 h, cell viability dropped to 71% in the presence of free Dox, whereas PG–Dox, PG–Trp –Dox and PG–$Trp_2$– Dox demonstrated a lower toxicity (95, 91 and 83%

respectively). However, cell viability decreased significantly in the presence of PG–$Trp_3$ – Dox to 63%, to levels lower than those of free Dox. Moreover, a significant difference (Kruskal–Wallis, $p < .05$) emerged between free Dox and PG–$Trp_x$ – Dox. Assuming that only the released free Dox can interact with DNA molecules to cause cytotoxicity, the weaker toxicity of PG–Dox, PG–Trp–Dox and PG–$Trp_2$–Dox may be ascribed to the low amount of Dox released from the PG–Dox surface (Figure 4.12a) at pH 5.4 over 24 h. The attachment of Trp, $Trp_2$ and especially $Trp_3$ to PG's surface caused significantly higher toxicity than with PG–Dox, as may be partly explained by data in Figure 4.13. After 48 h, cell viability decreased significantly for all samples containing Dox, and the incubation of cells with free Dox, PG–Dox, PG–Trp–Dox, PG–$Trp_2$–Dox and PG–$Trp_3$–Dox resulted in respective decreases of 37%, 76%, 64%, 51% and 24% in cell viability compared to 24 h. The absence of a positive control affects the assay's sensitivity as it is essential to confirm the sensitivity.

In summary, PG–$Trp_3$–Dox may be a promising nano-carrier for delivering Dox that can overcome drug resistance in cancer cells. Dox not only binds tightly with PG–tripeptides at a physiological pH but can also release its load at lower pH i.e. in late endocytosis. Acidic conditions of the endosomal–lysosomal component are likely the chief driving force for Dox's release inside cancer cells; however, introducing tripeptides improved its release and, in turn, its toxicity.

### 4.5.5.3. Intracellular Dox

Figure 4.14 illustrates the presence of Dox (i.e. red fluorescence) inside cells from free Dox, PG–Dox and PG–$Trp_x$–Dox in MDA-MB-231 cells. For all treatments, an intense Dox fluorescence was observed mostly in the cytoplasm, and to some extent in the nuclei. The overlay of PG–Dox showed weak red fluorescence in cells, especially compared to PG–$Trp_3$-

DOX. Considering the PG-based particles only, fluorescence intensity appeared to increase from PG–Dox to PG–$Trp_3$-DOX; the fluorescence intensity of the latter approaching that of DOX alone. Earlier reports showed that the fluorescence of Dox could be quenched in presence of graphene due to the $\pi-\pi$ stacking with PG [78, 333]. The intracellular Dox fluorescence intensity (red colour) was significantly higher for PG-$Trp_3$-Dox compared to PG-Trp-Dox, PG-$Trp_2$-Dox and free Dox. Endocytosis is likely to be involved in the delivery of the PG based particles i.e. cellular uptake and transport in cytoplasm. In the nuclei (blue colour area), the fluorescence intensity of free Dox (red colour) appeared to be higher than PG-Trp-Dox, PG-$Trp_2$-Dox and PG-$Trp_3$-Dox, which may be caused by the delayed Dox release from the PG sheets [334].

Based on our data on drug release (Section 4.5.5.1), Dox's pH-dependent release behaviour is likely to assist drug release during the endocytic process. Its release rate at pH 5.5 was significantly higher than that at pH 7.4, possibly due to weakened hydrogen bonds between Dox and PG–$Trp_x$. Taken together, those images confirm the idea that a PG-based delivery system can contribute to delivering drugs into cells [335]. Previous work suggested that the cell viability data obtained by using MTS assay may be inconsistent as graphene can interfere with MTS resulting in optical interferences, induced adsorption and electron transfer; all of which is likely to prevent appropriate evaluation of graphene toxicity[336]. Finally, although not sufficient to directly support every step of this process, intracellular Dox fluorescent results are consistent with such an interpretation. The release mechanism of the Dox from PG-$Trp_x$-Dox requires further investigation.

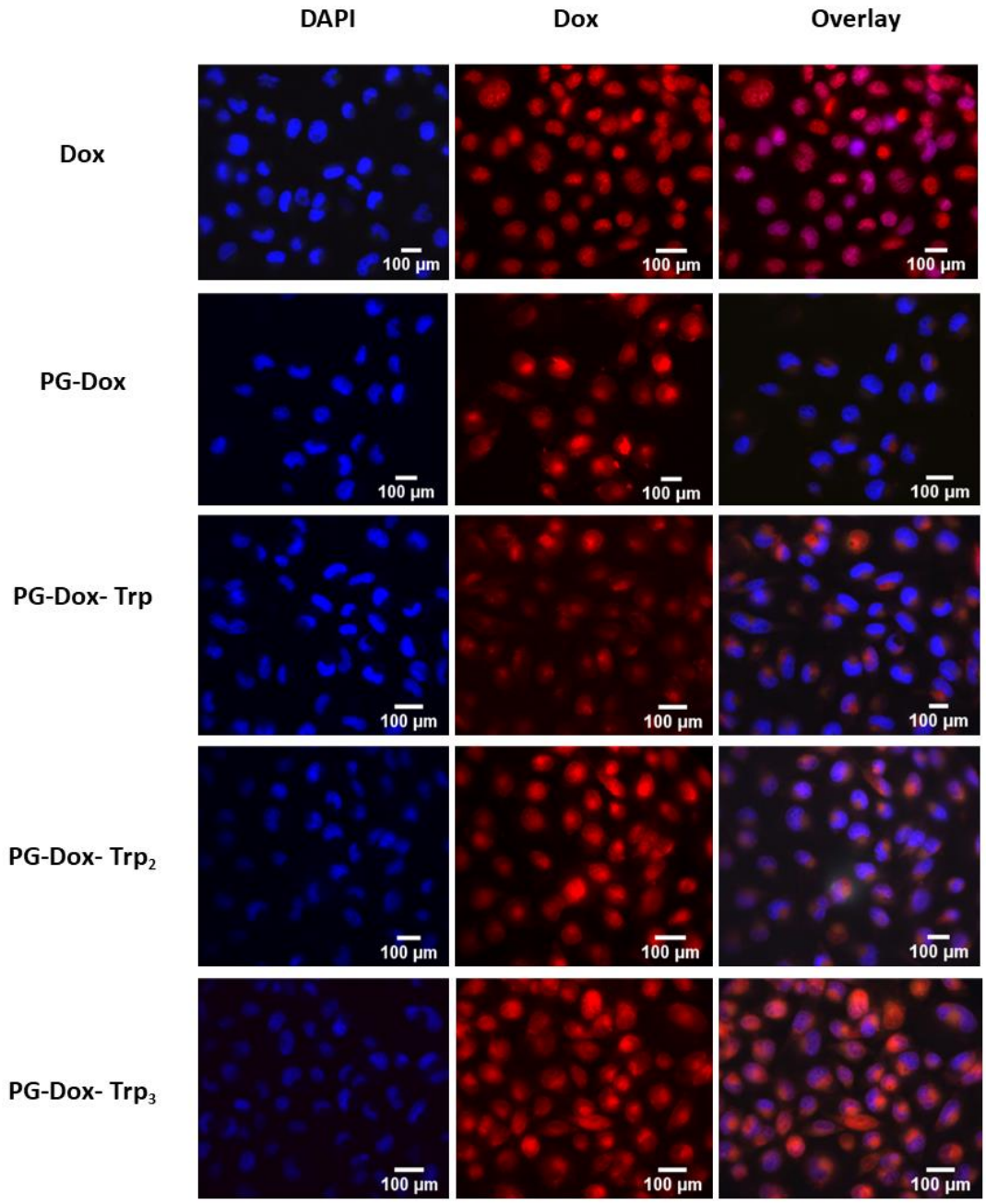


**Figure 4. 14-** Representative fluorescence images of MDA-MB-231 treated with free Dox, PG–Dox and PG–Trpx –Dox incubated for 48 h with MDA-MB-231 cells were seeded at 5 × $10^3$ cells per well in six-well chamber slides. The cells were then washed with PBS (pH 7.4) and fixed with paraformaldehyde for 5 min at 25 °C. The final concentration of Dox in all cells was equivalent to 50 µg/mL. Blue colour indicates DAPI (nuclei stain) and the red colour represents Dox. Scale bars: 100 µm.

## 4.6. Conclusion

Seeking to demonstrate the potential of PG–Trp peptides as vehicles for drug delivery, we found that short tryptophan peptides (i.e. dipeptides and tripeptides) could functionalise PG to form stable suspensions with reduced toxicity. However, those results clearly depended upon the length of the peptide. Indeed, the tripeptide, $Trp_3$, created a complex with PG with the most negative zeta potential, which resulted in the highest concentration of PG in suspension after 4 weeks and the smallest particles in suspension. The influence of size also manifested when the thickness of PG flakes decreased from multilayer to single layer—for example, from no Trp to $Trp_3$—as revealed by both AFM and Raman spectroscopy. In particular, Raman spectroscopy confirmed the presence of a single layer of PG flakes in $Trp_3$, in which the 2D peak's intensity exceeded the G peak's intensity, and the $I_{2d}$-to-$I_G$ ratio was greater than in the PG sample.

Dox was used as a model drug to test PG–$Trp_x$ as potential vehicles for drug delivery. Dox's LE was greatest in PG–$Trp_3$, owing to PG's surface modification by peptides. Meanwhile, its release depended upon the pH, which was larger at pH 5.4 than at pH 7.4. An MTS assay suggested that PG–$Trp_2$– Dox and PG–$Trp_3$–Dox reduced the viability of MDA-MB-231 cells more than PG–Dox and PG–Trp–Dox but to levels similar to those achieved with free Dox.

Although our results are preliminary, especially the ones regarding toxicity and drug release, they nevertheless highlight the potential of simple amino acids and their short peptides to create stable suspensions of PG.

*Research Article*

# 5. Characterisation of graphene oxide for use in biomedical applications

Fai A. Alkathiri[a], Catriona McCallion[a], Alexander P. Golovanov[b], John Burthem[c], Richard A. Bryce[a, *] and Alain Pluen[a *]

[a] *Division of Pharmacy and Optometry, School of Health Sciences, University of Manchester, Manchester, UK*

[b] *Manchester Institute of Biotechnology, and School of Chemistry, Faculty of Science and Engineering, University of Manchester, Manchester, UK*

[c] *Division of Cancer Sciences, University of Manchester, Manchester, UK*

Corresponding Authors

*Alain Pluen, Division of Pharmacy and Optometry, School of Health Sciences, University of Manchester, Manchester, M13 9PT, U.K. Email: Alain.Pluen@manchester.ac.uk, Tel: (0)161-275-1792

*Richard Bryce, Division of Pharmacy and Optometry, School of Health Sciences, University of Manchester, Manchester, M13 9PT, U.K. Email: Richard.Bryce@manchester.ac.uk, Tel: (0)161-275-8345

## 5.1. Abstract

Graphene oxide (GO) represents a promising class of drug carriers, the characterisation of which has received extraordinary attention, before the suspension deliver in vivo. GO has been widely used in the biomedical sphere than pristine graphene due to the presence of oxygen functional group, which makes it easy to attach to drugs and ligands. The inherent fluorescence of GO can be used to improve suspension characterisation; raster image correlation spectroscopy (RICS) can be used as a technique to characterise the distribution of flake sizes present in suspension. In our study, GO samples were studied under various conditions, including sonication power, after washing and dispersion in various media. The highest sonication power revealed a more uniform distribution of GO flakes and the washed GO (wGO) samples, which had less small particles. Because washing removes the impurities, it aids in extracting GO flakes only as carriers. Under brightfield optical microscopy and atomic force microscopy (AFM) to determine the morphology of GO flakes, the wGO sample showed single layers of GO flakes, whereas unwashed GO (uwGO) samples had multiple layers of GO. Also, the results showed that AFM cannot measure flakes larger than 10 um; however, optical microscopy can measure flakes up to 100 um on substrate. Whereas dynamic light scattering (DLS) and raster image correlation spectroscopy (RICS) can be used to assess the behaviour of GO flakes in biologically relevant media at different ionic strengths and concentrations of saline, phosphate buffer saline (PBS) and phosphate buffer. The finding showed when the ionic strength increases, the lake size increase and could be due to GO's aggregation at high concentrations of saline. Furthermore, DLS cannot capture flakes more than 10 um; however, it can assess the quality of GO suspension via the correlation curve method. By contrast, RICS is an alternative approach that can be used to measure large flakes and evaluate the behaviour of GO in media. Our results indicate that RICS is able to capture a broader range of flake sizes (i.e. up to 100 um) and can measure GO flakes similar to optical microscopy but in media.

## 5.2. Introduction

Of all types of chemically modified graphene, GO is the most highly oxidised form, consisting of a layer of graphene only one atom thick that contains epoxide (–O–) groups, hydroxyl(–OH) groups and carboxylic acid groups on GO basal plane [19]. Peripheral carboxylate groups influence the GO's pH-dependent negative surface charge and, consequently, the colloidal stability of GO [21]. Polar but uncharged, hydroxyl and epoxide groups on GO's basal plane allow hydrogen bonding and other surface reactions [10]. Unmodified areas on the basal plane contain free surface π–electrons, which are hydrophobic and hence capable of π–π interactions available for non-covalent functionalisation and drug loading. Thus GO may be viewed as an amphiphilic molecule, i.e. it may be adsorbed onto interfaces and reduce interfacial as well as surface tension; it could potentially be used as a surfactant in aqueous solutions to stabilise hydrophobic molecules, including anticancer drugs [13, 22].

GO is typically synthesised by using Hummer's method or some variation of it. As demonstrated in Figure 5.1, the method involves treating graphite flakes with potassium permanganate, sodium nitrate and sulphuric acid, followed by a water rinse, after which the mixture is stirred for 2 h. The reaction is often terminated with hydrogen peroxide, and the majority of procedures require several steps of centrifugation in order to remove all of the oxidative starting material and any unreacted graphite or unexfoliated flakes of graphite oxide [19, 337, 338]. The resulting suspension is distinguished from pristine graphene by its hydrophilicity, fluorescence and insulating properties.

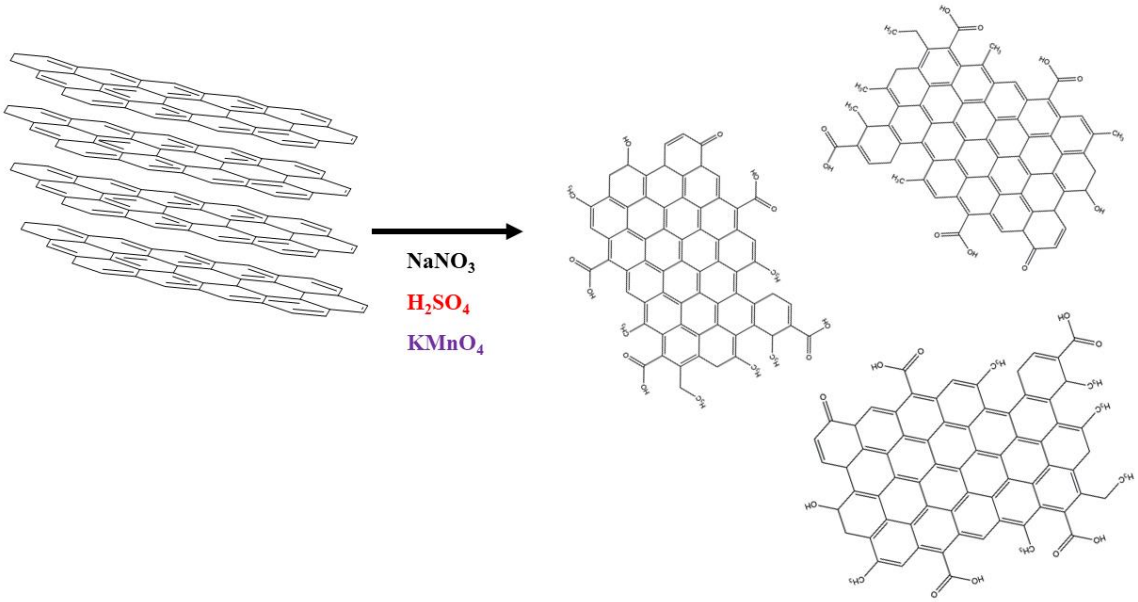


**Figure 5. 1**- Preparation of GO via chemical oxidation of graphite by Hummer's method to produce GO, using oxidizing agent including $NaNO_3$, $H_2SO_4$ and $KMnO_4$ adapted from Ruoff et al. [19].

Each GO flake has extremely heterogeneous surface chemistry, and, in turn, GO suspensions are highly polydisperse in terms of flake size. The features of the flakes also often differ significantly among preparations, even if prepared by the same manufacturer which may pose problems for their use in biomedical applications. Indeed nanoparticles used in biological applications should be very carefully characterised so that observed behaviour can be correlated with the initial physicochemical properties.

The structure of GO flakes results in significant differences in their optoelectronic properties compared with pristine graphene. Altough the exact structure of GO is still debated [339], two major models have been proposed. The first is the Lerf–Klinowski model (Figure 5.2), in which graphene's polyaromatic basal plane is heterogeneously functionalised with hydroxyl, epoxy and carboxylic acid groups [19, 340]. By contrast, the second is a two-component model of a

weakly oxidised GO flake's basal plane with carboxylic acids on its edges and highly functionalised oxidative debris adsorbed on its surface [36].

In the Lerf–Klinowski model, the $sp^2$-hybridised carbon structure causes the electrons to disperse linearly in pristine graphene, and the existence of oxygenated functional groups disrupts the structure with $sp^3$ domains, which produces isolated $sp^2$ clusters and, in turn, affects the flakes' insulating properties [3, 340]. The heterogeneity of the flakes' functionalisation means that these clusters have various sizes of flakes; it is believed that the electron–hole pair recombination in the isolated electronic states cause GO's photoluminescence [340]. By comparison, in the two-component model, GO's photoluminescent properties derive from oxidative debris on weakly oxidised graphene flake surfaces [36], and the heterogeneity of the debris causes GO's broadband photoluminescence. The two-component model gained support following experimental proof that oxidative debris and poorly oxidised graphene sheets may be split after base washing with NaOH solution [36]. After separating, the oxidative debris showed significantly more intense fluorescence, with emission peaks that had blue-shifted compared with the original GO, whereas the weakly oxidised flakes showed no fluorescence. Such outcomes were attributed to the quenching phenomena that occurs as the debris is adsorbed [341].

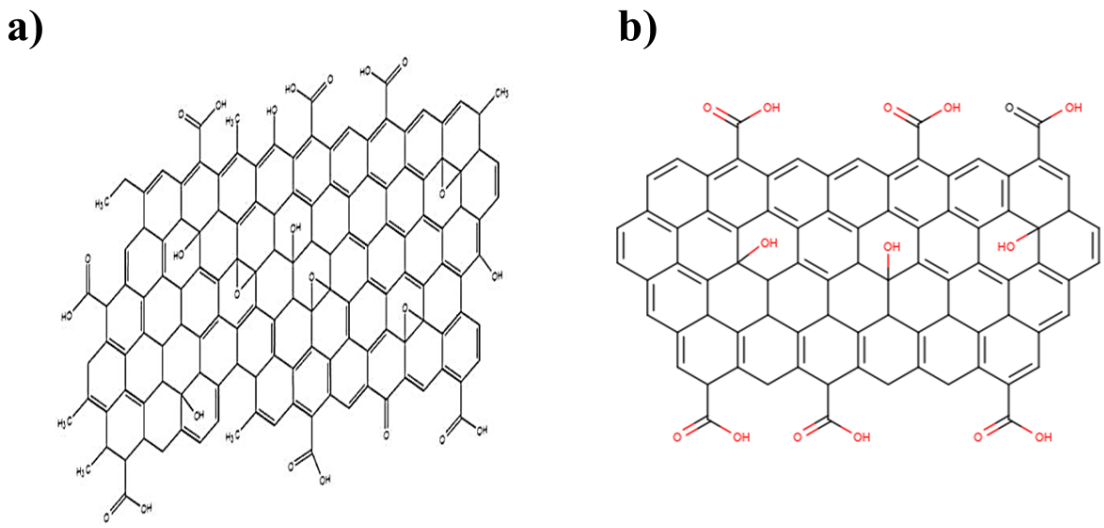


**Figure 5. 2-** Chemical structure of a) Lerf–Klinowski and b) two-component model of GO adapted from[35].

Recent studies have revealed, however, that the high-resolution structural characterisation of GO is closer to the Lerf–Klinowski model than the two-component model [342]. High-resolution transmission electron microscopy can be performed at high temperatures to eliminate surface contaminants that are ubiquitous on GO and, to a lesser extent, pristine graphene under atmospheric environments. However, it can also hinder efforts to characterise the structure of GO flakes in sufficient detail. In those efforts, studies have revealed a nano-crystalline structure (i.e. grain size of approx. 2 $nm^2$) separated by defects, involving both oxygenated functional groups and more than six-member rings [342]. That finding supports a structure similar to that in the Lerf–Klinowski model and thus challenges the two-component model, which, instead of eliminating adsorbed material, proposes the use of base washing that mostly changes the structure of GO flakes [339]. Therefore, regardless of debate over GO's structure and, by extension, the possible origins of its fluorescence, GO is generally recognised

to emit broadband photoluminescence. Research suggests that fluorescence can be excited from 325 to 600 nm, accompanied by emissions ranging from 400 to 1100 nm [72, 343, 344]. In particular, Luo *et al.* detected peak fluorescence between 700 and 850 nm following excitation from 580 to 600 nm [344], whereas Shang *et al.* [345] detected peak fluorescence between 600 and 680 nm after excitation from 380 to 440 nm.

GO is traditionally characterised by a series of techniques, including optical microscopy, atomic force microscopy (AFM) and dynamic light scattering (DLS). However, even when combined, those methods often fail to provide a complete picture of samples, both regarding the size of flakes and their behaviour in complex, biologically relevant media. Among the reasons why, only a limited the range of flake sizes can be easily observed with AFM and DLS. Beyond that, for objects with lateral dimensions exceeding 5 μm, DLS cannot be used, while objects with sizes exceeding 1 μm often cannot be easily measured. By comparison, AFM is time-consuming, and most set-ups do not allow accurately measuring areas greater than 10 × 10 μm, which complicates capturing images of flakes with large lateral dimensions or large samples. On top of that, both optical microscopy and AFM involve the immobilisation of flakes on a substrate and thus cannot be used to determine the behaviour of GO flakes in suspension. As an alternative method, raster image correlation spectroscopy (RICS) is a fluorescence technique used to measure the size and movement of fluorescent bodies. RICS has been used in studies geared towards examining protein aggregation and cell trafficking [70, 346] and can be deployed to calculate a wider array of object sizes than DLS. By taking advantage of GO's inherent fluorescence, characterisation methods such as RICS can be applied to fully characterise GO flakes in suspension prior to their introduction into cells.

To summarise, only few methods can be used to characterise GO, due to not only the range of sizes that can be obtained but also the often prolonged timescales needed. In our research, by exploiting GO's intrinsic fluorescence, we sought to find ways to overcome those limitations

by using other characterisation techniques and, in turn, provide a well-characterised GO sample before using it *in vivo.*

To achieve those aims, GO samples were characterised by using the traditional techniques of optical microscopy, AFM and DLS, and, once their limitations were demonstrated, by using RICS for comparison. Among the results, RICS allowed capturing the full range of flake sizes and the interactions of flakes with relevant biological media. Given GO's widely discussed instability without further functionalisation in biologically relevant media, such functionalisation was required before the suspensions could be delivered *in vivo*[347, 348]. PEG is known to prevent the adsorption of serum proteins on GO [349] and has been frequently used to that purpose with bio-nanoparticles. In our experiment, GO flakes were PEGylated with 10 kDa of branched PEG with primary amine termini to enhance their stability in biologically relevant media. The presence of the weakly positive amine functional groups was appealing due to the easy attachment of other functional molecules, including targeting ligands, and because earlier work has indicated that amine functionalised GO was less thrombogenic [162], which is essential for the intended function of the flakes.

Following traditional methods of functionalising GO using polyethylene glycol (PEG) and a fluorescence-based technique (i.e. RICS), we studied both the surface chemistry of the flakes and their behaviour in suspension.

## 5.3. Experiment

### 5.3.1. Materials

Graphene oxide (GO) dispersions in water were purchased from Graphenea (Spain). Four-arm, amine-terminated poly(ethylene oxide) with an average $M_n$ of 10,000 (typically 10,000–12,000), *N*-(3-dimethylaminopropyl)-*N'*-ethylcarbodiimide hydrochloride (EDC) and the

Kaiser Test Kit were all purchased from Sigma Aldrich (UK). Vivaspin centrifuge ultrafiltration tubes with membranes with a molecular weight cut-off of 30 kDa were purchased from Sartorius (UK), whereas Cornin Falcon round-bottom polystyrene tubes for FACS analysis were purchased from Fisher Scientific (UK).

## 5.3.2. Chemical methods

### 5.3.2.1. Graphene oxide purification

Centrifugation was performed using the Avanti J-30I high-performance centrifuge and Eppendorf MiniSpin® (Beckman Coulter, US). After centrifugation at low speed (3893 × *g*) for 2 h, the supernatant was retained to remove any aggregates and unoxidised graphitic material [271]. Next, each suspension was subjected to 5% (v/v) hydrochloric acid (HCl) solution [72] to remove any residual metal ions possibly left over from initial oxidation. After 2 h of being stirred at room temperature (RT), each suspension was diluted using Milli-Q water and subjected to repeated steps of washing via centrifugation at 17,000 × *g* for 45 min per step with distilled warm water until the supernatant reached a neutral pH. All of those procedures were performed to remove residual HCl, metal ion chlorides and any other by-products of Hummer's method, including mellitic acids [73].

### *5.3.2.2. PEGylation*

For PEGylation, we followed Yang *et al.*'s [350] protocol, albeit with specific changes to improve the GO's affinity to the PEG chain and to reduce the probability of cross-linking between the GO flakes. In the presence of EDC purchased from Sigma Aldrich (UK), the GO

suspensions were stirred in distilled water to activate the GO carboxyl groups and thus make them susceptible to amide coupling, as shown in Figure 5.3.

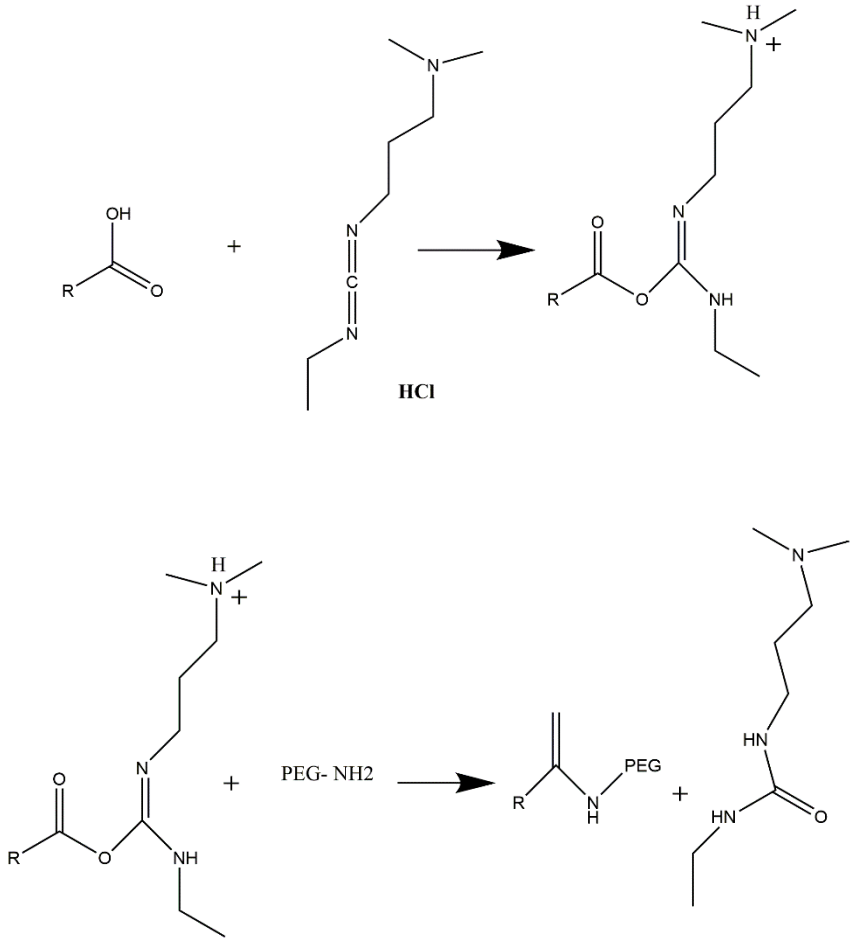


**Figure 5. 3-** Formation of an amide bond using EDC (carbodiimide ) crosslinking chemistry [351].

Because EDC is hygroscopic and degrades in the presence of water, the container was left to equilibrate at room temperature before opening in order to prevent condensation from forming within the container. After a small amount of distilled water was mixed with amine-terminated PEG, the activated GO was gradually added to the PEG using a peristaltic pump in a sonication bath in order to introduce an excess of PEG and thereby avoid cross-linking.

Following 70 min of sonication, the mixture was left stirring overnight. Then, the suspension was washed in a centrifuge tube of the Vivaspin filter from Sartorius (UK) until the filtrate was free of residual PEG chains. The filtrate was examined using the Kaiser test kit purchased from Sigma Aldrich (UK) according to the manufacturer's protocol—that is, a drop of pyridine and potassium cyanide were added, followed by a drop of ninhydrin in *n*-butanol, followed by phenol in *n*-butanol, and the mixture was heated at 110 °C for 5 min. A colour change to deep blue or purple (i.e. Ruhemann's purple) suggested the existence of primary amines and that the suspensions needed to be washed again.

### 5.3.3. Statistical methods

Statistical analysis was presented using GraphPad Prism (GraphPad Software Inc., USA) or Origin Pro (OriginLab, USA). Because most populations of GO flakes were non-normal (i.e. skewed) and with a range of sample sizes, non-parametric tests were used with few exceptions. The Mann–Whitney test was used to compare only two samples, while the Kruskal–Wallis test was used for multiple comparisons; such tests can be interpreted as non-parametric extensions of the *t* test and Analysis of variance (ANOVA), respectively.

## 5.4. Results

### 5.4.1. Graphene oxide characterisation

Two GO preparations were initially characterised—unwashed GO (uwGO) and washed GO (wGO)—by using traditional methods amply described in the literature [66, 275, 352-355]. The techniques used focused primarily on the physical properties of the flakes, including size and thickness, as well as the behaviour of the suspensions in various media.

#### 5.4.1.1. Traditional characterisation techniques

### Characterisation of flake dimensions using optical microscopy

Figure 5.9 shows representative images of uwGO and wGO from optical microscopy. The flakes contrasting the background the most (bright blue) were thick, multilayer ones, whereas those with no significant background contrast were thinner, single flakes or flakes in only a few layers.

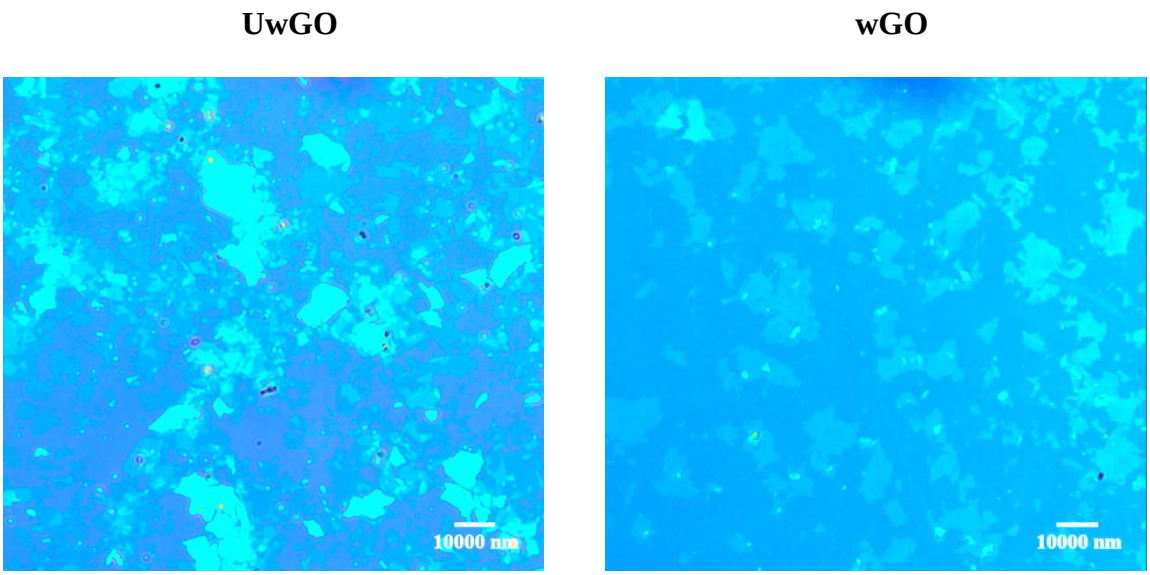


**Figure 5. 4-** Representative images of a) uwGO and b) wGO at 100% sonication power found by using reflective optical microscopy of a GO flake deposited on a silicon oxide substrate using spin coating (scale bar: 10,000 nm). The background is dark blue and the GO flakes are bright blue.

Figure 5.10 summarises the distributions of the calculated lateral dimensions for uwGO and wGO as a function of the sonication power. Lateral dimensions were determined with reference to the major axes of the flakes, and a non-parametric rank-based significance test (i.e. Kruskal–

Wallis multiple comparisons test) was conducted to assess whether the median lateral dimension varied significantly between sonication powers for each preparation. Ultimately, the difference was significant ($p < .0001$) for all of the preparations, and increasing the sonication power to 100% decreased the median lateral dimension of both preparations (Table 5.1). Therefore, significantly different distributions (Mann–Whitney, $p < .0001$) between uwGO and wGO emerged, which indicated that the washing process had significantly influenced the distributions.

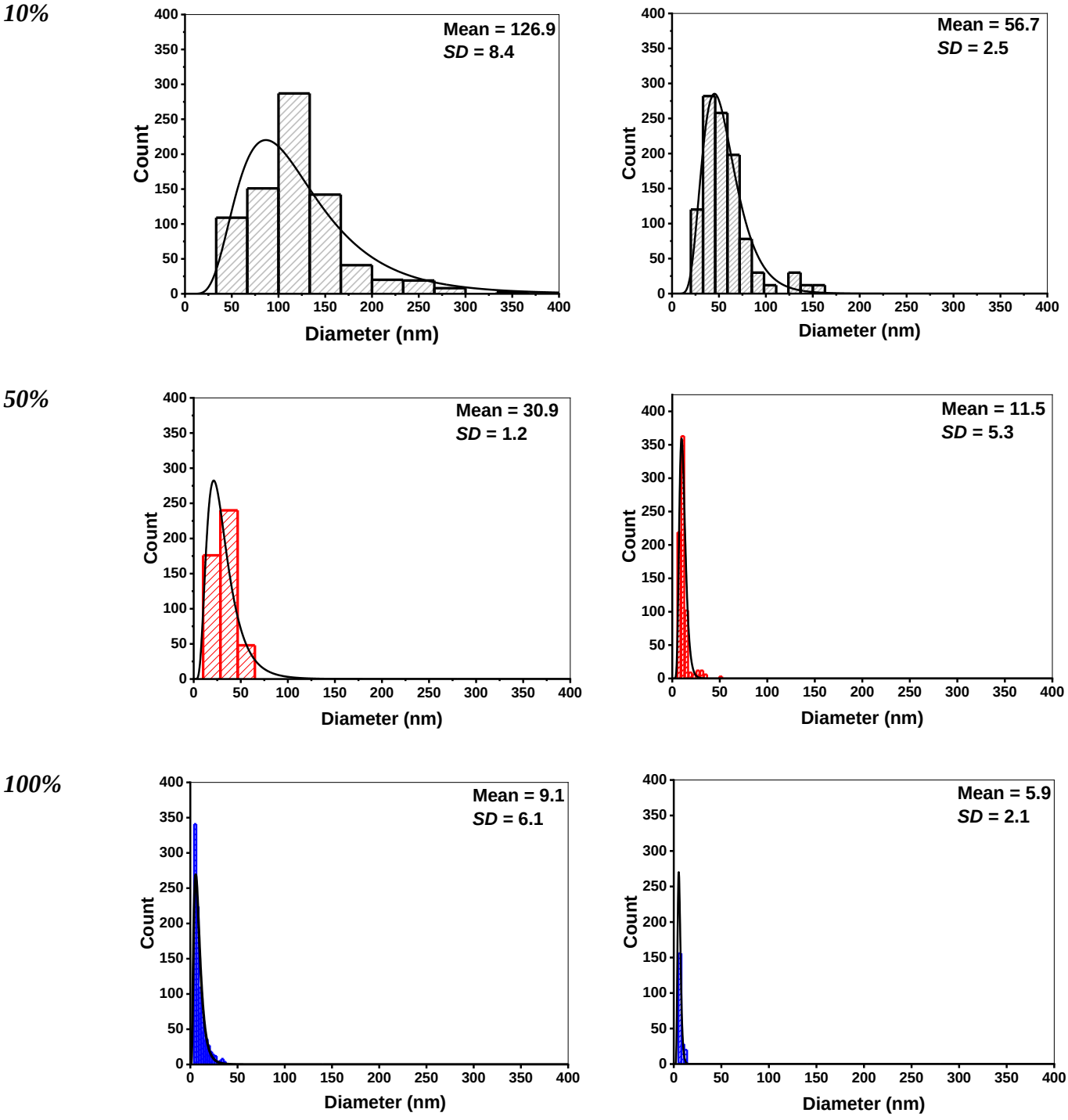


**Figure 5. 5-** Distributions of diameters for uwGO and wGO determined by optical microscopy 10%, 50% and 100% sonication powers, with a log(normal) distribution fitted to each.

## Flake morphology

Although AFM is commonly used to define both the thickness and lateral dimensions of GO flakes, images of objects with lateral dimensions exceeding 10 µm, which is far beyond the technique's limits, are not easily obtained, even though the sizes are quite common in highly polydisperse GO suspensions [356]. As a solution, reflective optical microscopy can be used in conjunction with AFM to enable the measurement of larger flakes. Thus, in our experiment, all flakes were measured after being deposited on silicon wafers with an oxide layer of 290 nm, which allowed the visualisation of flakes immobilised on the surface by using reflective optical microscopy [275, 357].

## Flake dimensions using atomic force microscopy

Using AFM, representative images of both uwGO and wGO were taken in regions between large flakes that were visible with optical microscopy, as shown in Figure 5.11.

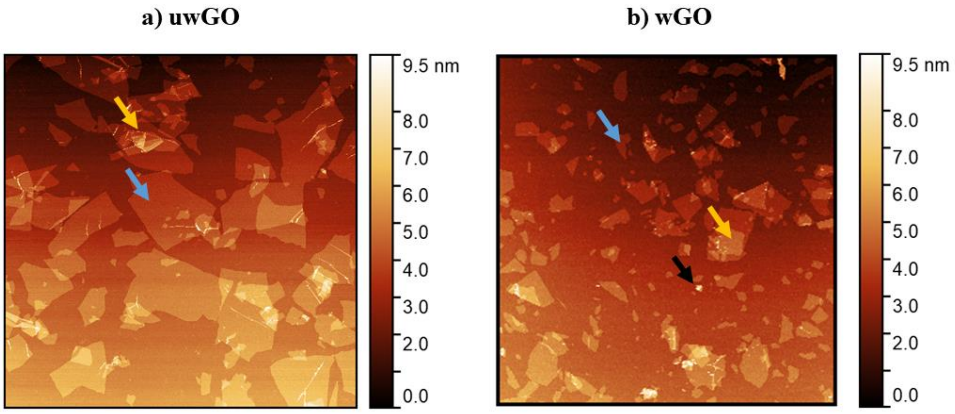


**Figure 5. 6**- Representative AFM images of a) uwGO and b) wGO taken using a Bruker MultiMode in ScanAsyst mode, deposited onto silicon wafers with a 290-nm oxide layer using spin coating. Single-layered , thick or aggregated GO flakes and bright spots indicated by blue, yellow and black arrow respectively.

A wide range of flake sizes was observed for uwGO (Figure 5.11a); many were large (i.e. >500 nm), and most were single-layered, as indicated with blue arrows in Figure 5.11. The wGO sample, presented in Figure 5.11b, was strikingly similar to the uwGO sample, with primarily single-layered flakes with median lateral dimensions (i.e. 170 nm), as shown in Table 5.1. Although fewer thick or aggregated flakes were observed, as indicated by yellow arrows, and some bright spots, shown by the black arrows in Figure 5.11b, may suggest the possible presence of remaining impurities, the median was observed to decrease significantly (Mann–Whitney, $p < .0001$), as detailed in Table 5.1. Overall, such results show that the washing process generated higher-quality samples, marked by somewhat decreased heterogeneity and possibly fewer contaminants that could affect their toxicological profile.

Particle analysis was performed to determine the dimensions of flakes according to the two primary axes for both preparations; their distributions appear in Figure 5.12. As data from both optical microscopy and AFM reveal, increasing the sonicating power to 100% decreased the average diameter of the flake for not only wGO (optical microscopy and AFM median diameters: 380 nm and 170 nm, respectively) but also uwGO (optical microscopy and AFM median diameters: 530 nm and 570 nm, respectively). As mentioned, wGO flakes have a smaller average diameter and a reduced size distribution. Although the median in the uwGO distribution appeared to exceed that in the wGO distribution, as shown in Table 5.1, the distribution for the wGO preparation was less heterogeneous. Thus, significantly different distributions (Kruskal–Wallis, $p < .0001$) in sonication powers for each preparation suggest that the sonication and washing processes significantly influenced the distributions. Of course, the regions in which AFM was performed were limited by the suitability of the flakes in the sample. As a consequence, when exceptionally large or exceptionally thick flakes were present in the GO samples, AFM could not be easily performed and required using the results of optical microscopy as well.

The images taken using AFM and reflective optical microscopy provided data (Figure 5.12) about the exact morphology of the suspended flakes, including their lateral dimensions, shape and thickness [358], as well as information about the existence of any impurities on their surfaces. Nevertheless, the limitations imposed by both methods, especially AFM, complicated determining whether the overall distribution provided a representative view of the distributions of flake size.

**Table 5. 1**- Median lateral dimensions at different sonication powers for uwGO and wGO using optical microscopy and AFM.

| **Sonication power (%)** | **Median lateral dimension (nm)** | | | |
|---|---|---|---|---|
| | **Optical microscopy** | | **AFM** | |
| | **uwGO** | **wGO** | **uwGO** | **wGO** |
| **10** | 16,100 | 11,600 | 5,200 | 4,700 |
| **50** | 3,600 | 1,800 | 2,100 | 1,600 |
| **100** | 530 | 380 | 570 | 170 |

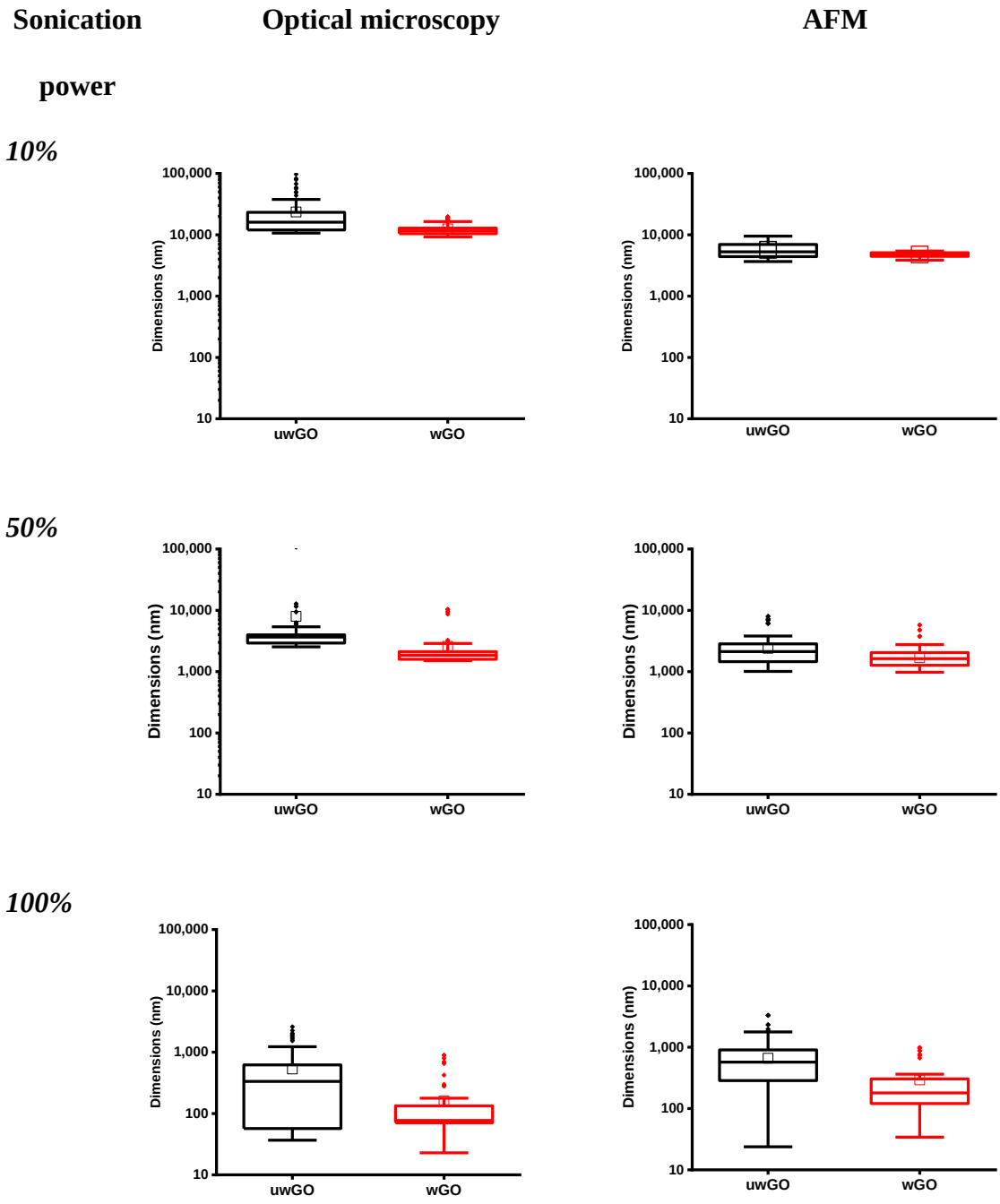


**Figure 5. 7**-Lateral dimension of uwGO and wGO at different sonication powers using a) optical microscopy and b) AFM. The figure shows a box and whisker plot, in which extended whiskers represent the edges of the 1st and 4th quartiles, edges represent the 2nd and 3rd quartiles, a bisecting line represents the median, □ represents the mean, and the solid diamonds represent the outliers.

## Characterisation of flake size and behaviour in suspension

Scattering techniques such as DLS are often used to rapidly assay sizes of GO flakes in suspension [66, 238, 359]. In our experiment, optical microscopy revealed that many of the lateral dimensions of the flakes exceeded 100 μm at the lowest sonication power (Figure 5.4), which was far beyond the maximum achieved with DLS. However, for a more complete representation, studies often match DLS data with those yielded by a direct imaging technique such as optical microscopy, AFM or transmission electron microscopy (TEM) [66]. Figure 5.14 presents a summary of flake sizes determined by DLS for both the uwGO and wGO samples. Using water, different ionic strengths of NaCl (i.e. 10, 50 and 150 mM) and the same ionic strength of NaCl dispersed in phosphate buffer (10 mM, pH 7.4) were chosen to assess how the apparent $R_h$ of flakes changed in the presence of ions and buffering agents commonly used in cell culture. The quality of the correlation curves was evaluated and placed below the graph that presents the distributions (Figure 5.14).

In water, the distributions differed significantly (Mann–Whitney $p$ <.05) for both preparations at different sonication powers. Moreover, the apparent $R_h$ for both preparations decreased as the sonication power increased, with uwGO having a median reduced from 927 nm to 229 nm, while that of wGO reduced from 919 nm to 302 nm. Upon adding 10 mM and 50 mM NaCl, no significant difference surfaced between those with water and those with NaCl. Nevertheless, the distributions were narrower and significantly different (Mann–Whitney $p$ < .0001) with 150 mM NaCl, and the median of apparent $R_h$ at 100% sonication power increased to 1309 nm and 1383 nm for uwGO and wGO, respectively. The overall distribution did not change significantly for either uwGO or wGO at 10% sonication power and for the different NaCl concentrations, although the distributions at 50% and 100% sonication power for different ionic

strengths of NaCl presented a significant difference for uwGO versus wGO, as revealed by Kruskal–Wallis multiple comparisons.

In the presence of phosphate-buffered sodium (PBS) (10 mM, pH 7.4) and 10 mM or 50 mM NaCl, no significant difference in the apparent $R_h$ was observed compared with the sample dispersed in water, which indicates that altered pH did not affect the distributions. Nevertheless, when the concentration of NaCl increased to 150 mM in PBS, the distributions became significantly different (Mann–Whitney, $p < .0001$) from distributions in the sample dispersed in water, and the results showed an increase in the median to 2651 nm and 1648 nm for uwGO and wGO, respectively. Furthermore, a significant difference arose between those dispersed in salt and those dispersed in salt and PBS (Mann–Whitney, $p < .05$).

## Apparent hydrodynamic radii of the graphene oxide preparations

The flake sizes found using AFM and described in Section 1.4.1.1.1 (Figure 5.12) were changed into $R_h$ by assuming that the lateral dimensions determined the size of the solvent sphere occupied by the suspended flakes. For all preparations, even though the ranges in size from both techniques were similar, the distributions differed significantly (uwGO: Mann–Whitney, $p < .0001$; wGO: Mann–Whitney, $p < .0001$). For DLS, the sample size was larger than that for AFM imaging; thus, the size distribution may be more representative. At the same time, the oblate geometry of the flakes was tentatively attributed to inconsistencies in measurement [66]. As expected, the distributions observed with optical microscopy (Figure 5.12) did not capture flakes with exceedingly large lateral dimensions. Statistical interpretation of samples using DLS could be valid if 10000 events were recorded for each sample, because of the distribution of sizes is not weighted by the concentration of each flake size.

For the distribution of $R_h$ measured for all uwGO and wGO preparations (Figure 5.14), $R_h$ was observed with preparations in water and was far smaller than what we observed with AFM

[360]. Although the oblate geometry of the flakes may have allowed other degrees of freedom of the suspended flakes to contribute to the results, including by flake bending and wrinkling, we did not test that hypothesis.

## Relationship between suspension quality and dispersion media

Aside from measurements of the apparent $R_h$ for the GO flakes appearing in the suspensions, each correlation curve was evaluated in terms of quality, as explained in Section 1.3.3.3. Quantities were defined as a proportion of the total number of records taken. In Figure 5.7, the measurement proportions were designated “poor” (red), “satisfactory” (yellow) or “good” (green) and thus provide additional information regarding GO’s aggregation and precipitation in suspension.

As shown in Figure 5.14, for all preparations most of the correlation curves were no more than satisfactory, even if the flakes in the suspensions appeared stable in water. By increasing the ionic strength and PBS (10 mM, pH 7.4) in the presence of saline (50 mM and 150 mM NaCl), the purchased GO might have decreased the quality of the samples. However, in PBS in 10 mM and 50 mM NaCl, the correlation curves improved considerably and were good. At the same time, the quality of the correlation curves for wGO suspensions became substantially worse in the presence of ionic species and buffering agents. As all correlation curves were rejected in 150 mM NaCl and PBS (10 mM, pH 7.4) with (150 mM NaCl) for both uwGO and wGO, the overall quality did not significantly improve in the presence of the phosphate buffer. Thus, adding ionic species and buffering agents probably result in aggregation, and, the presence of salt may affect the polydispersity of GO suspensions, which concurs with past findings [209, 361].

## Variation in apparent hydrodynamic radii with changing dispersion media

As shown in Figure 5.14, for each sample the median $R_h$ increased as the ionic strength rose for both uwGO and wGO. Moreover, at low sonication power, the preparations dispersed in water; 10 mM NaCl with PBS tended to have a flattened log(normal) distribution for $0 \leq R_h \leq$ 500 nm. It was difficult to observe a small $R_h$ at higher ionic strength (i.e. 150 mM NaCl and 150 mM NaCl in PBS), because GO aggregated in the presence of such high concentrations, and the distribution was closer than in the samples in water.

Irreversible aggregation can be easily initiated by introducing an electrolyte that can neutralise GO's surface charges. Upon being suspended in aqueous NaCl solution (final concentration, 150 mM), GO's immediate precipitation could be detected visually (Figure 5.13) and by DLS (Figure 5.14). For instance, at 100% sonication power, small GO flakes in water (i.e. $R_h$, approximately 229 nm and 301 nm for uwGO and wGO, respectively) changed into larger aggregates in 150 mM NaCl (i.e. $R_h$, approximately 1.6 μm and 1.3 μm for uwGO and wGO, respectively). However, at the lowest salt concentration (i.e. 10 mM), no significant difference emerged between those suspended in water and those suspended in 10 mM NaCl (Mann–Whitney, $p < 0.05$), as shown in Figure 5.14 ( median $R_h$, approximately 261 nm and 353 nm for uwGO and wGO, respectively), which suggests that dispersions of GO could tolerate small amounts of electrolyte [362, 363].

## Influence of sonication power on apparent hydrodynamic radii

Regarding the relationship between sonication power and average flake size, a significant difference (Mann–Whitney test, $p < .1$) was observed between the uwGO and wGO samples. The uwGO samples also had a median $R_h$ in water at a lowest sonication power (i.e. 10%) of 957 nm, which exceeded the highest sonication power's (i.e. 100%) median of 229 nm.

Meanwhile, for the wGO, the median $R_h$ was 597.2 nm at the lowest power and 201.3 nm at the highest. Upon sonication, the quality of the correlation curve improved, as did the particle size distribution, which showed homogeneous samples with fewer larger flakes.

The results presented in this section indicate that none of the traditional techniques applied in the experiment can allow the full characterisation of GO flakes required for their use in biomedical applications. Measuring the lateral dimensions of the flakes apparent in preparations was particularly hampered due to the heterogeneity of the sample and the size limits of the techniques used. An alternative approach employing the inherent fluorescence of GO to allow the use of RICS was therefore assessed.

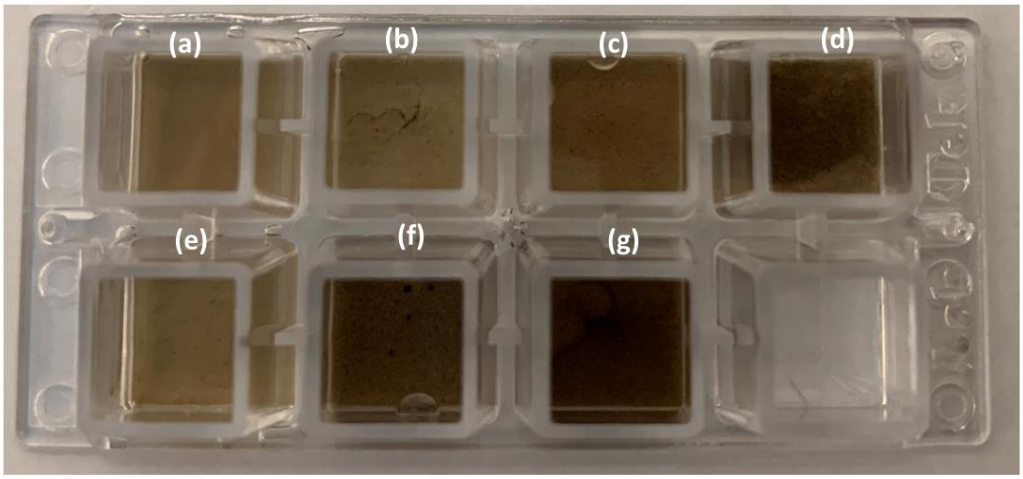


**Figure 5. 8**- GO flakes suspended in a) water, b) 10 mM NaCl + PBS, c) 50 mM NaCl + PBS, d) 150 mM NaCl + PBS, e) 10 mM NaCl, f) 50 mM NaCl and g) 150 mM NaCl. Samples were diluted to approximately 50 μg/mL.

| | Water | 10 mM NaCl | 50 mM NaCl | 150 mM NaCl |
|---|---|---|---|---|
| DLS | 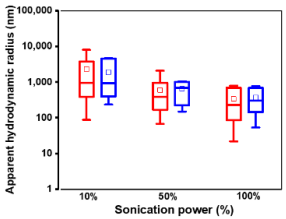 | 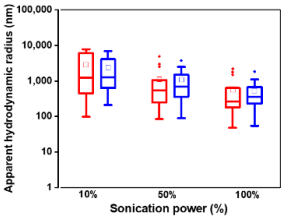 | 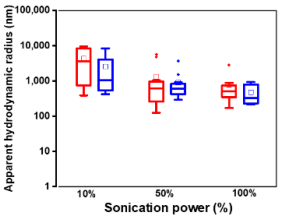 | 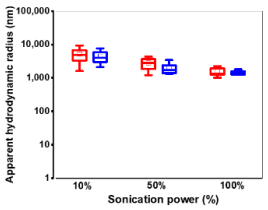 |
| | | PBS + 10 mM NaCl | PBS + 50 mM NaCl | PBS + 150 mM NaCl |
| | | 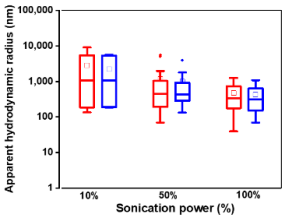 | 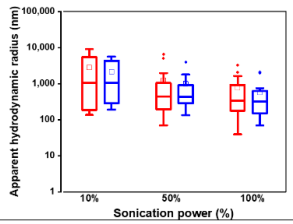 | 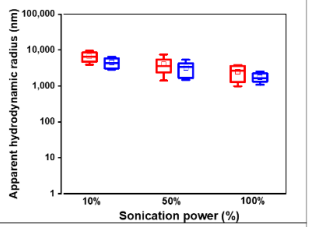 |
| | Water | 10 mM NaCl | 50 mM NaCl | 150 mM NaCl |
| RICS | 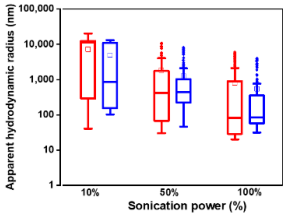 | 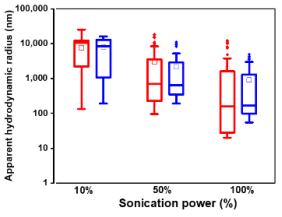 | 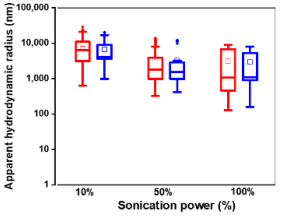 | 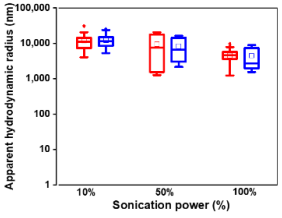 |
| | | PBS + 10 mM NaCl | PBS + 50 mM NaCl | PBS + 150 mM NaCl |
| | | 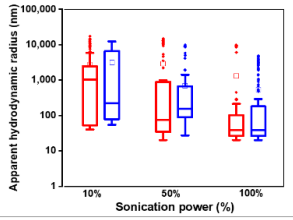 | 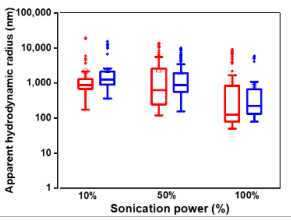 | 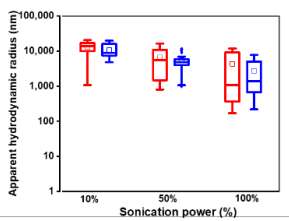 |

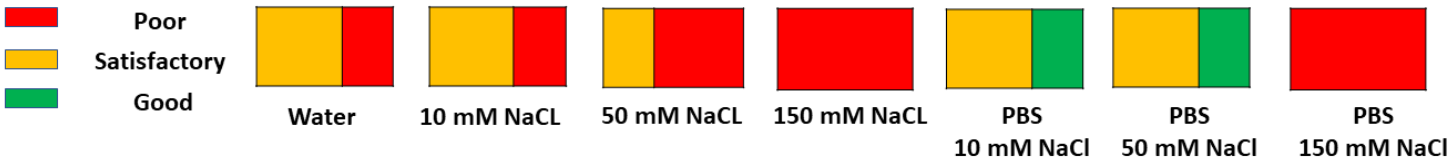


**Figure 5. 9-** Distributions of apparent Rh for uwGO and wGO determined by using DLS and RICS, in red for uwGO and in blue for wGO, along with the quality of the suspensions found using the correlation curve method: a) water, b) 10 mM NaCl, c) 50 mM NaCl, d) 150 mM NaCl, e) 10 mM phosphate buffer (pH 7.4), f) 50 mM NaCl dispersed in 10 mM phosphate buffer and g) 150 mM NaCl dispersed in 10 mM phosphate buffer.

#### 5.4.1.2. Using graphene oxide's intrinsic fluorescence for characterisation

### Raster image correlation spectroscopy to enhance the characterisation of flake size

RICS is a method used to determine the dynamics of fluorescent or fluorescently labelled bodies using a confocal microscope. Because RICS can be applied to calculate the dynamics of small, fast-moving bodies and larger, slower ones [364] by using both laser raster scanning and sequential image stacking of a 2D focal area [69], it can be mobilised to calculate particle dynamics within a broader range of sizes and in more complex or viscous media. Consequently, RICS is considered to be more suitable than either the combination of optical microscopy and AFM or DLS for a broad, high-throughput measurement of the lateral dimensions of flakes.

As with DLS, RICS requires using the Stokes–Einstein equation to obtain the $R_h$ from the self-diffusion coefficient ($D_s$). In-house software [70] was used to develop a diffusion coefficient for each region of interest, which was later changed to $R_h$. The $R_h$ distributions for both uwGO and wGO at different sonication powers appear in Figure 5.14.

RICS allowed capturing a far larger distribution of flake sizes than DLS did [365]. Indeed, it could capture flake sizes up to 97 μm in the uwGO preparation, which was within the range captured with optical microscopy but not with any other technique. The in-house software ManICS generated an $R^2$ value for every $D$ value based upon the goodness of the 2D autocorrelation curve. The mean $R^2$ value outside the confidence ellipse was 0.7, which we used as a criterion ($R^2 > 0.7$) for rejecting outliers. Thus, the measurements in which the $R^2$ value was less than 0.7 were rejected.

RICS was used to characterise the distribution of flake sizes present in suspension. GO was dispersed using different concentrations of NaCl (i.e. 10, 50 and 150 mM) and the same ionic strength of NaCl dispersed in PBS (i.e. 10 mM, pH 7.4) to investigate whether aggregation occurred. The distributions appear in Figure 5.14.

A non-parametric rank-based significance test (i.e. Mann–Whitney) was performed to assess whether the distributions varied significantly for the uwGO and wGO preparations. In water, for both preparations at different sonication powers, the difference was significant (Mann–Whitney, $p < .05$), which agreed well with the result obtained with DLS. Once the sonication power was increased to 100%, the median $R_h$ values for uwGO and wGO (i.e. 83 nm and 80 nm) were far smaller than those observed at lower sonication powers for both uwGO and wGO (i.e. 11.3 µm and 866 nm). When GO was suspended in 10 mM NaCl, no significant variation with those suspended in water occurred, and the overall distribution did not change significantly, whereas a significant difference was observed in 50 mM and 150 mM NaCl (Mann–Whitney, $p < .0001$), as was a narrow distribution, compared with those in water. Thus, the median $R_h$ increased in 150 mM NaCl relative to the GO flakes suspended in water: to 4.5 µm and 2.7 µm for uwGO and wGO, respectively, at 100% sonication power. That outcome may be due to electrostatically induced aggregation, as corroborated by literature reporting that GO flakes suspended in different strengths of potassium chloride ranging from 50 mM to 360 mM induced aggregation. Moreover, that nano-sized GO remained dispersed could be due to their pronounced Brownian motion relative to large flakes [366]. Comparing the results of the dispersion of flakes in different concentrations of NaCl in the presence of PBS to those in water, the distributions were significantly different (Mann–Whitney, $p < .0001$). In particular, the median $R_h$ increased to 1.3 µm and 1.0 µm for uwGO and wGO, respectively, in 150 mM NaCl at the highest sonication power.

The distribution of both preparations in different concentrations of NaCl with PBS was also significantly different (Mann–Whitney $p < .0001$). The median $R_h$ in 150 mM NaCl decreased from 4.5 μm to 1.1 μm in 150 mM NaCl with PBS in the uwGO sample and from 2.7 μm to 1.4 μm for wGO, both at the highest sonication power. Notably, the distribution of GO flakes for both uwGO and wGO using RICS was wider than in DLS, which agrees with past findings [70]. A smaller median $R_h$ (i.e. 80 nm) was observed in the wGO preparation than in the uwGO preparation in water at a high sonication power, which also occurred in the measurements determined with AFM and especially DLS.

A significant difference between the results achieved with RICS and DLS was that the median $R_h$ increased over the range of ionic strength studied. Again, the distribution captured larger flakes with lateral dimensions exceeding 10 μm observed in optical microscopy as well as nanoscale objects found using AFM. Although the oxidative functional groups of GO were used for functionalisation—that is, the same parameters used for non-functionalised GO—the flakes remained fluorescent, with a strong signal obtained in the stack of 30 images taken.

### 5.4.2. Graphene oxide functionalisation

Several research groups have used PEG to functionalise GO flakes in order to improve their stability and biocompatibility as well as to adjust their functionality [349, 367-370].

#### 5.4.2.1. Graphene oxide surface chemistry

After PEG conjugation, the surface chemistry of both the functionalised and non-functionalised GO flakes was assessed using Fourier transform infrared (FTIR) spectroscopy, and the FTIR spectra were recorded using a Bruker tensor 37 instrument (Bruker, UK). The FTIR spectra of GO, PEG and GO–PEG in Figure 5.15 were scanned between 400 and 4000 $cm^{-1}$ and recorded

as the average of 24 scans at 4 $cm^{-1}$ resolution, with air used as a reference background [302]. For each sample, three replicates were recorded, and each sample took 3–5 min to scan. The platform was cleaned with isopropyl alcohol between samples. In GO's FTIR spectrum, the wide peaks of approximately 3417 $cm^{-1}$ and approximately 1735 $cm^{-1}$ corresponded to the stretching vibrations of the carbonyl and carboxyl groups O–H and C=O, respectively. Meanwhile, the peak at approximately 1624 $cm^{-1}$ correlated to C=C, while the peaks at approximately 1395 $cm^{-1}$ and approximately 1056 $cm^{-1}$ were attributed to the C–O bonds [371]. By comparison, in PEG's FTIR spectrum, the sharp peaks at 2889 $cm^{-1}$, 1630 $cm^{-1}$ and 1111 $cm^{-1}$ seemed to relate to the stretching vibrations of C–H, C=O and C–O, respectively. Beyond that, peaks of the C–H deformation vibrations were in the region of 1465 $cm^{-1}$ and 1340 $cm^{-1}$, while peaks in region of 1284 $cm^{-1}$ and 1242 $cm^{-1}$ corresponded to the O–H bending vibrations, which indicated a pure PEG. As shown in Figure 5.15, the major functional groups of each material were almost entirely retained in GO–PEG. The results of FTIR spectroscopy thus indicated C=O and O–H groups in GO and PEG [372], meaning that the main functional group in the sample clearly existed in GO–PEG's final FTIR spectrum.

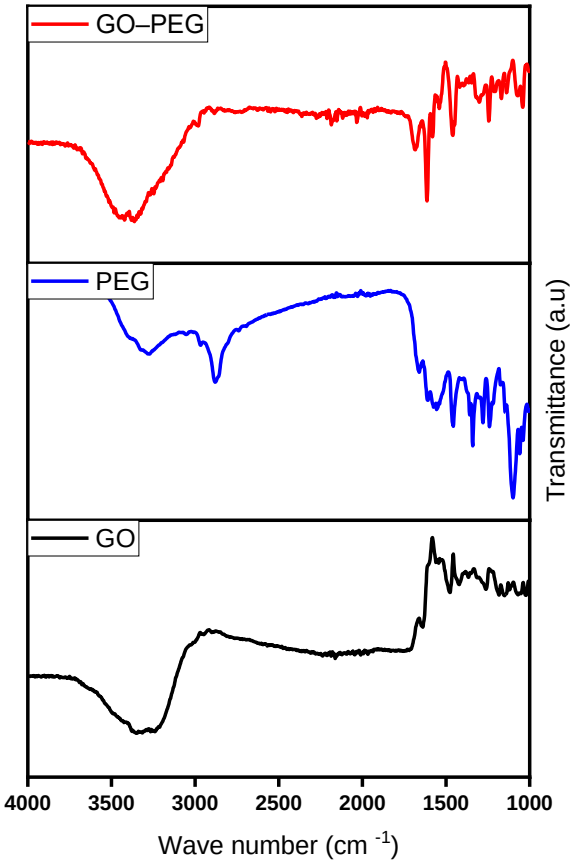


**Figure 5. 10-** Fourier transform infrared (FTIR) spectra of a) GO (black), b) PEG (blue) and GO–PEG (red). The FTIR spectra were recorded between 400 to 4000 cm-1. Each spectrum was obtained using 24 scans at a resolution of 4 $cm^{-1}$.

### 5.4.2.2. Characterisation of functionalised GO using established methods

As described in Section 1.5, to determine the morphology of the GO flakes, the suspensions were spin-coated onto silicon wafers with an oxide layer; representative images from optical microscopy appear in Figure 5.16. The lateral dimensions of the flakes were measured with reference to images of optical microscopy and AFM, the distributions for which appear in Figure 5.17.

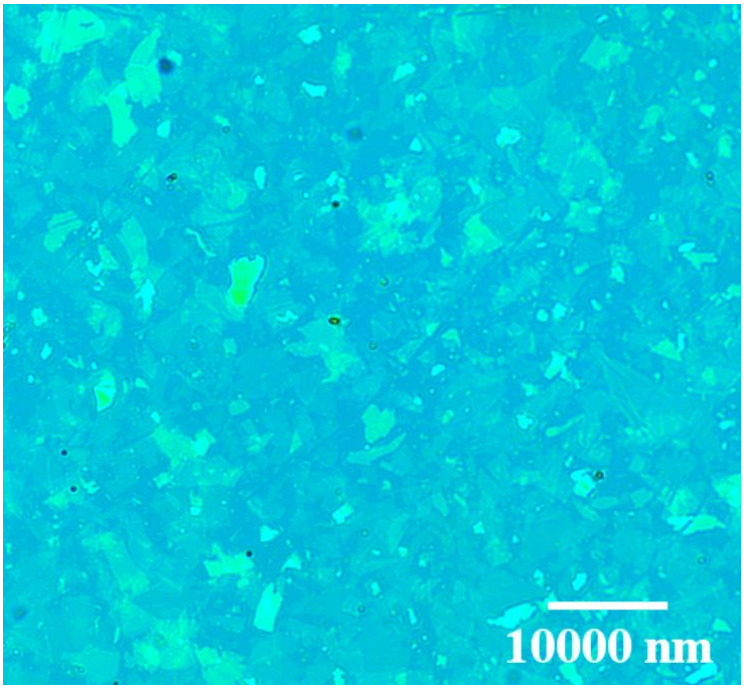


**Figure 5. 11**- Representative image of GO–PEG (10 kDa) found by using reflective optical microscopy. The background is dark blue and the GO flakes are bright blue.

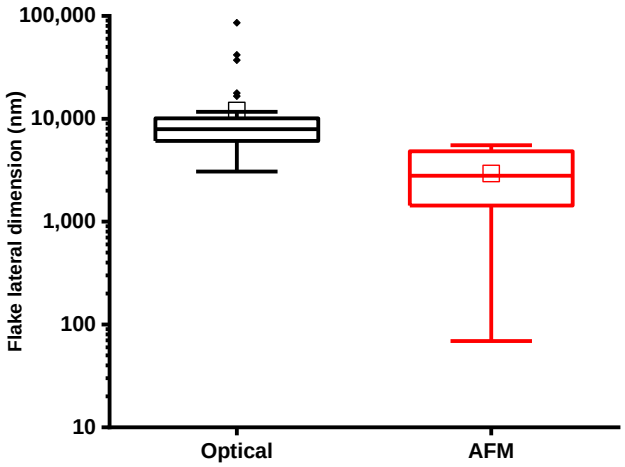


**Figure 5. 12**- Distribution of the lateral dimensions of GO–PEG flakes measured with optical microscopy and AFM. Distributions are represented using box and whisker plots, with the whiskers representing the 1st and 4th quartiles and the box representing the 2nd and 3rd quartiles, bisected by the median. The symbol □ indicates the mean and the solid diamonds represent outliers.

The distributions shown in Figure 5.17 confirm not only the limits of both techniques but also the need to use them in parallel to characterise larger flakes. In addition, images from AFM provided information on the extent of flake functionalisation. The linkage of PEG molecules with GO flakes is observable on large flakes as small bright spots distributed across the surface of the flakes. GO flakes have been proposed to primarily present carboxylic acid groups at their edges [19], with the majority of observed PEG chains appearing across their surfaces. In addition, on large flakes where it was easiest to detect functional molecules, coverage appeared sparse.

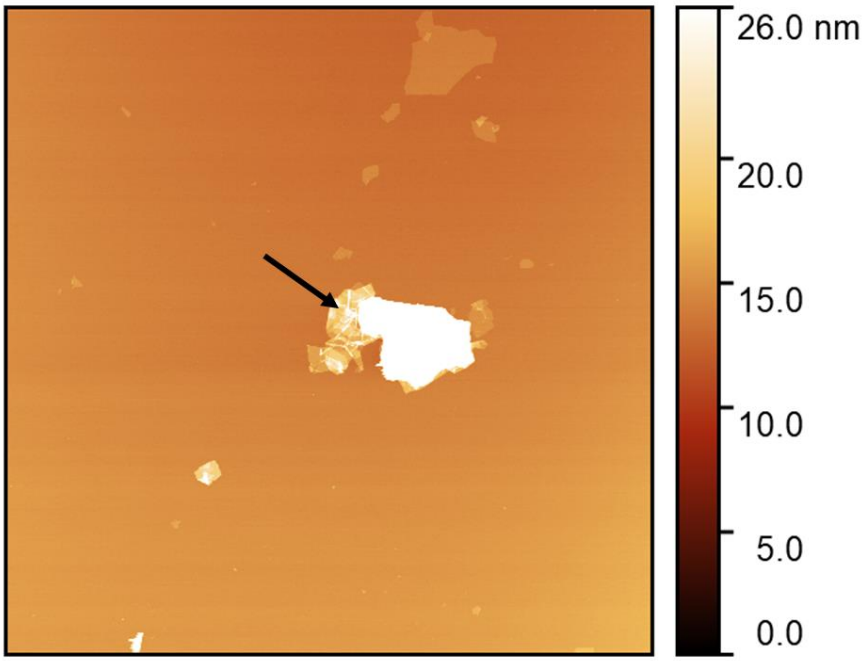


**Figure 5. 13-** Representative AFM images of GO–PEG (10 kDa) and functionalisation that seems to be sparse and mostly on the flakes basal A highlighted area indicated by black arrow that could either be PEG functionalisation or small but highly functionalised GO flake(s).

To make the flakes more stable in biologically relevant media, conjugation with PEG chains was performed to avoid aggregation and recognition by macrophages. Thus, to determine the success of functionalisation, the flakes were assessed using both traditional scattering techniques and fluorescence techniques, as described in Section 1.5.

## Scattering methods of characterising flake size and behaviour in suspension

After functionalisation, the size of the GO flakes in suspension was determined using DLS in different dispersion media including water, different ionic strengths of NaCl (i.e. 10, 50 and 150 mM) and different concentrations of NaCl (i.e. 10, 50 and 150 mM) in PBS (10 mM, pH 7.4).

The distributions were significantly different (Mann–Whitney, $p < .05$) for the sample dispersed in 150 mM NaCl and 150 mM NaCl in PBS compared to the sample in water. Additionally, the median $R_h$ for 150 mM NaCl sample was larger than in water (i.e. 278 nm and 169 nm, respectively), and upon the addition of PBS to 150 mM NaCl, the median $R_h$ increased from 169 to 372 nm compared with water. Although no significant difference emerged between those dispersed in low ionic strength (i.e. 10 mM and 50 mM NaCl) compared with water, also no significant variation occurred between salt and PBS compared with salt only; the median $R_h$ for 150 mM NaCl was smaller than that for 150 mM NaCl with PBS (i.e. 278 nm), while that of 150 mM NaCl in PBS was 372 nm. The distributions were significantly different (Mann–Whitney, $p < .05$) compared with wGO at 100% sonication power in water. Moreover, the median flake size of the PEGylated GO was less (i.e. 169 nm) than wGO (i.e. 301 nm), and at 150 mM NaCl, the size distribution was narrow. The distributions became broader when functionalised GO was measured in 10 mM NaCl with PBS.

To assess the quality of the suspensions, the quality of the DLS correlation curves in all of the dispersion media were examined. About 95% of the measurements were good for PEGylated GO, and none were rejected; moreover, the overall quality of the suspension improved compared with the unfunctionalised GO in both the uwGO and wGO samples. At that point, RICS was used on the PEGylated GO, as explained in Section 1.5, to further assess those observations and to obtain a more representative distribution of flake sizes.

#### 5.4.2.3. Characterisation of functionalised GO by using fluorescence techniques

Section 1.2.3 describes how using the inherent fluorescence of the GO flakes to determine the flake sizes in a suspension and their interactions with surrounding media can be achieved. The same approach was taken to examine the PEGylated flake sizes and their behaviour in physiologically relevant media.

## Raster image correlation spectroscopy for characterising PEGylated graphene oxide

Measurements were taken using the ionic strength of NaCl at different concentrations (i.e. 10, 50 and 150 mM) and the same ionic strength dispersed in PBS (10 mM, pH 7.4) to examine whether aggregation occurred; the distributions appear in Figure 5.19. Although the oxidative functional groups of GO were used for functionalisation, the flakes remained fluorescent, and a strong signal was found in the stack of 30 images taken with the same parameters used for non-functionalised GO.

The GO flakes dispersed in water demonstrated an $R_h$ median of 122 nm, which was less than the $R_h$ median of flakes in different NaCl concentrations and in NaCl in PBS. While the distributions differed significantly in 150 mM NaCl and 150 mM NaCl with PBS (Mann–Whitney, $p < .0001$) relative to water, the median $R_h$ increased to 279 nm and 254 nm for 150 mM NaCl and 150 mM NaCl with PBS, respectively.

In water, a significant difference occurred with DLS versus RICS (Mann–Whitney, $p < .05$): The median $R_h$ changed from 169 nm to 122.3 nm. Although significant difference appeared between DLS and RICS at different ionic strengths of NaCl, when PBS was added to the same range of ionic strengths of NaCl, no significant difference between DLS and RICS surfaced except for those dispersed in 150 mM NaCl in the presence of PBS (Mann–Whitney, $p < .05$). The median $R_h$ of GO–PEG dispersed in 150 mM NaCl with PBS observed using RICS provided surprising results, for the median $R_h$ observed (254 nm) was less than that observed in DLS (i.e. 372 nm). Additionally, the median $R_h$ observed in 150 mM NaCl with PBS in both techniques was higher than in water, which also occurred with unfunctionalised GO, as detailed in Section 1.5..

Again, in optical microscopy, the distribution captured larger flakes with lateral dimensions greater than 10 μm as well as nanoscale objects detected using AFM. The median $R_h$ of the PEGylated flakes in water was 122.3 nm, which was less than that of wGO, which had a median of 235.0 nm.

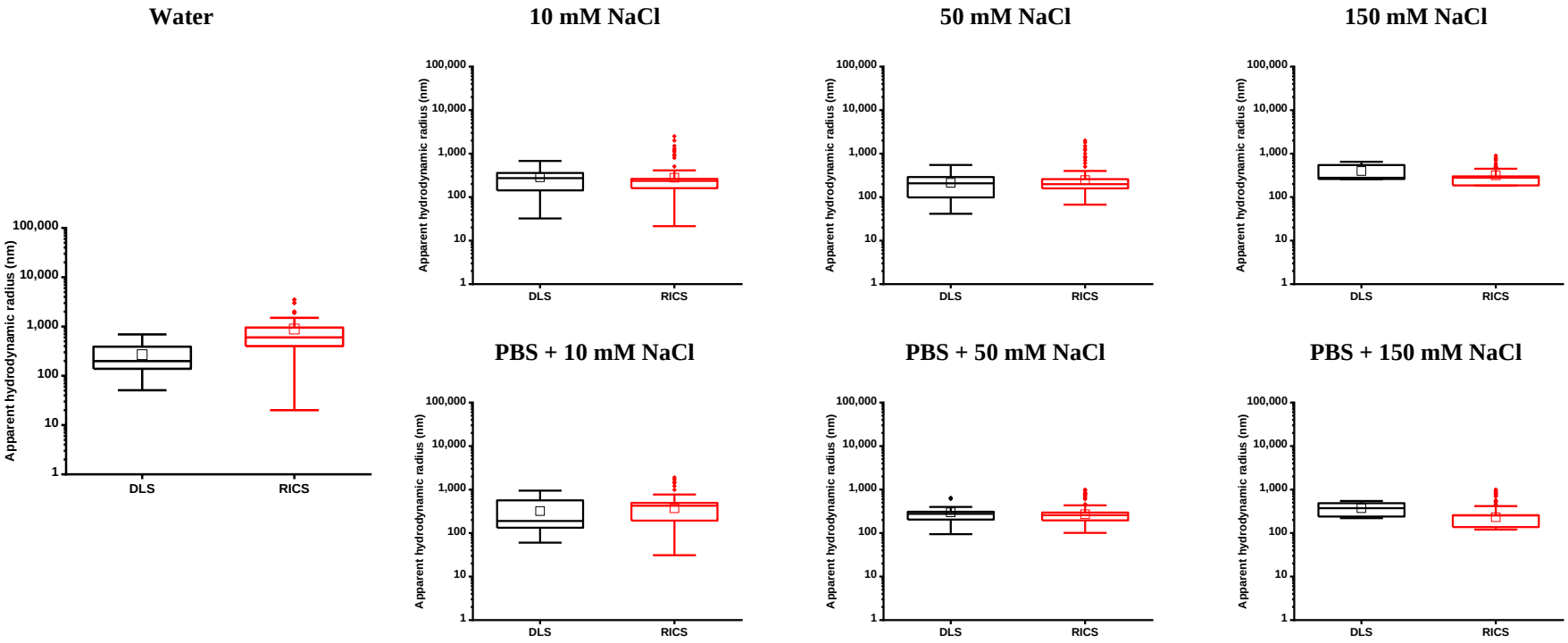


**Figure 5. 14-** Distribution of apparent $R_h$ present in GO functionalised with 10 kDa PEG, determined using DLS and RICS in different media. Distributions are represented using box and whisker plots, with the whiskers representing the 1st and 4th quartiles and the box representing the 2nd and 3rd quartiles, bisected by the median. □ indicates the arithmetic mean, and the solid diamonds indicate outliers.

## 5.5. Discussion

Commercially purchased GO was purified and functionalised using techniques detailed in the literature to enhance biocompatibility [271, 351]. Given GO's inherent fluorescence, the extensive characterisation of the samples was undertaken to determine whether RICS could be used as an orthogonal technique.

### 5.5.1. Comparative analysis of methods of characterising graphene oxide

The results of the experiment revealed that current methods used to characterise GO cannot be used to easily quantify the full range of GO flakes, meaning that orthogonal techniques may be useful to confirm the ranges suggested by existing techniques. To that purpose, DLS was used in conjunction with RICS. Solution-based techniques for characterising GO suspensions are advantageous, because they characterise flakes *in situ*, the population sizes of samples studied are statistically significant, and the measurement time is often rapid.

Similar to DLS, RICS uses the Stokes–Einstein equation [69], which assumes that the particles being studied are hard spheres, such that their only degrees of freedom are translational and their diffusion characteristics in all Cartesian coordinates are symmetrical. Furthermore, because thin flakes such as GO flakes have both rotational and translational degrees of freedom, the diffusion-related properties of the flake's basal plane will be asymmetrical for diffusion, which is either normal or tangential to the flake basal plane [373]. Moreover, the exceptional flexibility of the flakes can cause bending and wrinkling diffusion. Such measurements can therefore reflect the influence of edge-on diffusion (i.e. diffusion tangential to the basal plane) or the twisting and wrinkling of the flakes. Despite the lack of similar findings when using DLS to determine GO, as is commonly done, research on the scattering profiles of oblate objects in DLS has indicated that an object's inherent flexibility can affect the correlation curve

[374] and, in turn, the distribution of $R_h$ calculated. The enhanced stability of GO–PEG in ionic solution was confirmed by measuring the flakes via RICS; however, the flake distribution determined using RICS after GO–PEG suspension dispersed in 150 mM NaCl showed that the median and range of $R_h$ detected were greater than those observed in pure water. Such results were likely due to the electrostatically induced aggregation of ionic species, which depended upon the surface charge and concentration of ionic species, because GO's aggregation was induced in the presence of electrolyte and increased with the pH due to the gradual ionisation of the surface of GO's functional groups. Furthermore, the absence of electrolytes at different ranges of pH likely fully impeded GO's aggregation [366, 375]. Several techniques for characterising GO and graphene reported in the literature include alternative methods of determining flake size and the stability of suspensions. Among them, TEM affords many of the advantages of AFM, including the direct visualisation of nanoscale objects; however, such methods are time-consuming to reach significance in sampling [66, 267, 271, 353, 376, 377]. Nevertheless, the technique can allow calculating from sub-nanometre ranges to micron-scale ranges, depending on the set-up, which explains the extremely short wavelengths of electrons. Furthermore, the area of interest that the method can capture is far larger than that accommodated by AFM, whereas the full range of flake sizes cannot be taken in one image and generally requires magnification to be performed [378]. As a method of determining the sizes of flakes, TEM [379] is thus a strong alternative to optical microscopy and AFM, although its particular set-up renders it somewhat impractical in many laboratories and can cause beam damage to the flakes throughout measurement, especially high-resolution ones [380]. By contrast, although RICS is a more effective, high-performance technique for analysing GO, its requirements underscore the significant challenges of using GO in biological applications. Owing to the significant polydispersity of the samples, the flakes are extremely difficult to characterise using standard techniques, which is particularly problematic for biomedical

applications such as drug delivery. Furthermore, RICS can characterise larger aggregates and flakes of up to a few microns, contrary to DLS, which is suitable for investigating flakes and aggregates of up to 100 nm in size. RICS could thus be used as an orthogonal technique in the analysis of GO's aggregation.

### 5.5.2. Preparation of graphene oxide for biomedical applications

Multiple steps were taken to prepare GO for biomedical applications. Initially, purification was applied to remove any thick unreacted flakes or residual contaminants, after which GO flakes were broken up by sonication in aqueous dispersions using different sonication powers. Following purification and sonication, the average lateral dimensions of the GO flakes decreased as measured by RICS (Figure 5.14), optical microscopy and AFM (Figure 5.12), while the thickness of the flakes decreased according to AFM and optical microscopy. Nevertheless, the distribution of lateral sizes in purified GO was more condensed, with both upper and lower limits of distribution reaching the median. Such outcomes stress the importance of using combination approaches (i.e. orthogonal techniques) such as DLS and RICS to determine the distribution of flake sizes in order to obtain a representative view of the GO flakes (Figure 5.14).

In our experiment, the PEGylated GO flakes were successfully characterised by using FTIR and AFM, as well as by studying the stability of the flakes in ionic solutions via both DLS and RICS. The GO–PEG findings detected with AFM, however, demonstrated that PEGylation was sparse, particularly on the larger flakes, and not significantly seen at the edges of the flakes, where most carboxylic acids on the flakes are assumed to reside [19, 36]. Furthermore, the experimental protocol for PEGylation involved using the slow addition of GO flakes activated with EDC to an excess of PEG in order to minimise cross-linking and increase the affinity of GO to the PEG chains. Although EDC is attractive partly because of its water solubility, the

activated ester of the carboxylic acids hydrolyse over time, which can cause a less complete level of surface functionalisation than required. In our experiments, that characteristic may have contributed to the aggregation of some of the flakes at high ionic strength. PEGylation entails the use of sonication, which causes the scission of GO flakes [351, 381, 382]; however, after PEGylation, the suspensions are washed frequently to eliminate all excess EDC and PEG, typically in a membrane filter centrifuge tube. The flakes tend to jam the membrane pores inside the centrifuge tube; thus, the tube requires regular agitation to resuspend the flakes. Even so, it remains unclear whether such agitation is an effective solution for selecting the size of flakes, because the smallest may remain stuck in the membranes. It is possible that some limited cross-linking between the flakes may have occurred in PEGylation. However, the stability of the suspensions and the absence of clear evidence in the AFM images suggests that extensive cross-linking is unlikely. Nevertheless, the overlap of flakes, which frequently occurs in spin-coating, may make characterising the GO flakes difficult.

## 5.6. Conclusion

We examined GO and functionalised GO using traditional characterisation techniques to assess the size and morphology of GO flakes. However, because the traditional methods were unable to capture the full range of flake sizes, a novel orthogonal technique, RICS, was used to assess the inherent fluorescence of GO and measure flakes within a wider range of sizes in more complex media than DLS. In all, RICS was superior to the combination of optical microscopy and AFM, which can be used to examine flake size and morphology but not the behaviour of flakes in different media. Our study thus further illuminated the applicability of RICS as a novel fluorescence-based method of fully characterising GO flakes in suspension before their use in biomedical applications.

# 6. General conclusions

At its core, this thesis has investigated the potential application of graphene-based materials in drug delivery. Employing theoretical and experimental methods, the initial work examined the possible use of pristine graphene (PG) in conjunction with amino acids used as novel exfoliating and suspending agents. The chief dynamic analysed was the relationship between the amino acid structure and the graphene flakes, especially regarding their combined ability to generate high yields of exfoliated graphene, the stability of the suspensions and the thickness of the resulting flakes. Moreover, a single amino acid molecule adheres to graphene with the preference of L-Trp > L-Tyr > L-Val, both in gas-phase and in solution. This concurs with previous studies for $n$ = 1 graphene systems by Sanyal et al.[225] and Goel et al.[266] and appears to reflect the size and hydrophobicity of the amino acids. The greater π−π stacking ability of L-Trp side-chains compared to L-Tyr has been well documented[227]. However, for more concentrated amino acid solutions, there is a predicted propensity for amino acid clustering as well as intermolecular steric effects that appear to hinder interaction with the graphene flake as its surface saturates with amino acid; the preference for interaction becomes L-Trp > L-Val > L-Tyr in gas-phase and solution This was followed by evaluating the ability of these three amino acids to suspend and exfoliate pristine graphene experimentally. To that end, sonication methods similar to ones described in the literature were employed[383-385]. Although all three amino acids tested—tryptophan, tyrosine and valine—exfoliated and suspended only a few layers of PG flakes in water, the aromatic amino acids were noticeably more effective than valine on a per molar basis. Beyond that, tryptophan created slightly thinner flakes than tyrosine—mean thicknesses were 6.4 and 7.5 nm, respectively—and the most stable suspensions after 4 weeks. The thicknesses of the PG flakes is lower than the thickness in the literature using DMF ( ~ 3μm)[386]. With high concentrations of aromatic amino acids e.g.

tryptophan and tyrosine, the suspensions become increasingly unstable and exhibited visible signs of precipitation at the bottom of the vessels. Those outcomes align with findings of graphene−water molecular dynamics simulations showing increased concentrations of aromatic amino acids, as well as self-aggregation and reduced PG binding efficiency. Exfoliating PG with those aromatic amino acids produced nano-flakes with diameters less than 50 nm and thus far smaller than most living cells. In fact, the fairly consistent distribution of the diameters was similar to the distribution of the thickness of the cellular membranes. On the whole, the findings thus indicate the potential of amino acids to exfoliate and suspend PG, which marks a step towards developing non-toxic graphene-based vehicles for drug delivery and other *in vivo* applications.

In follow-up research, the work presented in chapter 4 focused on synthesising a novel, uniformly small PG–peptide drug carrier with good biocompatibility and stability. Throughout the simulations, the increased amount of peptide residue attached to PG's surface revealed that Trp3 stacked to PG's surface more than the single Trp. Raising the number of peptides to 12 also revealed that Trp3 covered PG more thoroughly than Trp and Trp2. The experimental data of the mean flake thickness measured using AFM was within the predicted range, based on graphene layer thicknesses reported in other research involving AFM [305, 306], thereby suggesting that the method is a reliable predictor of flake thickness in the system tested. In the three types of peptides, flakes in the monopeptide preparation were the thickest, whereas those in the tripeptide preparation were the thinnest. Those data were compared with other thicknesses derived from Raman spectroscopy. The Raman spectra could be used to distinguish single-layer and bilayer graphene from multilayer graphene (≥3 layers), and bulk graphite could be distinguished by the Raman fingerprints of the 2D bond [311]. The ratio of intensities of $I_{2D}$ to $I_G$ increased from PG to PG–$Trp_3$, thereby indicating a significant increase in the intensity of the 2D peak and a decrease in the G peak, both owing to an increased number of

PG layers. After PG's functionalisation with Trp, the $I_{2D}$-to-$I_G$ ratio increased due to the increased intensity of the 2D band. Such outcomes suggest that adding the functional groups of $Trp_2$ and $Trp_3$ by functionalising PG restores the $sp^2$ hybridisation on the structure of PG. DLS confirmed the instability of the PG flakes samples in the no Trp samples, and the difficulty of redispersing the flakes after aggregation suggested that aggregation was irreversible. Even immediately after preparation, the apparent $R_h$ of the flakes were far greater than those in $Trp_3$. However, it should be mentioned that DLS depends upon observed diffusion times, which are necessarily affected by any molecules surrounding the surface, including multiple layers of peptides in the solution. Zeta potential analysis confirmed that $Trp_3$ produced a very stable suspension immediately after preparation and after 4 weeks. Concentrations of PG in suspensions immediately after preparation did not demonstrate any major trends concerning type of peptides, whereas the $Trp_3$ sample had more PG flakes remaining in suspension after 4 weeks. Also after 4 weeks, concentrations in suspensions declined significantly in the PG sample, even beneath concentrations immediately after preparation, and was accompanied by visible aggregates of PG at the bottom of the vial. After 4 weeks, the concentration of particles decreased in all cases. However, that outcome was far more important for PG particles, because the concentration of PG–$Trp_3$ particles remained approximately 75% of the initial value compared with only 30% for PG particles [312]. Dox's loading onto PG is likely due to simple π–π, similar to that with carbon nanotubes. However, compared with single-walled carbon nanotubes for drug loading via π–π stacking, PG is inexpensive and beneficial for scalability [17]. Dox can be loaded non-covalently onto PG, and its loose binding may rely on weak Dox–Dox interactions [314]. Given all of the above, the mass ratio 1:1 was used for the remainder of the experiments to achieve effective Dox loading and lessen Dox waste. The biocompatible PG–peptides obtained indeed demonstrated high aqueous solubility and stability in various physiological media. Moreover, they exhibited a high drug loading capacity due to their large

surface areas and strong π–π interactions. Moreover, the increased zeta potential might be due to the addition of amino groups in Dox after the binding of Dox to PG particles[323]. Dox's release from PG and PG–$Trp_x$ was clearly pH-dependent, for it appeared to be more limited at pH 7.4 than at pH 5.4. For drug release at pH 5.4, $n < 0.5$ a Fickian diffusion is suggested, which was related to the fast drug release as *n* changed from 0.53 to 0.34 for PG and PG–$Trp_3$ , the *k* value was increased from 1.5 to 15.3, which clearly showed more drug released in the PG-$Trp_3$ sample. Whereas, at pH 7.4 PBS, $n > 0.5$ is non-Fickian with a value of *n* ranging from 0.57 and 0.60 for PG and PG–$Trp_x$ [331]. The *k* value increased slightly from 1.2 to 2.5 at pH 7.4, which is lower than pH 5.4, thus indicated less Dox released at pH 7.4. The *in vitro* cell viability of free Dox, PG, PG–$Trp_x$ , PG–Dox and PG–$Trp_x$–Dox was tested against the breast cancer cell line MDA-MB-231. The cell viability remained above 95% after 24 h and 48 h following treatment with PG, PG–Trp, PG–$Trp_2$ and PG–$Trp_3$, thereby indicating that PG–$Trp_x$ particles are not toxic to those cells. After 24 h, cell viability dropped to 71% in the presence of free Dox, whereas PG– Dox, PG–Trp –Dox and PG–$Trp_2$– Dox demonstrated lower toxicity (95, 91 and 83%, respectively). However, cell viability decreased significantly in the presence of PG–$Trp_3$ – Dox to 63%, to levels lower than those of free Dox. After 48 h, cell viability decreased significantly for all samples containing Dox, and the incubation of cells with free Dox, PG–Dox, PG–Trp–Dox, PG–$Trp_2$–Dox and PG–$Trp_3$–Dox resulted in respective decreases of 37%, 76%, 64%, 51% and 24% in cell viability compared to 24 h. Dox not only binds tightly with PG–tripeptides at a physiological pH but can also release its load at lower pH i.e. in late endocytosis. Acidic conditions of the endosomal–lysosomal component are likely the chief driving force for Dox's release inside cancer cells; however, introducing tripeptides improved its release and, in turn, its toxicity. As such, the material was tested for drug delivery, the overlay of PG–Dox showed weak red fluorescence in cells, especially compared to PG–$Trp_3$-DOX. Considering the PG-based particles only, fluorescence intensity

appeared to increase from PG–Dox to PG–$Trp_3$-DOX; the fluorescence intensity of the latter approaching that of DOX alone. The results suggested that it was absorbed by MDA-MB-231 cells and could thus serve as a drug carrier. Furthermore, the release of Dox from PG–peptide in the cells seemed to be sustained when mediated by PG–peptide, which may have potential advantages for enhancing therapeutic efficacy. However, the limitations imposed by both MTS assay and the intracellular uptake of Dox were, therefore, further investigation using a more accurate technique, including WST-8. At any rate, the strategy devised paves the way for preparing graphene with good biocompatibility and solubility that can double as a promising platform for examining the biological applications of graphene.

Last, the proposed use of GO as a therapeutic drug carrier derived from its more common use in biomedical applications, as shown in the literature as described in Chapter1, and from its flexible structure in terms of functionalisation due to its polyaromatic basal plane and oxygenated functional groups. However, whereas part of the study for the thesis was designed to examine single amino acids used with non-functionalised PG material with highly controlled lateral dimensions, GO formed by employing Hummer's method is reportedly highly heterogeneous, both chemically and physically[19]. Thus, a substantial portion of the study focused on characterising and assessing GO, with special attention to whether the reported heterogeneity could be reduced. GO samples were characterised by using the traditional techniques of optical microscopy, AFM and DLS. However, even when combined, those methods often fail to provide a complete picture of samples, both regarding the size of flakes and their behaviour in complex, biologically relevant media. Among the reasons why only a limited range of flake sizes can be easily observed with AFM and DLS. Beyond that, for objects with lateral dimensions exceeding 5 μm, DLS cannot be used, while objects with sizes exceeding 1 μm often cannot be easily measured. By comparison, AFM is time-consuming.

Most set-ups do not allow accurately measuring areas greater than 10 × 10 μm, which complicates capturing images of flakes with large lateral dimensions or large samples.

On top of that, both optical microscopy and AFM involve the immobilisation of flakes on a substrate and thus cannot be used to determine the behaviour of GO flakes in suspension. Among the results, the existing methods tested could not offer adequate data about the overall distribution of flake sizes due to the polydispersity of the samples. The flakes' inherent fluorescence was investigated with raster image correlation spectroscopy (RICS) to determine the apparent hydrodynamic radii of each sample. The wide ranges of sizes that could be determined using the method were assessed with both optical microscopy and atomic force microscopy, which provided distributions that could be compared directly between preparations. Although the GO used was obtained commercially, additional purification and functionalisation were performed in order to enhance its biocompatibility. The preliminary steps of purification resulted in a less laterally polydisperse suspension with thinner flakes and fewer residual impurities. After PEGylation, the suspension also demonstrated enhanced stability in biologically relevant media; however, the apparent hydrodynamic radii, as determined by RICS, were larger than those assessed in the purified suspension.

Nevertheless, PEGylated flakes were more biocompatible than the non-functional suspensions. Although non-functionalised GO seemed to prompt cellular agglutination and activate macrophages, cells treated with PEGylated GO maintained healthy morphologies and showed little change in viability while at rest. Those results underscore the need to additionally functionalise the flakes. Because the dimensions were greater than desired—some outlier flakes had dimensions exceeding 10 μm, which has been pinpointed as a significant factor of toxicity—that feature was not as significant as the surface chemistry of the GO flakes.

Despite PEGylated GO's improved stability and biocompatibility, the problems associated with regulating its size and surface chemistry, even before characterising the prepared

suspension, mean that a considerable amount of work remains to be done before the material can be considered appropriate for use in drug delivery. Moreover, debates regarding GO's exact surface chemistry indicate additional challenges with characterising the material. Such challenges have not arisen with assessing other nanoparticles used for drug delivery, because manufacturing approaches (e.g., extrusion) to regulate the size of liposomes, added to the wide range of monomeric components used for building polymeric nanoparticles, cause nanoparticles to be highly monodisperse in size and with carefully controlled chemistry that can be adapted to the work under investigation. Unlike research on liposomes and polymers, investigations into graphene are quite new, and for that reason, improving production methods to achieve significantly better-characterised samples of graphene is crucial, particularly in biology. For example, RICS can be used in quantifying the aggregation and diffusion behaviour of proteins. By extension, it allows semi-quantitatively profiling aggregate sub-populations by constructing 3D contour plots of concentrations of populations and their related diffusion coefficients, as well as the statistical interpretation of aggregate sub-populations contained within samples.

# 7. Reference


[1] K. S. Novoselov *et al.*, "Electric Field Effect in Atomically Thin Carbon Films," *Science,* vol. 306, no. 5696, pp. 666-669, 2004.

[2] H. K. Chae *et al.*, "A route to high surface area, porosity and inclusion of large molecules in crystals," *Nature,* 10.1038/nature02311 vol. 427, no. 6974, pp. 523-527, 02/05/print 2004.

[3] K. P. Loh, Q. Bao, P. K. Ang, and J. Yang, "The chemistry of graphene," *Journal of Materials Chemistry,* 10.1039/B920539J vol. 20, no. 12, pp. 2277-2289, 2010.

[4] K. S. Novoselov, V. I. Falko, L. Colombo, P. R. Gellert, M. G. Schwab, and K. Kim, "A roadmap for graphene," *Nature,* 10.1038/nature11458 vol. 490, no. 7419, pp. 192-200, 10/11/print 2012.

[5] M. J. Allen, V. C. Tung, and R. B. Kaner, "Honeycomb Carbon: A Review of Graphene," *Chemical Reviews,* vol. 110, no. 1, pp. 132-145, 2010/01/13 2010.

[6] B. Zhang, Y. Wang, and G. Zhai, "Biomedical applications of the graphene-based materials," *Materials Science and Engineering: C,* vol. 61, pp. 953-964, 4/1/ 2016.

[7] V. Singh, D. Joung, L. Zhai, S. Das, S. I. Khondaker, and S. Seal, "Graphene based materials: Past, present and future," *Progress in Materials Science,* vol. 56, no. 8, pp. 1178-1271, 2011/10/01/ 2011.

[8] W. Choi, I. Lahiri, R. Seelaboyina, and Y. S. Kang, "Synthesis of Graphene and Its Applications: A Review," *Critical Reviews in Solid State and Materials Sciences,* vol. 35, no. 1, pp. 52-71, 2010/02/11 2010.

[9] M. S. A. Bhuyan, M. N. Uddin, M. M. Islam, F. A. Bipasha, and S. S. Hossain, "Synthesis of graphene," *International Nano Letters,* journal article vol. 6, no. 2, pp. 65-83, June 01 2016.

[10] J. Liu, L. Cui, and D. Losic, "Graphene and graphene oxide as new nanocarriers for drug delivery applications," *Acta Biomaterialia,* vol. 9, no. 12, pp. 9243-9257, 2013/12/01/ 2013.

[11] W. S. Hummers and R. E. Offeman, "Preparation of Graphitic Oxide," *Journal of the American Chemical Society,* vol. 80, no. 6, pp. 1339-1339, 1958/03/01 1958.

[12] S. Pei and H.-M. Cheng, "The reduction of graphene oxide," *Carbon,* vol. 50, no. 9, pp. 3210-3228, 8// 2012.

[13] Y. Zhu *et al.*, "Graphene and Graphene Oxide: Synthesis, Properties, and Applications," *Advanced Materials,* vol. 22, no. 35, pp. 3906-3924, 2010.

[14] P. Bazylewski, S. Van Middelkoop, R. Divigalpitiya, and G. Fanchini, "Few-layer molybdenum disulfide nanosheets functionalized with l-cysteine for selective capture of Cd2+ ions," *FlatChem,* vol. 11, pp. 15-23, 2018/09/01/ 2018.

[15] H. C. Schniepp *et al.*, "Functionalized Single Graphene Sheets Derived from Splitting Graphite Oxide," *The Journal of Physical Chemistry B,* vol. 110, no. 17, pp. 8535-8539, 2006/05/01 2006.

[16] H. Dong *et al.*, "A Versatile Multicomponent Assembly via β-cyclodextrin Host–Guest Chemistry on Graphene for Biomedical Applications," *Small,* vol. 9, no. 3, pp. 446-456, 2013.

[17] L. Rodríguez-Pérez, M. a. Á. Herranz, and N. Martín, "The chemistry of pristine graphene," *Chemical Communications,* 10.1039/C3CC38950B vol. 49, no. 36, pp. 3721-3735, 2013.

[18] D. W. Boukhvalov and M. I. Katsnelson, "Chemical functionalization of graphene," *Journal of Physics: Condensed Matter,* vol. 21, no. 34, p. 344205, 2009.

[19] D. R. Dreyer, S. Park, C. W. Bielawski, and R. S. Ruoff, "The chemistry of graphene oxide," *Chemical Society Reviews,* 10.1039/B917103G vol. 39, no. 1, pp. 228-240, 2010.

[20] C. K. Chua and M. Pumera, "Chemical reduction of graphene oxide: a synthetic chemistry viewpoint," *Chemical Society Reviews,* 10.1039/C3CS60303B vol. 43, no. 1, pp. 291-312, 2014.

[21] S. Park *et al.*, "Colloidal Suspensions of Highly Reduced Graphene Oxide in a Wide Variety of Organic Solvents," *Nano Letters,* vol. 9, no. 4, pp. 1593-1597, 2009/04/08 2009.

[22] J. Kim, L. J. Cote, F. Kim, W. Yuan, K. R. Shull, and J. Huang, "Graphene Oxide Sheets at Interfaces," *Journal of the American Chemical Society,* vol. 132, no. 23, pp. 8180-8186, 2010/06/16 2010.
[23] T. Szabó *et al.*, "Evolution of Surface Functional Groups in a Series of Progressively Oxidized Graphite Oxides," *Chemistry of Materials,* vol. 18, no. 11, pp. 2740-2749, 2006/05/01 2006.
[24] K. R. Paton *et al.*, "Scalable production of large quantities of defect-free few-layer graphene by shear exfoliation in liquids," *Nat Mater,* Article vol. 13, no. 6, pp. 624-630, 06//print 2014.
[25] V. León, A. M. Rodriguez, P. Prieto, M. Prato, and E. Vázquez, "Exfoliation of Graphite with Triazine Derivatives under Ball-Milling Conditions: Preparation of Few-Layer Graphene via Selective Noncovalent Interactions," *ACS Nano,* vol. 8, no. 1, pp. 563-571, 2014/01/28 2014.
[26] W. Zhao, F. Wu, H. Wu, and G. Chen, "Preparation of colloidal dispersions of graphene sheets in organic solvents by using ball milling," *J. Nanomaterials,* vol. 2010, pp. 1-4, 2010.
[27] D. W. Johnson, B. P. Dobson, and K. S. Coleman, "A manufacturing perspective on graphene dispersions," *Current Opinion in Colloid & Interface Science,* vol. 20, no. 5–6, pp. 367-382, 10// 2015.
[28] T. Nakajima and Y. Matsuo, "Formation process and structure of graphite oxide," *Carbon,* vol. 32, no. 3, pp. 469-475, 1994/01/01/ 1994.
[29] J. B. Oostinga, H. B. Heersche, X. Liu, A. F. Morpurgo, and L. M. K. Vandersypen, "Gate-induced insulating state in bilayer graphene devices," *Nat Mater,* 10.1038/nmat2082 vol. 7, no. 2, pp. 151-157, 02//print 2008.
[30] J. L. Capelo-Martínez, *Ultrasound in Chemistry: Analytical Applications*. 2009, pp. 1-157.
[31] T. Leong, M. Ashokkumar, and S. Kentish, "The fundamentals of power ultrasound - A review," *Acoustics Australia,* vol. 39, 08/01 2011.
[32] Q. Yu, J. Lian, S. Siriponglert, H. Li, Y. P. Chen, and S.-S. Pei, "Graphene segregated on Ni surfaces and transferred to insulators," *Applied Physics Letters,* vol. 93, no. 11, p. 113103, 2008.
[33] H. He, T. Riedl, A. Lerf, and J. Klinowski, "Solid-State NMR Studies of the Structure of Graphite Oxide," *The Journal of Physical Chemistry,* vol. 100, no. 51, pp. 19954-19958, 1996/01/01 1996.
[34] A. O'Neill, U. Khan, P. N. Nirmalraj, J. Boland, and J. N. Coleman, "Graphene Dispersion and Exfoliation in Low Boiling Point Solvents," *The Journal of Physical Chemistry C,* vol. 115, no. 13, pp. 5422-5428, 2011/04/07 2011.
[35] A. Lerf, H. He, M. Forster, and J. Klinowski, "Structure of Graphite Oxide Revisited," *The Journal of Physical Chemistry B,* vol. 102, no. 23, pp. 4477-4482, 1998/06/01 1998.
[36] J. P. Rourke *et al.*, "The Real Graphene Oxide Revealed: Stripping the Oxidative Debris from the Graphene-like Sheets," *Angewandte Chemie International Edition,* vol. 50, no. 14, pp. 3173-3177, 2011.
[37] M. V. Bracamonte, G. I. Lacconi, S. E. Urreta, and L. E. F. Foa Torres, "On the Nature of Defects in Liquid-Phase Exfoliated Graphene," *The Journal of Physical Chemistry C,* vol. 118, no. 28, pp. 15455-15459, 2014/07/17 2014.
[38] L. Liu, Z. Shen, M. Yi, X. Zhang, and S. Ma, "A green, rapid and size-controlled production of high-quality graphene sheets by hydrodynamic forces," *RSC Advances,* 10.1039/C4RA05635C vol. 4, no. 69, pp. 36464-36470, 2014.
[39] A. P. A. Raju *et al.*, "Dispersal of pristine graphene for biological studies," *RSC Advances,* 10.1039/C6RA12195K vol. 6, no. 73, pp. 69551-69559, 2016.
[40] M. Yi, Z. Shen, S. Liang, L. Liu, X. Zhang, and S. Ma, "Water can stably disperse liquid-exfoliated graphene," *Chemical Communications,* 10.1039/C3CC46457A vol. 49, no. 94, pp. 11059-11061, 2013.
[41] K. B. Ricardo, A. Sendecki, and H. Liu, "Surfactant-free exfoliation of graphite in aqueous solutions," *Chemical Communications,* 10.1039/C3CC49273G vol. 50, no. 21, pp. 2751-2754, 2014.

[42] G. Bepete *et al.*, "Surfactant-free single-layer graphene in water," *Nat Chem,* Article vol. 9, no. 4, pp. 347-352, 04//print 2017.
[43] D. A. Dikin *et al.*, "Preparation and characterization of graphene oxide paper," *Nature,* 10.1038/nature06016 vol. 448, no. 7152, pp. 457-460, 07/26/print 2007.
[44] C. Shan, H. Yang, D. Han, Q. Zhang, A. Ivaska, and L. Niu, "Water-Soluble Graphene Covalently Functionalized by Biocompatible Poly-l-lysine," *Langmuir,* vol. 25, no. 20, pp. 12030-12033, 2009/10/20 2009.
[45] G. Gollavelli and Y.-C. Ling, "Multi-functional graphene as an in vitro and in vivo imaging probe," *Biomaterials,* vol. 33, no. 8, pp. 2532-2545, 3// 2012.
[46] A. Wang *et al.*, "Covalent functionalization of reduced graphene oxide with porphyrin by means of diazonium chemistry for nonlinear optical performance," (in eng), *Scientific reports,* vol. 6, pp. 23325-23325, 2016.
[47] E. Bekyarova *et al.*, "Chemical Modification of Epitaxial Graphene: Spontaneous Grafting of Aryl Groups," *Journal of the American Chemical Society,* vol. 131, no. 4, pp. 1336-1337, 2009/02/04 2009.
[48] S. Stankovich, R. D. Piner, S. T. Nguyen, and R. S. Ruoff, "Synthesis and exfoliation of isocyanate-treated graphene oxide nanoplatelets," *Carbon,* vol. 44, no. 15, pp. 3342-3347, 12// 2006.
[49] D.-D. Zhang, S.-Z. Zu, and B.-H. Han, "Inorganic–organic hybrid porous materials based on graphite oxide sheets," *Carbon,* vol. 47, no. 13, pp. 2993-3000, 11// 2009.
[50] J. Liu *et al.*, "Synthesis, Characterization, and Multilayer Assembly of pH Sensitive Graphene−Polymer Nanocomposites," *Langmuir,* vol. 26, no. 12, pp. 10068-10075, 2010/06/15 2010.
[51] L. Feng, S. Zhang, and Z. Liu, "Graphene based gene transfection," *Nanoscale,* 10.1039/C0NR00680G vol. 3, no. 3, pp. 1252-1257, 2011.
[52] M. Terrones *et al.*, "Interphases in Graphene Polymer-based Nanocomposites: Achievements and Challenges," *Advanced Materials,* vol. 23, no. 44, pp. 5302-5310, 2011.
[53] S. Stankovich, R. D. Piner, X. Chen, N. Wu, S. T. Nguyen, and R. S. Ruoff, "Stable aqueous dispersions of graphitic nanoplatelets via the reduction of exfoliated graphite oxide in the presence of poly(sodium 4-styrenesulfonate)," *Journal of Materials Chemistry,* 10.1039/B512799H vol. 16, no. 2, pp. 155-158, 2006.
[54] L. Guardia *et al.*, "High-throughput production of pristine graphene in an aqueous dispersion assisted by non-ionic surfactants," *Carbon,* vol. 49, no. 5, pp. 1653-1662, 4// 2011.
[55] A. G. Hsieh, C. Punckt, S. Korkut, and I. A. Aksay, "Adsorption of Sodium Dodecyl Sulfate on Functionalized Graphene Measured by Conductometric Titration," *The Journal of Physical Chemistry B,* vol. 117, no. 26, pp. 7950-7958, 2013/07/03 2013.
[56] A. G. Hsieh, S. Korkut, C. Punckt, and I. A. Aksay, "Dispersion Stability of Functionalized Graphene in Aqueous Sodium Dodecyl Sulfate Solutions," *Langmuir,* vol. 29, no. 48, pp. 14831-14838, 2013/12/03 2013.
[57] M. J. Fernández-Merino *et al.*, "Investigating the influence of surfactants on the stabilization of aqueous reduced graphene oxide dispersions and the characteristics of their composite films," *Carbon,* vol. 50, no. 9, pp. 3184-3194, 8// 2012.
[58] H. Wang, B. Xia, Y. Yan, N. Li, J.-Y. Wang, and X. Wang, "Water-Soluble Polymer Exfoliated Graphene: As Catalyst Support and Sensor," *The Journal of Physical Chemistry B,* vol. 117, no. 18, pp. 5606-5613, 2013/05/09 2013.
[59] A. S. Wajid *et al.*, "Polymer-stabilized graphene dispersions at high concentrations in organic solvents for composite production," *Carbon,* vol. 50, no. 2, pp. 526-534, 2// 2012.
[60] A. B. Bourlinos, V. Georgakilas, R. Zboril, T. A. Steriotis, A. K. Stubos, and C. Trapalis, "Aqueous-phase exfoliation of graphite in the presence of polyvinylpyrrolidone for the production of water-soluble graphenes," *Solid State Communications,* vol. 149, no. 47–48, pp. 2172-2176, 12// 2009.

[61] E. Ou *et al.*, "High concentration and stable few-layer graphene dispersions prepared by the exfoliation of graphite in different organic solvents," *RSC Advances,* 10.1039/C3RA40602D vol. 3, no. 24, pp. 9490-9499, 2013.
[62] S. Yoon and I. In, "Role of poly(N-vinyl-2-pyrrolidone) as stabilizer for dispersion of graphene via hydrophobic interaction," *Journal of Materials Science,* journal article vol. 46, no. 5, pp. 1316-1321, 2011.
[63] P. Demircioglu, "3.17 Topological Evaluation of Surfaces in Relation to Surface Finish," in *Comprehensive Materials Finishing*, M. S. J. Hashmi, Ed. Oxford: Elsevier, 2017, pp. 243-260.
[64] "Introduction to Colloid and Surface Chemistry, Fourth Edition, D. J. Shaw. Butterworth/Heinemann, Oxford, 1992. pp. vii + 306. $27.95. (ISBN 0-7506-1182-0)," *Journal of Dispersion Science and Technology,* vol. 15, no. 1, pp. 119-119, 1994/01/01 1994.
[65] J. Koetz and S. Kosmella, "Polyelectrolytes and Nanoparticles," *Polyelectrolytes and Nanoparticles, by J. Koetz and S. Kosmella. Berlin: Springer, 2007. ISBN: 978-3-540-46381-8,* 01/01 2007.
[66] M. Lotya, A. Rakovich, J. F. Donegan, and J. N. Coleman, "Measuring the lateral size of liquid-exfoliated nanosheets with dynamic light scattering," *Nanotechnology,* vol. 24, no. 26, p. 265703, 2013/06/03 2013.
[67] M. I. Mishchenko, "Electromagnetic scattering by nonspherical particles: A tutorial review," *Journal of Quantitative Spectroscopy and Radiative Transfer,* vol. 110, no. 11, pp. 808-832, 2009/07/01/ 2009.
[68] M. A. Digman, P. Sengupta, P. W. Wiseman, C. M. Brown, A. R. Horwitz, and E. Gratton, "Fluctuation Correlation Spectroscopy with a Laser-Scanning Microscope: Exploiting the Hidden Time Structure," *Biophysical Journal,* vol. 88, no. 5, pp. L33-L36, 2005/05/01/ 2005.
[69] M. A. Digman, C. M. Brown, P. Sengupta, P. W. Wiseman, A. R. Horwitz, and E. Gratton, "Measuring Fast Dynamics in Solutions and Cells with a Laser Scanning Microscope," *Biophysical Journal,* vol. 89, no. 2, pp. 1317-1327, 2005.
[70] Z. Hamrang, A. Pluen, E. Zindy, and D. Clarke, "Raster image correlation spectroscopy as a novel tool for the quantitative assessment of protein diffusional behaviour in solution," *Journal of Pharmaceutical Sciences,* vol. 101, no. 6, pp. 2082-2093, 2012.
[71] S. Goenka, V. Sant, and S. Sant, "Graphene-based nanomaterials for drug delivery and tissue engineering," *Journal of Controlled Release,* vol. 173, pp. 75-88, 2014/01/10/ 2014.
[72] X. Sun *et al.*, "Nano-Graphene Oxide for Cellular Imaging and Drug Delivery," (in eng), *Nano research,* vol. 1, no. 3, pp. 203-212, 2008.
[73] S. Syama and P. V. Mohanan, "Comprehensive Application of Graphene: Emphasis on Biomedical Concerns," *Nano-Micro Letters,* vol. 11, no. 1, p. 6, 2019/01/12 2019.
[74] D. Bitounis, H. Ali-Boucetta, B. H. Hong, D.-H. Min, and K. Kostarelos, "Prospects and Challenges of Graphene in Biomedical Applications," *Advanced Materials,* vol. 25, no. 16, pp. 2258-2268, 2013.
[75] K. Yang, L. Feng, X. Shi, and Z. Liu, "Nano-graphene in biomedicine: theranostic applications," *Chemical Society Reviews,* 10.1039/C2CS35342C vol. 42, no. 2, pp. 530-547, 2013.
[76] D. de Melo-Diogo *et al.*, "POxylated graphene oxide nanomaterials for combination chemo-phototherapy of breast cancer cells," *European Journal of Pharmaceutics and Biopharmaceutics,* vol. 131, pp. 162-169, 2018/10/01/ 2018.
[77] G. Bottari *et al.*, "Chemical functionalization and characterization of graphene-based materials," *Chemical Society Reviews,* 10.1039/C7CS00229G vol. 46, no. 15, pp. 4464-4500, 2017.
[78] Z. Liu, J. T. Robinson, X. Sun, and H. Dai, "PEGylated nanographene oxide for delivery of water-insoluble cancer drugs," (in eng), *Journal of the American Chemical Society,* vol. 130, no. 33, pp. 10876-10877, 2008.

[79] J. T. Robinson *et al.*, "Ultrasmall Reduced Graphene Oxide with High Near-Infrared Absorbance for Photothermal Therapy," *Journal of the American Chemical Society,* vol. 133, no. 17, pp. 6825-6831, 2011/05/04 2011.

[80] M. T. Mart nez *et al.*, "Modifications of single-wall carbon nanotubes upon oxidative purification treatments," *Nanotechnology,* vol. 14, no. 7, pp. 691-695, 2003/05/01 2003.

[81] V. Georgakilas, K. Kordatos, M. Prato, D. M. Guldi, M. Holzinger, and A. Hirsch, "Organic Functionalization of Carbon Nanotubes," *Journal of the American Chemical Society,* vol. 124, no. 5, pp. 760-761, 2002/02/01 2002.

[82] V. Georgakilas *et al.*, "Functionalization of Graphene: Covalent and Non-Covalent Approaches, Derivatives and Applications," *Chemical Reviews,* vol. 112, no. 11, pp. 6156-6214, 2012/11/14 2012.

[83] J. Park *et al.*, "PEGylated PLGA nanoparticles for the improved delivery of doxorubicin," *Nanomedicine: Nanotechnology, Biology and Medicine,* vol. 5, no. 4, pp. 410-418, 2009/12/01/ 2009.

[84] X. Yang, X. Zhang, Z. Liu, Y. Ma, Y. Huang, and Y. Chen, "High-Efficiency Loading and Controlled Release of Doxorubicin Hydrochloride on Graphene Oxide," *The Journal of Physical Chemistry C,* vol. 112, no. 45, pp. 17554-17558, 2008/11/13 2008.

[85] N. G. Sahoo *et al.*, "Functionalized carbon nanomaterials as nanocarriers for loading and delivery of a poorly water-soluble anticancer drug: a comparative study," *Chemical Communications,* 10.1039/C1CC00075F vol. 47, no. 18, pp. 5235-5237, 2011.

[86] L. Zhang, Z. Lu, Q. Zhao, J. Huang, H. Shen, and Z. Zhang, "Enhanced Chemotherapy Efficacy by Sequential Delivery of siRNA and Anticancer Drugs Using PEI-Grafted Graphene Oxide," *Small,* vol. 7, no. 4, pp. 460-464, 2011.

[87] B. Chen, M. Liu, L. Zhang, J. Huang, J. Yao, and Z. Zhang, "Polyethylenimine-functionalized graphene oxide as an efficient gene delivery vector," *Journal of Materials Chemistry,* 10.1039/C1JM10341E vol. 21, no. 21, pp. 7736-7741, 2011.

[88] Y. Pan, H. Bao, N. G. Sahoo, T. Wu, and L. Li, "Water-Soluble Poly(N-isopropylacrylamide)–Graphene Sheets Synthesized via Click Chemistry for Drug Delivery," *Advanced Functional Materials,* vol. 21, no. 14, pp. 2754-2763, 2011.

[89] J. Gao *et al.*, "Functionalized graphene oxide modified polysebacic anhydride as drug carrier for levofloxacin controlled release," *RSC Advances,* Article vol. 1, no. 9, pp. 1737-1744, 2011.

[90] V. K. Rana *et al.*, "Synthesis and Drug-Delivery Behavior of Chitosan-Functionalized Graphene Oxide Hybrid Nanosheets," *Macromolecular Materials and Engineering,* vol. 296, no. 2, pp. 131-140, 2011.

[91] D. Depan, J. Shah, and R. D. K. Misra, "Controlled release of drug from folate-decorated and graphene mediated drug delivery system: Synthesis, loading efficiency, and drug release response," *Materials Science and Engineering: C,* vol. 31, no. 7, pp. 1305-1312, 2011/10/10/ 2011.

[92] H. Hu, J. Yu, Y. Li, J. Zhao, and H. Dong, "Engineering of a novel pluronic F127/graphene nanohybrid for pH responsive drug delivery," *Journal of Biomedical Materials Research Part A,* vol. 100A, no. 1, pp. 141-148, 2012.

[93] M. Kakran, N. G. Sahoo, H. Bao, Y. Pan, and L. Li, "Functionalized Graphene Oxide as Nanocarrier for Loading and Delivery of Ellagic Acid," *Current Medicinal Chemistry,* vol. 18, no. 29, pp. 4503-4512, 2011.

[94] G. Wei *et al.*, "Covalent Modification of Reduced Graphene Oxide by Means of Diazonium Chemistry and Use as a Drug-Delivery System," *Chemistry – A European Journal,* vol. 18, no. 46, pp. 14708-14716, 2012.

[95] L. Zhang, J. Xia, Q. Zhao, L. Liu, and Z. Zhang, "Functional Graphene Oxide as a Nanocarrier for Controlled Loading and Targeted Delivery of Mixed Anticancer Drugs," *Small,* vol. 6, no. 4, pp. 537-544, 2010.

[96] Y. Yang, Y.-M. Zhang, Y. Chen, D. Zhao, J.-T. Chen, and Y. Liu, "Construction of a Graphene Oxide Based Noncovalent Multiple Nanosupramolecular Assembly as a Scaffold for Drug Delivery," *Chemistry – A European Journal,* vol. 18, no. 14, pp. 4208-4215, 2012.
[97] X. T. Zheng and C. M. Li, "Restoring Basal Planes of Graphene Oxides for Highly Efficient Loading and Delivery of β-Lapachone," *Molecular Pharmaceutics,* vol. 9, no. 3, pp. 615-621, 2012/03/05 2012.
[98] X. Huang, X. Qi, F. Boey, and H. Zhang, "Graphene-based composites," *Chemical Society Reviews,* 10.1039/C1CS15078B vol. 41, no. 2, pp. 666-686, 2012.
[99] J. Shen *et al.*, "Facile synthesis and application of Ag-chemically converted graphene nanocomposite," *Nano Research,* journal article vol. 3, no. 5, pp. 339-349, 2010.
[100] W. Chen, P. Yi, Y. Zhang, L. Zhang, Z. Deng, and Z. Zhang, "Composites of Aminodextran-Coated Fe3O4 Nanoparticles and Graphene Oxide for Cellular Magnetic Resonance Imaging," *ACS Applied Materials & Interfaces,* vol. 3, no. 10, pp. 4085-4091, 2011/10/26 2011.
[101] X. Yang, X. Zhang, Y. Ma, Y. Huang, Y. Wang, and Y. Chen, "Superparamagnetic graphene oxide-Fe3O4nanoparticles hybrid for controlled targeted drug carriers," *Journal of Materials Chemistry,* 10.1039/B821416F vol. 19, no. 18, pp. 2710-2714, 2009.
[102] X. Ma *et al.*, "A functionalized graphene oxide-iron oxide nanocomposite for magnetically targeted drug delivery, photothermal therapy, and magnetic resonance imaging," *Nano Research,* journal article vol. 5, no. 3, pp. 199-212, 2012.
[103] N. A. Hussien, N. Işıklan, and M. Türk, "Aptamer-functionalized magnetic graphene oxide nanocarrier for targeted drug delivery of paclitaxel," *Materials Chemistry and Physics,* vol. 211, pp. 479-488, 2018/06/01/ 2018.
[104] A. Ciesielski and P. Samorì, "Supramolecular Approaches to Graphene: From Self-Assembly to Molecule-Assisted Liquid-Phase Exfoliation," *Advanced Materials,* vol. 28, no. 29, pp. 6030-6051, 2016.
[105] K. Liu, J.-J. Zhang, F.-F. Cheng, T.-T. Zheng, C. Wang, and J.-J. Zhu, "Green and facile synthesis of highly biocompatible graphene nanosheets and its application for cellular imaging and drug delivery," *Journal of Materials Chemistry,* 10.1039/C1JM10749F vol. 21, no. 32, pp. 12034-12040, 2011.
[106] M. H. Zainal-Abidin, M. Hayyan, G. C. Ngoh, and W. F. Wong, "Doxorubicin Loading on Functional Graphene as a Promising Nanocarrier Using Ternary Deep Eutectic Solvent Systems," (in eng), *ACS omega,* vol. 5, no. 3, pp. 1656-1668, 2020.
[107] H. Song *et al.*, "Folic Acid-Chitosan Conjugated Nanoparticles for Improving Tumor-Targeted Drug Delivery," *BioMed research international,* vol. 2013, p. 723158, 10/26 2013.
[108] C. Wang, J. Li, C. Amatore, Y. Chen, H. Jiang, and X. Wang, "Gold nanoclusters and graphene nanocomposites for drug delivery and imaging of cancer cells," *Angewandte Chemie,* vol. 50 49, pp. 11644-8, 2011.
[109] J. Yan *et al.*, "Antitumor Effect of GO-PEG-DOX Complex on EMT-6 Mouse Breast Cancer Cells," (in eng), *Cancer Biother Radiopharm,* vol. 33, no. 4, pp. 125-130, May 2018.
[110] H. Wen *et al.*, "Engineered Redox-Responsive PEG Detachment Mechanism in PEGylated Nano-Graphene Oxide for Intracellular Drug Delivery," *Small,* vol. 8, no. 5, pp. 760-769, 2012.
[111] G. Liu *et al.*, "Transferrin Modified Graphene Oxide for Glioma-Targeted Drug Delivery: In Vitro and in Vivo Evaluations," *ACS Applied Materials & Interfaces,* vol. 5, no. 15, pp. 6909-6914, 2013/08/14 2013.
[112] H. Bao *et al.*, "Chitosan-functionalized graphene oxide as a nanocarrier for drug and gene delivery," (in eng), *Small,* vol. 7, no. 11, pp. 1569-78, Jun 6 2011.
[113] L. Zhou, W. Wang, J. Tang, J.-H. Zhou, H.-J. Jiang, and J. Shen, "Graphene Oxide Noncovalent Photosensitizer and Its Anticancer Activity In Vitro," *Chemistry – A European Journal,* vol. 17, no. 43, pp. 12084-12091, 2011.
[114] P. Huang *et al.*, "Folic Acid-conjugated Graphene Oxide loaded with Photosensitizers for Targeting Photodynamic Therapy," (in eng), *Theranostics,* vol. 1, pp. 240-250, 2011.

[115] Y.-J. Lu *et al.*, "Improving thermal stability and efficacy of BCNU in treating glioma cells using PAA-functionalized graphene oxide," (in eng), *International journal of nanomedicine,* vol. 7, pp. 1737-1747, 2012.
[116] C. Wang, J. Li, C. Amatore, Y. Chen, H. Jiang, and X.-M. Wang, "Gold Nanoclusters and Graphene Nanocomposites for Drug Delivery and Imaging of Cancer Cells," *Angewandte Chemie International Edition,* vol. 50, no. 49, pp. 11644-11648, 2011.
[117] Y. Park, S. Park, and I. In, "Direct noncovalent conjugation of folic acid on reduced graphene oxide as anticancer drug carrier," *Journal of Industrial and Engineering Chemistry,* vol. 30, 06/01 2015.
[118] W. Miao *et al.*, "Cholesteryl hyaluronic acid-coated, reduced graphene oxide nanosheets for anti-cancer drug delivery," *Biomaterials,* vol. 34, no. 37, pp. 9638-9647, 2013/12/01/ 2013.
[119] X. Shi *et al.*, "Heparin-reduced graphene oxide nanocomposites for curcumin delivery: in vitro, in vivo and molecular dynamics simulation study," (in eng), *Biomater Sci,* vol. 7, no. 3, pp. 1011-1027, Feb 26 2019.
[120] R. Justin and B. Chen, "Strong and conductive chitosan–reduced graphene oxide nanocomposites for transdermal drug delivery," *Journal of Materials Chemistry B,* 10.1039/C4TB00390J vol. 2, no. 24, pp. 3759-3770, 2014.
[121] N. Gupta *et al.*, "Site-specific delivery of a natural chemotherapeutic agent to human lung cancer cells using biotinylated 2D rGO nanocarriers," *Materials Science and Engineering: C,* vol. 112, p. 110884, 2020/07/01/ 2020.
[122] W.-G. La *et al.*, "Delivery of bone morphogenetic protein-2 and substance P using graphene oxide for bone regeneration," (in eng), *International journal of nanomedicine,* vol. 9 Suppl 1, no. Suppl 1, pp. 107-116, 2014.
[123] F. Emadi, A. Amini, A. Gholami, and Y. Ghasemi, "Functionalized Graphene Oxide with Chitosan for Protein Nanocarriers to Protect against Enzymatic Cleavage and Retain Collagenase Activity," *Scientific Reports,* vol. 7, no. 1, p. 42258, 2017/02/10 2017.
[124] O. Akhavan and E. Ghaderi, "Toxicity of Graphene and Graphene Oxide Nanowalls Against Bacteria," *ACS Nano,* vol. 4, no. 10, pp. 5731-5736, 2010/10/26 2010.
[125] S. Liu *et al.*, "Antibacterial Activity of Graphite, Graphite Oxide, Graphene Oxide, and Reduced Graphene Oxide: Membrane and Oxidative Stress," *ACS Nano,* vol. 5, no. 9, pp. 6971-6980, 2011/09/27 2011.
[126] X. Guo and N. Mei, "Assessment of the toxic potential of graphene family nanomaterials," (in eng), *Journal of food and drug analysis,* vol. 22, no. 1, pp. 105-115, 2014.
[127] K. Krishnamoorthy, M. Veerapandian, L.-H. Zhang, K. Yun, and S. J. Kim, "Antibacterial Efficiency of Graphene Nanosheets against Pathogenic Bacteria via Lipid Peroxidation," *The Journal of Physical Chemistry C,* vol. 116, no. 32, pp. 17280-17287, 2012/08/16 2012.
[128] J. Li *et al.*, "Antibacterial activity of large-area monolayer graphene film manipulated by charge transfer," *Scientific Reports,* vol. 4, no. 1, p. 4359, 2014/03/12 2014.
[129] I. Zarafu *et al.*, "Antimicrobial Features of Organic Functionalized Graphene-Oxide with Selected Amines," *Materials,* vol. 11, no. 9, p. 1704, 2018.
[130] L. Hou *et al.*, "Smart nanocomposite hydrogels based on azo crosslinked graphene oxide for oral colon-specific drug delivery," *Nanotechnology,* vol. 27, no. 31, p. 315105, 2016/06/27 2016.
[131] O. N. Ruiz *et al.*, "Graphene Oxide: A Nonspecific Enhancer of Cellular Growth," *ACS Nano,* vol. 5, no. 10, pp. 8100-8107, 2011/10/25 2011.
[132] M. Di Giulio *et al.*, "Antimicrobial and Antibiofilm Efficacy of Graphene Oxide against Chronic Wound Microorganisms," *Antimicrobial Agents and Chemotherapy,* vol. 62, no. 7, pp. e00547-18, 2018.
[133] H. E. Karahan *et al.*, "Graphene Materials in Antimicrobial Nanomedicine: Current Status and Future Perspectives," *Advanced Healthcare Materials,* vol. 7, no. 13, p. 1701406, 2018.

[134] S.-R. Ryoo, Y.-K. Kim, M.-H. Kim, and D.-H. Min, "Behaviors of NIH-3T3 Fibroblasts on Graphene/Carbon Nanotubes: Proliferation, Focal Adhesion, and Gene Transfection Studies," *ACS Nano,* vol. 4, no. 11, pp. 6587-6598, 2010/11/23 2010.
[135] M. Kalbacova, A. Broz, J. Kong, and M. Kalbac, "Graphene substrates promote adherence of human osteoblasts and mesenchymal stromal cells," *Carbon,* vol. 48, no. 15, pp. 4323-4329, 2010/12/01/ 2010.
[136] C. X. Guo, X. T. Zheng, Z. S. Lu, X. W. Lou, and C. M. Li, "Biointerface by Cell Growth on Layered Graphene–Artificial Peroxidase–Protein Nanostructure for In Situ Quantitative Molecular Detection," *Advanced Materials,* vol. 22, no. 45, pp. 5164-5167, 2010.
[137] R. Guazzo *et al.*, "Graphene-Based Nanomaterials for Tissue Engineering in the Dental Field," (in eng), *Nanomaterials (Basel, Switzerland),* vol. 8, no. 5, p. 349, 2018.
[138] W. C. Lee *et al.*, "Origin of Enhanced Stem Cell Growth and Differentiation on Graphene and Graphene Oxide," *ACS Nano,* vol. 5, no. 9, pp. 7334-7341, 2011/09/27 2011.
[139] N. Li *et al.*, "The promotion of neurite sprouting and outgrowth of mouse hippocampal cells in culture by graphene substrates," *Biomaterials,* vol. 32, no. 35, pp. 9374-9382, 2011/12/01/ 2011.
[140] H. Fan *et al.*, "Fabrication, Mechanical Properties, and Biocompatibility of Graphene-Reinforced Chitosan Composites," *Biomacromolecules,* vol. 11, no. 9, pp. 2345-2351, 2010/09/13 2010.
[141] S. Sayyar, E. Murray, B. C. Thompson, S. Gambhir, D. L. Officer, and G. G. Wallace, "Covalently linked biocompatible graphene/polycaprolactone composites for tissue engineering," *Carbon,* vol. 52, pp. 296-304, 2013/02/01/ 2013.
[142] H. N. Lim, N. M. Huang, S. S. Lim, I. Harrison, and C. H. Chia, "Fabrication and characterization of graphene hydrogel via hydrothermal approach as a scaffold for preliminary study of cell growth," (in eng), *International journal of nanomedicine,* vol. 6, pp. 1817-1823, 2011.
[143] G. Yang, J. Su, J. Gao, X. Hu, C. Geng, and Q. Fu, "Fabrication of well-controlled porous foams of graphene oxide modified poly(propylene-carbonate) using supercritical carbon dioxide and its potential tissue engineering applications," *The Journal of Supercritical Fluids,* vol. 73, pp. 1-9, 2013/01/01/ 2013.
[144] S. Shah, P. T. Yin, T. M. Uehara, S.-T. D. Chueng, L. Yang, and K.-B. Lee, "Guiding Stem Cell Differentiation into Oligodendrocytes Using Graphene-Nanofiber Hybrid Scaffolds," *Advanced Materials,* vol. 26, no. 22, pp. 3673-3680, 2014.
[145] S. Saravanan *et al.*, "Graphene Oxide-Gold Nanosheets Containing Chitosan Scaffold Improves Ventricular Contractility and Function After Implantation into Infarcted Heart," *Scientific Reports,* vol. 8, no. 1, p. 15069, 2018/10/10 2018.
[146] G. Zhao *et al.*, "Reduced graphene oxide functionalized nanofibrous silk fibroin matrices for engineering excitable tissues," *NPG Asia Materials,* vol. 10, no. 10, pp. 982-994, 2018/10/01 2018.
[147] S. R. Shin *et al.*, "Reduced Graphene Oxide-GelMA Hybrid Hydrogels as Scaffolds for Cardiac Tissue Engineering," *Small,* vol. 12, no. 27, pp. 3677-3689, 2016.
[148] M. H. Norahan, M. Amroon, R. Ghahremanzadeh, M. Mahmoodi, and N. Baheiraei, "Electroactive graphene oxide-incorporated collagen assisting vascularization for cardiac tissue engineering," *Journal of Biomedical Materials Research Part A,* vol. 107, no. 1, pp. 204-219, 2019.
[149] P. Hitscherich *et al.*, "Electroactive graphene composite scaffolds for cardiac tissue engineering," *Journal of Biomedical Materials Research Part A,* vol. 106, no. 11, pp. 2923-2933, 2018.
[150] S. Malik *et al.*, "Graphene composites with dental and biomedical applicability," *Beilstein Journal of Nanotechnology,* vol. 9, pp. 801-808, 03/05 2018.

[151] V. Rosa *et al.*, "Graphene oxide-based substrate: physical and surface characterization, cytocompatibility and differentiation potential of dental pulp stem cells," *Dental Materials,* vol. 32, no. 8, pp. 1019-1025, 2016/08/01/ 2016.
[152] G. Y. Chen, D. W. P. Pang, S. M. Hwang, H. Y. Tuan, and Y. C. Hu, "A graphene-based platform for induced pluripotent stem cells culture and differentiation," *Biomaterials,* vol. 33, no. 2, pp. 418-427, 2012/01/01/ 2012.
[153] Y. Chang *et al.*, "In vitro toxicity evaluation of graphene oxide on A549 cells," *Toxicology Letters,* vol. 200, no. 3, pp. 201-210, 2/5/ 2011.
[154] K.-H. Liao, Y.-S. Lin, C. W. Macosko, and C. L. Haynes, "Cytotoxicity of Graphene Oxide and Graphene in Human Erythrocytes and Skin Fibroblasts," *ACS Applied Materials & Interfaces,* vol. 3, no. 7, pp. 2607-2615, 2011/07/27 2011.
[155] K. Wang *et al.*, "Biocompatibility of Graphene Oxide," *Nanoscale Res Lett,* journal article vol. 6, no. 1, p. 8, 2010.
[156] H. Ali-Boucetta, D. Bitounis, R. Raveendran-Nair, A. Servant, J. Van den Bossche, and K. Kostarelos, "Purified Graphene Oxide Dispersions Lack In Vitro Cytotoxicity and In Vivo Pathogenicity," *Advanced healthcare materials,* vol. 2, 03/01 2013.
[157] X. Zhang *et al.*, "Distribution and biocompatibility studies of graphene oxide in mice after intravenous administration," *Carbon,* vol. 49, no. 3, pp. 986-995, 3// 2011.
[158] W. Hu *et al.*, "Graphene-Based Antibacterial Paper," *ACS Nano,* vol. 4, no. 7, pp. 4317-4323, 2010/07/27 2010.
[159] M. C. Duch *et al.*, "Minimizing Oxidation and Stable Nanoscale Dispersion Improves the Biocompatibility of Graphene in the Lung," *Nano Letters,* vol. 11, no. 12, pp. 5201-5207, 2011/12/14 2011.
[160] K. Yang, S. Zhang, G. Zhang, X. Sun, S.-T. Lee, and Z. Liu, "Graphene in Mice: Ultrahigh In Vivo Tumor Uptake and Efficient Photothermal Therapy," *Nano Letters,* vol. 10, no. 9, pp. 3318-3323, 2010/09/08 2010.
[161] K. Yang, J. Wan, S. Zhang, Y. Zhang, S.-T. Lee, and Z. Liu, "In Vivo Pharmacokinetics, Long-Term Biodistribution, and Toxicology of PEGylated Graphene in Mice," *ACS Nano,* vol. 5, no. 1, pp. 516-522, 2011/01/25 2011.
[162] S. K. Singh, M. K. Singh, P. P. Kulkarni, V. K. Sonkar, J. J. A. Grácio, and D. Dash, "Amine-Modified Graphene: Thrombo-Protective Safer Alternative to Graphene Oxide for Biomedical Applications," *ACS Nano,* vol. 6, no. 3, pp. 2731-2740, 2012/03/27 2012.
[163] D. Chen, H. Zhang, Y. Liu, and J. Li, "Graphene and its derivatives for the development of solar cells, photoelectrochemical, and photocatalytic applications," *Energy & Environmental Science,* 10.1039/C3EE23586F vol. 6, no. 5, pp. 1362-1387, 2013.
[164] C. Xu, Y. Cao, R. Kumar, X. Wu, X. Wang, and K. Scott, "A polybenzimidazole/sulfonated graphite oxide composite membrane for high temperature polymer electrolyte membrane fuel cells," *Journal of Materials Chemistry,* 10.1039/C1JM11159K vol. 21, no. 30, pp. 11359-11364, 2011.
[165] H. Chang and H. Wu, "Graphene-based nanocomposites: preparation, functionalization, and energy and environmental applications," *Energy & Environmental Science,* 10.1039/C3EE42518E vol. 6, no. 12, pp. 3483-3507, 2013.
[166] O. Akhavan, E. Ghaderi, and R. Rahighi, "Toward Single-DNA Electrochemical Biosensing by Graphene Nanowalls," *ACS Nano,* vol. 6, no. 4, pp. 2904-2916, 2012/04/24 2012.
[167] T. Kuila, S. Bose, A. K. Mishra, P. Khanra, N. H. Kim, and J. H. Lee, "Chemical functionalization of graphene and its applications," *Progress in Materials Science,* vol. 57, no. 7, pp. 1061-1105, 9// 2012.
[168] J. Shen, N. Li, M. Shi, Y. Hu, and M. Ye, "Covalent synthesis of organophilic chemically functionalized graphene sheets," *Journal of Colloid and Interface Science,* vol. 348, no. 2, pp. 377-383, 8/15/ 2010.

[169] Y.-K. Yang *et al.*, "Non-covalently modified graphene sheets by imidazolium ionic liquids for multifunctional polymer nanocomposites," *Journal of Materials Chemistry,* 10.1039/C2JM16006D vol. 22, no. 12, pp. 5666-5675, 2012.
[170] M. Born and R. Oppenheimer, "Zur Quantentheorie der Molekeln," *Annalen der Physik,* vol. 389, no. 20, pp. 457-484, 1927.
[171] W. L. Jorgensen, J. Chandrasekhar, J. D. Madura, R. W. Impey, and M. L. Klein, "Comparison of simple potential functions for simulating liquid water," *The Journal of Chemical Physics,* vol. 79, no. 2, pp. 926-935, 1983.
[172] H. J. C. Berendsen, J. P. M. Postma, W. F. van Gunsteren, and J. Hermans, "Interaction Models for Water in Relation to Protein Hydration," in *Intermolecular Forces: Proceedings of the Fourteenth Jerusalem Symposium on Quantum Chemistry and Biochemistry Held in Jerusalem, Israel, April 13–16, 1981*, B. Pullman, Ed. Dordrecht: Springer Netherlands, 1981, pp. 331-342.
[173] P. E. Smith and B. M. Pettitt, "Modeling Solvent in Biomolecular Systems," *The Journal of Physical Chemistry,* vol. 98, no. 39, pp. 9700-9711, 1994/09/01 1994.
[174] T. Darden, D. York, and L. Pedersen, "Particle mesh Ewald: An N·log(N) method for Ewald sums in large systems," *The Journal of Chemical Physics,* vol. 98, no. 12, pp. 10089-10092, 1993.
[175] A. Y. Toukmaji and J. A. Board, "Ewald summation techniques in perspective: a survey," *Computer Physics Communications,* vol. 95, no. 2, pp. 73-92, 1996/06/01 1996.
[176] H. J. C. Berendsen, J. P. M. Postma, W. F. v. Gunsteren, A. DiNola, and J. R. Haak, "Molecular dynamics with coupling to an external bath," *The Journal of Chemical Physics,* vol. 81, no. 8, pp. 3684-3690, 1984.
[177] S. Nosé, "A unified formulation of the constant temperature molecular dynamics methods," *The Journal of Chemical Physics,* vol. 81, no. 1, pp. 511-519, 1984.
[178] H. C. Andersen, "Molecular dynamics simulations at constant pressure and/or temperature," *The Journal of Chemical Physics,* vol. 72, no. 4, pp. 2384-2393, 1980.
[179] R. J. Loncharich, B. R. Brooks, and R. W. Pastor, "Langevin dynamics of peptides: The frictional dependence of isomerization rates of N-acetylalanyl-N'-methylamide," *Biopolymers,* vol. 32, no. 5, pp. 523-535, 1992.
[180] B. M. Pettitt, V. A. Makarov, and B. K. Andrews, "Protein hydration density: theory, simulations and crystallography," *Current Opinion in Structural Biology,* vol. 8, no. 2, pp. 218-221, 1998/04/01 1998.
[181] B. Roux, "Computational Studies of the Gramicidin Channel," *Accounts of Chemical Research,* vol. 35, no. 6, pp. 366-375, 2002/06/01 2002.
[182] P. J. Bond and M. S. P. Sansom, "The simulation approach to bacterial outer membrane proteins (Review)," *Molecular Membrane Biology,* vol. 21, no. 3, pp. 151-161, 2004/01/01 2004.
[183] G. Tiana, F. Simona, G. M. S. De Mori, R. A. Broglia, and G. Colombo, "Understanding the determinants of stability and folding of small globular proteins from their energetics," *Protein Science,* vol. 13, no. 1, pp. 113-124, 2004.
[184] W. Wang, O. Donini, C. M. Reyes, and P. A. Kollman, "Biomolecular Simulations: Recent Developments in Force Fields, Simulations of Enzyme Catalysis, Protein-Ligand, Protein-Protein, and Protein-Nucleic Acid Noncovalent Interactions," *Annual Review of Biophysics and Biomolecular Structure,* vol. 30, no. 1, pp. 211-243, 2001.
[185] A. Warshel, "Computer Simulations of Enzyme Catalysis: Methods, Progress, and Insights," *Annual Review of Biophysics and Biomolecular Structure,* vol. 32, no. 1, pp. 425-443, 2003.
[186] R. Day and V. Daggett, "All-Atom Simulations Of Protein Folding And Unfolding," in *Advances in Protein Chemistry*, vol. Volume 66: Academic Press, 2003, pp. 373-403.
[187] V. Daggett, "Protein Folding−Simulation," *Chemical Reviews,* vol. 106, no. 5, pp. 1898-1916, 2006/05/01 2006.
[188] H. W. Kim *et al.*, "Restoring allosterism with compensatory mutations in hemoglobin," (in eng), *Proc Natl Acad Sci U S A,* vol. 91, no. 24, pp. 11547-51, Nov 22 1994.

[189] A. H. Elcock, "Molecular simulations of diffusion and association in multimacromolecular systems," (in eng), *Methods Enzymol,* vol. 383, pp. 166-98, 2004.
[190] C. F. Wong and A. J. McCammon, "Protein simulation and drug design," (in eng), *Adv Protein Chem,* vol. 66, pp. 87-121, 2003.
[191] P. Koehl and M. Levitt, "De novo protein design. I. In search of stability and specificity," (in eng), *J Mol Biol,* vol. 293, no. 5, pp. 1161-81, Nov 12 1999.
[192] A. T. Brunger and P. D. Adams, "Molecular dynamics applied to X-ray structure refinement," (in eng), *Acc Chem Res,* vol. 35, no. 6, pp. 404-12, Jun 2002.
[193] J. P. Linge, M. A. Williams, C. A. Spronk, A. M. Bonvin, and M. Nilges, "Refinement of protein structures in explicit solvent," (in eng), *Proteins,* vol. 50, no. 3, pp. 496-506, Feb 15 2003.
[194] H. Fan and A. E. Mark, "Refinement of homology-based protein structures by molecular dynamics simulation techniques," (in eng), *Protein Sci,* vol. 13, no. 1, pp. 211-20, Jan 2004.
[195] J. W. Ponder and D. A. Case, "Force fields for protein simulations," (in eng), *Adv Protein Chem,* vol. 66, pp. 27-85, 2003.
[196] A. D. Mackerell, Jr., "Empirical force fields for biological macromolecules: overview and issues," (in eng), *J Comput Chem,* vol. 25, no. 13, pp. 1584-604, Oct 2004.
[197] C. S. Ewig, T. S. Thacher, and A. T. Hagler, "Derivation of Class II Force Fields. 7. Nonbonded Force Field Parameters for Organic Compounds," *The Journal of Physical Chemistry B,* vol. 103, no. 33, pp. 6998-7014, 1999/08/01 1999.
[198] S. A. Adcock and J. A. McCammon, "Molecular Dynamics: Survey of Methods for Simulating the Activity of Proteins," *Chemical Reviews,* vol. 106, no. 5, pp. 1589-1615, 2006/05/01 2006.
[199] C. I. Bayly, P. Cieplak, W. Cornell, and P. A. Kollman, "A well-behaved electrostatic potential based method using charge restraints for deriving atomic charges: the RESP model," *The Journal of Physical Chemistry,* vol. 97, no. 40, pp. 10269-10280, 1993/10/01 1993.
[200] R. J. Woods and R. Chappelle, "Restrained electrostatic potential atomic partial charges for condensed-phase simulations of carbohydrates," *Journal of Molecular Structure-theochem - J MOL STRUC-THEOCHEM,* vol. 527, pp. 149-156, 08/01 2000.
[201] J. Wang, R. M. Wolf, J. W. Caldwell, P. A. Kollman, and D. A. Case, "Development and testing of a general amber force field," (in eng), *J Comput Chem,* vol. 25, no. 9, pp. 1157-74, Jul 15 2004.
[202] M. Ramezanpour, S. S. W. Leung, K. H. Delgado-Magnero, B. Y. M. Bashe, J. Thewalt, and D. P. Tieleman, "Computational and experimental approaches for investigating nanoparticle-based drug delivery systems," *Biochimica et Biophysica Acta (BBA) - Biomembranes,* vol. 1858, no. 7, Part B, pp. 1688-1709, 7// 2016.
[203] D. A. Case *et al.*, "The Amber biomolecular simulation programs," *Journal of Computational Chemistry,* vol. 26, no. 16, pp. 1668-1688, 2005.
[204] B. Hess, C. Kutzner, D. van der Spoel, and E. Lindahl, "GROMACS 4: Algorithms for Highly Efficient, Load-Balanced, and Scalable Molecular Simulation," *Journal of Chemical Theory and Computation,* vol. 4, no. 3, pp. 435-447, 2008/03/01 2008.
[205] B. R. Brooks *et al.*, "CHARMM: The biomolecular simulation program," *Journal of Computational Chemistry,* vol. 30, no. 10, pp. 1545-1614, 2009.
[206] S. Plimpton, "Fast Parallel Algorithms for Short-Range Molecular Dynamics," *Journal of Computational Physics,* vol. 117, no. 1, pp. 1-19, 1995/03/01 1995.
[207] J. C. Phillips *et al.*, "Scalable molecular dynamics with NAMD," *Journal of Computational Chemistry,* vol. 26, no. 16, pp. 1781-1802, 2005.
[208] H. He, J. Klinowski, M. Forster, and A. Lerf, "A new structural model for graphite oxide," *Chemical Physics Letters,* vol. 287, no. 1–2, pp. 53-56, 4/24/ 1998.
[209] C.-J. Shih, S. Lin, R. Sharma, M. S. Strano, and D. Blankschtein, "Understanding the pH-Dependent Behavior of Graphene Oxide Aqueous Solutions: A Comparative Experimental and Molecular Dynamics Simulation Study," *Langmuir,* vol. 28, no. 1, pp. 235-241, 2012/01/10 2012.

[210] R. M. Abolfath and K. Cho, "Computational Studies for Reduced Graphene Oxide in Hydrogen-Rich Environment," *The Journal of Physical Chemistry A,* vol. 116, no. 7, pp. 1820-1827, 2012/02/23 2012.
[211] B. Narayanan *et al.*, "Carbon monoxide-induced reduction and healing of graphene oxide," *Journal of Vacuum Science & Technology A,* vol. 31, no. 4, p. 040601, 2013.
[212] N. Wei, C. Lv, and Z. Xu, "Wetting of Graphene Oxide: A Molecular Dynamics Study," *Langmuir,* vol. 30, no. 12, pp. 3572-3578, 2014/04/01 2014.
[213] F. Taherian, V. Marcon, N. F. A. van der Vegt, and F. Leroy, "What Is the Contact Angle of Water on Graphene?," *Langmuir,* vol. 29, no. 5, pp. 1457-1465, 2013/02/05 2013.
[214] C.-J. Shih *et al.*, "Breakdown in the Wetting Transparency of Graphene," *Physical Review Letters,* vol. 109, no. 17, p. 176101, 10/24/ 2012.
[215] M. Pykal, P. Jurecka, F. Karlicky, and M. Otyepka, "Modelling of graphene functionalization," *Physical Chemistry Chemical Physics,* 10.1039/C5CP03599F vol. 18, no. 9, pp. 6351-6372, 2016.
[216] P. Lazar *et al.*, "Adsorption of Small Organic Molecules on Graphene," *Journal of the American Chemical Society,* vol. 135, no. 16, pp. 6372-6377, 2013/04/24 2013.
[217] G. R. Jenness and K. D. Jordan, "DF-DFT-SAPT Investigation of the Interaction of a Water Molecule to Coronene and Dodecabenzocoronene: Implications for the Water−Graphite Interaction," *The Journal of Physical Chemistry C,* vol. 113, no. 23, pp. 10242-10248, 2009/06/11 2009.
[218] M. Rubeš, P. Nachtigall, J. Vondrášek, and O. Bludský, "Structure and Stability of the Water−Graphite Complexes," *The Journal of Physical Chemistry C,* vol. 113, no. 19, pp. 8412-8419, 2009/05/14 2009.
[219] A. Schlierf *et al.*, "Nanoscale insight into the exfoliation mechanism of graphene with organic dyes: effect of charge, dipole and molecular structure," *Nanoscale,* 10.1039/C3NR00258F vol. 5, no. 10, pp. 4205-4216, 2013.
[220] P.-P. Zhou and R.-Q. Zhang, "Physisorption of benzene derivatives on graphene: critical roles of steric and stereoelectronic effects of the substituent," *Physical Chemistry Chemical Physics,* 10.1039/C4CP05973E vol. 17, no. 18, pp. 12185-12193, 2015.
[221] Y. H. Lu, W. Chen, Y. P. Feng, and P. M. He, "Tuning the Electronic Structure of Graphene by an Organic Molecule," *The Journal of Physical Chemistry B,* vol. 113, no. 1, pp. 2-5, 2009/01/08 2009.
[222] Q. Li *et al.*, "Fluorination of Graphene Enhances Friction Due to Increased Corrugation," *Nano Letters,* vol. 14, no. 9, pp. 5212-5217, 2014/09/10 2014.
[223] X. Sun, Z. Feng, T. Hou, and Y. Li, "Mechanism of Graphene Oxide as an Enzyme Inhibitor from Molecular Dynamics Simulations," *ACS Applied Materials & Interfaces,* vol. 6, no. 10, pp. 7153-7163, 2014/05/28 2014.
[224] A. N. Camden, S. A. Barr, and R. J. Berry, "Simulations of Peptide-Graphene Interactions in Explicit Water," *The Journal of Physical Chemistry B,* vol. 117, no. 37, pp. 10691-10697, 2013/09/19 2013.
[225] H. Vovusha, S. Sanyal, and B. Sanyal, "Interaction of Nucleobases and Aromatic Amino Acids with Graphene Oxide and Graphene Flakes," *The Journal of Physical Chemistry Letters,* vol. 4, no. 21, pp. 3710-3718, 2013/11/07 2013.
[226] W. Qin, X. Li, W.-W. Bian, X.-J. Fan, and J.-Y. Qi, "Density functional theory calculations and molecular dynamics simulations of the adsorption of biomolecules on graphene surfaces," *Biomaterials,* vol. 31, no. 5, pp. 1007-1016, 2010/02/01/ 2010.
[227] C. Rajesh, C. Majumder, H. Mizuseki, and Y. Kawazoe, "A theoretical study on the interaction of aromatic amino acids with graphene and single walled carbon nanotube," *The Journal of Chemical Physics,* vol. 130, no. 12, p. 124911, 2009.
[228] C. Cazorla, "Ab initio study of the binding of collagen amino acids to graphene and A-doped (A = H, Ca) graphene," *Thin Solid Films,* vol. 518, no. 23, pp. 6951-6961, 9/30/ 2010.

[229] "Crystal structure of l-valine hydrochloride monohydrate*," in *Zeitschrift für Kristallographie* vol. 128, ed, 1969, p. 339.
[230] G. Gorgolis and C. Galiotis, "Graphene aerogels: a review," *2D Materials,* vol. 4, no. 3, p. 032001, 2017/06/22 2017.
[231] L. Xu *et al.*, "Superhydrophobic and superoleophilic graphene aerogel prepared by facile chemical reduction," *Journal of Materials Chemistry A,* 10.1039/C5TA00383K vol. 3, no. 14, pp. 7498-7504, 2015.
[232] C.-H. Lu, H.-H. Yang, C.-L. Zhu, X. Chen, and G.-N. Chen, "A Graphene Platform for Sensing Biomolecules," *Angewandte Chemie International Edition,* vol. 48, no. 26, pp. 4785-4787, 2009.
[233] Y. Xuan *et al.*, "Atomic-layer-deposited nanostructures for graphene-based nanoelectronics," *Applied Physics Letters,* vol. 92, no. 1, p. 013101, 2008.
[234] L. Qu, Y. Liu, J.-B. Baek, and L. Dai, "Nitrogen-Doped Graphene as Efficient Metal-Free Electrocatalyst for Oxygen Reduction in Fuel Cells," *ACS Nano,* vol. 4, no. 3, pp. 1321-1326, 2010/03/23 2010.
[235] J. Zhang *et al.*, "Graphene Oxide as a Matrix for Enzyme Immobilization," *Langmuir,* vol. 26, no. 9, pp. 6083-6085, 2010/05/04 2010.
[236] D. Y. Lee, Z. Khatun, J.-H. Lee, Y.-k. Lee, and I. In, "Blood Compatible Graphene/Heparin Conjugate through Noncovalent Chemistry," *Biomacromolecules,* vol. 12, no. 2, pp. 336-341, 2011/02/14 2011.
[237] H. Lei *et al.*, "Adsorption of double-stranded DNA to graphene oxide preventing enzymatic digestion," *Nanoscale,* 10.1039/C1NR10617A vol. 3, no. 9, pp. 3888-3892, 2011.
[238] H. Bao *et al.*, "Chitosan-Functionalized Graphene Oxide as a Nanocarrier for Drug and Gene Delivery," *Small,* vol. 7, no. 11, pp. 1569-1578, 2011.
[239] R. Alqus, S. J. Eichhorn, and R. A. Bryce, "Molecular Dynamics of Cellulose Amphiphilicity at the Graphene–Water Interface," *Biomacromolecules,* vol. 16, no. 6, pp. 1771-1783, 2015/06/08 2015.
[240] Y. Li, M. Liao, and J. Zhou, "Catechol and Its Derivatives Adhesion on Graphene: Insights from Molecular Dynamics Simulations," *The Journal of Physical Chemistry C,* vol. 122, no. 40, pp. 22965-22974, 2018/10/11 2018.
[241] E. V. Bichenkova, A. P. A. Raju, K. K. Burusco, I. A. Kinloch, K. S. Novoselov, and D. J. Clarke, "NMR detects molecular interactions of graphene with aromatic and aliphatic hydrocarbons in water," *2D Materials,* vol. 5, no. 1, p. 015003, 2017/10/03 2017.
[242] N. Tisawat *et al.*, "Enhancement performance of carbon electrode for supercapacitors by quinone derivatives loading via solvent-free method," *Applied Surface Science,* 2019/05/21/ 2019.
[243] U.S. Food and Drug Administration. (2018, December 20,). *GRAS Notices*. Available: https://www.accessdata.fda.gov/scripts/fdcc/?set=GRASNotices
[244] A. Chakraborty, J. C. Boer, C. Selomulya, and M. Plebanski, "Amino Acid Functionalized Inorganic Nanoparticles as Cutting-Edge Therapeutic and Diagnostic Agents," (in eng), *Bioconjug Chem,* vol. 29, no. 3, pp. 657-671, Mar 21 2018.
[245] P. R. Selvakannan, S. Mandal, S. Phadtare, and M. Sastry, *Capping of Gold Nanoparticles by the Amino Acid Lysine Renders Them Water-Dispersible*. 2003, p. 3545.
[246] W. Zhou *et al.*, "Surface functionalization of graphene oxide by amino acids for Thermomyces lanuginosus lipase adsorption," *Journal of Colloid and Interface Science,* vol. 546, pp. 211-220, 2019/06/15/ 2019.
[247] D. Chen, L. Li, and L. Guo, "An environment-friendly preparation of reduced graphene oxide nanosheets via amino acid," *Nanotechnology,* vol. 22, no. 32, p. 325601, 2011/07/14 2011.
[248] J. Guo, L. Ren, R. Wang, C. Zhang, Y. Yang, and T. Liu, "Water dispersible graphene noncovalently functionalized with tryptophan and its poly(vinyl alcohol) nanocomposite," *Composites Part B: Engineering,* vol. 42, no. 8, pp. 2130-2135, 2011/12/01/ 2011.

[249] S. Mallakpour, A. Abdolmaleki, and S. Borandeh, "Covalently functionalized graphene sheets with biocompatible natural amino acids," *Applied Surface Science,* vol. 307, pp. 533-542, 2014/07/15/ 2014.
[250] W. Humphrey, A. Dalke, and K. Schulten, "VMD: Visual molecular dynamics," *Journal of Molecular Graphics,* vol. 14, no. 1, pp. 33-38, 1996/02/01/ 1996.
[251] J. Wang, R. M. Wolf, J. W. Caldwell, P. A. Kollman, and D. A. Case, "Development and testing of a general amber force field," *Journal of computational chemistry,* vol. 25, no. 9, pp. 1157-1174, 2004.
[252] J. A. Maier, C. Martinez, K. Kasavajhala, L. Wickstrom, K. E. Hauser, and C. Simmerling, "ff14SB: Improving the Accuracy of Protein Side Chain and Backbone Parameters from ff99SB," *Journal of Chemical Theory and Computation,* vol. 11, no. 8, pp. 3696-3713, 2015/08/11 2015.
[253] D. Case *et al.*, *Amber 16, University of California, San Francisco*. 2016.
[254] J.-P. Ryckaert, G. Ciccotti, and H. J. C. Berendsen, "Numerical integration of the cartesian equations of motion of a system with constraints: molecular dynamics of n-alkanes," *Journal of Computational Physics,* vol. 23, no. 3, pp. 327-341, 1977/03/01 1977.
[255] M. P. Allen and D. J. Tildesley, *Computer simulation of liquids*. Oxford university press, 2017.
[256] D. R. Roe and T. E. Cheatham, "PTRAJ and CPPTRAJ: Software for Processing and Analysis of Molecular Dynamics Trajectory Data," *Journal of Chemical Theory and Computation,* vol. 9, no. 7, pp. 3084-3095, 2013/07/09 2013.
[257] M. J. Frisch *et al.*, "Gaussian 16 Rev. B.01," ed. Wallingford, CT, 2016.
[258] P. Jurečka, J. Černý, P. Hobza, and D. R. Salahub, "Density functional theory augmented with an empirical dispersion term. Interaction energies and geometries of 80 noncovalent complexes compared with ab initio quantum mechanics calculations," *Journal of Computational Chemistry,* vol. 28, no. 2, pp. 555-569, 2007.
[259] M. Korth, "Third-generation hydrogen-bonding corrections for semiempirical QM methods and force fields," *Journal of Chemical Theory and Computation,* vol. 6, no. 12, pp. 3808-3816, 2010.
[260] S. Conti and M. Cecchini, "Accurate and Efficient Calculation of the Desorption Energy of Small Molecules from Graphene," *The Journal of Physical Chemistry C,* vol. 119, no. 4, pp. 1867-1879, 2015/01/29 2015.
[261] J.-D. Chai and M. Head-Gordon, "Long-range corrected hybrid density functionals with damped atom–atom dispersion corrections," *Physical Chemistry Chemical Physics,* vol. 10, no. 44, pp. 6615-6620, 2008.
[262] C. Backes *et al.*, "Spectroscopic metrics allow in situ measurement of mean size and thickness of liquid-exfoliated few-layer graphene nanosheets," *Nanoscale,* 10.1039/C5NR08047A vol. 8, no. 7, pp. 4311-4323, 2016.
[263] T. E. Needham, A. N. Paruta, and R. J. Gerraughty, "Solubility of Amino Acids in Pure Solvent Systems," *Journal of Pharmaceutical Sciences,* vol. 60, no. 4, pp. 565-567, 1971/04/01/ 1971.
[264] THE MERCK INDEX. (2019,Jaunuary 28). *an encyclopedia of chemicals, drugs and biologicals,* . Available: https://www.rsc.org/merck-index?e=1%20[
[265] A. V. Marenich, C. J. Cramer, and D. G. Truhlar, "Universal Solvation Model Based on Solute Electron Density and on a Continuum Model of the Solvent Defined by the Bulk Dielectric Constant and Atomic Surface Tensions," *The Journal of Physical Chemistry B,* vol. 113, no. 18, pp. 6378-6396, 2009/05/07 2009.
[266] P. Singla, M. Riyaz, S. Singhal, and N. Goel, "Theoretical study of adsorption of amino acids on graphene and BN sheet in gas and aqueous phase with empirical DFT dispersion correction," *Physical Chemistry Chemical Physics,* 10.1039/C5CP07078C vol. 18, no. 7, pp. 5597-5604, 2016.
[267] M. Lotya, P. J. King, U. Khan, S. De, and J. N. Coleman, "High-Concentration, Surfactant-Stabilized Graphene Dispersions," *ACS Nano,* vol. 4, no. 6, pp. 3155-3162, 2010/06/22 2010.

[268] S. Wang, M. Yi, and Z. Shen, "The effect of surfactants and their concentration on the liquid exfoliation of graphene," *RSC advances,* vol. 6, no. 61, pp. 56705-56710, 2016.
[269] Y. J. Lee *et al.*, "Structural rearrangement and dispersion of functionalized graphene sheets in aqueous solutions," *Colloids and Interface Science Communications,* vol. 8, pp. 1-5, 2015.
[270] D. A. Jasim, C. Ménard-Moyon, D. Bégin, A. Bianco, and K. Kostarelos, "Tissue distribution and urinary excretion of intravenously administered chemically functionalized graphene oxide sheets," *Chemical Science,* 10.1039/C5SC00114E vol. 6, no. 7, pp. 3952-3964, 2015.
[271] H. Ali-Boucetta, D. Bitounis, R. Raveendran-Nair, A. Servant, J. Van den Bossche, and K. Kostarelos, "Purified Graphene Oxide Dispersions Lack In Vitro Cytotoxicity and In Vivo Pathogenicity," *Advanced Healthcare Materials,* vol. 2, no. 3, pp. 433-441, 2013.
[272] C. McCallion, J. Burthem, K. Rees-Unwin, A. Golovanov, and A. Pluen, "Graphene in therapeutics delivery: Problems, solutions and future opportunities," *European Journal of Pharmaceutics and Biopharmaceutics,* vol. 104, pp. 235-250, 2016/07/01/ 2016.
[273] P. Blake *et al.*, "Making graphene visible," *Applied Physics Letters,* vol. 91, no. 6, p. 063124, 2007.
[274] Z. Chen, Y.-M. Lin, M. J. Rooks, and P. Avouris, "Graphene nano-ribbon electronics," *Physica E: Low-dimensional Systems and Nanostructures,* vol. 40, no. 2, pp. 228-232, 2007/12/01/ 2007.
[275] C. Casiraghi *et al.*, "Rayleigh Imaging of Graphene and Graphene Layers," *Nano Letters,* vol. 7, no. 9, pp. 2711-2717, 2007/09/01 2007.
[276] M. Lotya *et al.*, "Liquid Phase Production of Graphene by Exfoliation of Graphite in Surfactant/Water Solutions," *Journal of the American Chemical Society,* vol. 131, no. 10, pp. 3611-3620, 2009/03/18 2009.
[277] D. Boukhvalov and M. Katsnelson, "Chemical functionalization of graphene," *Journal of physics. Condensed matter : an Institute of Physics journal,* vol. 21, p. 344205, 08/26 2009.
[278] M. Singh *et al.*, "Tuneable Physicochemical Properties of Thermally Annealed Graphene Oxide Powder and Thin Films," *Journal of Nanoscience and Nanotechnology,* vol. 18, no. 3, pp. 1763-1771, // 2018.
[279] S.-Y. Wu, S. S. A. An, and J. Hulme, "Current applications of graphene oxide in nanomedicine," (in eng), *International journal of nanomedicine,* vol. 10 Spec Iss, no. Spec Iss, pp. 9-24, 2015.
[280] J. B. Oostinga, H. B. Heersche, X. Liu, A. F. Morpurgo, and L. M. K. Vandersypen, "Gate-induced insulating state in bilayer graphene devices," *Nature Materials,* vol. 7, no. 2, pp. 151-157, 2008/02/01 2008.
[281] A. Gallagher, U. Khan, P. Nirmalraj, J. Boland, and J. Coleman, "Graphene Dispersion and Exfoliation in Low Boiling Point Solvents," *The Journal of Physical Chemistry C,* vol. 115, 03/14 2011.
[282] V. Bracamonte, G. Lacconi, S. Urreta, and L. Foa Torres, "On the Nature of Defects in Liquid-Phase Exfoliated Graphene," *The Journal of Physical Chemistry C,* 06/25 2014.
[283] R. Durge, R. V. Kshirsagar, and P. Tambe, "Effect of Sonication Energy on the Yield of Graphene Nanosheets by Liquid-phase Exfoliation of Graphite," *Procedia Engineering,* vol. 97, pp. 1457-1465, 2014/01/01/ 2014.
[284] F. A. Alkathiri, C. McCallion, A. P. Golovanov, J. Burthem, A. Pluen, and R. A. Bryce, "Solvation of Pristine Graphene Using Amino Acids: A Molecular Simulation and Experimental Analysis," *The Journal of Physical Chemistry C,* vol. 123, no. 50, pp. 30234-30244, 2019/12/19 2019.
[285] C. M. Rubert Pérez, N. Stephanopoulos, S. Sur, S. S. Lee, C. Newcomb, and S. I. Stupp, "The Powerful Functions of Peptide-Based Bioactive Matrices for Regenerative Medicine," *Annals of Biomedical Engineering,* vol. 43, no. 3, pp. 501-514, 2015/03/01 2015.
[286] K. Nawara *et al.*, "Adsorption of Doxorubicin onto Citrate-Stabilized Magnetic Nanoparticles," *The Journal of Physical Chemistry C,* vol. 116, no. 9, pp. 5598-5609, 2012/03/08 2012.
[287] H. Cortés-Funes and C. Coronado, "Role of anthracyclines in the era of targeted therapy," *Cardiovascular Toxicology,* vol. 7, no. 2, pp. 56-60, 2007/06/01 2007.

[288] J. Shi, P. W. Kantoff, R. Wooster, and O. C. Farokhzad, "Cancer nanomedicine: progress, challenges and opportunities," *Nature Reviews Cancer,* vol. 17, no. 1, pp. 20-37, 2017/01/01 2017.

[289] C. Chittasupho, K. Lirdprapamongkol, P. Kewsuwan, and N. Sarisuta, "Targeted delivery of doxorubicin to A549 lung cancer cells by CXCR4 antagonist conjugated PLGA nanoparticles," *European Journal of Pharmaceutics and Biopharmaceutics,* vol. 88, no. 2, pp. 529-538, 2014/10/01/ 2014.

[290] S. Biswas, N. S. Dodwadkar, P. P. Deshpande, S. Parab, and V. P. Torchilin, "Surface functionalization of doxorubicin-loaded liposomes with octa-arginine for enhanced anticancer activity," *European Journal of Pharmaceutics and Biopharmaceutics,* vol. 84, no. 3, pp. 517-525, 2013/08/01/ 2013.

[291] N. Zhao, M. C. Woodle, and A. J. Mixson, "Advances in delivery systems for doxorubicin," (in eng), *Journal of nanomedicine & nanotechnology,* vol. 9, no. 5, p. 519, 2018.

[292] K. Greish, "Enhanced Permeability and Retention (EPR) Effect for Anticancer Nanomedicine Drug Targeting," in *Cancer Nanotechnology: Methods and Protocols*, S. R. Grobmyer and B. M. Moudgil, Eds. Totowa, NJ: Humana Press, 2010, pp. 25-37.

[293] C. Schindler *et al.*, "Exosomal delivery of doxorubicin enables rapid cell entry and enhanced in vitro potency," (in eng), *PloS one,* vol. 14, no. 3, pp. e0214545-e0214545, 2019.

[294] W. D. Cornell *et al.*, "A Second Generation Force Field for the Simulation of Proteins, Nucleic Acids, and Organic Molecules," *Journal of the American Chemical Society,* vol. 117, no. 19, pp. 5179-5197, 1995/05/01 1995.

[295] P. H. Hünenberger, "Thermostat Algorithms for Molecular Dynamics Simulations," in *Advanced Computer Simulation: Approaches for Soft Matter Sciences I*, C. Dr. Holm and K. Prof. Dr. Kremer, Eds. Berlin, Heidelberg: Springer Berlin Heidelberg, 2005, pp. 105-149.

[296] S. Shah *et al.*, "Fluorescence properties of doxorubicin in PBS buffer and PVA films," (in eng), *Journal of photochemistry and photobiology. B, Biology,* vol. 170, pp. 65-69, 2017.

[297] K. Radotić, T. B. Melø, R. M. Leblanc, Y. A. Yousef, and K. R. Naqvi, "Fluorescence and phosphorescence of tryptophan in peptides of different length and sequence," *Journal of Photochemistry and Photobiology B: Biology,* vol. 157, pp. 120-128, 2016/04/01/ 2016.

[298] P. Mohan and N. Rapoport, "Doxorubicin as a Molecular Nanotheranostic Agent: Effect of Doxorubicin Encapsulation in Micelles or Nanoemulsions on the Ultrasound-Mediated Intracellular Delivery and Nuclear Trafficking," *Molecular Pharmaceutics,* vol. 7, no. 6, pp. 1959-1973, 2010/12/06 2010.

[299] K. Lee, Y. Choi, K. Kim, H.-J. Koo, and J. Choi, "Quantification of Unknown Nanoscale Biomolecules Using the Average-Weight-Difference Method," *Applied Sciences,* vol. 9, no. 1, p. 130, 2019.

[300] L. M. Malard, M. A. Pimenta, G. Dresselhaus, and M. S. Dresselhaus, "Raman spectroscopy in graphene," *Physics Reports,* vol. 473, no. 5, pp. 51-87, 2009/04/01/ 2009.

[301] I. Calizo, I. Bejenari, G. Liu, and A. Balandin, "Ultraviolet Raman microscopy of single and multilayer graphene," *Journal of Applied Physics,* vol. 106, pp. 043509-043509, 09/01 2009.

[302] E. Aliyev, V. Filiz, M. M. Khan, Y. J. Lee, C. Abetz, and V. Abetz, "Structural Characterization of Graphene Oxide: Surface Functional Groups and Fractionated Oxidative Debris," (in eng), *Nanomaterials (Basel, Switzerland),* vol. 9, no. 8, p. 1180, 2019.

[303] T. M. Buttke, J. A. McCubrey, and T. C. Owen, "Use of an aqueous soluble tetrazolium/formazan assay to measure viability and proliferation of lymphokine-dependent cell lines," *Journal of Immunological Methods,* vol. 157, no. 1, pp. 233-240, 1993/01/04/ 1993.

[304] X. Zeng, R. Morgenstern, and A. M. Nyström, "Nanoparticle-directed sub-cellular localization of doxorubicin and the sensitization breast cancer cells by circumventing GST-Mediated drug resistance," *Biomaterials,* vol. 35, no. 4, pp. 1227-1239, 2014/01/01/ 2014.

[305] H. Wang *et al.*, "Preparation of Graphene Sheets by Electrochemical Exfoliation of Graphite in Confined Space and Their Application in Transparent Conductive Films," *ACS Applied Materials & Interfaces,* vol. 9, 09/13 2017.

[306] Z. Shen, J. Li, M. Yi, X. Zhang, and S. Ma, "Preparation of graphene by jet cavitation," *Nanotechnology,* vol. 22, p. 365306, 09/07 2011.

[307] A. C. Ferrari *et al.*, "Raman Spectrum of Graphene and Graphene Layers," *Physical Review Letters,* vol. 97, no. 18, p. 187401, 10/30/ 2006.

[308] R. Muzyka, S. Drewniak, T. Pustelny, M. Chrubasik, and G. Gryglewicz, "Characterization of Graphite Oxide and Reduced Graphene Oxide Obtained from Different Graphite Precursors and Oxidized by Different Methods Using Raman Spectroscopy," (in eng), *Materials (Basel, Switzerland),* vol. 11, no. 7, p. 1050, 2018.

[309] R. P. Vidano, D. B. Fischbach, L. J. Willis, and T. M. Loehr, "Observation of Raman band shifting with excitation wavelength for carbons and graphites," *Solid State Communications,* Article vol. 39, no. 2, pp. 341-344, 1981.

[310] S. G. Prolongo, A. Jimenez-Suarez, R. Moriche, and A. Ureña, "In situ processing of epoxy composites reinforced with graphene nanoplatelets," *Composites Science and Technology,* vol. 86, pp. 185-191, 2013/09/24/ 2013.

[311] A. C. Ferrari *et al.*, "Raman Spectrum of Graphene and Graphene Layers," *Physical review letters,* vol. 97, p. 187401, 12/01 2006.

[312] P. Das, I. Pan, E. Cohen, and M. Reches, "Self-assembly of a metallo-peptide into a drug delivery system using a “switch on” displacement strategy," *Journal of Materials Chemistry B,* 10.1039/C8TB01483C vol. 6, no. 48, pp. 8228-8237, 2018.

[313] M. Z. Tonel, M. O. Martins, I. Zanella, R. B. Pontes, and S. B. Fagan, "A first-principles study of the interaction of doxorubicin with graphene," *Computational and Theoretical Chemistry,* vol. 1115, pp. 270-275, 2017/09/01/ 2017.

[314] Z. Liu *et al.*, "Switching off the interactions between graphene oxide and doxorubicin using vitamin C: combining simplicity and efficiency in drug delivery," *Journal of Materials Chemistry B,* 10.1039/C7TB03063K vol. 6, no. 8, pp. 1251-1259, 2018.

[315] K. A. Janes, M. P. Fresneau, A. Marazuela, A. Fabra, and M. a. J. Alonso, "Chitosan nanoparticles as delivery systems for doxorubicin," *Journal of Controlled Release,* vol. 73, no. 2, pp. 255-267, 2001/06/15/ 2001.

[316] K. Kataoka *et al.*, "Doxorubicin-loaded poly(ethylene glycol)-poly(??-benzyl-L-aspartate) copolymer micelles: Their pharmaceutical characteristics and biological significance," *Journal of Controlled Release,* vol. 64, pp. 143-153, 03/01 2000.

[317] R. K. Subedi, K. W. Kang, and H.-K. Choi, "Preparation and characterization of solid lipid nanoparticles loaded with doxorubicin," *European Journal of Pharmaceutical Sciences,* vol. 37, no. 3, pp. 508-513, 2009/06/28/ 2009.

[318] H. Bao *et al.*, *Chitosan-Functionalized Graphene Oxide as a Nanocarrier for Drug and Gene Delivery*. 2011, pp. 1569-78.

[319] V. Rana *et al.*, "Synthesis and Drug-Delivery Behavior of Chitosan-Functionalized Graphene Oxide Hybrid Nanosheets," *Macromolecular Materials and Engineering,* vol. 296, pp. 131-140, 02/14 2011.

[320] Y. Wang, Z. Li, J. Wang, J. Li, and Y. Lin, "Graphene and graphene oxide: biofunctionalization and applications in biotechnology," (in eng), *Trends in biotechnology,* vol. 29, no. 5, pp. 205-212, 2011.

[321] X. Yang, X. Zhang, Z. Liu, Y. Ma, Y. Huang, and Y. Chen, "High-Efficiency Loading and Controlled Release of Doxorubicin Hydrochloride on Graphene Oxide," *Journal of Physical Chemistry C - J PHYS CHEM C,* vol. 112, 11/13 2008.

[322] D. Depan, S. Js, and R. D. K. Misra, "Controlled release of drug from folate-decorated and graphene mediated drug delivery system: Synthesis, loading efficiency, and drug release response," *Materials Science and Engineering: C,* vol. 31, pp. 1305-1312, 10/01 2011.

[323] X. Pei *et al.*, "PEGylated nano-graphene oxide as a nanocarrier for delivering mixed anticancer drugs to improve anticancer activity," (in eng), *Scientific reports,* vol. 10, no. 1, pp. 2717-2717, 2020.
[324] D. Ayodhya, M. Venkatesham, A. Santoshi kumari, G. Bhagavanth Reddy, and G. Veerabhadram, "One-pot sonochemical synthesis of CdS nanoparticles: photocatalytic and electrical properties," *International Journal of Industrial Chemistry,* vol. 6, no. 4, pp. 261-271, 2015/11/01 2015.
[325] B. B. Ivanova, "IR-LD spectroscopic characterization of l-Tryptophan containing dipeptides," *Spectrochimica Acta Part A: Molecular and Biomolecular Spectroscopy,* vol. 64, no. 4, pp. 931-938, 2006/07/01/ 2006.
[326] I. J. Macha *et al.*, "Drug Delivery From Polymer-Based Nanopharmaceuticals—An Experimental Study Complemented by Simulations of Selected Diffusion Processes," (in English), *Frontiers in Bioengineering and Biotechnology,* Original Research vol. 7, no. 37, 2019-March-08 2019.
[327] T. Murakami, K. Ajima, J. Miyawaki, M. Yudasaka, S. Iijima, and K. Shiba, "Drug-Loaded Carbon Nanohorns: Adsorption and Release of Dexamethasone in Vitro," *Molecular Pharmaceutics,* vol. 1, no. 6, pp. 399-405, 2004/11/01 2004.
[328] A. Choucair, P. Lim Soo, and A. Eisenberg, "Active Loading and Tunable Release of Doxorubicin from Block Copolymer Vesicles," *Langmuir,* vol. 21, no. 20, pp. 9308-9313, 2005/09/01 2005.
[329] R. S. Langer and N. A. Peppas, "Present and future applications of biomaterials in controlled drug delivery systems," *Biomaterials,* vol. 2, no. 4, pp. 201-214, 1981/10/01/ 1981.
[330] J. S. Vrentas, C. M. Jarzebski, and J. L. Duda, "A Deborah number for diffusion in polymer-solvent systems," *AIChE Journal,* vol. 21, no. 5, pp. 894-901, 1975.
[331] X. Z. Shu and K. J. Zhu, "Controlled drug release properties of ionically cross-linked chitosan beads: the influence of anion structure," *International Journal of Pharmaceutics,* vol. 233, no. 1, pp. 217-225, 2002/02/21/ 2002.
[332] T. A. Hilder and J. M. Hill, "Modeling the Loading and Unloading of Drugs into Nanotubes," *Small,* vol. 5, no. 3, pp. 300-308, 2009.
[333] Z. Liu, X. Sun, N. Nakayama-Ratchford, and H. Dai, "Supramolecular Chemistry on Water-Soluble Carbon Nanotubes for Drug Loading and Delivery," *ACS Nano,* vol. 1, no. 1, pp. 50-56, 2007/08/01 2007.
[334] C. Wang *et al.*, "Enhancing Cell Nucleus Accumulation and DNA Cleavage Activity of Anti-Cancer Drug via Graphene Quantum Dots," *Scientific Reports,* vol. 3, no. 1, p. 2852, 2013/10/04 2013.
[335] X. Yang *et al.*, "Multi-functionalized graphene oxide based anticancer drug-carrier with dual-targeting function and pH-sensitivity," *Journal of Materials Chemistry,* 10.1039/C0JM02494E vol. 21, no. 10, pp. 3448-3454, 2011.
[336] G. Jiao *et al.*, "Limitations of MTT and CCK-8 assay for evaluation of graphene cytotoxicity," *RSC Advances,* 10.1039/C5RA08958A vol. 5, no. 66, pp. 53240-53244, 2015.
[337] D. Li, M. B. Müller, S. Gilje, R. B. Kaner, and G. G. Wallace, "Processable aqueous dispersions of graphene nanosheets," *Nature Nanotechnology,* vol. 3, no. 2, pp. 101-105, 2008/02/01 2008.
[338] A. Gopal, "A Simple Approach to Stepwise Synthesis of Graphene Oxide Nanomaterial," *Journal of Nanomedicine & Nanotechnology,* vol. 6, p. 1000253, 01/01 2015.
[339] A. M. Dimiev and T. A. Polson, "Contesting the two-component structural model of graphene oxide and reexamining the chemistry of graphene oxide in basic media," *Carbon,* vol. 93, pp. 544-554, 2015/11/01/ 2015.
[340] K. P. Loh, Q. Bao, G. Eda, and M. Chhowalla, "Graphene oxide as a chemically tunable platform for optical applications," *Nature Chemistry,* vol. 2, no. 12, pp. 1015-1024, 2010/12/01 2010.

[341] H. R. Thomas, C. Vallés, R. J. Young, I. A. Kinloch, N. R. Wilson, and J. P. Rourke, "Identifying the fluorescence of graphene oxide," *Journal of Materials Chemistry C,* 10.1039/C2TC00234E vol. 1, no. 2, pp. 338-342, 2013.

[342] S. H. Dave, C. Gong, A. W. Robertson, J. H. Warner, and J. C. Grossman, "Chemistry and Structure of Graphene Oxide via Direct Imaging," *ACS Nano,* vol. 10, no. 8, pp. 7515-7522, 2016/08/23 2016.

[343] C.-T. Chien *et al.*, "Tunable Photoluminescence from Graphene Oxide," *Angewandte Chemie International Edition,* vol. 51, no. 27, pp. 6662-6666, 2012.

[344] Z. Luo, P. M. Vora, E. J. Mele, A. T. C. Johnson, and J. M. Kikkawa, "Photoluminescence and band gap modulation in graphene oxide," *Applied Physics Letters,* vol. 94, no. 11, p. 111909, 2009.

[345] J. Shang, L. Ma, J. Li, W. Ai, T. Yu, and G. G. Gurzadyan, "The Origin of Fluorescence from Graphene Oxide," *Scientific Reports,* vol. 2, no. 1, p. 792, 2012/11/09 2012.

[346] Z. Hamrang *et al.*, "Characterisation of Stress-Induced Aggregate Size Distributions and Morphological Changes of a Bi-Specific Antibody Using Orthogonal Techniques," *Journal of Pharmaceutical Sciences,* vol. 104, no. 8, pp. 2473-2481, 2015.

[347] Z. Xu, S. Wang, Y. Li, M. Wang, P. Shi, and X. Huang, "Covalent Functionalization of Graphene Oxide with Biocompatible Poly(ethylene glycol) for Delivery of Paclitaxel," *ACS Applied Materials & Interfaces,* vol. 6, no. 19, pp. 17268-17276, 2014/10/08 2014.

[348] M. Xu *et al.*, "Improved In Vitro and In Vivo Biocompatibility of Graphene Oxide through Surface Modification: Poly(Acrylic Acid)-Functionalization is Superior to PEGylation," *ACS Nano,* vol. 10, no. 3, pp. 3267-3281, 2016/03/22 2016.

[349] X. Tan *et al.*, "Functionalization of Graphene Oxide Generates a Unique Interface for Selective Serum Protein Interactions," *ACS Applied Materials & Interfaces,* vol. 5, no. 4, pp. 1370-1377, 2013/02/27 2013.

[350] K. Yang, L. Feng, H. Hong, W. Cai, and Z. Liu, "Preparation and functionalization of graphene nanocomposites for biomedical applications," (in eng), *Nat Protoc,* vol. 8, no. 12, pp. 2392-403, Dec 2013.

[351] K. Yang, L. Feng, H. Hong, W. Cai, and Z. Liu, "Preparation and functionalization of graphene nanocomposites for biomedical applications," (in eng), *Nature protocols,* vol. 8, no. 12, pp. 2392-2403, 2013.

[352] X. Cao *et al.*, "Functionalized Graphene Oxide with Hepatocyte Targeting as Anti-Tumor Drug and Gene Intracellular Transporters," *Journal of Nanoscience and Nanotechnology,* vol. 15, no. 3, pp. 2052-2059, // 2015.

[353] R. Imani, S. H. Emami, and S. Faghihi, "Nano-graphene oxide carboxylation for efficient bioconjugation applications: a quantitative optimization approach," *Journal of Nanoparticle Research,* journal article vol. 17, no. 2, p. 88, February 13 2015.

[354] R. Imani, S. H. Emami, and S. Faghihi, "Synthesis and characterization of an octaarginine functionalized graphene oxide nano-carrier for gene delivery applications," *Physical Chemistry Chemical Physics,* 10.1039/C4CP04301D vol. 17, no. 9, pp. 6328-6339, 2015.

[355] T. Lammel, P. Boisseaux, M.-L. Fernández-Cruz, and J. M. Navas, "Internalization and cytotoxicity of graphene oxide and carboxyl graphene nanoplatelets in the human hepatocellular carcinoma cell line Hep G2," (in eng), *Particle and fibre toxicology,* vol. 10, pp. 27-27, 2013.

[356] S. Sinha Ray, "4 - Techniques for characterizing the structure and properties of polymer nanocomposites," in *Environmentally Friendly Polymer Nanocomposites*, S. Sinha Ray, Ed.: Woodhead Publishing, 2013, pp. 74-88.

[357] J. H. Warner, F. Schäffel, A. Bachmatiuk, and M. H. Rümmeli, "Chapter 5 - Characterisation Techniques," in *Graphene*, J. H. Warner, F. Schäffel, A. Bachmatiuk, and M. H. Rümmeli, Eds.: Elsevier, 2013, pp. 229-332.

[358] A. Kröner and T. Hirsch, "Current Trends in the Optical Characterization of Two-Dimensional Carbon Nanomaterials," (in eng), *Frontiers in chemistry,* vol. 7, pp. 927-927, 2020.
[359] M. J. Feito *et al.*, "In vitro evaluation of graphene oxide nanosheets on immune function," *Journal of Colloid and Interface Science,* vol. 432, pp. 221-228, 2014/10/15/ 2014.
[360] P. Eaton *et al.*, "A direct comparison of experimental methods to measure dimensions of synthetic nanoparticles," *Ultramicroscopy,* vol. 182, pp. 179-190, 2017/11/01/ 2017.
[361] M. Wang *et al.*, "The dispersion and aggregation of graphene oxide in aqueous media," *Nanoscale,* 10.1039/C6NR03503E vol. 8, no. 30, pp. 14587-14592, 2016.
[362] Z. Hua, Z. Tang, X. Bai, J. Zhang, L. Yu, and H. Cheng, "Aggregation and resuspension of graphene oxide in simulated natural surface aquatic environments," *Environmental Pollution,* vol. 205, pp. 161-169, 2015/10/01/ 2015.
[363] B. J. Hong, O. C. Compton, Z. An, I. Eryazici, and S. T. Nguyen, "Successful stabilization of graphene oxide in electrolyte solutions: enhancement of biofunctionalization and cellular uptake," (in eng), *ACS nano,* vol. 6, no. 1, pp. 63-73, 2012.
[364] Z. Hamrang *et al.*, "Characterisation of Stress-Induced Aggregate Size Distributions and Morphological Changes of a Bi-Specific Antibody Using Orthogonal Techniques," (in eng), *J Pharm Sci,* vol. 104, no. 8, pp. 2473-81, Aug 2015.
[365] A. Hawe, D. Weinbuch, S. Zölls, A. Reichel, and J. F. Carpenter, "Chapter 10 - Submicrometer, micrometer and visible particle analysis in biopharmaceutical research and development," in *Biophysical Characterization of Proteins in Developing Biopharmaceuticals (Second Edition)*, D. J. Houde and S. A. Berkowitz, Eds.: Elsevier, 2020, pp. 285-310.
[366] T. Szabo, P. Maroni, and I. Szilagyi, "Size-dependent aggregation of graphene oxide," *Carbon,* vol. 160, pp. 145-155, 2020/04/30/ 2020.
[367] Y. Li *et al.*, "Surface Coating-Dependent Cytotoxicity and Degradation of Graphene Derivatives: Towards the Design of Non-Toxic, Degradable Nano-Graphene," *Small,* vol. 10, no. 8, pp. 1544-1554, 2014.
[368] A. Chandra, S. Deshpande, D. B. Shinde, V. K. Pillai, and N. Singh, "Mitigating the Cytotoxicity of Graphene Quantum Dots and Enhancing Their Applications in Bioimaging and Drug Delivery," *ACS Macro Letters,* vol. 3, no. 10, pp. 1064-1068, 2014/10/21 2014.
[369] L. Feng, K. Li, X. Shi, M. Gao, J. Liu, and Z. Liu, "Smart pH-Responsive Nanocarriers Based on Nano-Graphene Oxide for Combined Chemo- and Photothermal Therapy Overcoming Drug Resistance," *Advanced Healthcare Materials,* vol. 3, no. 8, pp. 1261-1271, 2014.
[370] T. L. Moore, R. Podilakrishna, A. Rao, and F. Alexis, "Systemic Administration of Polymer-Coated Nano-Graphene to Deliver Drugs to Glioblastoma," *Particle & Particle Systems Characterization,* vol. 31, no. 8, pp. 886-894, 2014.
[371] Sudesh, N. Kumar, S. Das, C. Bernhard, and G. D. Varma, "Effect of graphene oxide doping on superconducting properties of bulk MgB2," *Superconductor Science and Technology,* vol. 26, no. 9, p. 095008, 2013/07/29 2013.
[372] C. Wang *et al.*, "Graphene oxide stabilized polyethylene glycol for heat storage," *Physical Chemistry Chemical Physics,* 10.1039/C2CP41988B vol. 14, no. 38, pp. 13233-13238, 2012.
[373] S. Fujime and K. Kubota, "Dynamic light scattering from dilute suspensions of thin discs and thin rods as limiting forms of cylinder, ellipsoid and ellipsoidal shell of revolution," *Biophysical Chemistry,* vol. 23, no. 1, pp. 1-13, 1985/11/01/ 1985.
[374] K. Kubota, Y. Tominaga, S. Fujime, J. Otomo, and A. Ikegami, "Dynamic light scattering study of suspensions of purple membrane," *Biophysical Chemistry,* vol. 23, no. 1, pp. 15-29, 1985/11/01/ 1985.
[375] X. Wen *et al.*, "Cation-induced coagulation in graphene oxide suspensions," *Materials Today Chemistry,* vol. 13, pp. 139-146, 2019/09/01/ 2019.
[376] C. K. Chua, A. Ambrosi, and M. Pumera, "Graphene oxide reduction by standard industrial reducing agent: thiourea dioxide," *Journal of Materials Chemistry,* 10.1039/C2JM16054D vol. 22, no. 22, pp. 11054-11061, 2012.

[377] M. Chu *et al.*, "Biocompatible polyethylenimine-graft-dextran catiomer for highly efficient gene delivery assisted by a nuclear targeting ligand," *Polymer Chemistry,* 10.1039/C3PY21092H vol. 4, no. 8, pp. 2528-2539, 2013.
[378] D. Williams and C. Carter, *Transmission Electron Microscopy: A Textbook for Materials Science*. 2009.
[379] Z. Zhang, H. C. Schniepp, and D. H. Adamson, "Characterization of graphene oxide: Variations in reported approaches," *Carbon,* vol. 154, pp. 510-521, 2019/12/01/ 2019.
[380] R. S. Pantelic, J. C. Meyer, U. Kaiser, and H. Stahlberg, "The application of graphene as a sample support in transmission electron microscopy," *Solid State Communications,* vol. 152, no. 15, pp. 1375-1382, 2012/08/01/ 2012.
[381] J. Russier *et al.*, "Evidencing the mask effect of graphene oxide: a comparative study on primary human and murine phagocytic cells," *Nanoscale,* 10.1039/C3NR03543C vol. 5, no. 22, pp. 11234-11247, 2013.
[382] S. K. Singh *et al.*, "Thrombus Inducing Property of Atomically Thin Graphene Oxide Sheets," *ACS Nano,* vol. 5, no. 6, pp. 4987-4996, 2011/06/28 2011.
[383] P. Turner, M. Hodnett, R. Dorey, and J. D. Carey, "Controlled Sonication as a Route to in-situ Graphene Flake Size Control," *Scientific Reports,* vol. 9, no. 1, p. 8710, 2019/06/18 2019.
[384] A. V. Tyurnina *et al.*, "Ultrasonic exfoliation of graphene in water: A key parameter study," *Carbon,* vol. 168, pp. 737-747, 2020/10/30/ 2020.
[385] S. Park and R. S. Ruoff, "Chemical methods for the production of graphenes," *Nature Nanotechnology,* vol. 4, no. 4, pp. 217-224, 2009/04/01 2009.
[386] V. Georgakilas *et al.*, "Graphene nanobuds: Synthesis and selective organic derivatisation," *Carbon,* vol. 110, pp. 51-55, 2016/12/01/ 2016.

# 8.Appendix

**Table 8. 1-** Summary of systems simulated by MD.

| System | Box size (Å$^3$) | Total number of atoms |
|---|---|---|
| **G(Trp)$_1$** | 43 × 44 × 34 | 4,551 |
| **G(Trp)$_6$** | 56 × 68 × 53 | 16,035 |
| **G(Trp)$_{12}$** | 68 × 68 × 63 | 21,519 |
| **G(Trp)$_{24}$** | 81 × 77 × 79 | 40,887 |
| **G(Tyr)$_1$** | 44 × 34 × 43 | 4,593 |
| **G(Tyr)$_6$** | 53 × 59 × 66 | 15,567 |
| **G(Tyr)$_{12}$** | 57 × 63 × 60 | 17,304 |
| **G(Tyr)$_{24}$** | 72 × 76 × 73 | 32,916 |
| **G(Val)$_1$** | 43 × 29 × 44 | 4,245 |
| **G(Val)$_6$** | 53 × 65 × 54 | 14,769 |
| **G(Val)$_{12}$** | 58 × 65 × 57 | 17,568 |
| **G(Val)$_{24}$** | 59 × 74 × 63 | 21,915 |

**Table 8. 2-** Average per amino acid interaction energy, ΔE, and its dispersion energy component, $\Delta E_{disp}$ , of pristine graphene, computed at the PM7 and ω B97XB97X-D/def2-SVP levels of theory in the gas phase. All energies in kcal/mol.

| | DFT | | PM7 | |
|---|---|---|---|---|
| **System** | **ΔE** | **$\Delta E_{disp}$** | **ΔE** | **$\Delta E_{disp}$** |
| **G(Trp)$_1$** | -26.2 ± 1.7 | -22.3 ± 1.7 | -30.5 ± 1.3 | -27.6 ± 0.9 |
| **G(Trp)$_6$** | -21.2 ± 1.7 | -19.2 ± 2.9 | -24.5 ± 1.5 | -22.6 ± 0.1 |
| **G(Tyr)$_1$** | -21.2 ± 2.6 | -17.8 ± 2.3 | -24.5 ± 2.8 | -22.5 ± 1.6 |
| **G(Tyr)$_6$** | -15.8 ± 2.7 | -24.0 ± 2.9 | -18.6 ± 2.0 | -16.3 ± 2.8 |
| **G(Val)$_1$** | -8.7 ± 5.8 | -5.7 ± 1.4 | -11.0 ± 1.3 | -8.7 ± 4.1 |
| **G(Val)$_6$** | -7.6 ± 0.9 | -7.0 ± 0.7 | -10.0 ± 0.2 | -8.4 ± 1.8 |

**Table 8. 3**-Average distance of amino acid groups from graphene surface (in Å), from MD simulation of G(X)$_n$ for X = Trp, Tyr and Val. Block average errors in parentheses. Average angle $\Theta$ (in degrees) between graphene plane normal and side-chain vector of amino acid (see Methods for definition), from MD trajectory.

| **System** | **Sidechain** | **$CO_2$** | **$NH_3$** | **Θ** |
|---|---|---|---|---|
| **G(Trp)$_n$** | 4.5 (0.0) | 6.9 (0.1) | 6.8 (0.0) | 89.8 (0.4) |
| **G(Tyr)$_n$** | 4.5 (0.1) | 6.6 (0.3) | 6.5 (0.0) | 108.7 (32.1) |
| **G(Val)$_n$** | 4.6 (0.1) | 5.8 (0.1) | 6.1 (0.2) | 86.4 (10.2) |

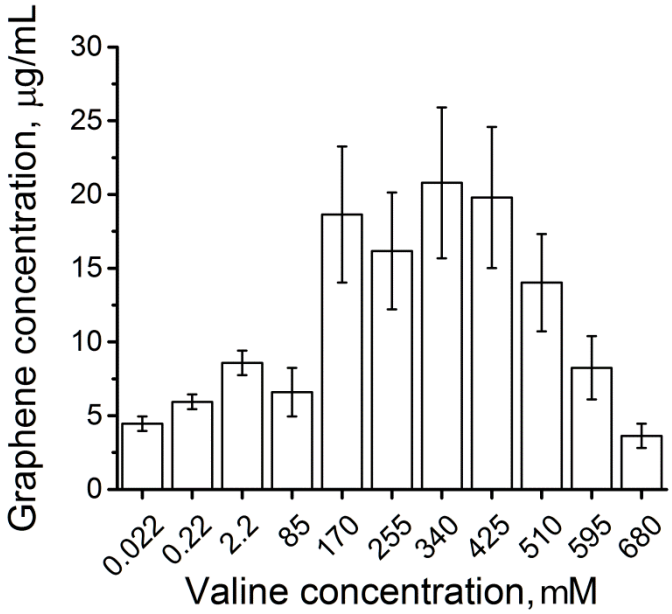


**Figure 8. 1**- Concentrations of graphene prepared from graphite exfoliated in Val solutions in water. These results were obtained using UV-vis absorption spectroscopy at wavelength of 750 nm. Error bars indicate the standard deviation of triplicate measurements of different samples.

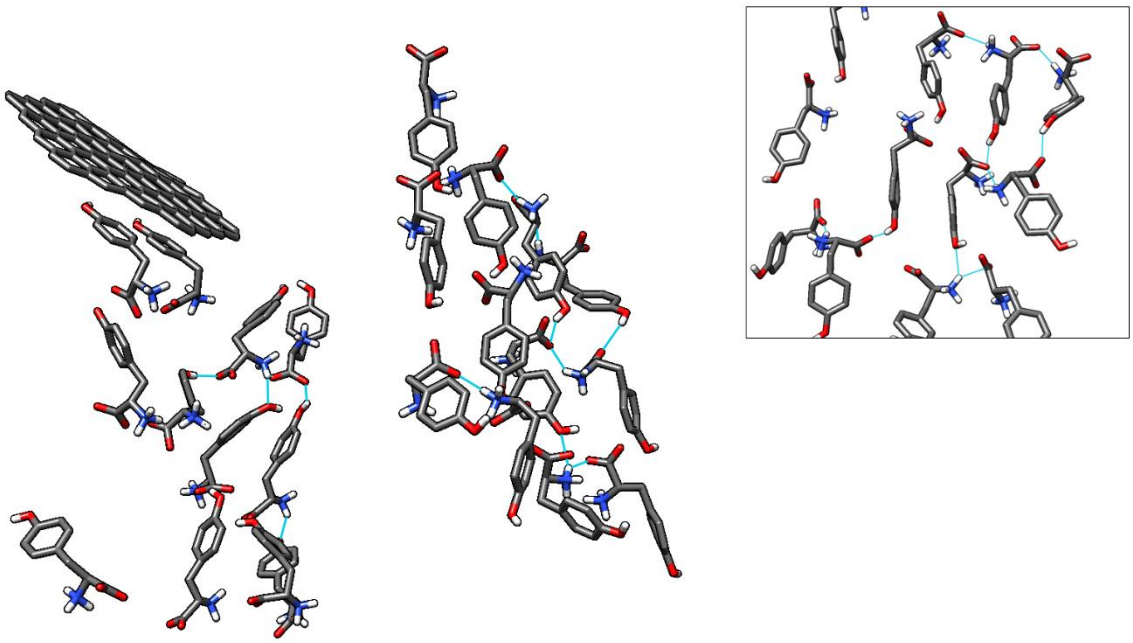

**Figure 8. 2-** Snapshots showing inter-molecular hydrogen bonding via the phenol OH group of its sidechain.

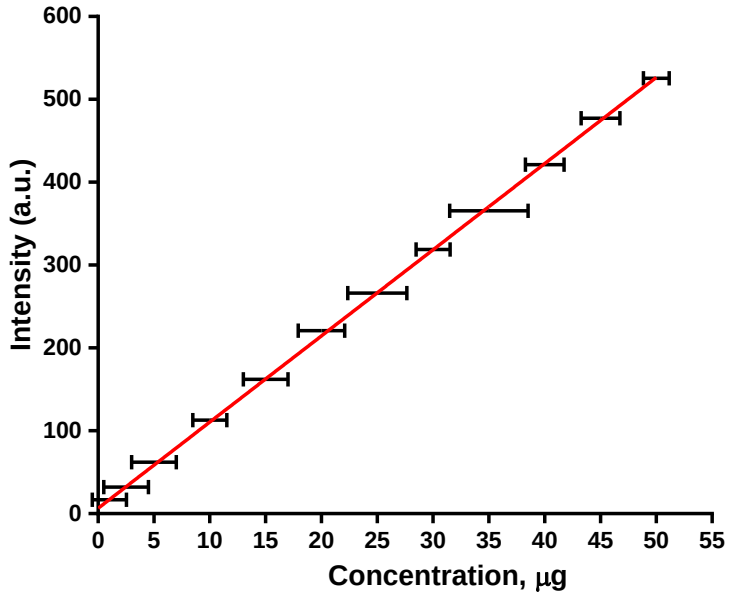


**Figure 8. 3**- The standard calibration curve of Dox in PBS at pH 5.4 using fluorescence spectrophotometer at excitation and emission wavelengths of 470 nm and 600 nm for Dox.

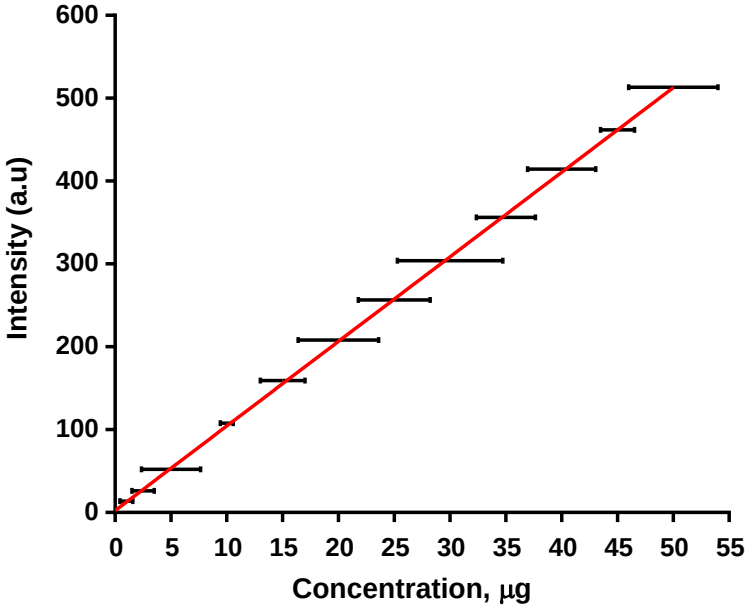


**Figure 8. 4**- The standard calibration curve of Dox in PBS at pH 7.4 using fluorescence spectrophotometer at excitation and emission wavelengths of 470 nm and 600 nm for Dox.

**Table 8. 4-** Raman spectra of PG, PG–Trp, PG–Trp2 and PG–Trp3.

| Sample | G band | | D band | | 2D band | | $I_{2D}/I_G$ |
|---|---|---|---|---|---|---|---|
| | **Peak position ($cm^{-1}$)** | **Intensity** | **Peak position ($cm^{-1}$)** | **Intensity** | **Peak position ($cm^{-1}$)** | **Intensity** | |
| **PG** | **1581.1** | 20,121.7 | **1333.8** | 8907.5 | **2688.1** | 14,702.8 | 0.7 |
| **PG–Trp** | **1579.4** | 19,321.5 | **1333.8** | 8107.5 | **2688.1** | 16,815.4 | 0.8 |
| **PG–Trp$_2$** | **1576.0** | 10,321.7 | **1333.8** | 5107.5 | **2678.1** | 18,902.2 | 1.8 |
| **PG–Trp$_3$** | **1589.7** | 8321.1 | **1335.6** | 3082.9 | **2675.1** | 20,149.8 | 2.4 |